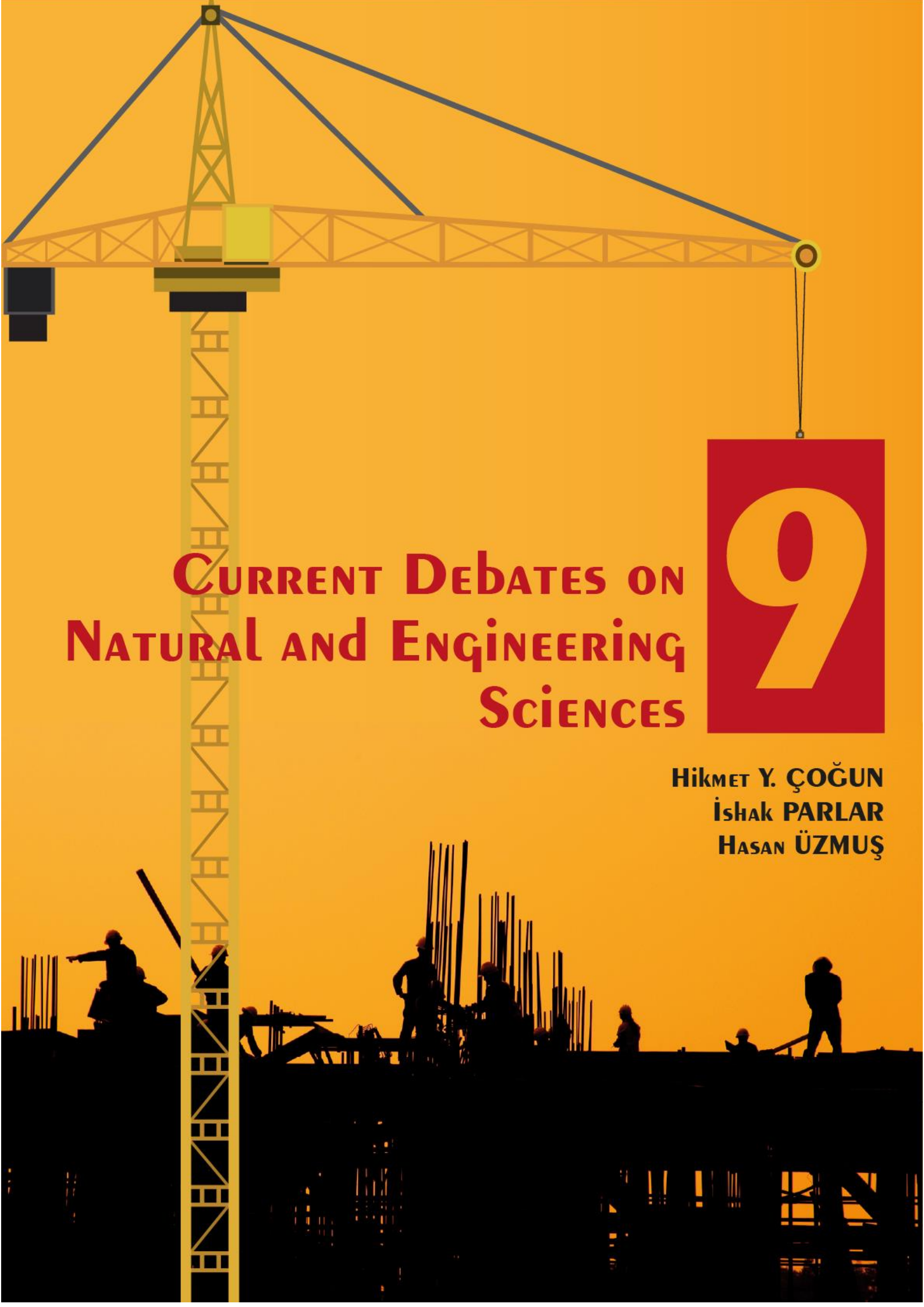

Current Debates on Natural and Engineering Sciences

9

Hikmet Y. ÇOĞUN
İshak PARLAR
Hasan ÜZMUŞ

ISBN:

1st Edition

25 Haziran 2023

Current Debates on Natural and Engineering Sciences 9

Editors

Hikmet Y. ÇOĞUN

İshak PARLAR

Hasan ÜZMUŞ

Publisher
Engin DEVREZ
Bilgin Kültür Sanat Yayınları
Certificate No: 20193
Selanik Cd. No: 68/10 06640 Kızılay / Ankara
Phone: 0 (312) 419 85 67 – Fax: 0 (312) 419 85 68
www.bilginkultursanat.com
bilginkultursanat@gmail.com

Contents

A Study on Third Order Rational Difference Equation

Mehmet Emre ERDOĞAN

Introduction

It is an interesting problem to find the asymptotic stability of positive solutions when approaching the equilibrium point for the difference equations. Real-life problems involving the difference equation are encountered in population biology, physics, financial and economic models, etc. The studies carried out to contribute to the theory of difference equations until today have focused on nonlinear difference equations. For example:

(Elsayed et al., 2017) investigated the global stability and the periodicity of the solutions of the recursive sequence

$$x_{n+1} = ax_n + bx_{n-1} + \frac{c + dx_{n-2}}{e + fx_{n-2}}.$$

(El-Dessoky & Al-Basyouni, 2019) deal with the global stability of the solutions, the boundedness and the periodic character of the nonlinear difference equation

$$x_{n+1} = \alpha x_n + \beta x_{n-l} + \gamma x_{n-k} + \frac{ax_n x_{n-k}}{bx_n + cx_{n-l} + dx_{n-k}}$$

(Elsayed & Alghamdi, 2019) studied the dynamics and stability behavior of the solutions of the second order nonlinear difference equation

$$x_{n+1} = ax_n + \frac{bx_n + cx_{n-1}}{d + ex_n x_{n-1}}$$

(Nirmaladevi & Karthikeyan, 2017) discussed about the periodicity of the difference equation

$$y_{n+1} = Py_n + Qy_{n-k} + Ry_{n-l} + \frac{by_{n-k}}{dy_{n-k} - ey_{n-l}}$$

(El-Moneam & Zayed, 2014) studied the boundedness and the global stability of the positive solutions of the following nonlinear difference equation

$$x_{n+1} = Ax_n + Bx_{n-k} + Cx_{n-l} + \frac{bx_n x_{n-k} x_{n-l}}{dx_{n-k} - ex_{n-l}}$$

(Elsayed & Gafel, 2022) investigated the behavior of the solutions of the following rational difference equation

$$x_{n+1} = ax_n + bx_{n-1} + \frac{cx_n + dx_{n-1}}{e + fx_{n-1}}$$

For other related studies on the subject, see (Khaliq et al., 2022) (Erdogan, 2020).

In this study, our aim is to examine the global asymptotic stability of the solutions of the nonlinear difference equation

$$x_{n+1} = \alpha x_{n-1} + \beta x_{n-2} + \frac{\gamma x_{n-1} + \theta x_{n-2}}{\phi + \varphi x_{n-1}} \tag{1}$$

where the initial conditions x_{-2}, x_{-1} and x_0 are positive real numbers and $\alpha, \beta, \gamma, \theta, \phi$ and φ are positive real numbers

Let us give some definitions and theorems that we need.

Definition 1. (Camouzis & Ladas, 2007) Let I be some interval of real numbers and let

$$f : I^3 \to I$$

be a continuously differentiable function.

Then for every set of initial conditions $x_0, x_{-1}, x_{-2} \in I$, the difference equation

$$x_{n+1} = f(x_n, x_{n-1}, x_{n-2}), \ n = 0,1,\ldots \tag{2}$$

has a unique solution $\{x_n\}_{n=-2}^{\infty}$.

A point $\bar{x} \in I$ is called an equilibrium point of (2) if

$$\bar{x} = f(\bar{x}, \bar{x}, \bar{x});$$

that is,

$$x_n = \bar{x} \text{ for } n \geq 0$$

is a solution of Eq.(2), or equivalently, $\bar{x}$ is a fixed point of f.

Definition 2. (Camouzis & Ladas, 2007) Let $\bar{x}$ be an equilibrium point of Eq.(2).

(i) The equilibrium $\bar{x}$ of Eq.(2) is called locally stable if for every $\grave{o} > 0$, there exists $\delta > 0$ such that for all $x_0, x_{-1}, x_{-2} \in I$ with $|x_0 - \bar{x}| + |x_{-1} - \bar{x}| + |x_{-2} - \bar{x}| < \delta$, we have

$$|x_n - \bar{x}| < \grave{o} \text{ for all } n \geq -2.$$

(ii) The equilibrium $\bar{x}$ of Eq.(2) is called locally asymptotically stable if it is locally stable, and if there exists $\gamma > 0$ such that for all $x_0, x_{-1}, x_{-2} \in I$ with $|x_0 - \bar{x}| + |x_{-1} - \bar{x}| + |x_{-2} - \bar{x}| < \gamma$, we have

$$\lim_{n\to\infty} x_n = \bar{x}.$$

(iii) The equilibrium $\bar{x}$ of Eq.(2) is called global attractor if for every $x_0, x_{-1}, x_{-2} \in I$ we have

$\lim_{n\to\infty} x_n = \bar{x}.$

(iv) The equilibrium $\bar{x}$ of Eq.(2) is called global asymptotically stable if it is locally stable and a global attractor.

(v) The equilibrium $\bar{x}$ of Eq.(2) is called unstable if it is not stable.

(vi) The equilibrium $\bar{x}$ of Eq.(2) is called source or a repeller, if there exists $r > 0$ such that for all $x_0, x_{-1}, x_{-2} \in I$ with $0 < |x_0 - \bar{x}| + |x_{-1} - \bar{x}| + |x_{-2} - \bar{x}| < r$, there exists $N \geq 1$ such that

$|x_N - \bar{x}| \geq r.$

The linearized equation of (2) about the equilibrium point $\bar{x}$ is

$$y_{n+1} = p_1 y_n + p_2 y_{n-1} + p_3 y_{n-2}, \quad n = 0,1,... \tag{3}$$

where

$$p_1 = \frac{\partial f}{\partial x_n}(\bar{x}, \bar{x}, \bar{x})$$
$$p_2 = \frac{\partial f}{\partial x_{n-1}}(\bar{x}, \bar{x}, \bar{x})$$
$$p_3 = \frac{\partial f}{\partial x_{n-2}}(\bar{x}, \bar{x}, \bar{x})$$

The characteristic equation of (3) is

$$\lambda^3 - p_1\lambda^2 - p_2\lambda - p_3 = 0 \tag{4}$$

Theorem 1. (Camouzis & Ladas, 2007) Assume that $p_i \in \square$, $i = 1,2,...$. Then

$$\sum_{i=1}^{3} |p_i| < 1,$$

is a sufficient condition for the asymptotic stability of (4)

Theorem 2. (Camouzis & Ladas, 2007) Let $[p,q]$ be an interval of real numbers and assume that $f : [p,q]^2 \to [p,q]$ is a continuous function satisfying the following properties:

(a) $f(x,y)$ is non-decreasing in $y \in [p,q]$ for each $x \in [p,q]$, and non-increasing in $x \in [p,q]$ for each $y \in [p,q]$;

(b) If $(m,M) \in [p,q] \times [p,q]$ is a solution of the system

$M = f(m,M)$ and $m = f(M,m)$

then $m = M$. Thus the difference equation has a unique equilibrium $\bar{x} \in [p,q]$ and every solution converges to $\bar{x}$.

Stability Analysis of Eq.(1)

In this section we investigate the stability of Equation (1) under the assumptions. The equilibrium points of Eq.(1) are obtained by

$$\overline{x} = \alpha\overline{x} + \beta x + \frac{\gamma\overline{x} + \theta\overline{x}}{\phi + \varphi\overline{x}},$$

so the equilibrium points of Eq.(1) are $\overline{x}_1 = 0$ and $\overline{x}_2 = \frac{\gamma+\theta}{\delta\varphi} - \frac{\phi}{\varphi}$ where $\delta = 1-\alpha-\beta \neq 0$. Also if $\gamma + \theta = \delta\phi$ then $\overline{x}_1 = 0$.

Let $f : (0,\infty)^2 \to (0,\infty)$ be a function defined by

$$f(u,v) = \alpha u + \beta v + \frac{\gamma u + \theta v}{\phi + \varphi u}.$$

Then

$$\frac{\partial f(u,v)}{\partial u} = \alpha + \frac{\gamma\phi - \varphi\theta v}{(\phi + \varphi u)^2},$$
$$\frac{\partial f(u,v)}{\partial v} = \beta + \frac{\theta}{\phi + \varphi v}$$

Theorem 3. The following statement are true.

i. If $\delta > 0$ and $\gamma + \theta < \phi\delta$, then equilibrium point $\overline{x}_1 = 0$ of Eq.(1) is locally asymptotically stable.

ii. If $\delta > 0$ and $\phi\delta < \gamma + \theta$ then the equilibrium point $\overline{x}_2 = \frac{\gamma+\theta}{\delta\varphi} - \frac{\phi}{\varphi}$ of Eq.(1) is locally asymptotically stable.

iii. If $\delta < 0$ then the equilibrium points of Eq. (1) are unstable.

Proof. The linearized equation of Eq.(1) about the equilibrium point $\overline{x}_1 = 0$ is

$$y_{n+1} = \left(\alpha + \frac{\gamma}{\phi}\right) y_{n-1} + \left(\beta + \frac{\theta}{\phi}\right) y_{n-2} \tag{5}$$

The characteristic equation of (5) is

$$\lambda^3 - \left(\alpha + \frac{\gamma}{\phi}\right)\lambda - \left(\beta + \frac{\theta}{\phi}\right) = 0$$

hence the proof of (i) follows Theorem 1.

For (ii),

The characteristic equation of Eq.(1) about the equilibrium point $\overline{x}_2 = \frac{\gamma+\theta}{\delta\varphi} - \frac{\phi}{\varphi}$ is

$$\lambda^3 - \left(\alpha + \frac{\delta(\phi\delta - \theta)}{\gamma + \theta}\right)\lambda - \left(\beta + \frac{\theta\delta}{\gamma + \theta}\right) = 0.$$

By the Theorem 1, Eq.(1) is asymptotically stable on $\bar{x}_2$ if $\left|\alpha + \frac{\delta(\phi\delta - \theta)}{\gamma + \theta}\right| + \left|\beta + \frac{\theta\delta}{\gamma + \theta}\right| < 1$. There are six cases about to consider.

Case (I) If $\delta > 0$ and $\phi\delta \geq \theta$, the inequality occurs as

$$\alpha + \frac{\delta(\phi\delta - \theta)}{\gamma + \theta} + \beta + \frac{\theta\delta}{\gamma + \theta} < 1$$

rearranging inequality we obtain

$$\phi\delta < \gamma + \theta.$$

Case (II) If $\delta > 0$ and $\alpha\frac{\gamma + \theta}{\delta} + \phi\delta > \theta > \phi\delta$, the inequality occurs as before

$$\alpha + \frac{\delta(\phi\delta - \theta)}{\gamma + \theta} + \beta + \frac{\theta\delta}{\gamma + \theta} < 1$$

so we find $\phi\delta < \gamma + \theta$ again.

Case (III) If $\delta > 0$ and $\theta > \alpha\frac{\gamma + \theta}{\delta} + \phi\delta$, the inequality occurs as

$$-\alpha - \frac{\delta(\phi\delta - \theta)}{\gamma + \theta} + \beta + \frac{\theta\delta}{\gamma + \theta} < 1.$$

This leads to

$$-2\alpha - \frac{\phi\delta^2 - 2\theta\delta}{\gamma + \theta} < 0 < \delta$$

Hence, the statement is a tautology.

Case (IV) If $\delta > 0$, $\theta = \alpha\frac{\gamma + \theta}{\delta} + \phi\delta$ and $\theta > \phi\delta$, the inequality occurs as

$$\beta + \frac{\theta\delta}{\gamma + \theta} < 1$$

which leads to $\gamma(\beta - 1) < \alpha\theta$. If we rewrite the inequality $\delta > 0$ will be

$$\begin{aligned} \delta &> 0 \\ 1 - \alpha - \beta &> 0 \\ 1 &> \alpha + \beta \\ 0 &> \alpha + \beta - 1 \\ 0 &> \beta - 1 \end{aligned}$$

so, $\gamma(\beta - 1) < 0 < \alpha\theta$ which is tautology.

Case (V) If $\delta < 0$ and $\beta + \frac{\theta\delta}{\gamma+\theta} > 0$, the inequality occurs as

$$\alpha + \frac{\delta(\phi\delta - \theta)}{\gamma+\theta} + \beta + \frac{\theta\delta}{\gamma+\theta} < 1$$

by rearranging inequality we conclude that $\phi\delta > \gamma + \theta$ which is contradiction to $\gamma + \theta > 0$ and $\phi\delta < 0$.

Case (VI) If $\delta < 0$ and $\beta + \frac{\theta\delta}{\gamma+\theta} < 0$, the inequality occurs as

$$\alpha + \frac{\delta(\phi\delta - \theta)}{\gamma+\theta} - \beta - \frac{\theta\delta}{\gamma+\theta} < 1$$
$$-2\beta(\gamma+\theta) + \delta(\phi\delta - \theta) < \delta$$

From $\beta + \frac{\theta\delta}{\gamma+\theta} < 0$, we can easily say that $\beta(\gamma+\theta) < -\theta\delta$. Thus,

$$2\theta\delta + \phi\delta^2 - 2\theta\delta < -2\beta(\gamma+\theta) + \delta(\phi\delta - 2\theta) < \delta$$
$$\phi\delta^2 < \delta$$

The inequality $\phi\delta^2 < \delta$ is contradiction to $\phi\delta^2 > 0$ and $\delta < 0$.

From Case (V) and Case(VI) δ should be positive. This completes the proof.

Theorem 4. If $(1+\alpha-\beta)\phi > \theta - \gamma$, then the equilibrium point $\bar{x}$ of Eq.(1) is global asymptotically stable

Proof. Let $M = f(m, M)$ and $m = f(M, m)$,

$$M = \alpha m + \beta M + \frac{\gamma m + \theta M}{\phi + \varphi m}$$
$$m = \alpha M + \beta m + \frac{\gamma M + \theta m}{\phi + \varphi M},$$

then

$$M(1-\beta)\phi + \varphi m M(1-\beta) = \alpha m\phi + \alpha\varphi m^2 + \gamma m + \theta M$$
$$m(1-\beta)\phi + \varphi m M(1-\beta) = \alpha M\phi + \alpha\varphi M^2 + \gamma M + \theta m$$

by substracting equations it gives,

$$(M-m)\left[(1-\beta)\phi + \alpha\phi + \alpha\varphi(M+m) + \gamma - \theta\right] = 0$$

since $(1+\alpha-\beta)\phi > \theta - \gamma$, then $M = m$. From Theorem 2 and Definition 2 the equilibrium point $\bar{x}$ of Eq.(1) is global asymptotically stable. Thus, the proof is completed.

Theorem 2.3. If $\gamma + \theta < \phi\delta$ then the solutions of Eq.(1) is bounded.

Proof. Let $\{x_n\}_{n=-2}^{\infty}$. be a solution of Eq.(1). Then

$$x_{n+1} = \alpha x_{n-1} + \beta x_{n-2} + \frac{\gamma x_{n-1} + \theta x_{n-2}}{\phi + \varphi x_{n-1}}$$
$$\leq \alpha x_{n-1} + \beta x_{n-2} + \frac{\gamma x_{n-1} + \theta x_{n-2}}{\phi}$$
$$\leq \left(\alpha + \frac{\gamma}{\phi}\right) x_{n-1} + \left(\beta + \frac{\theta}{\phi}\right) x_{n-2}$$

Let $\chi = \max\{x_{n-1}, x_{n-2}\}$. So,

$$x_{n+1} \leq \left(\alpha + \frac{\gamma}{\phi} + \beta + \frac{\theta}{\phi}\right)\chi$$

since $\gamma + \theta < \phi\delta$, the inequality holds the

$$\gamma + \theta < \phi(1 - \alpha - \beta)$$
$$\alpha + \beta + \frac{\gamma + \theta}{\phi} < 1.$$

which implies that $x_{n+1} < \max\{x_{n-1}, x_{n-2}\}$ for $n \geq 0$. Then

$$\lim_{n\to\infty} x_n = 0.$$

Thus the solutions of Eq. (1) are bounded. The proof is complete.

Computational Examples

Computational examples are provided in this section to show how the main results are valid. With the use of MATLAB, a graph of the solutions was created in order to better illustrate the numerical examples. These graphs are created using various starting conditions and parameter values.

- In Figure 1, the equilibrium point $\bar{x}_1$ of Eq. (1) is shown to be globally asymptotically stable under the initial conditions $x_{-2} = 3.456$, $x_{-1} = 7.879$, $x_0 = -4.57$ and the parameters $\alpha = 0.1$, $\beta = 0.2$, $\gamma = 2.24$, $\theta = 3.12$, $\phi = 9.65$ and $\varphi = 6.45$ that meet the condition $\gamma + \theta < \phi\delta$.

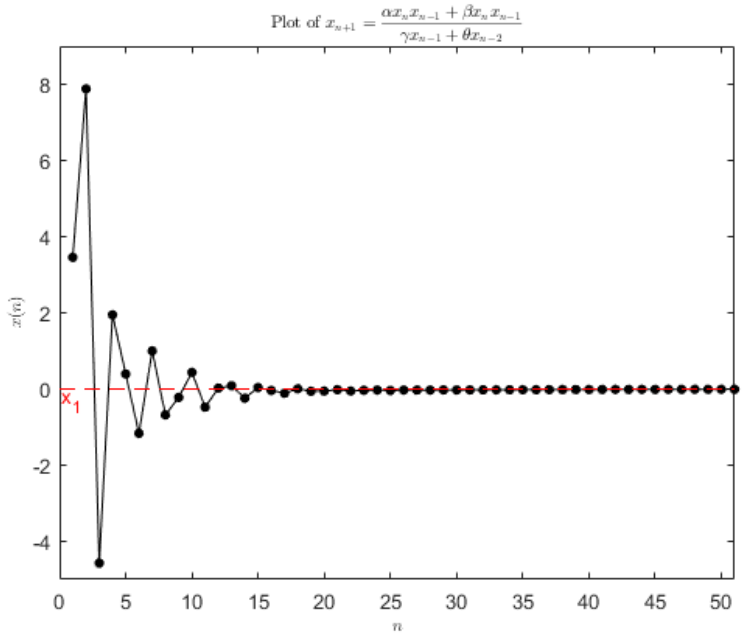

Figure 1: Stability of the solutions of Eq. (1) under the condition $\gamma + \theta < \phi\delta$.

- In Figure 2, the equilibrium point $\bar{x}_2$ of Eq. (1) is shown to be globally asymptotically stable under the initial conditions $x_{-2} = 3.456,\ x_{-1} = 7.879,\ x_0 = -4.57$ and the parameters $\alpha = 0.1,\ \beta = 0.2,\ \gamma = 5.24,\ \theta = 3.12,\ \phi = 2.65$ and $\varphi = 6.45$ that meet the condition $\gamma + \theta > \phi\delta$.

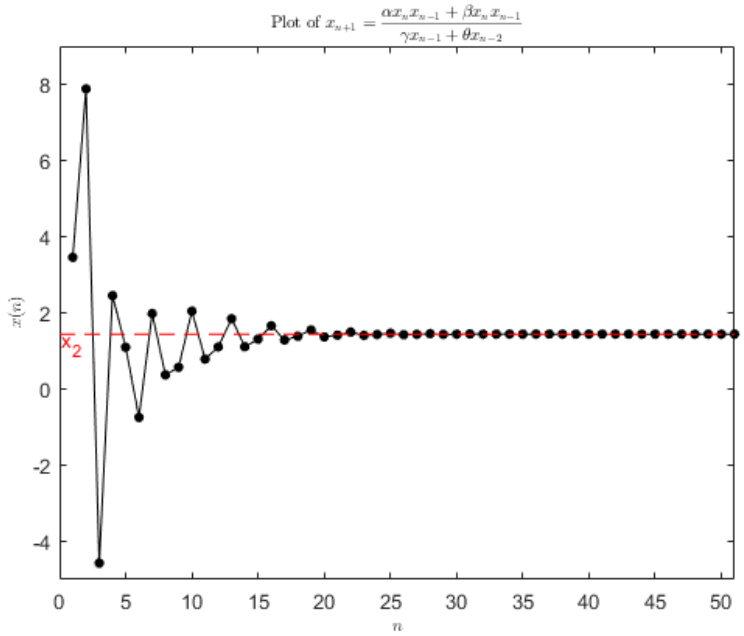

Figure 2: Stability of the solutions of Eq. (1) under the condition $\gamma + \theta > \phi\delta$.

- In Figure 3, Eq. (1) is shown to be unstable under the initial conditions $x_{-2} = 3.456,\ x_{-1} = 7.879,\ x_0 = -4.57$ and the parameters $\alpha = 0.8,\ \beta = 0.4,\ \gamma = 2.24,\ \theta = 3.12,\ \phi = 4.65$ and $\varphi = 2.45$ that meet the condition $\delta < 0$.

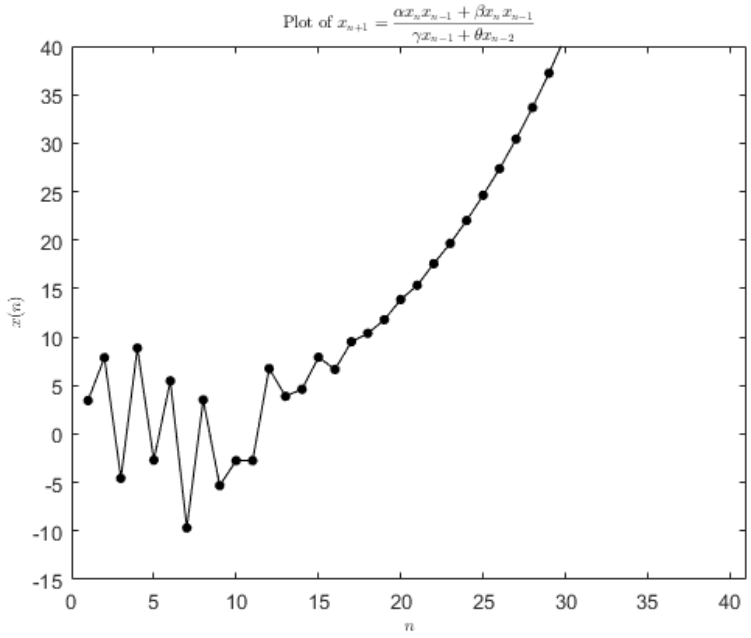

Figure 3: Unbounded solutions of Eq. (1) under the condition $\delta < 0$.

References

Camouzis, E., & Ladas, G. (2007). *Dynamics of Third-Order Rational Difference Equations with Open Problems and Conjectures.* New York: Chapman and Hall/CRC. https://doi.org/10.1201/9781584887669

El-Dessoky, M., & Al-Basyouni, K. S. (2019). On the Higher Order Difference Equation. *Journal of Computational Analysis and Applications, 27*(6), 1013-1022.

El-Moneam, M. A., & Zayed, E. M. (2014). Dynamics of the rational difference equation. *Dynamics of Continuous, Discrete and Impulsive Systems Series A: Mathematical Analysis, 21*, 317-331.

Elsayed, E. M., & Alghamdi, A. (2019). Qualitative behavior of a rational recursive sequence of second order. *Rocky Mountain Journal of Mathematics, 49*(7), 2135-2154. https://doi.org/10.1216/RMJ-2019-49-7-2135

Elsayed, E. M., & Gafel, H. S. (2022, 1 16). Dynamics And Global Stability Of Second Order Nonlinear Difference Equation. *Pan-American Journal of Mathematics, 1*, 1-16. https://doi.org/https://doi.org/10.28919/cpr-pajm/1-16

Elsayed, E. M., Alzahrani, F., & Alayachi, H. (2017, 23 7). Global Attractivity and the Periodic Nature of Third Order Rational Difference Equation. *Journal of Computational Analysis and Applications, 23*(7), 1230-1241.

Erdogan, M. E. (2020). Stability of the third order rational difference equation. *MANAS Journal of Engineering, 8*(1), 68-76.

Khaliq, A., Alam, M., & Hassan, S. (2022). Stability Chaos And Periodic Solution Of Delayed Rational Recursive. *Pan-American Journal of Mathematics, 1*, 1-15. https://doi.org/10.28919/cpr-pajm/1-15

Nirmaladevi, S., & Karthikeyan, N. (2017). Dynamics And Behavior Of Higher Order And Nonlinear Rational Difference Equation. *International Journal Of Advance Research And Innovative Ideas In Education, 3*(4), 2071-2079. https://doi.org/16.0415/IJARIIE-6261

Quantitative Analysis of the Effect of Quarantine on the Spread of COVID-19

Mehmet KOCABIYIK[1]
Mevlüde YAKIT ONGUN [2]

1.INTRODUCTION

COVID-19, short for coronavirus disease (2019), is caused by severe acute respiratory syndrome coronavirus 2 (SARS-CoV-2) (WHO,2019). The rate of spread of the virus is quite large. For this reason, its sphere of influence has expanded in a short time. Studies have been carried out to determine the dynamics of the virus. By determining the dynamics, it is aimed to intervene to reduce the spread of the virus. Mathematical models have been created for the virus spread system. Among these models, equations including the quarantine effect were also expressed.

Feng et al. (2020) examined the effects of COVID-19 on media and quarantine. Baleanu et al. (2020) took a new approach to the COVID-19 model and used the Caputo-Fabrizio derivative. They expressed the dynamics of the system of equations with the help of this derivative. Atangana (2020) created the system using novel fractal fractional derivatives. From this work, Atangana created the dynamics for the salvation of humanity before vaccination.

According to Babaei et al. (2021) developed the model system, which will be modified and used in this study. In their modeling, the authors used a type that includes quarantine data for COVID-19. The authors investigated the dynamics of this system using the Adams-Bashforth-Moulton predictor-corrector method for numerical simulations.

This model, which includes the quarantine factor from this study, has been expressed and modified with distributed order differential equations. The aim here is to use the density function of distributed order differential equations. It has been suggested to examine the different effects in a shorter time than the modeling right with the density function. Both ordinary order and fractional order differential equations can be expressed by the choice of density function. Thus, the dynamics of the system can be obtained easily with a single equation instead of several different equations.

Caputo defined distributed order differential equations in 1969 and conducted studies in 1995, including their areas of use. Afterwards, studies on this type of equations have increased due to the wide range of usage areas. Bagley and Torvik (2000) examined the solution of distributed order differential equations in their studies. Hartley and Lorenzo (2003) studied the definition of a fractional ordinal system based on continuous-order distributions.

In the early days, studies on numerical analysis were not seen in this type of equations. Recently, the increase in usage areas has led to the emergence of studies where these analyzes are also carried out. For some numerical studies and stability analysis, refer to the following resources; Diethelm and Ford (2009), Katsikadelis (2014), Li and Wu (2016), Aminikhah et al. (2013), Kocabıyık et al. (2021), Kocabıyık (2022), Kocabıyık and Ongun (2022) and Kocabıyık et al. (2022).

This study consists of four main sections. In the second section, basic definitions and concepts are given for fractional derivatives and distributed order differential equations. Also

[1] Res. Asst., Burdur Mehmet Akif Ersoy University, Department of Mathematics, Orcıd: 0000-0002- 7701-6946.
[2] Prof. Dr., Süleyman Demirel University, Department of Mathematics, Orcıd: 0000-0003-2363-9395.

in this section, the NSFD scheme and approximate Grünwald-Letnikov fractional derivative required for discretization are given. In the third section, the modified system has been discretized. Afterward, the numerical analyzes of the system are expressed with the help of graphics. In the fourth section, the conclusion part is included and the information about the obtained data is expressed.

2.BASIC DEFINITIONS AND CONCEPTS

Distributed order differential equations are a kind of general case of fractional order differential equations. For this reason, fractional differential equations are very important in terms of definition. In the first part of this chapter, different types of fractional derivatives are described. Then, with the help of these fractional derivatives, distributed order differential equations are expressed (Podlubny, 1999; Caputo, 2001).

In the second part of the chapter, the Nonstandard finite difference approach introduced by Mickens for discretization is expressed. Also in this section, the approximation method of the Grünwald-Letnikov derivative is defined for discretization (Dorciak, 1994; Mickens, 1989; Mickens, 1994; Meerschaert and Tadjeran, 2004).

2.1.Preliminary Information About Fractional Derivatives

Definition 2.1.1: (Podlubny, 1999) Let the function $h(t)$ be an integrable function in the interval $[u_1, u_2]$ with $k-1 < \alpha \leq k$ for $k \epsilon \mathbb{N}^+$. Riemann Liouville fractional derivative of order α is defined by

$$D_R^{\alpha} h(t) = \frac{1}{\Gamma(k-\alpha)} \frac{d^n}{dt^n} \int_{\alpha}^{t} \frac{h^{(k)}(v)}{(t-z)^{\alpha-k+1}} dv.$$

Definition 2.1.2: (Podlubny, 1999). Caputo fractional derivative of order α is given by

$$D_{CP}^{\alpha} h(t) = \frac{1}{\Gamma(k-\alpha)} \int_{\alpha}^{t} \frac{h^{(k)}(v)}{(t-z)^{\alpha-k+1}} dv,$$

where $\Gamma(.)$ is a Gamma function and h(t) is integrable function in the range $[u_1, u_2]\, with \;\; k \epsilon \mathbb{N}^+$ and $k-1 < \alpha \leq$ k.

Definition 2.1.3: (Podlubny, 1999) Suppose that the function $h^{(u)}$(t) is integrable function in the range $[u, t]$ and $u = 1,2,..,k+1-th$ times differentiable function. Grünwald-Letnikov fractional derivative of order α is described by

$$D_G^{\alpha} h(t) = \lim_{j \to 0} j^{-\alpha} \sum_{i=0}^{k} (-1)^i \binom{k}{i} h(t-ij).$$

Definition 2.1.4: (Caputo, 2001) The integral operator of distributed order differential equations is expressed as:

$$D_t^{d(\alpha)} h(t) = \int_{k_1}^{k_2} d(\alpha)\, D_t^{\alpha} h(t)\, d\alpha,$$

where $\alpha \epsilon (k_1, k_2)$, $\int_{k_1}^{k_2} d(\alpha) = m > 0$ and $d(\alpha)$ is as density function of distributed order differential equations. $D_t^{\alpha} h(t)$ expressed in the definition is the fractional derivative operator. So, the derivative operators above can be used here. It has been observed that different operators are used in different sources. In this study, the use of the Caputo derivative operator was preferred due to the existence of initial conditions. Distributed order derivatives are expressed as:

$$D_t^{d(\alpha)}h(t) = \sum_{i=1}^{n} \alpha^i \int_{k_1}^{k_2} d_i(\alpha)\, D_t^{i-\alpha}h(t)d\alpha + \sum_{j=0}^{n} b_j h^i(t).$$

Preliminary Information About Discretization

Definition 2.2.1: (Dorciak, 1994) Let $p_j^{\alpha} = \left(1 - \frac{1+\alpha}{j}\right) p_{j-1}^{\alpha},\ for\ j = 1,2,3, \dots,\ v = h^{-\alpha}$ and h is chosen quite small. The approximate Grünwald-Letnikov derivative formula for distributed order differential equations can be arranged as follows:

$$D_t^{\alpha}h(t) = \sum_{i=0}^{n} p_i^{\alpha} h(t_{n-r}),\quad n = 1,2,3, \dots.$$

Nonstandard finite difference (NSFD) schemes were described by Mickens. Its use for different systems of equations was also introduced by him. With this method, Mickens tried to eliminate instabilities. For this reason, he used the denominator function from his definition. It has been shown that indecisions can be removed by selecting the denominator function (Mickens, 1989; Mickens, 1994).

Definition 2.2.2: (Mickens, 1994) The NSFD scheme is defined as follows:

$$H(z) \to H(v_n),\quad v(t) \to v(t_n),\quad \frac{dv}{dt} \to \frac{v_{n+1} - v_n}{\eta}, t \to t_n,$$

where $\frac{dv}{dt} = H(\varphi, v)$ with $\varphi: parameter$ and η is a denominator function and it can be chosen as $\eta = \frac{1-e^{-ph}}{p}$.

The denominator function depends on the variable h, which is the step interval, and the variable p, which can be found with the equilibrium point, respectively. Thus, with these definitions and expressions, the NSFD scheme can be used in distributed order differential equations with the help of the Grünwald-Letnikov approximate derivative formula (Meerschaert and Tadjeran, 2004).

3.QUANTITATIVE ANALYSIS OF THE EFFECT OF QUARANTINE ON THE SPREAD OF COVID-19

The population in the equation system given in the study was expressed with seven different groups (Babaei et al., 2021):

S: People who are susceptible or exposed to the virus,

I: Infected individuals with symptoms,

N: Those who are infected with the virus but have no symptoms,

S^q: Susceptible individuals in quarantine,

Q: Infected individuals in quarantine,

H: Infected individuals in the hospital,

R: Individuals who have recovered.

The modified model of the effect of Quarantine on the Spread of COVID-19 model can be given as:

$$D_t^{u(\alpha)}S(t) = B - (cp_t\,(1-q)(1-\rho) + cp_t(1-q)\rho + cqp_t + (1-p_t)cq)\big(I(t) + t_r N(t)\big)S(t) + \lambda S^q(t) - dS(t),$$

$$D_t^{u(\alpha)}I(t) = p_t c\rho(1-q)S(t)\big(I(t) + t_r N(t)\big) - (t_1 + r_1 + a_1)I(t),$$

$$D_t^{u(\alpha)}N(t) = p_t c(1-q)(1-\rho)S(t)\big(I(t)+t_r N(t)\big) - (r_2+a_2)N(t),$$
$$D_t^{u(\alpha)}S^q(t) = (1-p_t)cqS(t)\big(I(t)+t_r N(t)\big) - (\lambda+d)S^q(t),$$
$$D_t^{u(\alpha)}Q(t) = p_t cqS(t)\big(I(t)+t_r N(t)\big) - (t_2+a_3)Q(t),$$
$$D_t^{u(\alpha)}H(t) = t_1 I(t) + t_2 Q(t) - (a_2+r_3)H(t),$$
$$D_t^{u(\alpha)}R(t) = r_1 I(t) + r_2 N(t) + r_3 H(t) - a_4 R(t),$$

where, B is the birth rate of the population. c is the contact ratio. t_r indicates the transmission rate and p_t indicates the transmission probability per contact. q indicates the rate at which susceptible individuals are quarantined. t_1 and t_2 represent the rates of passage of symptomatic infected individuals and quarantined susceptible individuals into the quarantined infected compartment, respectively. r_1, r_2, and r_3 are the recovery rates of infected persons with symptoms, infected persons without symptoms, and quarantined infected persons, respectively. d naturally denotes mortality rates. ρ is the probability of occurrence of symptoms among infected individuals.

λ indicates the rate at which quarantined uninfected persons are released into the community. a_1, a_2, a_3, and a_4 represent the rates at which virus was removed from compartments I, N, Q, and R.

If a nonstandard discretization scheme is applied to the modified distributed order model of the impact of quarantine on the spread of COVID-19, the discretized version is obtained as follows:

$$\sum_{i=1}^{l}\frac{u(\alpha_i)}{l}\sum_{j=0}^{n+1}p_j^{\alpha_i}S_{n+1-j} = B - A_1(I_n + t_r N_n)S_{n+1} + \lambda {S^q}_n - dS_{n+1},$$

$$\sum_{i=1}^{l}\frac{u(\alpha_i)}{l}\sum_{j=0}^{n+1}p_j^{\alpha_i}I_{n+1-j} = A_2(I_{n+1} + t_r N_n)S_n - (t_1+r_1+a_1)I_{n+1},$$

$$\sum_{i=1}^{l}\frac{u(\alpha_i)}{l}\sum_{j=0}^{n+1}p_j^{\alpha_i}N_{n+1-j} = A_3(I_n + t_r N_{n+1})S_n - (r_2+a_2)N_{n+1},$$

$$\sum_{i=1}^{l}\frac{u(\alpha_i)}{l}\sum_{j=0}^{n+1}p_j^{\alpha_i}{S^q}_{n+1-j} = A_4(I_n + t_r N_n)S_n - (\lambda+d){S^q}_{n+1},$$

$$\sum_{i=1}^{l}\frac{u(\alpha_i)}{l}\sum_{j=0}^{n+1}p_j^{\alpha_i}Q_{n+1-j} = A_5(I_n + t_r N_n)S_n - (t_2+a_3)Q_{n+1},$$

$$\sum_{i=1}^{l}\frac{u(\alpha_i)}{l}\sum_{j=0}^{n+1}p_j^{\alpha_i}H_{n+1-j} = t_1 I_n + t_2 Q_n - (a_2+r_3)H_{n+1},$$

$$\sum_{i=1}^{l}\frac{u(\alpha_i)}{l}\sum_{j=0}^{n+1}p_j^{\alpha_i}R_{n+1-j} = r_1 I_n + r_2 N_n + r_3 H_n - a_4 R_{n+1},$$

where A_1: $(cp_t\,(1-q)(1-\rho) + cp_t(1-q)\rho + cqp_t + (1-p_t)cq)$, A_2: $p_t c\rho(1-q)$, A_3: $p_t c(1-q)(1-\rho)$, A_4: $(1-p_t)cq$, and A_5: $p_t cq$.

The discretized system, with the Grünwald-Letnikov approximate derivative formula and the arrangement of the denominator functions described below, becomes as follows:

$$S_{n+1}\left(\sum_{i=1}^{l}\frac{u(\alpha_i)}{l}(\eta_1(h))^{-\alpha_i}+A_1(I_n+t_rN_n)+d\right)$$
$$=B+\lambda {S^q}_n-\sum_{i=1}^{l}\frac{u(\alpha_i)}{l}\left(\sum_{j=1}^{n+1}p_j^{\alpha_i}S_{n+1-j}\right),$$

$$I_{n+1}\left(\sum_{i=1}^{l}\frac{u(\alpha_i)}{l}(\eta_2(h))^{-\alpha_i}-A_2S_n+t_1+r_1+a_1\right)$$
$$=A_2t_rN_nS_n-\sum_{i=1}^{l}\frac{u(\alpha_i)}{l}\left(\sum_{j=1}^{n+1}p_j^{\alpha_i}I_{n+1-j}\right),$$

$$N_{n+1}\left(\sum_{i=1}^{l}\frac{u(\alpha_i)}{l}(\eta_3(h))^{-\alpha_i}+r_2+a_2+A_3t_rS_n\right)=A_3I_nS_n-\sum_{i=1}^{l}\frac{u(\alpha_i)}{l}\left(\sum_{j=1}^{n+1}p_j^{\alpha_i}N_{n+1-j}\right),$$

$${S^q}_{n+1}\left(\sum_{i=1}^{l}\frac{u(\alpha_i)}{l}(\eta_4(h))^{-\alpha_i}+\lambda+d\right)=A_4(I_n+t_rN_n)S_n-\sum_{i=1}^{l}\frac{u(\alpha_i)}{l}\left(\sum_{j=1}^{n+1}p_j^{\alpha_i}{S^q}_{n+1-j}\right),$$

$$Q_{n+1}\left(\sum_{i=1}^{l}\frac{u(\alpha_i)}{l}(\eta_5(h))^{-\alpha_i}+t_2+a_3\right)=A_5(I_n+t_rN_n)S_n-\sum_{i=1}^{l}\frac{u(\alpha_i)}{l}\left(\sum_{j=1}^{n+1}p_j^{\alpha_i}Q_{n+1-j}\right),$$

$$H_{n+1}\left(\sum_{i=1}^{l}\frac{u(\alpha_i)}{l}(\eta_6(h))^{-\alpha_i}+a_2+r_3\right)=t_1I_n+t_2Q_n-\sum_{i=1}^{l}\frac{u(\alpha_i)}{l}\left(\sum_{j=1}^{n+1}p_j^{\alpha_i}H_{n+1-j}\right),$$

$$R_{n+1}\left(\sum_{i=1}^{l}\frac{u(\alpha_i)}{l}(\eta_7(h))^{-\alpha_i}+a_4\right)=r_1I_n+r_2N_n+r_3H_n-\sum_{i=1}^{l}\frac{u(\alpha_i)}{l}\left(\sum_{j=1}^{n+1}p_j^{\alpha_i}R_{n+1-j}\right),$$

where, $i=1,\dots,7$ and $0<\alpha_i<1$, $p_0^{\alpha_i}=(\eta_i(h))^{-\alpha_i}$ and denominator functions are:

$$\eta_1(h)=\frac{1-e^{dh}}{d},\eta_2(h)=\frac{1-e^{(t_1+r_1+a_1)h}}{(t_1+r_1+a_1)},\eta_3(h)=\frac{1-e^{(r_2+a_2)h}}{(r_2+a_2)},\eta_4(h)=\frac{1-e^{(\lambda+d)h}}{(\lambda+d)},$$
$$\eta_5(h)=\frac{1-e^{(t_2+a_3)h}}{(t_2+a_3)},\eta_6(h)=\frac{1-e^{(a_2+r_3)h}}{(a_2+r_3)},\eta_7(h)=\frac{1-e^{a_4h}}{a_4}.$$

Thus, the discretized version of the COVID-19 system is obtained as follows:

$$S_{n+1}=\frac{B+\lambda {S^q}_n-\sum_{i=1}^{l}\frac{u(\alpha_i)}{l}\left(\sum_{j=1}^{n+1}p_j^{\alpha_i}S_{n+1-j}\right)}{\sum_{i=1}^{l}\frac{u(\alpha_i)}{l}(\eta_1(h))^{-\alpha_i}+A_1(I_n+t_rN_n)+d},$$

$$I_{n+1}=\frac{A_2t_rN_nS_n-\sum_{i=1}^{l}\frac{u(\alpha_i)}{l}\left(\sum_{j=1}^{n+1}p_j^{\alpha_i}I_{n+1-j}\right),}{\sum_{i=1}^{l}\frac{u(\alpha_i)}{l}(\eta_2(h))^{-\alpha_i}-A_2S_n+t_1+r_1+a_1},$$

$$N_{n+1} = \frac{A_3 I_n S_n - \sum_{i=1}^{l} \frac{u(\alpha_i)}{l} \left(\sum_{j=1}^{n+1} p_j^{\alpha_i} N_{n+1-j} \right)}{\sum_{i=1}^{l} \frac{u(\alpha_i)}{l} (\eta_3(h))^{-\alpha_i} + r_2 + a_2 + A_3 t_r S_n},$$

$$S^q{}_{n+1} = \frac{A_4 (I_n + t_r N_n) S_n - \sum_{i=1}^{l} \frac{u(\alpha_i)}{l} \left(\sum_{j=1}^{n+1} p_j^{\alpha_i} S^q{}_{n+1-j} \right)}{\sum_{i=1}^{l} \frac{u(\alpha_i)}{l} (\eta_4(h))^{-\alpha_i} + \lambda + d},$$

$$Q_{n+1} = \frac{A_5 (I_n + t_r N_n) S_n - \sum_{i=1}^{l} \frac{u(\alpha_i)}{l} \left(\sum_{j=1}^{n+1} p_j^{\alpha_i} Q_{n+1-j} \right)}{\sum_{i=1}^{l} \frac{u(\alpha_i)}{l} (\eta_5(h))^{-\alpha_i} + t_2 + a_3},$$

$$H_{n+1} = \frac{t_1 I_n + t_2 Q_n - \sum_{i=1}^{l} \frac{u(\alpha_i)}{l} \left(\sum_{j=1}^{n+1} p_j^{\alpha_i} H_{n+1-j} \right)}{\sum_{i=1}^{l} \frac{u(\alpha_i)}{l} (\eta_6(h))^{-\alpha_i} + a_2 + r_3},$$

$$R_{n+1} = \frac{r_1 I_n + r_2 N_n + r_3 H_n - \sum_{i=1}^{l} \frac{u(\alpha_i)}{l} \left(\sum_{j=1}^{n+1} p_j^{\alpha_i} R_{n+1-j} \right)}{\sum_{i=1}^{l} \frac{u(\alpha_i)}{l} (\eta_7(h))^{-\alpha_i} + a_4}.$$

If the following system of equations is solved to obtain the disease-free equilibrium point:

$$S_n - \frac{B + \lambda S^q{}_n - \sum_{i=1}^{l} \frac{u(\alpha_i)}{l} \left(\sum_{j=1}^{n+1} p_j^{\alpha_i} S_n \right)}{\sum_{i=1}^{l} \frac{u(\alpha_i)}{l} (\eta_1(h))^{-\alpha_i} + A_1 (I_n + t_r N_n) + d} = 0,$$

$$I_n - \frac{A_2 t_r N_n S_n - \sum_{i=1}^{l} \frac{u(\alpha_i)}{l} \left(\sum_{j=1}^{n+1} p_j^{\alpha_i} I_n \right),}{\sum_{i=1}^{l} \frac{u(\alpha_i)}{l} (\eta_2(h))^{-\alpha_i} - A_2 S_n + t_1 + r_1 + a_1} = 0,$$

$$N_n - \frac{A_3 I_n S_n - \sum_{i=1}^{l} \frac{u(\alpha_i)}{l} \left(\sum_{j=1}^{n+1} p_j^{\alpha_i} N_n \right)}{\sum_{i=1}^{l} \frac{u(\alpha_i)}{l} \left(\eta_3(h) \right)^{-\alpha_i} + r_2 + a_2 + A_3 t_r S_n} = 0,$$

$$S^q{}_n - \frac{A_4 (I_n + t_r N_n) S_n - \sum_{i=1}^{l} \frac{u(\alpha_i)}{l} \left(\sum_{j=1}^{n+1} p_j^{\alpha_i} S^q{}_n \right)}{\sum_{i=1}^{l} \frac{u(\alpha_i)}{l} (\eta_4(h))^{-\alpha_i} + \lambda + d} = 0,$$

$$Q_n - \frac{A_5 (I_n + t_r N_n) S_n - \sum_{i=1}^{l} \frac{u(\alpha_i)}{l} \left(\sum_{j=1}^{n+1} p_j^{\alpha_i} Q_n \right)}{\sum_{i=1}^{l} \frac{u(\alpha_i)}{l} (\eta_5(h))^{-\alpha_i} + t_2 + a_3} = 0,$$

$$H_n - \frac{t_1 I_n + t_2 Q_n - \sum_{i=1}^{l} \frac{u(\alpha_i)}{l} \left(\sum_{j=1}^{n+1} p_j^{\alpha_i} H_n \right)}{\sum_{i=1}^{l} \frac{u(\alpha_i)}{l} (\eta_6(h))^{-\alpha_i} + a_2 + r_3} = 0,$$

$$R_n - \frac{r_1 I_n + r_2 N_n + r_3 H_n - \sum_{i=1}^{l} \frac{u(\alpha_i)}{l} \left(\sum_{j=1}^{n+1} p_j^{\alpha_i} R_n \right)}{\sum_{i=1}^{l} \frac{u(\alpha_i)}{l} (\eta_7(h))^{-\alpha_i} + a_4} = 0.$$

The disease-free equilibrium point is obtained as:

$$E = \left(\frac{B}{\sum_{i=1}^{l} \frac{u(\alpha_i)}{l} \left(\eta_1(h)\right)^{-\alpha_i} + d + \sum_{i=1}^{l} \frac{u(\alpha_i)}{l} \left(\sum_{j=1}^{n+1} p_j^{\alpha_i}\right)}, 0,0,0,0,0,0 \right).$$

In this part of this section, some numerical simulations are presented to better understand the dynamic behavior of the distributed order COVID-19 model including the quarantine effect. Parameter estimates and selections are described below (Babaei et al., 2021):
$B = 6931614.27, c = 14.781, t_r = 0.5944, p_t = 2.1011\ 10^{-8}, q = 1.8887\ 10^{-7},$

$t_1 = 0.13266, t_2 = 0.1259, r_1 = 0.33029, r_2 = 0.13978, r_3 = 0.11624, d = \frac{1}{69.5},$

$\rho = 0.86834, \lambda = \frac{1}{14}, a_1 = 0.00723, a_2 = 1.7826\ 10^{-5}, a_3 = \frac{1}{68.5}, a_4 = 0.0144.$

Also, let's choose the initial conditions in the form (Babaei et al., 2021):

$$S(0) = 1108100, \quad I(0) = 27.679, \quad N(0) = 53.839, \quad S^q(0) = 739,$$
$$Q(0) = 1.1642, \quad H(0) = 1, \quad R(0) = 2.$$

Some of the numerical results of the discretized system on the effects of COVID-19 are expressed in graphs below.

First of all, in Figure 1, the choice of the density function and the effect of the solution are examined. As a result of this examination, it was seen that with the appropriate density function selection, the results were consistent with their ordinary and fractional states (Babaei et al., 2021).

Figures 2 and 3 show the results of how the data changes with the selection of the density function.

In Figures 4, 5 and 6, it is aimed to examine the effects on the system of equations in different situations. For this reason, it has been shown that external effects can be easily expressed in the system with the help of the density function. At the same time, as can be seen from the figures, it has been seen that the equilibrium point can be reached by choosing the density function.

All calculations and drawings in this section are calculated with the help of MATLAB package program.

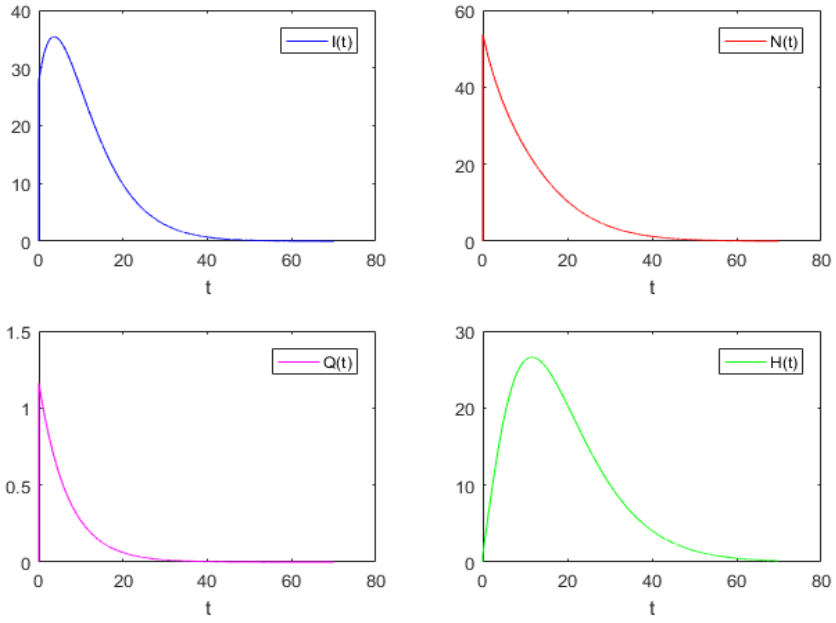

Figure 1. *Dynamics of the Effect of Quarantine on the Spread of COVID-19 for* $d(\alpha) = \Gamma(2 - 3\alpha/5)$.

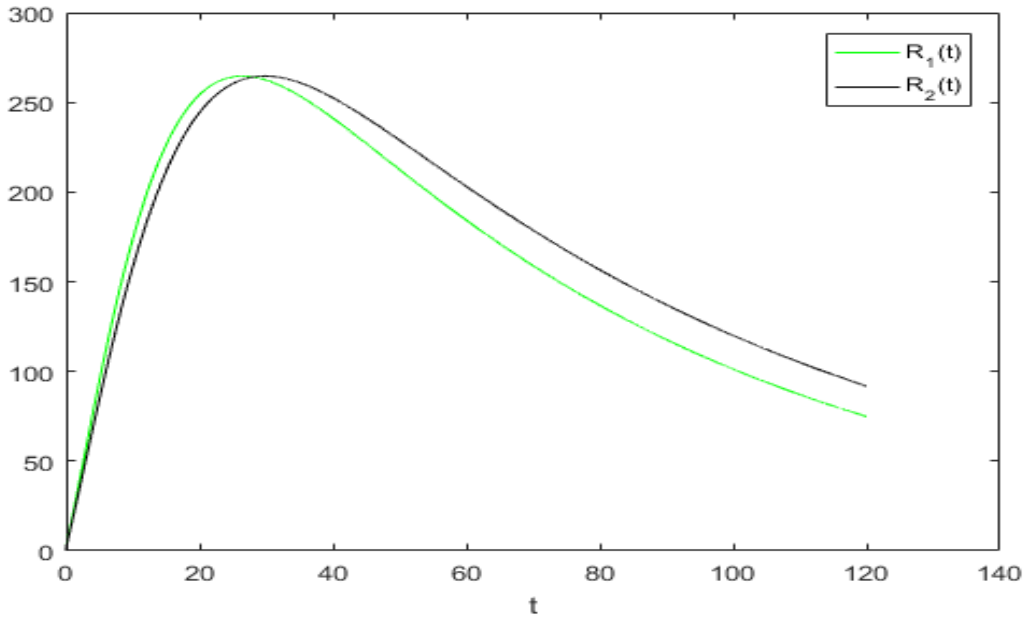

Figure 2. *Dynamics of Individuals who have recovered for different density functions* $d_1(\alpha) = \Gamma(1 + 2\alpha/7),\ and\ d_2(\alpha) = \Gamma(2 + \alpha)$.

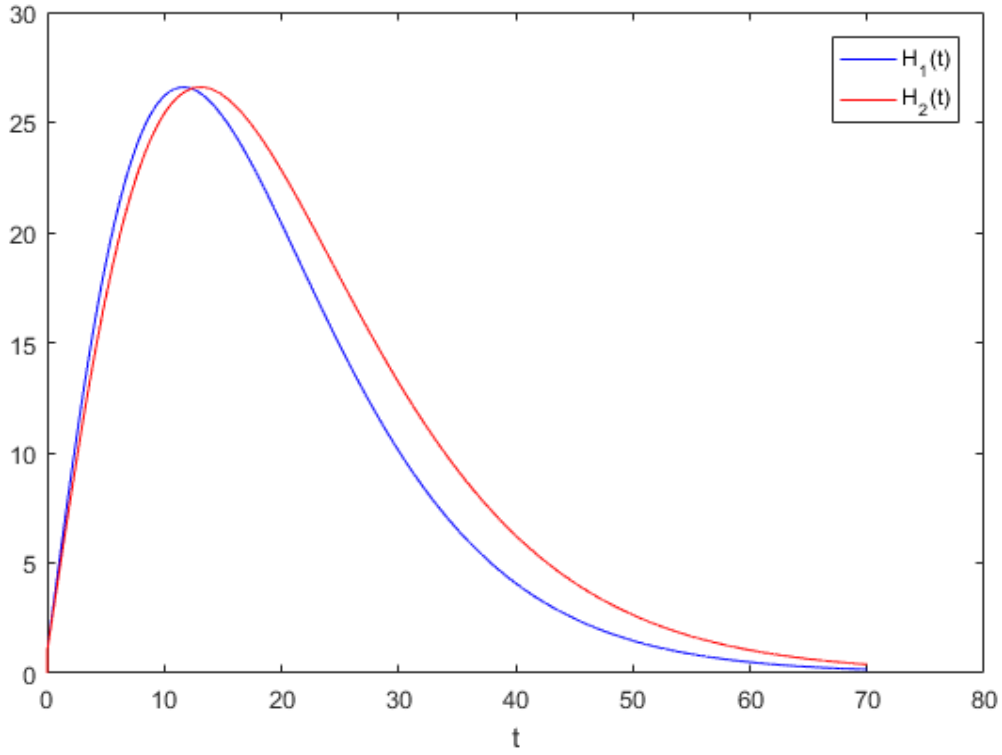

Figure 3. *Dynamics of Infected individuals in the hospital for different density functions* $d_1(\alpha) = \Gamma(2 - 3\alpha/5),\ and\ d_2(\alpha) = \Gamma(3 - \alpha).$

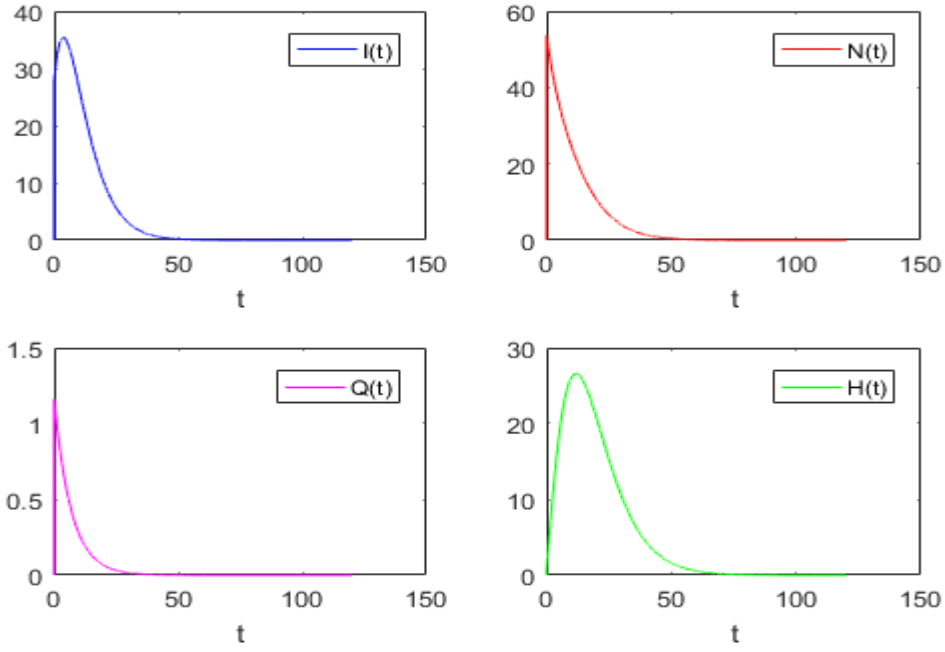

Figure 4. *Dynamics of the Effect of Quarantine on the Spread of COVID-19 for* $d(\alpha) = \Gamma(1 + 2\alpha/7).$

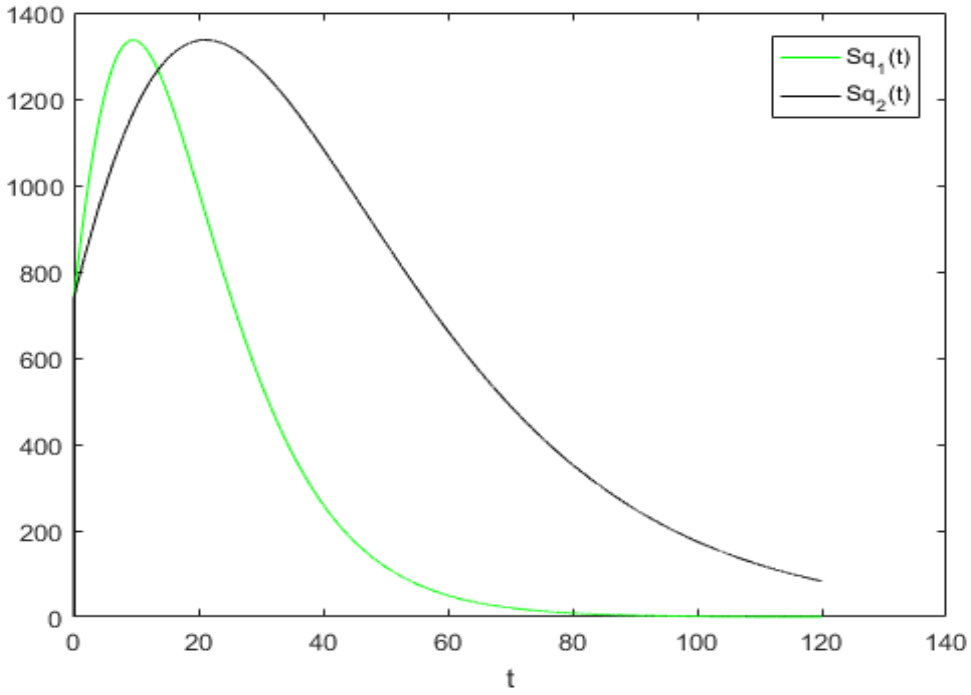

Figure 5. *Dynamics of Susceptible individuals in quarantine for different density functions* $d_1(\alpha) = \Gamma(1 + 2\alpha/7),\ and\ d_2(\alpha) = \Gamma(2 + \alpha)$.

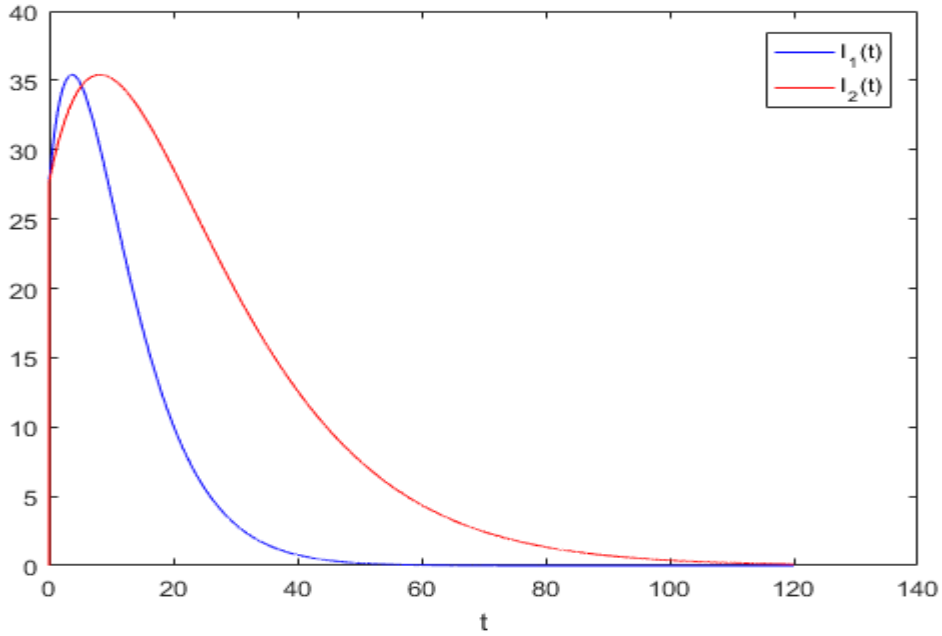

Figure 6. *Dynamics of Infected individuals with symptoms for different density functions* $d_1(\alpha) = \Gamma(1 + 2\alpha/7),\ and\ d_2(\alpha) = \Gamma(2 + \alpha)$.

4.CONCLUSION

In this study, a distributed-order coronavirus model has been created. In order to examine the effects of the disease in the quarantine situation, the quarantine factor is also included in the model. Thus, this modified equation system has been very effective in determining the dynamics of the disease. Because, the effects can be obtained quickly by choosing the density

function within the distributed order differential equations. The non-standard finite difference scheme is applied to the modified equation to determine the effects. Discretization is achieved with the help of this scheme. The Grünwald-Letnikov derivative operator is also used during discretization.

The equilibrium point was found with the discretized system. In the light of the data found, it has been seen that the use of numerical simulations and analysis of the equilibrium point in the coronavirus model of distributed order differential equations is also very effective. When the density function selection is compared with the previous study results, it is seen that the modified equation system gives very consistent results.

Thus, it has been seen that the coronavirus model can be expressed with distributed order differential equations. Consistency of the results showed that using such equations in modeling would save time in determining the dynamics. It is seen that the savings will be at a high level with the selection of the density function. In the light of the results obtained, it has been shown that the use of distributed order differential equations will contribute to the literature in modeling.

REFERENCES

Aminikhah, H., Refahi Sheikhani, A., Rezazadeh, H. (2013). Stability analysis of distributed order fractional Chen system. *The Scientific World Journal*, *2013*.

Atangana A. (2020). Modelling the spread of COVID-19 with new fractal-fractional operators: can the lockdown save mankind before vaccination? *Chaos Solitons Fractals*, 136:109860.

Bagley, R. L., Torvik, P. J. (2000). On the existence of the order domain and the solution of distributed order equations-Part I. *International Journal of Applied Mathematics*, *2*(7), 865-882.

Babaei, A., Ahmadi, M., Jafari, H., Liya, A. (2021). A mathematical model to examine the effect of quarantine on the spread of coronavirus. *Chaos, Solitons & Fractals*, *142*, 110418.

Baleanu, D., Mohammadi, H., Rezapour, S. A. (2020). fractional differential equation model for the COVID-19 transmission by using the Caputo–Fabrizio derivative. *Adv Differ Equ.*, 2020:299.

Caputo, M. (1969). Elasticita e dissipazione. Zanichelli.

Caputo, M. (1995). Mean fractional-order-derivatives differential equations and filters. Annali dell'Universita di Ferrara, 41(1), 73-84.

Caputo, M. (2001). Distributed order differential equations modelling dielectric induction and diffusion. Fractional Calculus and Applied Analysis, 4(4), 421-442.

Diethelm, K., Ford, N. J. (2009). Numerical analysis for distributed-order differential equations. *Journal of Computational and Applied Mathematics*, *225*(1), 96-104.

Dorciak L. (1994). Numerical models for simulation the fractional-order control systems, UEF-04-94, The Academy of Sciences, Institute of Experimental Physic, Kosice, Slovak Republic.

Feng L.X., Jing S.L., Hu S.K., Wang D.F., Huo H.F. (2020). Modelling the effects of media coverage and quarantine on the COVID-19 infections in the UK. *Math Bioscience Eng*, 17(4), 3618–3636.

Hartley, T. T., Lorenzo, C. F. (2003). Fractional-order system identification based on continuous order-distributions. *Signal processing*, *83*(11), 2287-2300.

Katsikadelis, J. T. (2014). Numerical solution of distributed order fractional differential equations. *Journal of Computational Physics*, *259*, 11-22.

Kocabiyik, M., Ongun, M. Y., Çetinkaya, İ.T. (2021). Standart olmayan sonlu fark metodu ile dağılımlı mertebeden SVIR modelinin nümerik analizi. *Balıkesir Üniversitesi Fen Bilimleri Enstitüsü Dergisi*, *23*(2), 577-591.

Kocabıyık, M. (2022). Nonstandard Discretization and Stability Analysis of a novel type Malaria-Ross Model . Journal of the Institute of Science and Technology , 12 (2) , 1023-1033 . DOI: 10.21597/jist.1026364

Kocabiyik, M., Ongun, M. Y., Çetinkaya, İ.T. (2022). An Application of Distributed Order Differential Equations to a HIV Infection Model, ISBN: 978-625-7799-69-0 1st Edition, 150.

Kocabiyik, M., Ongun, M. Y. (2022). Construction a distributed order smoking model and its nonstandard finite difference discretization.

Li, X. Y., Wu, B. Y. (2016). A numerical method for solving distributed order diffusion equations. *Applied Mathematics Letters*, *53*, 92-99.

Mickens, R. E. (1989). Exact solutions to a finite-difference model of a nonlinear reaction-advection equation: Implications for numerical analysis. *Numerical Methods for Partial Differential Equations*, *5*(4), 313-325.

Meerschaert, M. M., Tadjeran, C. (2004). Finite difference approximations for fractional advection–dispersion flow equations. *Journal of computational and applied mathematics*, *172*(1), 65-77.

Mickens, R. E. (1994). Nonstandard finite difference models of differential equations. World scientific.

Podlubny, I. (1999). Fractional differential equations: an introduction to fractional derivatives, fractional differential equations, to methods of their solution and some of their applications (Vol. 198). Elsevier.

World Health Organization (2019). Coronavirus disease 2019. https://www.who.int/health-topics/coronavirus

Iterations of Euler Totient Function

Emre Öztürk[1]

Introduction

In mathematics history, the prime numbers constitute very special and big area. These numbers considered of atoms of the numbers. Because, from Euclid to today, it is well-known any natural number can be represented by canonic decomposition of primes which is called the fundamental theorem of the arithmetic. Therefore, the primes play very crucial role to understand the numbers. Moreover, in "Elements" of Euclid, the finiteness of primes proved by a nice technic. Today, still his book inspires many mathematicians. After the Euclid and Pythagoras, prime numbers have been studied by many famous mathematicians, especially well-knowns are Fermat, Euler and Gauss. On the other hand, arithmetic functions in number theory played a role to understand the distribution of primes. Maybe the most well-known defined by Leonhard Euler, called today "Euler totient function" or "Euler phi function". While many of characterizations and properties of this function known but the iterations of the function still have many open questions. Like logarithm (study with small numbers instead of big numbers), study with "class" of numbers will be provide an advantage to understand the theory.

The first studies on iterations of totient function date back to 1929 by Pillai, (Pillai, 1929). Then, the first extensive study given by Shapiro, (Shapiro, 1943). His important contribution is to examine numbers by classification into the different classes and sections. Whereas he conjectured the smallest number of these classes is prime, Mills (Mills, 1943) gave a counterexample. Then by Catlin (Catlin, 1970), these numbers characterized. After Shapiro's study, many mathematicians improved his "class of numbers", for more detail, see (Bal and Bhatnagar, 2020) and (Noe, 2008).

In this study, we examine class of numbers with respect to iterations of totient function through the reference (Shapiro, 1943) and give some new identities depends on the function and the number character. **In section 4**, we use our results for apply to Fermat primes. **In the final section**, we give two procedure for calculate the iterations and classes of numbers. Moreover, in order to examine primes in class more efficiently, we consider the partition sets and give some examples.

Method

Definition 2.1 Let $n \geq 1$ is a natural number. Number of integers m that satisfy $1 \leq m \leq n$ and $(m, n) = 1$ is shown by $\phi(n)$, where ϕ is called as Euler's totient function.

Example 2.2 If we take $n = 15$, then $\phi(n) = \phi(15) = 8$. Because 1,2,4,7,8,11,13,14 are coprime with 15.

Example 2.3 For big numbers n, we can use Euler's identity. Let $n = {p_1}^{m_1} {p_2}^{m_2} \dots {p_k}^{m_k}$ where $p_1, p_2, \dots, p_k$ are distinct primes. Then, $\phi(n) = {p_1}^{m_1-1}(p_1 - 1){p_2}^{m_2-1}(p_2 - 1) \dots {p_k}^{m_k-1}(p_k - 1)$.

Therefore, we can easily calculate $\phi(10368)$. Since $10368 = 2^7 3^4$, $\phi(10368) = 2^6 \times 3^3 \times 2 = 3456$.

[1] Emre Öztürk, Dr., Turkish Court of Accounts, Data Analysis, emreozturk1471@gmail.com

Now, in accordance with (Shapiro, 1943), we give some basic concepts slightly different.

In the following discussion we shall consider a rather curious concept which arises very naturally from the iteration of the Euler ϕ function. Since $\phi(n)$ is defined as the number of positive integers, not exceeding n, which are prime to n, it follows immediately that for $n > 1, \phi(n) < n$. If we write $\phi^2(n) = \phi[\phi(n)], \phi^3(n) = \phi[\phi^2(n)], \dots, \phi^k(n) = \phi[\phi^{k-1}(n)]$, then we have

$$\phi^k(n) < \phi^{k-1}(n), \tag{2.1}$$

for $\phi^{k-1}(n) > 1$. Thus we see from Eq. (2.1) that by making k large enough we must always arrive at

$$\phi^k(n) = 1. \tag{2.2}$$

When Eq. (2.2) holds we shall say that n is of class k, and write this as $\varepsilon(n) = k$. Notice that, this definiton slightly different from definition of (Shapiro, 1943) by $\varepsilon(n) = C(n) + 1$. In fact, some authors studied properties of function ε, by different notations, for more details see [4] and [7].

Remark 2.4 From definition, $\varepsilon(1) = 0$, and $\varepsilon(2) = 1$.

Example 2.5 If we take $n = 12$ we obtain that $\phi(12) = 4, \phi^2(12) = 2, \phi^3(12) = 1$. Therefore, $\varepsilon(12) = 3$.

Iterations of Euler Totient Function

In this section, we derive some formulas for iterations of Euler totient function.

Lemma 3.1 Let m is a natural number and $n > 1$ is a positive integer. The following equation occurs:

$$\varepsilon\big(\phi^m(n)\big) = \varepsilon\big(\phi^{m+1}(n)\big) + 1.$$

Proof. Assume that $\varepsilon\big(\phi^{m+1}(n)\big) = t$. Then, by definition, t is the least natural number that satisfy $\phi^t\big(\phi^{m+1}(n)\big) = 1$. Hence,

$$\phi^t\big(\phi^{m+1}(n)\big) = \phi^{t+1}\big(\phi^m(n)\big) = 1,$$

which means

$$\varepsilon\big(\phi^m(n)\big) = t + 1. \tag{3.1}$$

From hypothesis and Eq. (3.1), it is written

$$\varepsilon\big(\phi^m(n)\big) = \varepsilon\big(\phi^{m+1}(n)\big) + 1,$$

which completes the proof.

Lemma 3.2 Let k is a natural number. Then,

$$\varepsilon(2^k) = k.$$

Proof. By straightforward calculations, we obtain

$$\begin{aligned} \phi(2^k) &= 2^{k-1} \\ \phi^2(2^k) &= 2^{k-2} \\ \phi^3(2^k) &= 2^{k-3} \\ &\vdots \end{aligned}$$

In the case of general form it is written,

$$\phi^r(2^k) = 2^{k-r}. \tag{3.2}$$

If we subs $r = k$ in Eq. (3.2) we obtain,

$$\phi^k(2^k) = 1.$$

Hence, $\varepsilon(2^k) = k$ which completes the proof.

Table 1. List of class of exponentials from 1 to 22.

1^k	2^k	3^k	4^k	5^k	6^k	7^k	8^k	9^k	10^k	11^k
0	k	$k+1$	$2k$	$2k+1$	$2k$	$2k+1$	$3k$	$2k+1$	$3k$	$3k+1$
12^k	13^k	14^k	15^k	16^k	17^k	18^k	19^k	20^k	21^k	22^k
$3k$	$3k+1$	$3k$	$3k+1$	$4k$	$4k+1$	$3k$	$3k+1$	$4k$	$3k+1$	$4k$

Theorem 3.3 Assume that n is a positive integer, and $k < \varepsilon(n)$ is an arbitrary natural number. In this case, we have

$$\varepsilon(n) = \varepsilon\left(\phi^k(n)\right) + k. \tag{3.3}$$

Proof. For proof, we use induction onto Eq. (3.3). First, assume that $k = 1$ and $\varepsilon\left(\phi(n)\right) = t$. By definition, t is the least natural number that satisfy $\phi^t\left(\phi(n)\right) = 1$. This means $\phi^{t+1}(n) = 1$ and $\varepsilon(n) = t + 1$. Hence, for $k = 1$, Eq. (3.3) holds. Assume that for $k = m$ the equation holds. We must show it is true for $k = m + 1$. From our hypothesis $\varepsilon(n) = \varepsilon\left(\phi^m(n)\right) + m$. Moreover, according to Lemma 3.1, we write $\varepsilon\left(\phi^m(n)\right) = \varepsilon\left(\phi^{m+1}(n)\right) + 1$. Then, we obtain

$$\begin{aligned} \varepsilon(n) &= \varepsilon\left(\phi^m(n)\right) + m \\ &= \varepsilon\left(\phi^{m+1}(n)\right) + 1 + m \\ &= \varepsilon\left(\phi^{m+1}(n)\right) + (m+1), \end{aligned}$$

which is intended.

Example 3.4 Let us consider $n = 2^3 3^4 5^2$ and $k = 4$ at Theorem 3.3. Then, we obtain

$$\phi(n) = 2^5 3^3 5, \phi^2(n) = 2^7 3^2, \phi^3(n) = 2^7 3, \phi^4(n) = 2^7.$$

By Lemma 3.2 and Theorem 3.3, we obtain

$$\varepsilon(n) = \varepsilon\left(\phi^4(n)\right) + 4 = \varepsilon(2^7) + 4 = 11.$$

Lemma 3.5 (Shapiro, 1943) If either x or y is odd,

$$C(xy) = C(x) + C(y),$$

and if both x and y are even

$$C(xy) = C(x) + C(y) + 1.$$

Theorem 3.6 Let m and n are coprime. Then,

$$\varepsilon(mn) = \varepsilon(m) + \varepsilon(n) - 1.$$

Proof. Since m and n are coprime, one of those numbers is odd. Assume that m is odd, then it follows from Lemma 3.5 that $C(mn) = C(m) + C(n)$. Since $\varepsilon(n) = C(n) + 1$ and $\varepsilon(m) = C(m) + 1$ we obtain,

$$\varepsilon(mn) = (\varepsilon(m) - 1 + \varepsilon(n) - 1) + 1 = \varepsilon(m) + \varepsilon(n) - 1.$$

Corollary 3.7 Let m and n are coprime. Then,

$$\varepsilon((mn)^k) = \varepsilon(m^k) + \varepsilon(n^k) - 1.$$

Theorem 3.8 Let p is odd prime. Then,

$$\varepsilon(p^k) = k\varepsilon(p) - k + 1.$$

Proof. From Lemma 3.5, we obtain $C(p^k) = kC(p)$. Hence, $\varepsilon(p^k) = C(p^k) + 1 = kC(p) + 1 = k(\varepsilon(p) - 1) + 1$, and this completes the proof.

Theorem 3.9 Let m divides n. Then,

$$\varepsilon(mn) = 2\varepsilon(m) + \varepsilon(k) + \epsilon_{k,m},$$

where

	$\epsilon_{k,m}$
$Both\ m\ and\ k\ are\ odd$	-2
$m\ is\ even\ and\ k\ is\ odd$	-1
$Both\ m\ and\ k\ are\ even$	0

and $n = mk$.

Proof. *Case 1.* Assume that n is odd.

In this case, both m and k must be odd. Then, $C(mn) = 2C(m) + C(k)$. On the other hand, $\varepsilon(mn) = C(mn) + 1 = 2C(m) + C(k) + 1$. It follows from $C(m) = \varepsilon(m) - 1$ and $C(k) = \varepsilon(k) - 1$ that

$$\varepsilon(mn) = 2\varepsilon(m) + \varepsilon(k) - 2.$$

Case 2. Assume that n is even.

Case 2.1 Let m is even and k is odd. Then, immediately we obtain $C(mn) = 2C(m) + C(k) + 1$. Since $\varepsilon(mn) = C(mn) + 1 = 2C(m) + C(k) + 2$, it follows from $C(m) = \varepsilon(m) - 1$ and $C(k) = \varepsilon(k) - 1$ that

$$\varepsilon(mn) = 2\varepsilon(m) + \varepsilon(k) - 1.$$

Case 2.2 Let both m and k are even. Then, $C(mn) = 2C(m) + C(k) + 2$. Since $\varepsilon(mn) = C(mn) + 1 = 2C(m) + C(k) + 3$, it follows from $C(m) = \varepsilon(m) - 1$ and $C(k) = \varepsilon(k) - 1$ that

$$\varepsilon(mn) = 2\varepsilon(m) + \varepsilon(k).$$

which completes the proof.

Remark 3.10 In Theorem 3.9, if we consider m is odd and k is even then, we obtain $\varepsilon(mn) = 2\varepsilon(m) + \varepsilon(k) - 2$, similarly in Case 1.

Corollary 3.11 Let m divides n. Then,

$$\varepsilon(mn) = \varepsilon(m) + \varepsilon(n) + \epsilon_{m,n},$$

where

	$\epsilon_{m,n}$
$Both\ m\ and\ n\ are\ even$	0
$m\ is\ odd\ and\ n\ is\ even$	-1
$n\ is\ odd$	-1

Theorem 3.12 Let $n = {p_1}^{m_1}{p_2}^{m_2} \dots {p_k}^{m_k}$ where $p_1 = 2, p_2 = 3, p_3 = 5, \dots, p_k$ is sequence of first k prime. Then, the following holds:

$$\varepsilon(n) = m_1 + \sum_{j=2}^{k} m_j\big(\varepsilon(p_j) - 1\big). \tag{3.3}$$

Proof. By Theorem 3.6, we obtain

$$\varepsilon(n) = \varepsilon({p_1}^{m_1}) + \varepsilon({p_2}^{m_2}) + \cdots + \varepsilon({p_k}^{m_k}) - (k-1).$$

It follows from Lemma 3.2 and Theorem 3.8

$$\varepsilon(n) = m_1 + (m_2\varepsilon(p_2) - m_2 + 1) + (m_3\varepsilon(p_3) - m_3 + 1) + \cdots + (m_k\varepsilon(p_k) - m_k + 1) - (k-1),$$

and this implies

$$\varepsilon(n) = m_1 + (m_2\varepsilon(p_2) - m_2) + (m_3\varepsilon(p_3) - m_3) + \cdots + (m_k\varepsilon(p_k) - m_k),$$

which completes the proof.

Fermat Primes

Let k is a natural number. The well-known Fermat numbers are written by $F_k = 2^{2^k} + 1$. If F_k is prime then, F_k is called a Fermat prime. While F_k is prime for $0 \leq k \leq 4$, there is no exists another prime yet. Notice that, Euler showed that F_5 is divisible by 641. After Euler, whereas many mathematicians and computers determined composite Fermat numbers but hasn't found any different Fermat prime. There is a nice project about the current investigations and search of prime divisors of the Fermat numbers at web, see (Distributed Search for Fermat Number Divisors, 2023).
Now, let us investigate the class of Fermat primes.

Theorem 4.1 Let $n = 2^{2^k} + 1$ is a Fermat prime. Then, we have

$$\varepsilon(n) = 2^k + 1.$$

Proof. Assume that $n = 2^{2^k} + 1$ is a Fermat prime, then immediately we have $\phi(n) = 2^{2^k}$. From Lemma 3.1 and Lemma 3.2, we easily obtain the intended.

Theorem 4.2 Let $n = 2^{2^k} + 1$ is a Fermat prime. Then, the following satisfies:

$$\varepsilon(n^k) = \varepsilon((n-1)^k) + 1.$$

Proof. Let $n = 2^{2^k} + 1$ is a Fermat prime. Then, the following equations can be written:

$$\begin{aligned}
\phi((2^{2^k}+1)^k) &= (2^{2^k}+1)^{k-1}2^{2^k} \\
\phi^2((2^{2^k}+1)^k) &= (2^{2^k}+1)^{k-2}2^{2^k+2^k-1} \\
\phi^3((2^{2^k}+1)^k) &= (2^{2^k}+1)^{k-3}2^{2^k+2^k+2^k-2} \\
&\vdots
\end{aligned}$$

In the general case,

$$\phi^r\left((2^{2^k}+1)^k\right) = (2^{2^k}+1)^{k-r}2^{r2^k-(r-1)}. \tag{4.1}$$

If we subs $r = k$ in Eq. (4.1), we obtain $\phi^k((2^{2^k}+1)^k) = 2^{k2^k-(k-1)}$. From Theorem 3.3, it follows

$$\varepsilon(n^k) = k2^k + 1. \tag{4.2}$$

On the other hand,

$$\varepsilon((n-1)^k) = k2^k. \tag{4.3}$$

From Eq. (4.2) and Eq. (4.3) we obtain,

$$\varepsilon(n^k) = \varepsilon((n-1)^k) + 1,$$

which completes the proof.

Corollary 4.3 If $n = 2^{2^k} + 1$ and $\varepsilon(\phi^k(n)) \neq 2^k - k + 1$, then, n is composite.

Some Procedures and Results

In this section, we give two Maple procedure in order to calculate iterations of function and classes of numbers.

Procedure 5.1 The following procedure determines values of $\phi(n), \phi^2(n), \phi^3(n), \dots, \phi^k(n)$, depends on initial number of $n = x[1]$.

```
with(numtheory):
x[1]:= "enter any positive integer":
for i from 2 to 100 do x[i]:=phi(x[i-1]) od:
L := [seq(x[i],i=2..100)]:
for k from 1 to nops(L) do
if x[k]=1 then
A:= [seq(x[i],i=2..k)]: break; end if; end do;
print(A); nops(A);
```

```
with(numtheory):
mertebe:=proc(n)
local k,x,i,A,L;
x[1]:=n;
for i from 2 to 100 do x[i]:=phi(x[i-1]);
L := [seq(x[i],i=2..100)]:od:
for k from 1 to nops(L) do
if x[k]=1 then
A:= [seq(x[i],i=2..k)]: break; end if; end do;
nops(A):end:
hesapla:=proc(f)
local j,y,C; for j from 1 to f do;y[j]:=mertebe(j);
C:=[seq(y[j],j=1..f)]:od:end:
```

Procedure 5.2 *The following procedure lists class of numbers depends on given n.*

Table 2. *Class of numbers*

Class	Number of This Class
0	1,
1	2,
2	3, 4, 6,
3	5, 7, 8, 9, 10, 12, 14, 18,
4	11, 13, 15, 16, 19, 20, 21, 22, 24, 26, 27, 28, 30, 36, 38, 42, 54,
5	17, 23, 25, 29, 31, 32, 33, 34, 35, 37, 39, 40, 43, 44, 45, 46, 48, 49, 50, 52, 56, 57, 58, 60, 62, 63, 66, 70, 72, 74, 76, 78, 81, 84, 86, 90, 98, 108, 114, 126, 162,

6	41, 47, 51, 53, 55, 59, 61, 64, 65, 67, 68, 69, 71, 73, 75, 77, 79, 80, 82, 87, 88, 91, 92, 93, 94, 95, 96, 99, 100, 102, 104, 105, 106, 109, 110, 111, 112, 116, 117, 118, 120, 122, 124, 127, 129, 130, 132, 133, 134, 135, 138, 140, 142, 144, 146, 147, 148, 150, 152, 154, 156, 158, 163, 168, 171, 172, 174, 180, 182, 186, 189, 190, 196, 198, 210, 216, 218, 222, 228, 234, 243, 252, 254, 258, 266, 270, 294, 324, 326, 342, 378, 486,
7	83, 85, 89, 97, 101, 103, 107, 113,…
8	137, 168, 179, 187, 193,…
9	257, 289, 353,…
10	641, 685, 697,…

Table 3. *Smallest number of classes*

Class	Smallest number	Primality
1	2	Prime number
2	3	Fermat prime
3	5	Fermat prime
4	11	Prime number
5	17	Fermat prime
6	41	Prime number
7	83	Prime number
8	137	Prime number
9	257	Fermat prime
10	641	Divisor of F_5
11	1097	Prime number
12	2329	17×137
13	4369	17×257

Although Shapiro conjectured that all smallest number are prime with respect to their class, Mills (Mills, 1943) gave a counterexample which shows the conjecture is not true in general. Then, in 1970, Catlin (Catlin, 1970) proved that if the smallest number in a class is odd, then it can be factored into the product of other such numbers. Hence, these numbers are characterized totally. In fact, these numbers are belonging to sequence of A007755. For more detail, see (Sloane N. J. A., 2023).

In (Shapiro, 1943), Shapiro gives the bounds for $C(n)$ by

$$\frac{logn}{log2} > C(n) \geq \frac{log\,(n/2)}{log3}.$$

Since $\varepsilon(n) = C(n) + 1$, we obtain

$$log_3(3n/2) \leq \varepsilon(n) < log_2(2n). \tag{5.1}$$

From Eq. (6.1), we obtain

$$0{,}63k - 0{,}26 \leq \lim_{n \to 2^{k-1}} \varepsilon(n) < k, \tag{5.2}$$

where $log_3 2 \cong 0{,}63$. This result leads us to consider following:

This is interesting to consider the behaviour of (odd) primes which are belongs to following sets:

$$S_1 = \{x: 2 < x < 2^2\}, S_2 = \{x: 2^2 < x < 2^3\}, S_3 = \{x: 2^3 < x < 2^4\}, \dots, S_n = \{x: 2^n < x < 2^{n+1}\}.$$

Since $3 \in S_1$ and $3 < 2^2$, we can consider $k = 3$ in Eq. (5.2). Therefore, $1{,}63 \leq \varepsilon(3) < 3$ which obviously $\varepsilon(3) = 2$.

Another example; $61 \in S_3$ and $61 < 2^6$, we can consider $k = 7$ in Eq. (5.2). Therefore, $4{,}15 \leq \varepsilon(61) < 7$, which indicates $\varepsilon(61) = 5$ or $\varepsilon(61) = 6$. In fact, $\varepsilon(61) = 6$. For big primes this interval expands. For example, the Mersenne prime $M_7 = 524287 = 2^{19} - 1 < 2^{19}$. For $k = 20$ in Eq. (5.2), we obtain

$$12{,}34 \leq \varepsilon(M_7) < 20.$$

Then, $\varepsilon(M_7) \in \{13{,}14, \ldots, 19\}$. We note that $\varepsilon(M_7) = 15$.
If we consider minimum prime in S_k, that is, $p = 2^k + \theta$, where θ is odd, depends on the θ we determine the class. For example, if $\theta = 1$, then

$$\phi(p) = 2^k,$$

which gives $\varepsilon(p) = k + 1$. Since $\varepsilon(p) < k + 2$, p has the maximum class in S_k. We note that if $2^k + 1$ is prime then, k must be a power of 2, that is p is a Fermat prime. Hence, the Fermat primes belongs to maximum class in S_k. On the other hand, the maximum prime in S_k can be written by $q = 2^{k+1} - \alpha$, where α is odd, depends on the α we determine the class. For example, if $\alpha = 1$, then $k + 1$ must be prime. Because, if $2^n - 1$ is prime then n must be prime. This implies that k is even. Here this idea can be extended. As a result, considering the primes in the partition sets $S_1, S_2, \ldots$ will be helpful for determine the classes.
Now by previous results, we finish the section with the following conjectures:

Conjecture 5.3 By Procedure 5.2, it is easy to obtain $\varepsilon(F_5) = 30$ and $\varepsilon(F_6) = 57$. Therefore, it can be conjectured that the composite F_k Fermat numbers hold

$$\varepsilon(F_k) < 2^k.$$

Conjecture 5.4 $\varepsilon(F_k)$ is divisible by 3 when F_k is composite.

References

Bal H. S., & Bhatnagar G. (2020). Prime number conjectures from the Shapiro class structure, *Integers*, (20)

Catlin P. A. (1970) Concerning the iterated φ function, *Amer. Math. Monthly*, 77, 60–61.

Distributed Search for Fermat Number Divisors. (2023). http://www.fermatsearch.org/news.html Access Date:12/03/2023

Erdos P., & Granville A., &Pomerance C., & Spiro C. (1990). On the normal behavior of the iterates of some arithmetic functions, in: Analytic Number Theory, *Proceedings of a Conference in Honor of P. T. Bateman*, Birkhauser, Boston, 165-204.

Mills W. H. (1943). Iteration of the φ function, *Amer. Math. Monthly*, 50, 547–549.

Noe T.D. (2008). Primes in classes of the iterated totient function, *Journal of Integer Sequences*, 11

Pillai S. S. (1929). On a function connected with φ (n), Bull. Amer. Math. Soc. 35(6), 837–841.

Shapiro H. (1943). An arithmetic function arising from the φ function, *Amer. Math. Monthly*, 50, 18–30.

Sloane N. J. A. (2023). *The On-Line Encyclopedia of Integer Sequences*. https://oeis.org/ Access Date: 18/04/2023

A Study on the Comparison of the Parameter Estimation Methods in the Birnbaum-Saunders Distribution

Samet KAYA[1]
Esin KÖKSAL BABACAN[2]

1. Birnbaum-Saunders Distribution

The Birnbaum-Saunders distribution (BS) is a continuous probability distribution named after Birnbaum and Saunders in 1969. This distribution is also called the fatigue life distribution. The BS distribution was first suggested to model the defect that occurred as a result of growing cracks or failures on the surfaces of metallic parts in machines. The Birnbaum-Saunders distribution is an asymmetric and positively (right) skewed distribution used to model positive data. The Birnbaum-Saunders distribution generally has two parameters: shape (α) parameter and scale (β) parameter.

Considering the random variable T following a BS distribution with shape and scale parameters, $T \sim BS(\alpha, \beta)$, the probability density function is

$$f(t|\alpha,\beta) = \frac{1}{2\sqrt{2\pi}\alpha\beta}\left[\left(\frac{\beta}{t}\right)^{\frac{1}{2}} + \left(\frac{\beta}{t}\right)^{\frac{3}{2}}\right] \exp\left\{-\frac{1}{2\alpha^2}\left(\frac{t}{\beta} + \frac{\beta}{t} - 2\right)\right\}, \quad t > 0,\ \alpha,\beta > 0 \qquad (1)$$

and the distribution function is

$$F(t|\alpha,\beta) = \Phi\left(\frac{1}{\alpha}\left[\left(\frac{t}{\beta}\right)^{\frac{1}{2}} - \left(\frac{\beta}{t}\right)^{\frac{1}{2}}\right]\right), \quad t > 0,\ \alpha,\beta > 0\ . \qquad (2)$$

Here, Φ is the distribution function of the standard Normal distribution. The expected value and variance of the BS distribution are

$$E(T) = \beta\left(1 + \frac{1}{2}\alpha^2\right) \qquad Var(T) = (\alpha\beta)^2\left(1 + \frac{5}{4}\alpha^2\right) \qquad (3)$$

(Wang, M. et al., 2016 and Mohammadi, K. et al., 2017).

When the shape parameter (α) is constant and the scale parameter (β) takes different values, the graph of the probability density functions of the BS distribution is presented in Figure 1.

[1] Samet KAYA, Phd. Cand., The Scientific and Technological Research Council of Turkey,
[2] Esin KÖKSAL BABACAN, Assoc. Prof. Dr., Ankara University, Department of Statistics,

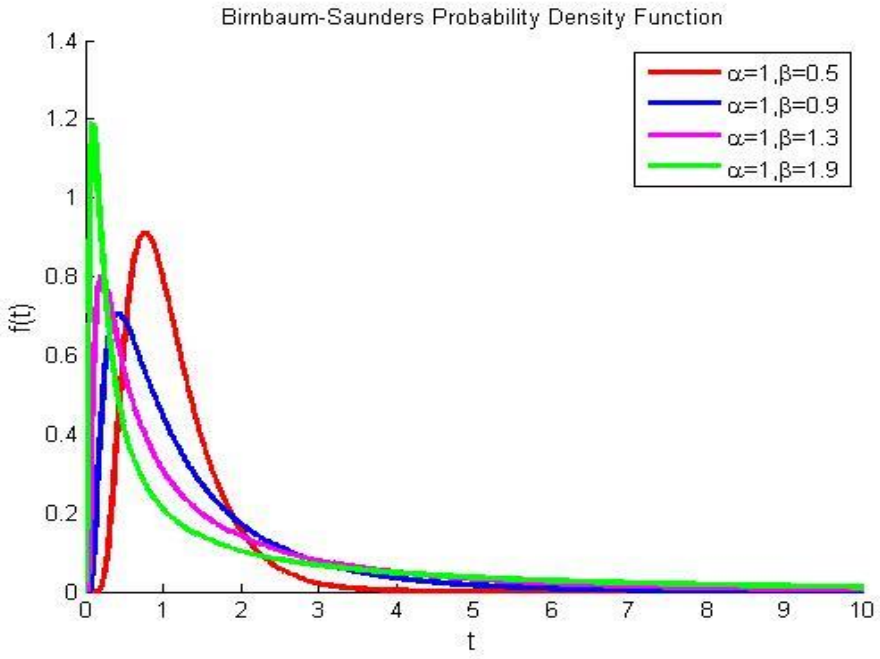

Figure 1- Probability Density Functions for different β values when the α value is constant

Likewise, when the scale parameter (β) is constant and the shape parameter (α) takes different values, the graph of the probability density functions of the Birnbaum-Saunders distribution is given in Figure 2.

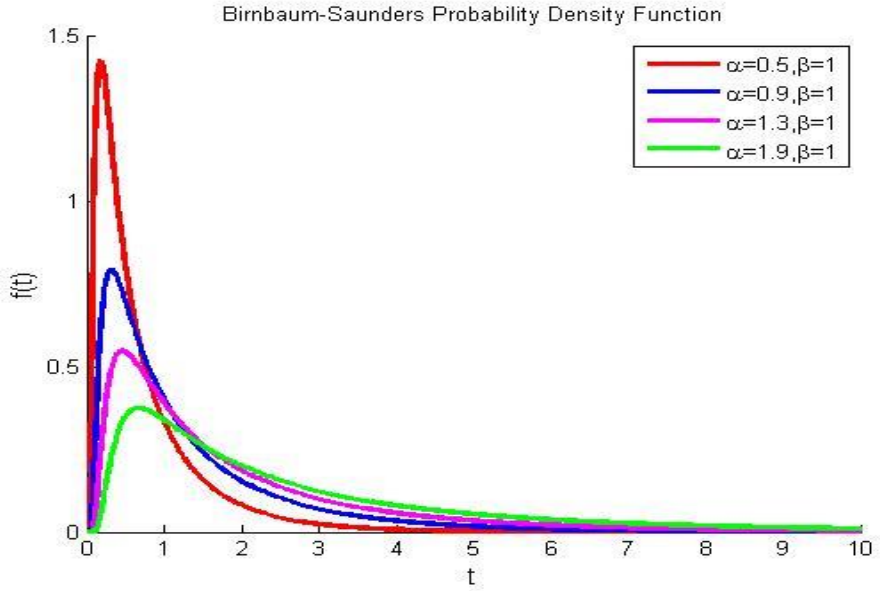

Figure 2- Probability Density Functions for different α values when the β value is constant

The BS distribution is widely used in many areas nowadays, such as water quality, agriculture, air pollution, wind velocity, business and economy, engineering sciences, environmental science, and medical science.

Regarding the BS distribution, scientific studies were conducted on the fatigue life of the 6061-T6 Aluminum coupons oscillated at 18 cycles per second by Birnbaum and Saunders (1969), the fatigue life in hours of bearings which are machine elements of a certain type

(supporting elements that decrease the friction between two machine elements in relative rotation) by Kundu et al. (2003), the tensile strength of carbon fibers in a procedure producing these fibers, which are used in fiber composite materials, by Pescim et al. (2014), the wind-related data belonging to 10 stations in the Ontario province of Canada by Mohammadi et al. (2017), the data on air pollutant concentration (SO_2) in the city of Santiago by Levia et al. (2018), and the deterioration time of a pair of disc electrodes immersed in insulating oil in an accelerated test by Sha (2018).

The rest of the paper is organized as follows. In section 2.1, maximum likelihood method is given to estimate the unknown parameters for BS Distribution. In Section 2.2, Bayesian estimation method is investigated. Section 2.2.1, estimations of the unknown BS parameters are obtained by using Lindley approximation. In Section 2.2.2, the MCMC method is explained and in subsection 2.2.2.1, the Metropolis-Hasting algorithm is given. In Section 3, a simulation study is presented to evaluate the performances of the estimators. Section 4, we use real data set to illustrate the estimation procedure developed in section 2. The last section, we make some conclusion about parameter estimation methods for BS distribution

2. Parameter Estimation in the Two-Parameter Birnbaum-Saunders Distribution

2.1 The Maximum Likelihood Method

Considering T as a random variable with a two-parameter BS distribution and $T_1, T_2, \dots, T_{\mathrm{n}}$ as an n-unit random sample taken from this distribution, the likelihood function is

$$L(\alpha,\beta|t_1,t_2,\dots,t_n)=\prod_{i=1}^{n}\left[\frac{1}{2\sqrt{2\pi}\alpha\beta}\left[\left(\frac{\beta}{t_i}\right)^{\frac{1}{2}}+\left(\frac{\beta}{t_i}\right)^{\frac{3}{2}}\right]\exp\left\{-\frac{1}{2\alpha^2}\left(\frac{t_i}{\beta}+\frac{\beta}{t_i}-2\right)\right\}\right]$$

$$=\left(\frac{1}{\sqrt{2\pi}}\right)^{n}\frac{1}{(2\alpha)^n}\frac{1}{\beta^n}\left[\prod_{i=1}^{n}\beta^{\frac{1}{2}}t_i^{-\frac{3}{2}}(t_i+\beta)\right]\exp\left\{-\frac{1}{2\alpha^2}\sum_{i=1}^{n}\left(\frac{t_i}{\beta}+\frac{\beta}{t_i}-2\right)\right\}$$

$$=\frac{1}{2^n}\frac{1}{(2\pi)^{n/2}}\frac{1}{\alpha^n}\frac{1}{\beta^{n/2}}\left[\prod_{i=1}^{n}t_i^{-\frac{3}{2}}(t_i+\beta)\right]\exp\left\{-\frac{1}{2\alpha^2}\sum_{i=1}^{n}\left(\frac{t_i}{\beta}+\frac{\beta}{t_i}-2\right)\right\} \quad (4)$$

When the logarithm of the likelihood function obtained in Equation (4) is taken,

$$LnL=-\frac{n}{2}\ln(2\pi)-n\ln(2)-n\ln(\alpha)-\frac{n}{2}\ln(\beta)-\frac{3}{2}\left(\sum_{i=1}^{n}lnt_i\right)+\sum_{i=1}^{n}ln(t_i+\beta)$$
$$-\frac{1}{2\alpha^2}\sum_{i=1}^{n}\left(\frac{t_i}{\beta}+\frac{\beta}{t_i}-2\right) \quad (5)$$

is obtained. When the partial derivative of Equation (5) is found with respect to α and equalized to zero,

$$\frac{\partial lnL}{\partial\alpha}=-\frac{n}{\alpha}+\frac{1}{\alpha^3}\left(\sum_{i=1}^{n}\left(\frac{t_i}{\beta}+\frac{\beta}{t_i}-2\right)\right)=0 \quad (6)$$

$$\alpha^2=\frac{\sum_{i=1}^{n}\left(\frac{t_i}{\beta}+\frac{\beta}{t_i}-2\right)}{n}=\frac{\sum_{i=1}^{n}t_i}{n\beta}+\frac{\beta\sum_{i=1}^{n}t_i^{-1}}{n}-2 \quad (7)$$

is obtained. Here, $s = \frac{\sum_{i=1}^{n} t_i}{n}$ and $k = \frac{\sum_{i=1}^{n} t_i^{-1}}{n}$ refer to the arithmetic and harmonic means of the sample, respectively (Mohammadi, K. et al., 2017). Accordingly, the maximum likelihood estimator of the α parameter is obtained as follows:

$$\hat{\alpha} = \left(\frac{s}{\hat{\beta}} + \frac{\hat{\beta}}{k} - 2\right)^{1/2} \tag{8}$$

To determine the maximum likelihood estimator of the β parameter, $\hat{\beta}$, the partial derivative of Equation (5) should be found with respect to β and equalized to zero. Accordingly,

$$\frac{\partial lnL}{\partial \beta} = -\frac{n}{2\beta} + \sum_{i=1}^{n} \frac{1}{(t_i+\beta)} - \frac{1}{2\alpha^2}\left(\sum_{i=1}^{n}\left(\frac{-t_i}{\beta^2} + \frac{1}{t_i}\right)\right) = 0 \tag{9}$$

To solve this equation, which is not linear according to $\hat{\beta}$, iterative methods can be used. The Newton-Raphson method is one of the commonly used methods.

2.2 The Bayesian Estimation Method

In the studies performed by Archar (1993) and Xu & Tang (2010), the Bayesian method was used in the Birnbaum-Saunders distribution, and an uninformative prior distribution was used as a prior distribution in the parameter estimation. In their studies, Archar (1993) and Wang et al. (2016) used the Inverse Gamma distribution as an informative prior distribution for α and β parameters.

In this study, inferences are made using the exponential distribution as a prior distribution for α and β parameters. Under the assumption of α and β parameters independent of each other, the prior probability density functions are built as follows:

$$\begin{aligned} \Pi_1(\alpha|\mathrm{c}) &= ce^{-c\alpha}, \quad \alpha > 0 \\ \Pi_2(\beta|\mathrm{b}) &= be^{-b\beta}, \quad \beta > 0 \end{aligned} \tag{12}$$

The likelihood function of the Birnbaum-Saunders distribution is stated as

$$L(\alpha,\beta|t_1,t_2,\dots,t_n) = \frac{1}{2^n}\frac{1}{(2\pi)^{n/2}}\frac{1}{\alpha^n}\frac{1}{\beta^{n/2}}\left[\prod_{i=1}^{n} t_i^{-\frac{3}{2}}(t_i+\beta)\right]\exp\left\{-\frac{1}{2\alpha^2}\sum_{i=1}^{n}\left(\frac{t_i}{\beta}+\frac{\beta}{t_i}-2\right)\right\} \tag{13}$$

in Equation (4). To obtain the Bayes estimator, the prior distribution is first multiplied by the likelihood function.

$$\begin{aligned} f(\alpha,\beta,t_1,t_2,\dots,t_n) &= \Pi_1(\alpha|\mathrm{c}) \times \Pi_2(\beta|\mathrm{b}) \times L(\alpha,\beta|t_1,t_2,\dots,t_n) \\ &= ce^{-c\alpha}be^{-b\beta}\,\frac{1}{2^n}\,\frac{1}{(2\pi)^{n/2}}\,\frac{1}{\alpha^n}\,\frac{1}{\beta^{n/2}}\left[\prod_{i=1}^{n} t_i^{-\frac{3}{2}}(t_i+\beta)\right]\exp\left\{-\frac{1}{2\alpha^2}\sum_{i=1}^{n}\left(\frac{t_i}{\beta}+\frac{\beta}{t_i}-2\right)\right\} \\ &= cbe^{-(c\alpha+b\beta)}\,\frac{1}{2^n}\,\frac{1}{(2\pi)^{n/2}}\,\frac{1}{\alpha^n}\,\frac{1}{\beta^{\frac{n}{2}}}\left[\prod_{i=1}^{n} t_i^{-\frac{3}{2}}(t_i+\beta)\right]\exp\left\{-\frac{1}{2\alpha^2}\sum_{i=1}^{n}\left(\frac{t_i}{\beta}+\frac{\beta}{t_i}-2\right)\right\} \end{aligned} \tag{14}$$

Then, the integral is taken with respect to both parameters, and the marginal likelihood of t is obtained.

$$\begin{aligned} f(t_1,t_2,\dots,t_n) &= \int_0^\infty\int_0^\infty f(\alpha,\beta,t_1,t_2,\dots,t_n)\,d\alpha d\beta \\ &= cb\,\frac{1}{2^n}\,\frac{1}{(2\pi)^{n/2}}\int_0^\infty\int_0^\infty \frac{1}{\alpha^n}\frac{1}{\beta^{\frac{n}{2}}}e^{-(c\alpha+b\beta)}\left[\prod_{i=1}^{n} t_i^{-\frac{3}{2}}(t_i+\beta)\right]\exp\left\{-\frac{1}{2\alpha^2}\sum_{i=1}^{n}\left(\frac{t_i}{\beta}+\frac{\beta}{t_i}-2\right)\right\}d\alpha\,d\beta \end{aligned} \tag{15}$$

In the last step, these are proportioned to each other, and the common posterior probability density function is obtained for both parameters in the following way:

$$f(\alpha,\beta|t_1,t_2,\dots,t_n) = \frac{cbe^{-(c\alpha+b\beta)}\frac{1}{2^n}\frac{1}{(2\pi)^{n/2}}\frac{1}{\alpha^n}\frac{1}{\beta^{\frac{n}{2}}}\left[\prod_{i=1}^{n} t_i^{-\frac{3}{2}}(t_i+\beta)\right]\exp\left\{-\frac{1}{2\alpha^2}\sum_{i=1}^{n}\left(\frac{t_i}{\beta}+\frac{\beta}{t_i}-2\right)\right\}}{\int_0^\infty\int_0^\infty cbe^{-(c\alpha+b\beta)}\frac{1}{2^n}\frac{1}{(2\pi)^{n/2}}\frac{1}{\alpha^n}\frac{1}{\beta^{\frac{n}{2}}}\left[\prod_{i=1}^{n} t_i^{-\frac{3}{2}}(t_i+\beta)\right]\exp\left\{-\frac{1}{2\alpha^2}\sum_{i=1}^{n}\left(\frac{t_i}{\beta}+\frac{\beta}{t_i}-2\right)\right\}d\alpha\,d\beta}$$

$$f(\alpha,\beta|t_1,t_2,\dots,t_n) = \frac{e^{-(c\alpha+b\beta)}\frac{1}{\alpha^n}\frac{1}{\beta^{\frac{n}{2}}}\left[\prod_{i=1}^{n} t_i^{-\frac{3}{2}}(t_i+\beta)\right]\exp\left\{-\frac{1}{2\alpha^2}\sum_{i=1}^{n}\left(\frac{t_i}{\beta}+\frac{\beta}{t_i}-2\right)\right\}}{\int_0^\infty\int_0^\infty e^{-(c\alpha+b\beta)}\frac{1}{\alpha^n}\frac{1}{\beta^{\frac{n}{2}}}\left[\prod_{i=1}^{n} t_i^{-\frac{3}{2}}(t_i+\beta)\right]\exp\left\{-\frac{1}{2\alpha^2}\sum_{i=1}^{n}\left(\frac{t_i}{\beta}+\frac{\beta}{t_i}-2\right)\right\}d\alpha\,d\beta} \quad (16)$$

To obtain posterior marginal probability density functions related to the parameters, the integral is taken with respect to the parameters, respectively. Thus, the marginal posterior probability density functions are obtained as

$$f_1(\alpha|t_1,t_2,\dots,t_n) = \int_0^\infty f(\alpha,\beta|t_1,t_2,\dots,t_n)\,d\beta = \int_0^\infty \frac{e^{-(c\alpha+b\beta)}\frac{1}{\alpha^n}\frac{1}{\beta^{\frac{n}{2}}}\left[\prod_{i=1}^{n} t_i^{-\frac{3}{2}}(t_i+\beta)\right]\exp\left\{-\frac{1}{2\alpha^2}\sum_{i=1}^{n}\left(\frac{t_i}{\beta}+\frac{\beta}{t_i}-2\right)\right\}}{\int_0^\infty\int_0^\infty e^{-(c\alpha+b\beta)}\frac{1}{\alpha^n}\frac{1}{\beta^{\frac{n}{2}}}\left[\prod_{i=1}^{n} t_i^{-\frac{3}{2}}(t_i+\beta)\right]\exp\left\{-\frac{1}{2\alpha^2}\sum_{i=1}^{n}\left(\frac{t_i}{\beta}+\frac{\beta}{t_i}-2\right)\right\}d\alpha\,d\beta}\,d\beta \quad (17)$$

and

$$f_2(\beta|t_1,t_2,\dots,t_n) = \int_0^\infty f(\alpha,\beta|t_1,t_2,\dots,t_n)\,d\alpha = \int_0^\infty \frac{e^{-(c\alpha+b\beta)}\frac{1}{\alpha^n}\frac{1}{\beta^{\frac{n}{2}}}\left[\prod_{i=1}^{n} t_i^{-\frac{3}{2}}(t_i+\beta)\right]\exp\left\{-\frac{1}{2\alpha^2}\sum_{i=1}^{n}\left(\frac{t_i}{\beta}+\frac{\beta}{t_i}-2\right)\right\}}{\int_0^\infty\int_0^\infty e^{-(c\alpha+b\beta)}\frac{1}{\alpha^n}\frac{1}{\beta^{\frac{n}{2}}}\left[\prod_{i=1}^{n} t_i^{-\frac{3}{2}}(t_i+\beta)\right]\exp\left\{-\frac{1}{2\alpha^2}\sum_{i=1}^{n}\left(\frac{t_i}{\beta}+\frac{\beta}{t_i}-2\right)\right\}d\alpha\,d\beta}\,d\alpha \quad (18)$$

Considering the estimators sought under the squared loss function as the expected values of these distributions, the expected values are obtained as

$$\hat{\alpha} = E(\alpha) = \int_0^\infty\int_0^\infty \frac{e^{-(c\alpha+b\beta)}\frac{1}{\alpha^{n-1}}\frac{1}{\beta^{\frac{n}{2}}}\left[\prod_{i=1}^{n} t_i^{-\frac{3}{2}}(t_i+\beta)\right]\exp\left\{-\frac{1}{2\alpha^2}\sum_{i=1}^{n}\left(\frac{t_i}{\beta}+\frac{\beta}{t_i}-2\right)\right\}}{\int_0^\infty\int_0^\infty e^{-(c\alpha+b\beta)}\frac{1}{\alpha^n}\frac{1}{\beta^{\frac{n}{2}}}\left[\prod_{i=1}^{n} t_i^{-\frac{3}{2}}(t_i+\beta)\right]\exp\left\{-\frac{1}{2\alpha^2}\sum_{i=1}^{n}\left(\frac{t_i}{\beta}+\frac{\beta}{t_i}-2\right)\right\}d\alpha\,d\beta}\,d\beta\,d\alpha$$

and

$$\hat{\beta} = E(\beta) = \int_0^\infty\int_0^\infty \frac{e^{-(c\alpha+b\beta)}\frac{1}{\alpha^n}\frac{1}{\beta^{\frac{n}{2}-1}}\left[\prod_{i=1}^{n} t_i^{-\frac{3}{2}}(t_i+\beta)\right]\exp\left\{-\frac{1}{2\alpha^2}\sum_{i=1}^{n}\left(\frac{t_i}{\beta}+\frac{\beta}{t_i}-2\right)\right\}}{\int_0^\infty\int_0^\infty e^{-(c\alpha+b\beta)}\frac{1}{\alpha^n}\frac{1}{\beta^{\frac{n}{2}}}\left[\prod_{i=1}^{n} t_i^{-\frac{3}{2}}(t_i+\beta)\right]\exp\left\{-\frac{1}{2\alpha^2}\sum_{i=1}^{n}\left(\frac{t_i}{\beta}+\frac{\beta}{t_i}-2\right)\right\}d\alpha\,d\beta}\,d\alpha\,d\beta \quad (19)$$

Numeric calculation methods can be used to solve such integrals. However, major errors and sample sensitivity are encountered when it is desired to obtain results using these methods. Instead, it will be more appropriate to apply the methods of the approaches developed for such cases. In this study, inferences are made using Lindley's approach. In Bayesian inference, the simulation methods developed to solve such integrals have been used in recent years. Using these methods, known as Markov chain Monte Carlo (MCMC) simulation methods, large samples are drawn from the posterior distribution, and these samples are used for inference. In this study, inferences were made using the Metropolis-Hastings algorithm, among the MCMC methods, and the results are compared with those obtained via Lindley's approach and the maximum likelihood method. To this end, Lindley's approach is first described, and the results are obtained for the BS distribution. Afterward, the Metropolis-Hastings algorithm of the MCMC methods is explained.

2.2.1. Lindley's Approach:

In general, difficulties arise in obtaining the Bayesian estimators expressed as the ratio of two integrals. The method of Lindley's approach is developed by Lindley (1980) regarding the approximate solution of the difficult integrals in multi-parameter distributions when n is large enough. When an informative prior distribution is used, the steps of Lindley's approach with regards to the BS distribution are obtained as follows.

$$g(\alpha,\beta) = ce^{-c\alpha} \times be^{-b\beta} \ , \quad log\big(g(\alpha,\beta)\big) = logc + logb - (c\alpha + b\beta)$$

$$g_1 = \frac{d\ log\big(g(\alpha,\beta)\big)}{d\alpha} = -c, \qquad g_2 = \frac{d\ ln\big(g(\alpha,\beta)\big)}{d\beta} = -b$$

The likelihood function and derivatives,

$$L(t_i,\beta,\alpha) = \frac{1}{2^n}\frac{1}{(2\pi)^{n/2}}\frac{1}{\alpha^n}\frac{1}{\beta^{n/2}}\left[\prod_{i=1}^{n} t_i^{-\frac{3}{2}}(t_i+\beta)\right]\exp\left\{-\frac{1}{2\alpha^2}\sum_{i=1}^{n}\left(\frac{t_i}{\beta}+\frac{\beta}{t_i}-2\right)\right\}$$

$$LnL = -\frac{n}{2}\ln(2\pi) - n\ln(2) - n\ln(\alpha) - \frac{n}{2}\ln(\beta) - \frac{3}{2}\left(\sum_{i=1}^{n} lnt_i\right) + \sum_{i=1}^{n} ln(t_i+\beta) - \frac{1}{2\alpha^2}\sum_{i=1}^{n}\left(\frac{t_i}{\beta}+\frac{\beta}{t_i}-2\right)$$

$$L_1 = \frac{dLnL}{d\alpha} = -\frac{n}{\alpha} + \frac{1}{\alpha^3}\left(\sum_{i=1}^{n}\left(\frac{t_i}{\beta}+\frac{\beta}{t_i}-2\right)\right)$$

$$L_{11} = \frac{d^2LnL}{d\alpha^2} = \frac{n}{\alpha^2} - \frac{3}{\alpha^4}\left(\sum_{i=1}^{n}\left(\frac{t_i}{\beta}+\frac{\beta}{t_i}-2\right)\right)$$

$$L_{111} = \frac{d^3LnL}{d\alpha^3} = -\frac{2n}{\alpha^3} + \frac{12}{\alpha^5}\left(\sum_{i=1}^{n}\left(\frac{t_i}{\beta}+\frac{\beta}{t_i}-2\right)\right)$$

$$L_2 = \frac{dLnL}{d\beta} = -\frac{n}{2\beta} + \sum_{i=1}^{n}\frac{1}{(t_i+\beta)} - \frac{1}{2\alpha^2}\left(\sum_{i=1}^{n}\left(\frac{-t_i}{\beta^2}+\frac{1}{t_i}\right)\right)$$

$$L_{22} = \frac{d^2LnL}{d\beta^2} = \frac{n}{2\beta^2} + \sum_{i=1}^{n}\frac{-1}{(t_i+\beta)^2} - \frac{1}{2\alpha^2}\left(\sum_{i=1}^{n}\left(\frac{2t_i}{\beta^3}\right)\right)$$

$$L_{222} = \frac{d^3LnL}{d\beta^3} = -\frac{n}{\beta^3} + \sum_{i=1}^{n}\frac{2(t_i+\beta)}{(t_i+\beta)^4} - \frac{1}{2\alpha^2}\left(\sum_{i=1}^{n}\left(\frac{-6t_i}{\beta^4}\right)\right)$$

$$L_{12} = L_{21} = \frac{d^2LnL}{d\alpha d\beta} = \frac{1}{\alpha^3}\left(\sum_{i=1}^{n}\left(\frac{-t_i}{\beta^2}+\frac{1}{t_i}\right)\right)$$

$$L_{211} = L_{121} = L_{112} = \frac{d^3LnL}{d\alpha^2 d\beta} = \frac{-3}{\alpha^4}\left(\sum_{i=1}^{n}\left(\frac{-t_i}{\beta^2}+\frac{1}{t_i}\right)\right)$$

$$L_{212} = L_{221} = L_{122} = \frac{d^3LnL}{d\alpha d\beta^2} = \frac{1}{\alpha^3}\left(\sum_{i=1}^{n}\left(\frac{2t_i}{\beta^3}\right)\right)$$

$$G_{ij} = \begin{bmatrix} L_{11} & L_{12} \\ L_{21} & L_{22} \end{bmatrix}^{-1}$$

$$G_{ij} = \frac{1}{\det(G_{ij})}\begin{bmatrix} L_{22} & -L_2 \\ -L_{21} & L_{11} \end{bmatrix}$$

$$= \frac{1}{\left(\frac{n}{\alpha^2} - \frac{3}{\alpha^4}\left(\sum_{i=1}^{n}\left(\frac{t_i}{\beta} + \frac{\beta}{t_i} - 2\right)\right)\right)\left(\frac{n}{2\beta^2} + \sum_{i=1}^{n}\frac{-1}{(t_i+\beta)^2} - \frac{1}{2\alpha^2}\left(\sum_{i=1}^{n}\left(\frac{2t_i}{\beta^3}\right)\right)\right) - \left(\frac{1}{\alpha^3}\left(\sum_{i=1}^{n}\left(\frac{-t_i}{\beta^2} + \frac{1}{t_i}\right)\right)\right)^2}$$

$$\begin{vmatrix} \frac{n}{2\beta^2} + \sum_{i=1}^{n}\frac{-1}{(t_i+\beta)^2} - \frac{1}{2\alpha^2}\left(\sum_{i=1}^{n}\left(\frac{2t_i}{\beta^3}\right)\right) & -\frac{1}{\alpha^3}\left(\sum_{i=1}^{n}\left(\frac{-t_i}{\beta^2} + \frac{1}{t_i}\right)\right) \\ -\frac{1}{\alpha^3}\left(\sum_{i=1}^{n}\left(\frac{-t_i}{\beta^2} + \frac{1}{t_i}\right)\right) & \frac{n}{\alpha^2} - \frac{3}{\alpha^4}\left(\sum_{i=1}^{n}\left(\frac{t_i}{\beta} + \frac{\beta}{t_i} - 2\right)\right) \end{vmatrix}$$

$$T = \left(\frac{n}{\alpha^2} - \frac{3}{\alpha^4}\left(\sum_{i=1}^{n}\left(\frac{t_i}{\beta} + \frac{\beta}{t_i} - 2\right)\right)\right)\left(-\frac{n}{2\beta^2} + \sum_{i=1}^{n}\frac{-1}{(t_i+\beta)^2} - \frac{1}{2\alpha^2}\left(\sum_{i=1}^{n}\left(\frac{2t_i}{\beta^3}\right)\right)\right) - \left(\frac{1}{\alpha^3}\left(\sum_{i=1}^{n}\left(\frac{-t_i}{\beta^2} + \frac{1}{t_i}\right)\right)\right)^2$$

$$U = \frac{n}{2\beta^2} + \sum_{i=1}^{n}\frac{-1}{(t_i+\beta)^2} - \frac{1}{2\alpha^2}\left(\sum_{i=1}^{n}\left(\frac{2t_i}{\beta^3}\right)\right)$$

$$V = -\frac{1}{\alpha^3}\left(\sum_{i=1}^{n}\left(\frac{-t_i}{\beta^2} + \frac{1}{t_i}\right)\right)$$

$$W = \frac{n}{\alpha^2} - \frac{3}{\alpha^4}\left(\sum_{i=1}^{n}\left(\frac{t_i}{\beta} + \frac{\beta}{t_i} - 2\right)\right)$$

$$G_{ij} = \begin{bmatrix} \frac{U}{T} & \frac{V}{T} \\ \frac{V}{T} & \frac{W}{T} \end{bmatrix}$$

If $\mathrm{U}(\alpha,\beta) = \alpha,\ U_1 = 1, U_2 = U_{12} = U_{21} = U_{11} = U_{22} = 0$

$$\hat{\alpha}_{BAYES} = \hat{\alpha}_{Mle} + G_{11}g_1 + G_{12}g_2 + \frac{1}{2}(L_{111}{G_{11}}^2 + 3L_{112}G_{11}G_{12} + L_{122}(G_{11}G_{22} + 2{G_{12}}^2) + L_{222}G_{12}G_{22})$$

If $\mathrm{U}(\alpha,\beta) = \beta,\ U_2 = 1, U_1 = U_{12} = U_{21} = U_{11} = U_{22} = 0$

$$\hat{\beta}_{BAYES} = \hat{\beta}_{Mle} + G_{21}g_1 + G_{22}g_2 + \frac{1}{2}\left(L_{222}{G_{22}}^2 + L_{112}(G_{11}G_{22} + 2{G_{12}}^2\right) + 3L_{122}G_{12}G_{22} + L_{111}G_{11}G_{12})$$

Here, $\hat{\alpha}_{Mle}$ and $\hat{\beta}_{Mle}$ are the maximum likelihood estimators of α and β parameters, respectively.

2.2.2 The Markov Chain Monte Carlo Methods

The most significant difficulty in the Bayesian approach is the use of integrals with high dimensions to obtain posterior distributions. In the calculation of integrals with high dimensions, the MCMC methods, which draw samples from complicated distributions using the simulation method, are first used by physicists. In recent years, they have been employed to solve many problems, particularly in the field of Bayesian statistics.

The Metropolis-Hastings algorithm and the Gibbs algorithm are the most used MCMC methods. Using these methods, samples are drawn from the relevant distribution, and then the sample means are calculated to find the expected values approximately.

2.2.2.1. The Metropolis-Hastings Algorithm

The Metropolis algorithm was generalized as a statistical simulation tool by Hastings (1970) and his student Peskun (1973, 1981) to overcome the multi-dimensionality problem brought together by the systematic Monte Carlo methods, as previously emphasized by Metropolis et al. (1953). The most important aspect distinguishing this algorithm from the Metropolis algorithm is its applicability to both symmetric and asymmetric distributions. Moreover, having asymmetric proposal distributions can be useful for increasing the convergence rate. The Metropolis-Hastings algorithm uses the probability of acceptance of

$$\alpha = \min\left(1, \frac{p(\theta^*)}{p(\theta^{t-1})}\,\frac{g(\theta^{t-1}|\theta^*)}{g(\theta^*|\theta^{t-1})}\right)$$

(Koç, 2020).

3. Application Studies

3.1 The Simulation Study

In this section, a program is written using MATLAB, and 100 trials are performed. The estimation results of the parameters of the BS distribution obtained via the maximum likelihood and Bayesian methods are compared. The sample size is selected as (n=30, 60, 90, 120, 150). When $\boldsymbol{\alpha = 2}$, $\boldsymbol{\beta = 3, 4, 5}$ is considered for each sample size, and the samples are produced through simulation.

In Lindley's approach and the Metropolis-Hastings method used in Bayesian inference, the exponential distribution is used as the prior distribution for unknown $\boldsymbol{\alpha}$ and $\boldsymbol{\beta}$ parameters. In the simulation study, the parameters of the prior distributions are selected as $\boldsymbol{c = 2}$ and $\boldsymbol{b = 2}$ while the numbers are produced.

To compare the performance of the estimation results obtained via the maximum likelihood method and Bayesian methods, the total mean squared error of both parameters is selected as a criterion. Accordingly, the selected criterion is calculated as follows:

$$\text{MSE} = \frac{(\boldsymbol{\beta}-\widehat{\boldsymbol{\beta}})^{\mathbf{2}}+(\boldsymbol{\gamma}-\widehat{\boldsymbol{\gamma}})^{\mathbf{2}}}{\boldsymbol{n}}$$

Accordingly, the simulation results are presented in the table below.

Table-1 Simulation results for α=2 and β=3,4,5

Parameter Values	n	Maximum Likelihood Method			Bayesian Method (Lindley's Approach)			Bayesian Method (MCMC)		
		$\widehat{\alpha}$	$\widehat{\beta}$	MSE	$\widehat{\alpha}$	$\widehat{\beta}$	MSE	$\widehat{\alpha}$	$\widehat{\beta}$	MSE
$\alpha = 2$ $\beta = 3$	30	2.033231	2.903830	0.463431	2.378851	2.995125	2.844704	2.080423	3.048188	0.489536
	60	2.088422	2.968531	0.238361	2.224810	2.992492	0.379010	2.118109	3.040453	0.252182
	90	1.998187	2.956300	0.147528	2.083621	2.965097	0.192451	2.020121	3.004934	0.152909
	120	2.030294	2.957421	0.121240	2.092607	2.963998	0.145285	2.052357	2.988867	0.124919
	150	2.012433	2.967696	0.086489	2.059872	2.972246	0.097276	2.028577	2.995835	0.089225
$\alpha = 2$ $\beta = 4$	30	1.999578	3.881979	0.601647	2.329217	3.885083	1.734017	2.045420	4.076068	0.653101
	60	1.982020	3.945078	0.313348	2.087386	3.948519	0.392303	2.013700	4.033043	0.330836
	90	2.050649	3.977124	0.161783	2.118436	3.978816	0.190577	2.073217	4.033412	0.167043
	120	1.964360	3.963736	0.128514	2.009450	3.964831	0.137404	1.999841	4.007540	0.133563
	150	2.031806	3.999533	0.115663	2.070249	4.000490	0.126040	2.043862	4.031660	0.122610
$\alpha = 2$ $\beta = 5$	30	2.065571	4.746797	0.884232	2.314588	4.750074	1.454636	2.125104	4.980367	0.901864
	60	2.063355	4.963706	0.367009	2.152887	4.495168	0.436567	2.095072	5.079223	0.394721
	90	2.016943	4.888693	0.256805	2.071258	4.889532	0.281650	2.035762	4.962406	0.250380
	120	1.995327	4.966306	0.179971	2.032211	4.966816	0.191649	2.008790	5.021907	0.190528
	150	1.996360	4.944510	0.165518	1.994605	4.944895	0.170212	1.999954	4.990478	0.170930

When the above-stated table is viewed, the estimates are observed to be quite close to the real values. The results of the Bayesian estimation obtained using the MCMC method are found to be closer to the real values compared to other estimation methods. As the number of samples increased, the mean squared error decreased for all methods. Since Lindley's approach is calculated using the maximum likelihood estimates, it gives results close to the maximum likelihood estimates, and the mean squared error is found to be quite big in small samples.

3.2 Real Data Application

In this section, an application study is carried out on the real data set, unlike the previous section. The data are taken from the article of Cooray and Ananda (2008). Kevlar 49/epoxy fibers with high strength used in fiber optic cables, plastic reinforcement and ropes are subjected to continuous pressure (at a tensile level of 90%), and their tension-failure lives are measured until their rupture. In this sense, 101 values including the rupture time of fibers are stated below. 0.01, 0.01, 0.02, 0.02, 0.02, 0.03, 0.03, 0.04, 0.05, 0.06, 0.07, 0.07,0.08, 0.09, 0.09, 0.1, 0.1, 0.11, 0.11, 0.12, 0.13, 0.18, 0.19, 0.2, 0.23, 0.24, 0.24, 0.29 , 0.34, 0.35, 0.36, 0.38, 0.4, 0.42, 0.43, 0.52, 0.54, 0.56, 0.6, 0.6, 0.63, 0.65, 0.67, 0.68, 0.72, 0.72, 0.72, 0.73, 0.79, 0.79, 0.8, 0.8, 0.83, 0.85, 0.9, 0.92, 0.95, 0.99, 1, 1.01, 1.02, 1.03, 1.05, 1.1, 1.1, 1.11, 1.15, 1.18, 1.2, 1.29, 1.31, 1.33, 1.34, 1.4, 1.43, 1.45, 1.5, 1.51, 1.52, 1.53, 1.54, 1.54, 1.55, 1.58, 1.60, 1.63, 1.64, 1.8, 1.8, 1.81, 2.02, 2.05, 2.14, 2.17, 2.33, 3.03, 3.03, 3.34, 4.2, 4.69, 7.89

The program is run for these data, and the following results are obtained.
Table-2 Parameter Estimation Results

Maximum Likelihood		Bayesian (Lindley's)		Bayesian (MCMC)	
$\widehat{\alpha}$	$\widehat{\beta}$	$\widehat{\alpha}$	$\widehat{\beta}$	$\widehat{\alpha}$	$\widehat{\beta}$
0.336199	1.843749	0.337676	1.836161	0.333175	1.870693

Concerning the results, the estimates obtained via the maximum likelihood method and the Bayesian estimates obtained using the MCMC method and Lindley's approach are close to each other. To observe the suitability of these estimation results for the model, the graphs of the probability density functions and the cumulative distribution functions of the data are presented below.

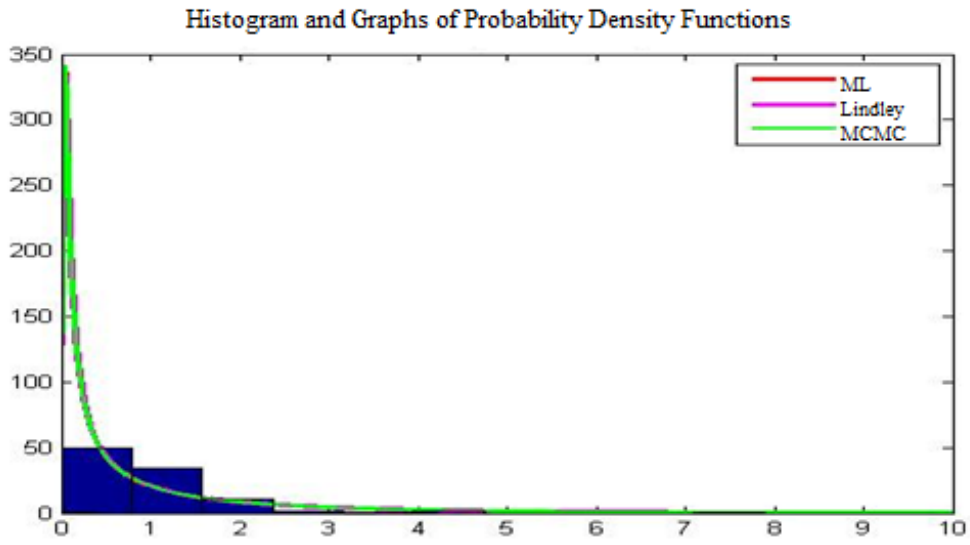

Figure-3 Histogram and Probability Density Functions Obtained with Estimates

It is observed that the graphs are in agreement with each other and with the histogram related to the data.

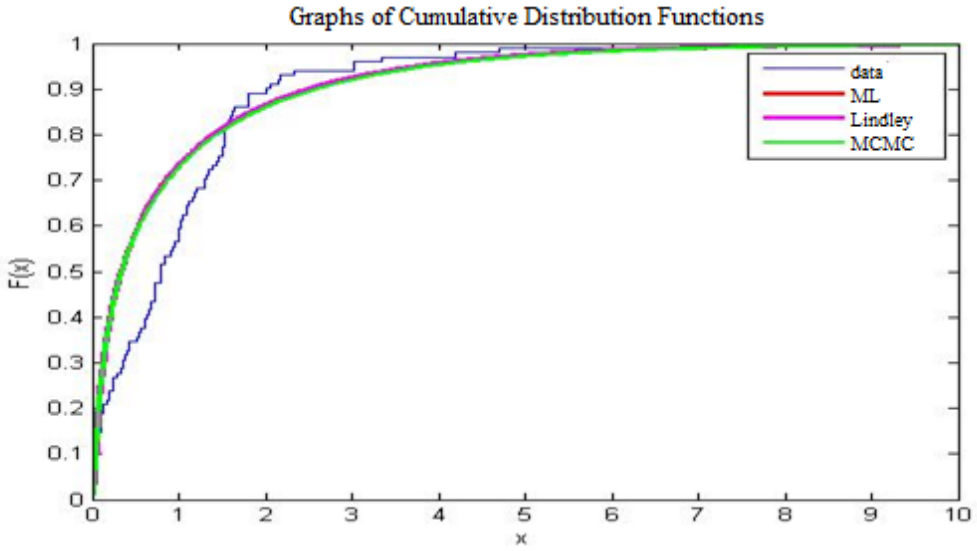

Figure-4 Empirical Distribution Function and Cumulative Distribution Functions Obtained with Estimates

In the graphs, all the three estimation methods used are observed to have produced results close to each other.

4. Conclusion

In this study, the BS distribution is first mentioned in general terms. Afterward, the maximum likelihood method and Bayesian method, which are used to estimate the parameters of the BS distribution, are explained. In Bayesian inference, the exponential distribution is used for calculations in the prior distributions related to the parameters. As a result of these calculations, the closed form of the posterior distribution could not be obtained, and therefore, the estimate values of the parameters are reached using Lindley's approach and the Metropolis-Hastings algorithms. The mean squared error criterion is employed to compare the estimation methods obtained.

In the simulation study, the program is run again and again for different sample sizes and different parameter values to make inferences. According to these estimation results, the mean squared error is observed to decrease for all the estimation methods as the number of samples increased. In Lindley's approach, the mean squared error is found big in small samples. The parameter estimation values obtained with estimators are observed to be close to the real parameter values. Since the maximum likelihood estimation is used in Lindley's approach, results are close to the maximum likelihood estimates in parameter estimations.

According to the results obtained in the real data study, parameter estimation values are close to each other. The graphs indicate that the results are compatible with the real data.

Regarding the simulation and real data, the results obtained using Lindley's and Metropolis-Hastings algorithms are similar to those obtained via the maximum likelihood method. In light of these results, it is possible to say that the Bayesian method can be used as an alternative to the maximum likelihood method.

References

Achcar, A. J., 1993. Inferences for the Birnbaum-Saunders fatigue life model using Bayesian methods. Computational Statistics & Data Analysis, 15 367-380 doi: 10.1016/0167-9473(93)90170-X

Bikramjit, B., Tiwari D., Kundu, D., Prasad, R. 2009. Is Weibull Distribution The Most Appropriate Statistical Strength Distribution for Brittle Materials. Ceramics International Journey 35 (2009), 237-246. doi: 10.1016/j.ceramint.2007.10.003

Birnbaum, W., Z., Saunders, S., C. 1969. Estimation for a Family of Life Distributions with Applications to Fatigue. Journal of Applied Probability, 6-2: 328-347 doi: 10.2307/3212004

Cooray, K., A. M. 2008. A Generalization of the Half-Normal Distribution with Applications to Lifetime Data. Communications in Statistics—Theory and Methods, 37:9, 1323-1337. doi: 10.1080/03610920701826088

Koç, Y., 2020. Weibull Dağılımının Parametrelerinin Bayesci Yöntemle Tahmini [The Estimation of the Weibull Distribution Parameters via the Bayesian Method]. Ankara Üniversitesi Fen Bilimleri Enstitüsü Yüksek Lisans Tezi

Leiva, V., Barros, M., Paula, G.A. and Sanhueza, A. 2008, Generalized Birnbaum-Saunders distributions applied to air pollutant concentration. Environmetrics, 19: 235-249. doi: 10.1002/env.861

Mohammadi, K., Alavi, O., McGowan, G. J., 2017. Use of Birnbaum-Saunders distribution for estimating wind speed and wind power probability distributions: A review. Energy Conversion and Management 143, 109–122. doi.:10.1016/j.enconman.2017.03.083

Ng., H.K.T., Kundu, D. and Balakrishnan, N. 2003. Modified moment estimation for the two-parameter Binbaum-Saunders distribution. Computational Statistics & Data Analysis. Vol:43, 283-298. doi:10.1016/S0167-9473(02)00254-2

Nwobi F. N., Ugomma. C. 2014. A Comparison of Methods for the Estimation of Weibull Distribution Parameters. Metodoloski Zvezki, Vol. 11, No. 1, 65-78.

Pescim, R., R., et al. 2014. The Kummer beta Birnbaum-Saunders: An alternative fatigue life distribution. Hacettepe Journal of Mathematics and Statistics. Vol:43(3), 473-510

Sha, N. 2018. Statistical Inference for Progressive Stress Accelerated Life Testing with Birnbaum-Saunders Distribution. Stats, 1, 189–203; doi:10.3390/stats1010014

Wang, M., Sun, X. and Park, C., 2016. Bayesian analysis of Birnbaum-Saunders distribution via the generalized ratio-of-uniform method. Comput Stat 31: 207–225. doi: 10.1007/s00180-015-0629-z

Xu, Y., et al. 2001. Optimization of sample number for Weibull function of brittle materials strength. Ceramics International Journey 27(2001) 239-241. doi:10.1016/S0272-8842(00)00056-0

Xu, A., Tang, Y., 2010. Reference analysis for Birnbaum-Saunders distribution. Computational Statistics and Data Analysis, Volume 54, Issue 1,185-192. doi:10.1016/j.csda.2009.08.004.

Rock Engineering Concept for Urban Development

Mehmet Kemal Gokay[1]

1. Introduction

In the definition of engineering, there are *"guiding instructions, orders"* that will enable the teams that make up the workforce to control their work and do it right, as well as scientifically based *"decisions"* made during the design phase of work and projects. From the first ages of history to the present, the people who provide engineering services have continued their profession by adding their own experiences to those previously transferred to them in order to fulfil their routine responsibilities in their work & projects. Experiences gained in different jobs & workplaces (in different projects) can have comprehensive features, with regional and local differences. Projects with different; purposes, boundaries, possibilities, outcomes, and working methods & workforces (chosen for relevant objectives), have shaped professions & engineering services over time with different engineering practices and decisions made by the contributing engineers. Occupations that developed in different parts of the world without being aware of each other have led to the differentiation of professions, which have developed for similar purposes, to offer outcomes (products) with different and unique experiences due to different raw material opportunities in different regions. This means that projects made to meet the different needs of people can have different solutions, and engineers can produce different solutions with different experiences. These experiences in the field of *"ground engineering"* have also manifested itself in the efforts spent in understanding (analysing) the mechanical behaviour of solid earth materials (Hudson & Harrison, 1997; Aydan, 2017; Das, 2019). When it comes to solid materials (substances); all natural solids *(rock/soil types)*, organic materials, manufactured metals and alloys, plastics, ceramics, bricks, etc. are somehow related to earth crust. Earth crust's main solid materials are rock masses and their generation and re-generation as rock formations from magma have been influenced by the interactions of climate, bioactivity, gravity, radiation, and magmatic activities in time have formed the rock/soil formations (earth's crust) around us. This rock formation mechanism is constantly being (searched) explored to find out economical potentials such as; cavities (voids, spaces) in the earth's crust, groundwater, mineral ores, energy resources (oil, natural gas, geothermal resources), etc.

When the strength of solid materials is considered, especially the strength properties of industrial products are among the most researched subjects. In other words, documentation on the mechanical behaviour of industrial products is more widely discussed due to the standards obeyed for their production. On the contrary; the analyses of the rock and soils that make up the earth's crust by measuring the strength and physical properties are limited to the studies carried out in the last 100 years. In previous years, works & projects done in/on rock and soil masses (or using these masses as materials) have emerged with the decisions and guidance of experienced, qualified people who had offered *"engineering works"*. The main concerns that come to the front in engineering fields show differences in cultures over the years with the

[1] Mehmet Kemal Gokay, Prof.Dr., Konya Technical University, Mining Engineering Department,

change of civilization. Today, in the current understanding in the field of engineering, three main concerns come to the front. It has been the basic principle to pay attention to these elements in engineering applications. These 3 concerns can be; minimizing the amount of energy used; conservation decisions & regulations regarding the environment and society; sustainability & protection measures for the raw materials used (or the earth crustal part that is in contact).

In fact, developing new technologies have created new needs and new production methods, while differentiating people and countries. With the new production methods and the cooperation of different professional groups, the engineers and the workforces in these areas have increased the communication among themselves, and new needs have enabled them to try to produce answers & solutions with different products or different possibilities. In this context, engineers have developed different methodologies to offer multiple choices and change raw material sources and products & services for sale to cope with demands in local and international markets. Concerning engineering projects *[that use the rock and soil formations as raw material sources (brick-tile-façade manufacturing activities, construction stones, soil filling materials, clay products, etc.) or as medium which supply stable spaces in/on them (like; infrastructures of cities, dams, bridges, highways, railways, airports, ports, underground and surface constructions, buildings, etc.)]* in different countries, they are being handled recently with participation from many countries through international cooperation efforts. That brings collateral knowledge and information sharing in common engineering experiences while special capabilities of companies and engineering experts have usually been kept private (patented).

One of the issues that should be emphasized at this stage is the increasing use of underground cavities opened for different purposes in the last century, in addition to underground mining activities. Although, the first settlements of humanity for the purpose of protection were caves or underground cavities. Underground spaces have continued to be opened and used for many different purposes over time. Today, the use of underground spaces has become a factor that will significantly affect modern urban planning. Digging underground comes reality with the different requirements & purposes of people; settlement spaces (underground cities), shopping malls, parking lots, transportation system tunnels, recreational (cultural & sportive) centres for social activity purposes, large or small scale commercial warehouses-depots, waste material or hazardous waste (i.e. radioactive wastes) storage volumes, etc. In the last 50 years, underground spaces have progressively started to be supplied commercially by obtaining official permissions near/under urban areas.

At this stage, the issue that should be especially emphasized is to ensure that the surface and underground usage of urban spaces should be included in official documentations (legislative data and documents compiled as “Building Information Modelling”, BIM, documentation. All the information related to urban structures regardless of its date of issue is valuable assets for the future of our settlements. It should always be remembered in BIM documentations that underground urban volumes (spaces) should be related directly to surface cadastral legislative land rights. At this point, it is important to note that underground urban spaces’ 3 Dimensional, 3D, extensions together with their surface connections should be located in/on “the lands” which have their surface/underground space usage rights. The *"living volumes"* in urban areas can be different under diverse climates, living conditions, religions, capabilities, and opportunities. Options in these habits are dependent on societies and their civilization requirements. Increase in population forces societies to handle new living structures (high buildings) including multiple living spaces. Surface land value increase in certain city

locations led also the engineers to design specially featured buildings which have more extensions in their height and depth. When we examine the surface and underground construction works, projects, in terms of stability, we observe two basic concepts emerge. The first concept includes stability of the structural elements of the buildings themselves. Their design/adjustment, and good implications (obeying engineering standards) directly influence the construction stability itself. Any malfunctions in these concerns give undesirable results, (may cause collapse of constructions). The second concept is related with structures' foundations and their behaviours. City planners, architects, civil engineers, geophysics, geotechnical and excavation engineers do their best to fulfil relevant procedures to have stable foundations. Rock/soil mechanics context in ground engineering play background (Terzaghi,.1943; Goodman, 1980; Hudson & Harrison, 1997; Gokay & Dogan, 2004; Wyllie, 2005; Atkinson, 2007; Das, 2019; Hoyos, etal., 2019; Gratchev, 2020) for the supplied decisions related with surface/underground urban spaces and their stability concerns.

2. Underground spaces in urban life

In the common construction industry, urban settlements' living volumes have been designed primarily above surface. However, there are also construction projects underground to form underground urban living spaces. Design and application efforts for underground tuff rock hotels and shopping centres in Nevsehir city (Turkey) are recent examples for this type of usage. On the contrary, the design aims have not always been the case for underground spaces. For example, the primary aims in mining activities and projects are extraction of ore bodies. In order to mine ore bodies, small/large stopes (spaces, volumes) are excavated in/on earth crust. During mining activities, it is primarily important to excavate stopes & galleries to remove required ore body parts to the ground surface with taking care of work&workplace stability (Brady & Brown, 2005) and safety. When the mining industry is under consideration, what can be the secondary usage options for abandoned mine facilities, specially surface/underground spaces.

Mining operations have been terminated after considering environmental and legal aspects. Main assets left behind are excavated volumes and groundwater (mine water) accumulated in them. Re-evaluation of them for secondary economic purposes has concerns in current market conditions. For example, Durham University (UK) has been researching currently on energy inputs from mine water to fulfil the abandoned mines through heat-pumps, (Adams, 2018). Volumes created in/on earth crust by mining operations have usually been deliberately demolished (collapsed) or backfilled after their economic usefulness. These operations usually provide stability for the other continual works at underground mines. However, there are numbers of underground mine volumes, spaces, and open mine pits which have kept their stability due to favourable surrounding rock formations. Another economic usage of these spaces have gradually emerged as "urban volumes". After performing mechanical stability *(long term)* evaluations (analyses) related to abandoned mine spaces in/on earth crust, secondary purpose usages of them re-designed as the market conditions led through. Rock mechanics knowledge and expertise play crucial roles in these evaluations. Stability of open pit slopes and underground mine spaces had usually been analysed and rock masses around these mine elements also had been measured & monitored for work & workplace safety concerns in mines. Therefore, extending the available data related to these spaces have provided valuable time dependent information for engineers during their secondary usage plans. Actually, urban surface/underground spaces should be deliberately planned for modern urban purposes, their stability issues, concerns, including static and dynamic (induced vibrations, quakes) force considerations must be evaluated deeply enough. The use of underground spaces

for urban purposes is not a new phenomenon. It is quite natural that underground spaces, *(which have been used whenever needed since the first days of humanity),* are included in urban settlement plans today. The importance of underground spaces, which are not handled other than infrastructure needs during the city planning in early periods of time for particular cities, has emerged drastically when the underground metro transportation planning started to be considered for those cities. In addition, the advantages of workplace and living volumes built on 5-10 sub-floor levels, which open & constructed towards the underground in crowded city areas, are at economical values that cannot be underestimated. With some projects implemented with the joint contributions of mining and civil engineering companies in some countries, the excavated spaces in/on rock masses (pits, quarries spaces, sublevel stopes, underground spaces, cavities etc.) left empty in the abandoned mine sites have been put into service for their secondary use after evaluating their stabilities in terms of rock mechanics. The best example is the Subtropolis underground facility which covers underground workspaces and warehouses near Kansas City, US. This abandoned but stable underground limestone mine has stopes which were excavated for limestone productions (Fig. 1). The importance of underground warehouses & tunnels with reduced risk against climatic and other dangerous interactions in the earth's crust is indispensable for today's urban settlements. It is important to note that surface/underground spaces (excavated purposely or abandoned mine spaces) in different parts of the world are presented to the Real-Estate sector for different social - cultural – economic purposes.

These spaces depicted for; *settlements, living apartments, houses, depots, hotels, shopping malls, energy production, manufacturing, large-scale factories, surface roads, rail-metro lines-stations, intercity bus stops-stations, garages, warehouses, tunnels, depots, civil-military shelter facilities, all kinds of culture-sports-social facilities etc.* should be planned in urban areas more carefully for future living standards. Special requirements of these facilities like drive-in entrances (Fig.1c) for engineered loading-hauling-transportation activities are vital and they should also be considered during city planning stages. In addition, including underground metro lines & stations, underground spaces located under "the registered surface land" have some difficulties in terms of "the land rights" concerns in some countries. Moreover, rock engineering related problems like stress & deformation redistribution due to underground spaces have produced surface deformations, subsidence, (more than the permission) which might cause dispute issues to be handled. Experiences gained in different countries have to be evaluated and used in new master-plans of urban settlements. These plans should cover all types of surface/underground settlements including 3D land ownership, rights, as well.

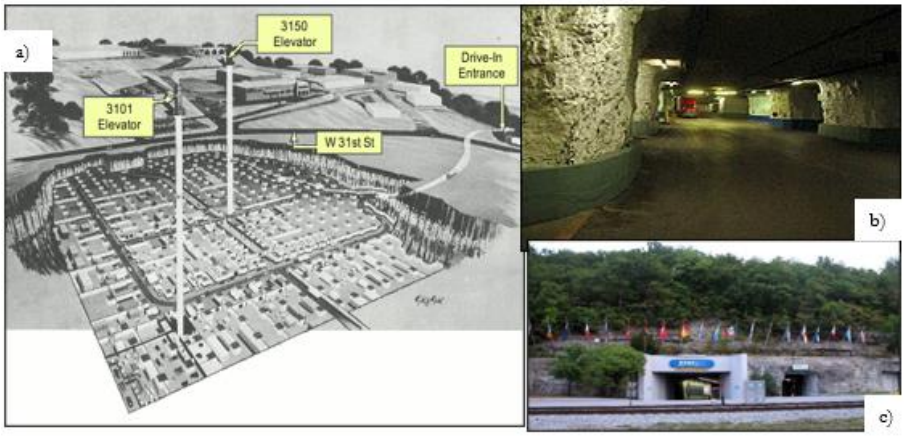

Figure 1. *a) Subtropolis, underground warehouse & storage facility at Kansas City, Missouri, US., (Historic Kansas City, 2022); b&c) Underground space & entrance view of Subtropolis facility, (Wikipedia, 2022).*

One of the examples that can be given to the reuse of surface/underground facilities in terms of urban planning is historical underground cities. Kaymakli, Ozkonak and Derinkuyu (Nevsehir, Turkey), underground cities are examples can be given here. These underground cities, which were excavated and served for different purposes in the past, have been rearranged and put into service as indispensable museums (cultural heritage and geo-sites) for tourism today (Aydan & Ulusay, 2003; Kultur portali, 2022). There are many underground spaces, cavities, excavated as underground city structures or underground shelters in many parts of the world. Mechanical behaviours of rock masses surrounding these underground spaces need to be evaluated before taking them into public service as historical museums. Alike underground mines, these museums have to be operated with official safety enforcements, which include also close observations of underground spaces' stabilities. Some of these

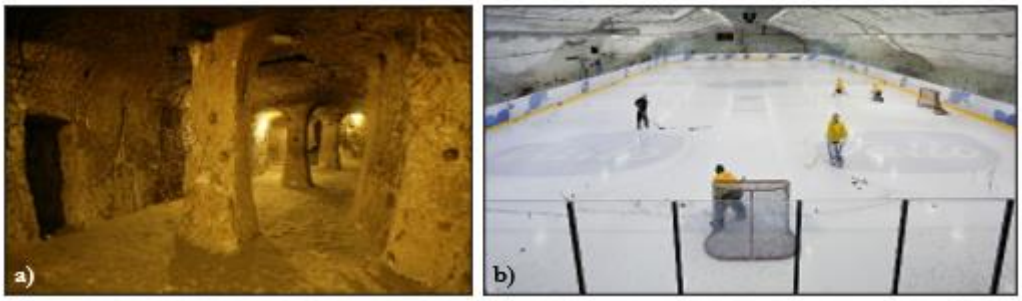

Figure 2. *Underground spaces used for urban activities; a) Underground city museum, Derinkuyu, Turkey, (Kultur portali, 2022). b) Underground ice-hockey sport facility, Helsinki, Finland, (Vähäaho, 2021).*

surface/underground spaces have places in the social-cultural heritage have been put into service as museums within the scope of the countries' socio-cultural heritage protection measures. There are also some underground space locations superimposed by current urban settlements. Actually, there are surface buildings, which have extra levels (basements) underground. But, in some cases surface structures have access passages to existing underground spaces, cavities, in surrounding rock masses. Urban areas which overlie historic underground settlements, caves, or historic mining activities might have surface structures having passages with them. Additionally, caves or excavated underground spaces have still been used in many urban localities in the world. Their usages have added advantages and generally there are common social senses, rules, formed in time for the usage of these underground spaces in those local societies, cultures. In fact, the reuse of abandoned underground mine cavities is not new. In Nottingham (UK), the basements of some houses (Bell, etal, 2009) have contact passages to warehouses, cellars, and shallow-depth galleries belonging to the mining activity that were previously exploited and abandoned underground at the same location. Similar situations can be considered for some houses in Nevsehir-Cappadocia (Turkey) region, which have contact with previously opened spaces of underground city systems. The history of underground spaces usage for urban purposes goes back to ancient times, but the idea of opening underground spaces as subway tunnels seemed like a miraculous solution for governing authorities of the populated cities. These samples, (requisites-resolutions cases) have given inspirations to city planners, architects, civil and ground engineers to design their futuristic cities together with current "carbon-zero" energy policies. Actually, engineers have recently started to design and implement more and more underground spaces in economically demanding locations.

It is important that designers and different groups of engineers should work together at all stages of urban life requirements. When the surface structures (buildings, bridges, dams, viaducts, etc.) are considered, decisions will be made about their foundation stabilities by

combining the knowledge & experience of civil and ground engineers. The stability of these structures should be analysed against static and dynamic loads (influences) so that their load carrying bodies and foundations should stay stable. It is of great importance that all engineering decisions needed in these analyses are made by people who have the authority to take responsibility in the relevant subject. The engineering branch that is missing in the decisions given is a situation that is expected to cause problems during planning or construction of the cities or their structures, buildings, or later. Apart from these facts, when examining the individual stability of constructed structures, their stabilities are also depending on the neighbouring surface/underground structures as well (Fig. 3). This reality presents the importance of urban planning. Surface structures and their social & environmental requirements may require re-evaluation to input underground spaces *(infrastructures, metro lines and their stations, cultural-sports centres, etc.)* into the city plans together with their stability interactions and land rights procedures.

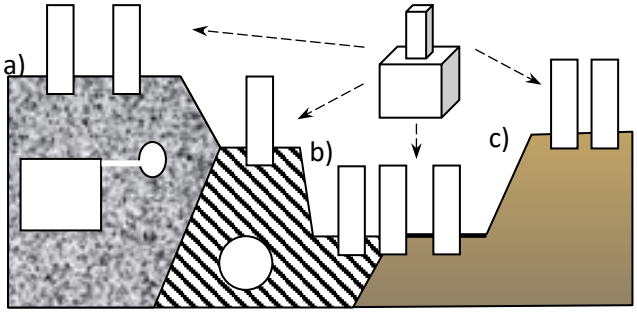

Figure 3. *Basic types of rock formations at foundations, a) Homogeneous rock mass, b) Laminated or fractures rock mass, c) Clay & Soil mass.*

As shown in Figure 3, the rock/soil masses at the foundations have vertically pressurized with their surface structures. The stresses exerted by the surface buildings on the ground, may provide deformations towards new voids, excavation, spaces to be opened next to them. These new spaces can be a new building foundation excavation *(in surface rock/soil masses)*, or an underground tunnel or cavity in the surrounding underground rock masses. It is therefore important to monitor the microscale deformations of the buildings and their foundations steadily, during & after their construction. While urban planning and urban construction rules are being put in place, it is important to set controlling teams to the locations where the planned structures are completed. These teams should measure the stresses and deformations that occur in these places on the basis of structures and their neighbourhoods. The data they collect can then be analysed regularly to monitor cities for any further instability cases. It is known that there are "Collapse prevention measurement programs" for the structures like; dams, bridges, tunnels, etc. It is important for the stability of the new futuristic cities that these types of measurement programs should be applied for urban areas. Engineering decisions to be made regarding the soil and rock engineering conditions of the foundations also include uncertainties arising from the natural properties of the earth's crust. For this reason, it is essential that the decisions about the foundation stability of the structures and the stability of the underground spaces are made by engineers who are trained in the relevant subjects, who are experts and who will take responsibilities. For these reasons, all processes and decisions should be taken in urban planning, excavation and construction activities according to available national and/or international "Engineering Standards". Eurocode 7 rules in this concern have gradually become common in Europe (EN 1997-1, 2011) which include risk assessments in designs due to the uncertain parameters. This fact is very important for earth crust (soil/rock masses) related engineering projects.

3. Underground spaces in use

The levels reached by the construction industry are presented with extreme examples made in the world. The basic requirements of the buildings constructed in urban settlements have not changed throughout history. These conditions can be listed as follows; ensuring the stability of living spaces; providing clean drinking water and food sources; safe discharge of solid-liquid-gas wastes; the suitability of safe and economical transportation manners; sustainable agricultural and industrial production areas in the immediate vicinity; existing natural-cultural-historical and sport areas; realities of socio-cultural activities. When urban developments are considered, the aims of civil engineering applications as surface structures immediately become apparent. Locations and aims of underground spaces are also important in city plans. As already mentioned before, tunnels, caves, abandoned mine spaces are apparent underground features which are already in use in different urban areas. Diamond & Kassel, (2018) provided historical perspective through; "an overview of the evolution of urban tunnels over a period of 6000 years". They focused on; "urban underground tunnels that make modern megacities possible". Galgaro etal., (2022) reported on underground food storage facilities. When it comes to storing food, the heat and humidity conditions of underground spaces are important. Because of this importance, these authors performed temperature variation analyses for the Rio Maggiore mine in Val diNon, (Trento, Italy) to evaluate reuse modelling of existing spaces. For similar abandoned mine conditions; when such a model and the other required measurement results are combined with underground space stability evaluations, reusing of the convenient underground abandoned mine (or mine sections) spaces have become economical assets to be considered. Evans, etal., (2008) have pointed out different aspects of underground spaces which should also be considered for current urbanisation and that were the aquifers and natural cavities within reservoir underground rock masses. They wrote about the secondary "use" of such spaces for new purposes. Among these uses, the purposes of “storage and disposal of different solids, liquids, gases and heat using different methods and practices” can also be considered. The modern life we live is intertwined with more underground spaces than in the old days. Successes in excavation, hauling, transportation, ventilation, lighting, groundwater discharging and other comfort technologies have increased the use of underground spaces as workplaces and/or residential areas. For instance, underground space designs supplied by Bicer (2012) and Ulusay etal., (2013) for Cappadocia (Nevsehir-Turkey) should also be examined on how underground spaces can be designed for commercial purposes. These design works include underground space plans for showrooms and restaurants in the volcanic tuff rock mass in this region. Similarly, underground cavities of different sizes (with different uses) for different purposes are already facilitated in some countries (Vähäaho, 2014; Ikavalko, etal,. 2016; Zhang,Z.,.2018; Zhang,P., 2018). The main driving aims can be listed here as; underground car parks *(protection against cold and hot weather)*; underground passages and shopping facilities *(pedestrian galleries under heavy traffic roads, protection against harsh cold/hot weather conditions)*; subway metro tunnels and stations *(protected-secure-fast underground transportation)*, underground shelters *(protection for civil-military purposes);* other cultural & sport centres *(supply protected-controlled-comforted locations).* Thus, dealing with underground space related engineering considerations, specially rock/soil mechanics studies and models have to be main research and consideration areas also in current city plan activities.

4. Surface settlements at rock/soil slopes

The mechanical behaviours of rock/soil masses at the foundations of surface constructions have supplied signs of their load bearing capacities. For this reason, ground engineers have conducted research on the formation and mechanical behaviour differences of the earth's crust (Goodman, 1980, Gokay, 1988).). In particular, the knowledge of rock engineering, geomechanics and soil mechanics experiences gained in different engineering applications have their responses in the city planning, civil and excavation & mining engineering applications (Hoek & Bray, 1977; Singh & Goel, 2011; Hu, 2021). Earth's crust is composed of rock formations and they have numerous generation-regeneration-deposition types and include many types of defects features. Rock mass defects zones including discontinuities, weaknesses, microcavities, and chemically alteration zones have defined their whole (mass) physical properties and mechanical behaviours. It is important for city planners and civil engineers to define rock masses and alluvium depositions (soil) at particular project sites. Morphology of earth surface and rock types in particular locations force the engineers to conduct test measurements to define safe settlement locations for urban areas. The gravitational force, quakes, weather influences (wind, water, temperature), biological influences, and chemical reactions are the main factors which impact surface/underground spaces, settlements. Some of these impacts are occasional on the urban structures, however if their (i.e; quakes, tournedos, tsunamis etc.), degree of influences are in high rates (high/low weather temperatures, floods, high wind speeds, etc.) they are problematic which engineers should develop necessity prevention measures. Some impacts on engineering spaces can get harmful levels in deterioration manners (in long periods of time). Rock mass weathering types developed due to the chemical reactions, biological influences, and radiation decompositions are these types of impacts. Gravity and tectonic forces on the other hand, constantly influences all substances on the earth. These two forces actually cause most of the discontinuities in rock masses. Gravity is also the main energy source of movements of water/rock/soil masses in downward direction. Landslides, rock slope failures, avalanches, rock falling disasters with/without extreme weather conditions (heavy winds, rains and snows, floods, quakes) are main driving cases for natural disaster prevention programs. When urban residential areas are considered, negative influences of gravity should be controlled & monitored carefully. Gravity pulls might create unstable circumstances for urban hillside settlements; it may cause collapse of weak roof rocks at underground spaces, it is the main drives of sinkhole disasters, it may also cause elevation differences (subsidence) due to the collapse of underground micro/macro rock voids, compactions.

Urban settlements in/on earth or at any other planets should be realised after understanding where the minimum expected crust displacements are. These analyses contain mainly rock/soil mechanics efforts together with geophysics in ground engineering professions. Stability of the surface structures, constructions, have usually been evaluated on the bases of their internal load carrying body strengths and their foundation steadiness. Stability evaluation of the settlement locations sometimes needs exceptional awareness of one particular concept of the ground engineering, such as; landslides, ground compaction, clay mineral types in soil mass, ground liquefaction, floor heaving, rock falls, rock slope failure, induced vibrations, load bearing capacity, quake shock expectation etc. For example; slope failure like presented in Figure 4 should be expected to be predicted through its previous indications at local rock/soil masses. These kinds of local slope failures, avalanches, have their earlier signs of the earth crust deformations. The signs can be changes in 3D stress/displacement values and that could be

determined by in-situ rock/soil measurement studies. After analysing the data collected through the targeted slope locations for certain period of time, ground engineers here should

Figure 4. *Hong Kong, Po-Shan Road landslide in 1972, presenting the danger of unstable ground conditions, (Photo by Geotechnical Control Office, Hong Kong Government), (Schuster & Highland, 2007).*

feel confident to report their predictions. It should also be noted that understanding and evaluating these early slope failure symptoms require responsible ground engineering professionals who documented their measurements, analyses and reports according to rock/soil mechanics concepts which track international engineering standards also. Settlements which have rock cliffs, rock/soil hillsides, slopes, should be ready for slope failures and avalanche problems. Therefore, ground engineers employed by local authorities are better equipped to monitor (by instrumented measurements) their urban areas including slopes for early predictions of dangerous conditions. In order to observe micro scale rock/soil displacements, groundwater conditions, (charge/discharge rates), rock mass stress fields at particular locations related in-situ measurement systems *(i.e; electrical earth resistivity, micro-displacement measurements, borehole inclinometer tests, borehole dilatometer & hydraulic stress tests, groundwater depth sensors etc.)* are required to be set. It is important to evaluate collected data for reliable landslide prediction. This ground engineering decision has its risks due to uncertainties in rock/ soil data originated due to their natural features. It should not be forgotten that, when the landslide was triggered and the slope started to slide, rock/soil masses at the sliding slope moved with the settlements on them. This disastrous final fact is always tried to be predicted by responsible ground engineers by taking early precautions & measures. Rock support applications provide additional strength to inclined rock slopes in their rehabilitation projects. Rock slope considerations could be one of the project items when rehabilitating natural rock slopes or abandoned open-pit slopes. Urban areas which have included these types of slopes can also be rehabilitated to their secondary usages. Joint engineering projects supplied by designers and engineers (*joint consultancy of mining-civil-geophysics-geomechanical-mechanical-electrical etc., engineers, city planners, architects, designers, social-art-cultural heritage experts, etc.)* provide economical outputs through these natural or abandoned mine sites. Figure 5 shows how the subject can be handled in a futuristic way. In these kinds of projects, existing data related to rock/soil masses around the rehabilitation sites might have been collected during an earlier period of time by local offices, mining companies etc. Thus, these data and the other data groups measured for rock/soil masses at the beginning of rehabilitation projects can be combined to provide stable surface/underground space combinations in/on rock masses for new city settlements, plans.

Figure 5. *Urban development at rehabilitated quarry pit. Hotel construction includes futuristic design options in Shanghai, China, (Tan, etal., 2019).*

5. Ground engineering decisions in urbanisation

It is most probable that planets, satellites like the moon, meteors, etc. have their solid crust formed through rock materials. If there are engineers dealing with rocks/soils mass stabilities anywhere, they have to make stability decisions on them for mining and civil engineering purposes. Rock masses have their complex structures and they have 3D discontinuity & weakness zone distributions in them. Due to their internal uncertainty features, mechanical properties of the rock masses can not be fully determined. The rock/soil properties could be tested according to available standards through samples obtained from surface/underground positioned rock masses. When the sample locations are recorded in 3D positioning systems, the size and types of rock masses and numbers of samples can be compared geostatistical manners to reach engineering decisions on their properties. However, rock masses have not been entirely modelled yet. Thus, their statistically averaged property values have not been considered completely valid. Therefore, rock engineers who should provide engineering decisions for urban settlements for example, must supply their decision reports together with risk evaluations (i.e; Eurocode 7 procedures). As it is obvious that, there is no way to test all concrete masses used in engineering structures as a whole. Similarly it is not possible to provide properties fully representing whole rock masses out of full-scale in-situ tests. There is no way to test all rock/soil masses as a whole, located as a foundation mass under particular engineered structure either. For this reason, it is obvious that engineering evaluations should be made to cover the risks of uncertainty while providing engineering decisions for surface/underground structures and their foundation rock/soil masses. Described risks in these decisions *(risk originated due to the strength of building materials-construction elements, risk due to concrete bodies, risk due to workforce quality, risk due to foundations, etc.)* should then be considered in order to prevent engineered structures' collapses. At this point it is important to mention the following statement wrote by Elmo & Stead (2020); "Even if engineers have unlimited

resources, the natural variability of rock mass, combined with limited rock mass knowledge in the early stages of a project, will still affect the design outcome by what we do effectively not knowing rather than knowing". Therefore, it is better to understand, there should always be a risk of catastrophe in engineered structures' stabilities which are constructed in/on, rock/soil masses as a part of urban settlement projects.

6. Conclusions

The living conditions of modern life in urban settlements have gradually changed with energy requirements and cost of living. The rate of population increase and convenient manners with new technologies have pushed societies to use all possible resources around city hot-spots by considering environmental precautions. Underground metro lines&stations and underground carparks&passages roads are accepted as normal plan elements in current city plans procedures. Settlements, historic or new development areas should have several factors to be favourable by modern lifestyle as well. However, the primary concern is the stability of the city structures (buildings, infrastructures etc.) and their foundations. Abandoned city centers are not a rare case in history due to natural hazards on these features' stabilities. Rock/soil masses around the human settlements (surface/underground spaces) also have their own behaviour differences. Think about modern subway systems, including underground tunnels and stations, they are part of existing modern cities. Passageways, shopping malls, parking lots, sports and cultural centers which gradually excavated in shallow depth are suitable places for people who live in compact apartments in crowded cities. These people are used to living at surface/underground apartment levels, and they are convenient with the usage of underground spaces listed above as far as they provide added opportunities. The use of underground spaces are currently evaluated as suitable living locations for very hot/cold weather conditions. Thus, urban settlement and its elements which should provide protection for human life should also be stable as structures and foundations for a long period of time. However, it should also be known that, there is no place in/on earth's crust where ground deformations are absent. Ground engineers have a duty here to localize areas where these displacements are acceptable (tolerable) according to international standards and legislative precautions. Rock/soil mechanics concepts (Triantafyllidis, 2020; Atalar & Cinicioglu, 2023) have emerged gradually to evaluate these decisions. The basis of the mechanical behavior and stabilities of urban structures cannot be understood without evaluating global, regional and local geologic and tectonic features of rock masses. Therefore, urban settlement plans should cover primarily in-situ deformation and stress measurements to localise suitable metropolitan areas. That means, foundation areas of the city buildings and structures must be examined in wider metropolitan projectiles. Then, the local foundation area of the projected civil structure should be analysed according to local data specially collected. After that, depending on the type of civil project *(hospital, school, apartment, bridge, dam, underground spaces, depots, etc.)*, at different rock and soil masses, their stability cases are considered and reported with engineering risks of threats according to current *"engineering standards*". Furthermore, it should also be borne in mind that national/international *engineering standards* have gradually been enhanced in time. So, following their procedures does not mean that the risks related to engineered structures are absent at all. Thus, supplying risk of stability concerns with engineered designs enlighten the people using those structures about the subjects. People living urban settlements, *(camps, villages, towns, cities, etc.)* should not contemplate that "engineered civil structures", are fully stable and they are 100% safe in their structure while they are using them.

References

Adams, C., Heat from abandoned mines: Developing legacy, Transactions-September 2018, North of England Institute of Mining and Mechanical Engineers, www.mininginstitute.org.uk, p4.

Atalar, C. and Cinicioglu, F., 5th International conference on new developments in soil mechanics and geotechnical engineering, (Eds.) Proceedings of ZM 2022, Lecture notes in Civil Eng. Vol305, Springer Nature, Switzerland AG, 2023, p502.

Atkinson, J., *The mechanics of soils and foundations*, Taylor&Francis Group, CRC Press, ISBN 978-0-415-36255-9, 2019, 2007, p442.

Aydan, O., *Time-dependency in rock mechanics and rock engineering*, Taylor&Francis Group, CRC Press, ISSN 2326-6872, 2017, p245.

Aydan, O. and Ulusay, R., Geotechnical and geoenvironmental characteristics of man-made underground structures in Cappadocia, Turkey, *Engineering Geology*, 69, pp245–272, 2003.

Bell, F.G., Culshaw, M.G., Forster, A. and Nathanail, C.P., The engineering geology of the Nottingham area, UK., *Engineering Geology for Tomorrow's Cities.* (Eds: Culshaw, et al.), Geological Society, London, Eng. Geology Special Publication, 22, pp1–24, 2009, doi: 10.1144/EGSP22.1 0267-9914/09.

Bicer, Z.O.P., An Example of the design and construction of rock cut places in Cappadocia: CEC, *Intercultural Understanding*, 2, pp35-44, 2012.

Brady, B.H.G. & Brown, E.T., *Rock mechanics for underground mining*. Kluwer Academic Publisher, ISBN 1-4020-2116-X. 2005, p628.

Das, B.M., *Advanced soil mechanics*, Taylor&Francis Group, CRC Press, ISBN 978-0-8153-7913-3, 2019, p712.

Diamond, R,S. and Kassel, B.G., A History of the urban underground tunnel (4000 B.C.E. - 1900 C.E.), *Journal of Transportation Technologies*, 8, pp11-43, 2018.

Elmo, D. and Stead, D., Disrupting rock engineering concepts: is there such a thing as a rock mass digital twin and are machines capable of learning rock mechanics? *Slope Stability*, p565, (Dight, PM. (ed.)), Australian Centre for Geomechanics, Perth, 2020, ISBN 978-0-9876389-7-7, doi:10.36487/ACG_repo/2025_34.

EN 1997-1, (English): Eurocode 7: Geotechnical design - Part 1: General rules [Authority: The European Union Per Regulation 305/2011, Directive 98/34/EC, Directive 2004/18/EC].

Evans, D., Highley, D., Gale, I., and Cowley, J., Underground storage, British Geological Survey, *Natural Environment Research Council, Mineral Planning Factsheet*, The Department for Communities and Local Government, DCLG-BGS Joint Mineral Programme, p22, 2008.

Galgaro, A., Santa, G.D., Cola, S., Cultrera, M., DeCarli, M., Conforti, F., Scotton, P., Viesi, D., and Fauri, M., Underground warehouses for food storage in the Dolomites (Eastern alps-Italy) and energy efficiency, *Tunnelling and Underground Space Technology*, 102, p13, 2022.

Gokay, M.K., Bearing capacity analysis of layered rock for an underground mine. *Master (MSc) thesis*, METU, Applied Science Institute, 1988, Ankara, Turkey.

Gokay, M.K. and Dogan, K., Contributions of rock mechanics in geomechanics research. 7th Regional rock Mechanics Symposium, Oct. 21-22, 2004, pp25- 33, Sivas, Turkey.

Goodman, R.E., *Introduction to Rock Mechanics*. John Willey & Sons, 1980, New York, US.

Gratchev, I., *Rock mechanics through project-based learning*, Taylor&Francis Group, CRC Press, ISBN 978-0-367-23219-1, 2020, p151.

Historic Kansas City, Downtown-Underground, www.historickansascity.org/wp-content/uploads/2013/10/down town-underground.png, Retrieved in Jan. 2022.

Hoek, E. & Bray, J.W., *Rock slope engineering*, The Institution of Mining and Metallurgy, ISBN 0-900488-36-0, 1977, p408,

Hoyos, L.R. & McCartney, J.S., *Novel issues on unsaturated soil mechanics and rock mechanics*, Proceedings of the 2cd GeoMEast international congress & exhibition on sustainable civil infrastructures, Egypt-2018, The official international congress of soil-structure interaction group in Egypt (SSIGE), ISSN 2366-3405, 2019, p227.

Hu, H., Chen, W. and Fu, J., *Rock mechanics and engineering, Prediction and control of landslides and geological disasters*, Eslevier Ltd., ISBN 978-0-12-822424-3, 2021, p407.

Hudson, J.A. & Harrison, J.P., *Engineering rock mechanics, An introduction to the principles*, Pergamon press, 1997, p443.

Ikavalko, O., Satola, I. and Hoivanen, R., *Helsinki, COST TU1206 Sub-Urban Report*, TU1206-WG1-007, (Eds:Saether, O.M. and Beylich, A.A.), March 2016, www,sub-urban.eu, p22.

Kultur portali, Derinkuyu underground city-Nevsehir, Ministry of Culture and Tourism, *Kultur portali, Gezilecek yerler*, Kultur ve Turizm Bakanligi, Turkey. Retrieved in Feb. 2022.

Schuster, R.L., and Highland, L.M., The third Hans Cloos lecture. Urban landslides: socioeconomic impacts and overview of mitigative strategies, *Bull Eng Geol Environment*, 66, pp1–27, 2007, doi:10.1007/s10064-006-0080-z.

Singh, B. & Goel, R.K., *Engineering rock mass classification, Tunneling, Foundations, and Landslides*, Elsevier Ltd., 2011, p365.

Tan, F., Jiao, Y.Y., Wang, H., Liu, Y., Tian, H., and Cheng, Y., Reclamation and reuse of abandoned quarry: A case study of Ice World & Water Park in Changsha, *Tunnelling and Underground Space technology*, 85, pp259-267, 2019.

Terzaghi, K., *Theoretical soil mechanics*, Wiley & Sons Press. 1943, p510.

Triantafyllidis, T,. Recent developments of soil mechanics and geomechanics in theory and practices, Springer, (Eds,) LNACM 91, ISSN 1613-7736, 2020, p409

Ulusay, R., Aydan, O., Genis, M., and Tano, H., Stability assessment of Avanos underground congress centre (Cappadocia, Turkey) in soft tuffs through ab integrated scheme of rock engineering methods, *Rock Mechanics and Rock Engineering*, 2013, 46, 6, pp1303-1321.

Vähäaho, I., *City of Helsinki, Helsinki urban underground spaces –Sustainable property development in Helsinki*, Real Estate Department, Geotechnical Division, Oct.2014, www.geotechnics.fi.

Vähäaho, I., *City of Helsinki, Helsinki urban underground spaces – Guidelines for visitors, (Urban Environment Brochures 2021:3,* (Ed., Vähäaho, I.), Head of Soil and Bedrock Unit, www.geotechnics.fi.

Wikipedia, SubTropolis, Kansas City, Missouri, US, www.en.wikipedia.org/wiki/ SubTropolis. Retrieved in Jan. 2022.

Wyllie, D.C., *Foundations on rock*, Taylor & Francis Group, ISBN 0-419-23210-9, 2005, p435.

Zhang, P., Japanese ways of developing urban underground recreation space, World Journal of Engineering and Technology, 2018, 6, pp504-517.

Zhang, Z., Study on urban underground streets in modern cities, American journal of Civil Engineering, 2018, 6, 2, pp60-67.

Evaluation of the Nutritional Benefits and Future Perspective of Hemp Seed Milk

Nour AWAD[1]
Mustafa MORTAŞ[2]

1. Introduction

The consumption of milk and milk products is rising quickly all across the world, and it is predicted that this trend will keep shifting in the same way going forward (Paul et al., 2019). Recently, due to milk allergies, lactose intolerance, as well a movement in consumer interest in plant-based alternatives, there has recently been a growing demand for vegan and vegetarian milk alternatives to bovine milk. This demand has contributed to a remarkable rise in the marketing of plant-based milk products such soymilk, and almond milk during the past ten years (Vanga et al., 2020). It was predicted that the global market for plant-based milk would generate US$ 13.24 billion in revenue in 2021 and to reach US$ 30.79 billion in total revenue by 2031(Besir et al., 2022). Besides, bovine milk revenues in the United States dropped 7% ($17.8 billion) in 2015 and were expected to drop a further eleven percent in 2020 (Singhal et al., 2017).

The main process for making plant-based milks involves extracting various raw materials (cereal, legume, nut, and seed) in water, which is then homogenized and thermally treated to extend shelf life and enhance stability (Besir et al., 2022). The term "milk" appears frequently in the beverage name, and they are created to mimic dairy milk in appearance. These plant-based products' nutritional value is influenced by their source, processing techniques, and fortification level (Singhal et al., 2017). Nowadays, hemp milk is viewed as an appealing substitute for dairy, soy, and nut milks since it is lactose free and has a low allergic potential due to ıts free of animal hormones and cholesterol (Wang et al., 2018). In 2018, the market for hemp seed beverages was worth over USD 185 million (Besir et al., 2022). Hemp (Cannabis sativa L.) is a herbaceous plant native to central Asia, belonging to the family *Cannabaceae*. Cannabis Sativa, which translates to "useful hemp" in Latin, is the same plant that both hemp and marijuana are derived from. The main distinction is in how much the concentration of delta-9-tetrahydrocannabinol (THC), marijuana's primary psychoactive ingredient. Compared to marijuana, which has 5% to 10% THC or higher, industrial hemp only contains 0.3% to 1.5% THC (Vahanvaty, 2009). Over the past few years, hemp and its derivatives, have gained popularity. The Plant Variety Database, which has 67 recognized variations, lists hemp as an agricultural plant species by the European Commission. France is the country that produces the most hemp seeds, accounting for over 60% of the world's total hemp output (Ignacio Alonso-Esteban et al., 2020). Hemp seeds and their food derivatives are being more widely consumed, particularly among vegans. Even though whole hemp seeds can be eaten (for example, as roasted seed snacks), they are mostly used as a raw material to make various products like hemp seed milk, flour, etc. Hence, one of the most popular products derived from industrial hemp seeds is hemp seed milk. Thus, whole or dehulled hemp seeds can be used to produce hemp milk. Most of the essential nutrients are present in hemp milk, which is regarded as being very

[1] Doktora öğr., Ondokuz Mayıs Üniversitesi, Gıda mühendisliği bölümü, ORCID:0000-0003-3441-9080

[2] Asst. Prof, Ondokuz Mayıs Üniversitesi, Gıda mühendisliği bölümü, ORCID:0000000203167768

healthy. According to studies, drinking hemp milk may result in lower levels of blood triacylglycerols, cholesterol, and thyroid hormones (Wang et al., 2018).

According to the literature, hemp milk has the following characteristics: it is unsweetened and unflavored, has a thick and creamy texture, and has a nuttier flavor that is comparable to the flavor of soy milk. Additionally, hemp seed milk has a low sodium content and is free of lactose, soy, gluten, cholesterol, and trans fats (Vahanvaty, 2009). Accordingly, the objective of this study is to evaluate the chemical composition, nutritional value and biological properties of hemp seed and milk according to the recent published studies.

2. Nutritional significance

Hemp seeds have a high proportion (16–19%) of readily digested complete protein and a rich supply of oil that provides a healthy balance of the key fatty acids linoleic (C18:2, n-6, LA), and linolenic (C18:3, n-3, LNA) acids. In particular, linoleic (-6) and -linolenic (-3) acids, which are best consumed in a 2:1 to 3:1 ratio needed for healthy human nutrition, are abundant in hemp seed oil (Wang et al., 2018). As well as, the components contain stearidonic (C18:4, n-3, SDA), palmitic acid (5–8%), and gamma-linolenic acid (C18:3, n-6, GLA)(1–3%), acids wich significantly contribute to the possible therapeutic efficacy (Chich_Owska et al., 2014). Additionally, the primary components of hemp seeds include lipids (25–35%), proteins (20–25%), carbohydrates (20–30%), insoluble fiber (10–15%), vitamin E (90 mg/100 g), and minerals (sodium, phosphorus, potassium, magnesium, calcium, sulfur, iron, and zinc)(Besir et al., 2022). The literature claims that phosphorus is the most prevalent mineral element and that it is present in larger concentrations in hulled seeds (1.1 g/100 g) than in whole seeds, along with potassium, magnesium, and zinc (Alonso-Esteban et al., 2022).

In a recent published study, a comparison between the chemical composition of whole and dehulled hemp seeds has been carried out. Accordıng to the results, both protein and fat content were higher in dehulled seeds. Dehulled seeds had a protein level of 26 g/100 g on average, compared to 20.4 g/100 g for whole seeds. Whole hemp seeds had a fat level between 29.1 and 32.66 g/100 g, while dehulled seeds had a fat content closer to or even greater than 50 g/100 g (Ignacio Alonso-Esteban et al., 2022). In the same study, whole hemp seeds had an energy content of 456 to 494 kcal/100 g, whereas dehulled seeds had an energy content of 589 to 621 kcal/100 g. Their higher fat content, is what gives them their increased energy value. Moreover, there were a slight differences in the total soluble sugars. The total soluble sugar content ranged from 3.14 to 4.62 g/100 g and 3.68 and 5.65 g/100 g in whole and dehulled hemp seeds, resperctively. The most prevalent soluble sugar in whole hemp seeds was sucrose. While fructose and glucose were absent from both seed types, sucrose and raffinose was dominant in dehulled seeds (Ignacio Alonso-Esteban et al., 2022).

Hemp milk can be produced by homogenizing crushed hemp seeds in water (1:5 w/v), and then filtering the resulting milk to remove any impurities (Wang et al., 2018). According to the literature, hemp seed milk has a protein content of 0.83–4%, a fat content of 1.25–3%, and a carbohydrate content of 2.5–20%. However, the total amounts of saturated and polyunsaturated fatty acids in hemp seed milk are, respectively, 0.428% and 4.173% (Besir et al., 2022). The protein present in hemp seeds is made up of 35% albumin, and 65% of the high-quality edestin protein, which is the most important protein found in any plant source. However, hemp seeds contain all the essential amino acids, with a high quantity of sulfur-containing amino acids (methionine and cysteine), which are often scarce in vegetable proteins (Vahanvaty, 2009). On another hand, hemp secondary metabolism produces a wide range of substances, including phenolic substances (mostly flavonoids, stilbenoids, and lignanamides), terpenoids, and alkaloids (Ignacio Alonso-Esteban et al., 2022).

3. Biological activities of hemp milk

Several studies have investigated the biological activities of hemp seeds. It has been reported that hemp seeds include bioactive substances that have biological potential, such as antioxidant,and antibacterial activities. As well as, cytotoxic characteristics, inflammatory bowel disease, rheumatoid arthritis, obesity, and Alzheimer's disease, which are just a few of the chronic conditions it helps prevent (Alonso-Esteban et al., 2022 ; Paul et al., 2019). These activities attribute to their content of phenolic compounds, mainly lignanamides (N-caffeoyltyramine, grossamide, cannabisin B, cannabisin F) that constituted 79%, while the content of flavonoids was only 2.8% (Alonso-Esteban et al., 2022 ; Sławińska & Olas, 2022). Interestingly, there is evidence that hemp lignanamides have cytotoxic effects on cancer cells. At a concentration of 50 g/mL, they drastically reduced the viability of the U-87 (human glioblastoma) cell line; this effect was noticeable after 24, 48, and 72 hours of incubation(Sławińska & Olas, 2022).

On another hand, studies on hemp seeds and cardiovascular disease are ongoing. High concentrations of the amino acid arginine found in hemp seed protein, which when ingested produces nitric oxide, which relaxes blood vessels and boosts circulation (Curl et al., 2020). Low levels of C-reactive protein, a sign of inflammation linked to heart disease and chronic inflammation, have been linked to arginine. However, hemp milk includes little quantities of hemp seed per serving, and the amount of arginine in hemp milk is minimal and may not have any preventive effects against cardiovascular disease, thus more study is required (Curl et al., 2020). In a released research, the effects of treating rats with hemp milk on insulin, thyroid hormone levels, and metabolic changes were examined (Chich_Owska et al., 2014). The purpose of the study was to search at the way hemp milk consumption changed body weight, internal organs weight, insulin and thyroid hormone serum concentrations, and blood lipid indices. According to the findings, consuming hemp milk significantly lowers blood triglyceride and cholesterol levels, including total, free, and esterified cholesterol. Additionally, rats used in experiments had their thyroid hormone levels significantly decrease (Chich_Owska et al., 2014).

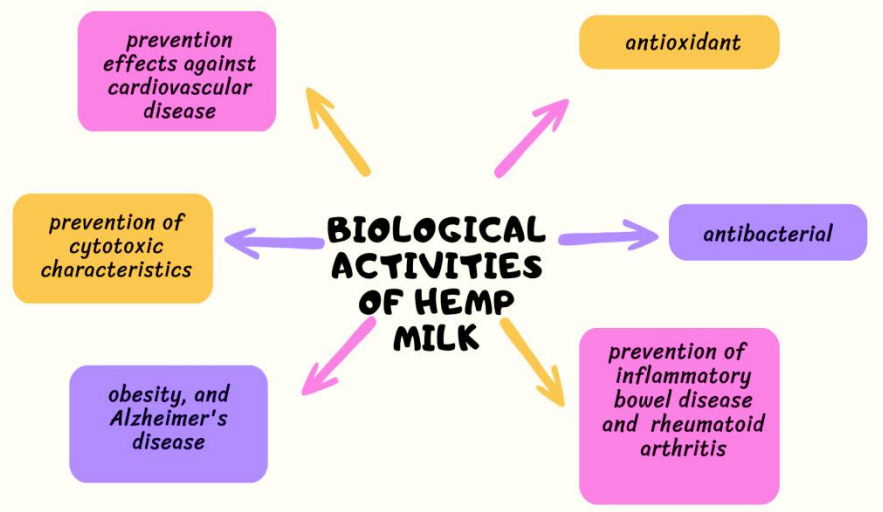

Figure 1. *Biological activities of hemp milk*

It is well known that some anti-nutrient elements in foods, including phytates and oxalates, which are contained in hemp seeds, may reduce the bioavailability of minerals. Thus, the primary type of phosphorus stored in seeds is phytic acid, which can form insoluble complexes with several cations, including calcium, magnesium, iron, and zinc (Alonso-Esteban

et al., 2022). However, during the production of hemp milk, to eliminate antinutritional elements and increase the digestibility and bioaccessibility of minerals, several physical procedures (boiling, soaking, sprouting, steam injection), chemical techniques (b-cyclo-dextrin trapping), and bioprocessing and biotechnological interventions (fermentation, enzyme processing) should be applied (Paul et al., 2019). Regarding hemp milk's phytic acid content, we couldn't find any information in the literature, and more future research is needed.

4. Comparison of hemp seed milk with other types plant milk

Bovine milk has far more of an impact than the plant-based alternatives across all criteria. Three times as much greenhouse gas emissions are produced, ten times as much land is required, two to twenty times as much freshwater is consumed, and the amount of eutrophication is noticeably higher (Ritchie, 2022). However, certain types of plant-based milk have a significant advantages over others. Either in terms of nutritional value, production cost or its impact on the environment **table 1**. In the following, there is a brief comparison between two types of plant based milk and hemp milk (Jessica Caporuscio, 2021: Ritchie, 2022).

4.1. Hemp milk Vs Soy milk

The popularity of soy milk is not surprising, considering its numerous health advantages. In terms of protein content, soy milk is about the same as dairy milk (8.25g per serving). Also it has high levels of essential monounsaturated and polyunsaturated fatty acids. Additionally, it contains plenty of fiber, phytochemicals, B vitamins, minerals (especially iron, calcium, and zinc), and unsaturated fatty acids (Paul et al., 2020). On another hand, soy milk contain isoflavones, soy compounds that may cause breast cancer in some women (Mollakhalili-Meybodi et al., 2022). As well as, high level of food allergens. Indeed, soybean is one of the "big 8" foods, which account for 90% of all food allergies caused by immunoglobulin E (Mollakhalili-Meybodi et al., 2022). According to studies, 14% of individuals who have health issues with bovine milk also have allergies to soy milk (Paul et al., 2020).

4.2. Hemp Milk VS Almond Milk

The global market for almond milk was valued at USD 5.2 billion in 2018; it is projected to increase at a CAGR of 14.3% in 2025. (*Global Industry Report, 2019-2025*). Almond milk has a considerable quantity of minerals, protein, monounsaturated fats, total dietary fiber, vitamin E, vitamin B complex, and total phenolic compounds. Additionally, almonds are also recognized as a source of anti-inflammatory, anti-tumor, and anti-hyperlipidemic chemicals (Paul et al., 2020).

However, the fatty acid content of almonds, has a significant role in the development of harmful bacteria including E. coli O157:H7 and L. monocytogenes. Although heat processing techniques can reduce infections, they can also significantly reduce nutritional value. Additionally, allergies to almonds are rather prevalent(Paul et al., 2020). On the other hand, almond milk has negative effects on the environment, particularly the water wastage. In contrast to hemp milk, which grows organically, uses very little water, and absorbs a lot of CO2, almonds take approximately a gallon of water per almond to grow, making them less sustainable (Ritchie, 2022).

Table. 1 *A comparison of the nutritional values of 240 milliliters (ml), and the health and environmental issues related to the consumption and production of of cow, hemp, soy and almond milk.*

Parameter	Bovine milk (whole)	Hemp milk	Soy milk	Almond milk
Calories	259	60	101	29
Protein	9 g	3 g	6.0 g	1.01 g
Total fat	10.99 g	4.51 g	3.5 g	2.50 g
Sugars	31.01 g	0 g	9.0 g	0 g
Calcium	300 mg	283 mg	451 mg	451 mg
Vitamin D	0 IU	0 IU	120 IU	101 IU
Health issues	-Lacose intolerence -Allergies to protein	-antinutritional factors	- food allergens -isoflavones compound which might cause breast cancer	- pathogenic bacteria - food allergens
Environmental impact	-high greenhouse gas emissions -high land use -high freshwater use - high level of eutrophication	-less freshwater use - absorbs a lot of CO2	-lesser freshwater use and eutrophication impact than dairy and almond milk.	- high freshwater use - has lower greenhouse gas emissions and uses less land than soy and dairy

5. Conclusions and future perspectives

The interest in consuming plant-based milk is increasing day after day for several reasons, including health, environmental, ethical, and others. Hemp milk is one of the plant based milk types that has gained a lot of attention in the past few years. Today's consumer has become more aware and keen to choose the best products available, in line with his needs and interests. Therefore, interest and demand for hemp milk is expected to increase more and more in the next few years. Nutritionally, hempseed has an ideal omega-6 to omega-3 PUFA ratio, a high quantity of essential amino acids, and proteins that are easy to digest, hence, it has the potential to be used as a nutraceutical in food, as well as it has no allergens, and this increases its preference over other types of plant milk. Last but not least, the production of hemp milk is sustainable as the plant needs small amounts of water to grow and consumes large amounts of carbon dioxide, which makes it environmentally friendly.

References

Alonso-Esteban, J. I., Torija-Isasa, M. E., & Sánchez-Mata, M. de C. (2022). Mineral elements and related antinutrients, in whole and hulled hemp (Cannabis sativa L.) seeds. *Journal of Food Composition and Analysis*, *109*, 104516. https://doi.org/10.1016/J.JFCA.2022.104516

Besir, A., Awad, N., Mortas, M., & Yazici, F. (2022). A Plant-Based Milk Type: Hemp Seed Milk. *Akademik Gida*, *20*(2), 170–184. https://doi.org/10.24323/AKADEMIK-GIDA.1149875

Caporuscio, J. (2021). *Almond Milk Market Size, Share | Global Industry Report, 2019-2025*. Medical News Today. https://www.grandviewresearch.com/industry-analysis/almond-milk-market

Chich_Owska, J., Kliber, A., Koz_Owska, J., Biskupski, M., & Grygorowicz, Z. (2014). *INSULIN, THYROID HORMONE LEVELS AND METABOLIC CHANGES AFTER TREATED RATS WITH HEMP MILK*.

Curl, S., Rivero-mendoza, D., & Dahl, W. J. (2020). Plant-Based Milks : Hemp. *UF | IFAS*, 1–4.

Ignacio Alonso-Esteban, J., José González-Fernández, M., Fabrikov, D., Torija-Isasa, E., de Cortes Sánchez-Mata, M., Luis Guil-Guerrero, J., Alonso-Esteban, J. I., Torija-Isasa, E., de Sánchez-Mata, M. C., González-Fernández, M. J., Fabrikov, D., & Guil-Guerrero, J. L. (2020). Hemp (Cannabis sativa L.) Varieties: Fatty Acid Profiles and Upgrading of γ-Linolenic Acid–Containing Hemp Seed Oils. *European Journal of Lipid Science and Technology*, *122*(7), 1900445. https://doi.org/10.1002/EJLT.201900445

Ignacio Alonso-Esteban, J., Pinela, J., Ciri, A., Calhelha, R. C., Sokovi, M., CFR Ferreira, I., Barros, L., Torija-Isasa, E., & de Cortes Sánchez-Mata, M. (2022). Chemical composition and biological activities of whole and dehulled hemp (Cannabis sativa L.) seeds. *Food Chemistry*, *374*, 131754. https://doi.org/10.1016/j.foodchem.2021.131754

Jessica Caporuscio. (2021). *Almond, hemp, oat, soy, and cow's milk: Which is best?* Medical News Today; Annual Reviews Inc. https://doi.org/10.1146/ANNUREV-PUBLHEALTH-031816-044437

Mollakhalili-Meybodi, N., Arab, M., & Zare, L. (2022). Harmful compounds of soy milk: characterization and reduction strategies. *Journal of Food Science and Technology*, *59*(10), 3723–3732. https://doi.org/10.1007/S13197-021-05249-4/FIGURES/2

Paul, A. A., Kumar, S., Kumar, V., & Sharma, R. (2019). Milk Analog: Plant based alternatives to conventional milk, production, potential and health concerns. *Https://Doi.Org/10.1080/10408398.2019.1674243*, *60*(18), 3005–3023. https://doi.org/10.1080/10408398.2019.1674243

Paul, A. A., Kumar, S., Kumar, V., & Sharma, R. (2020). Milk Analog: Plant based alternatives to conventional milk, production, potential and health concerns. *Critical Reviews in Food Science and Nutrition*, *60*(18), 3005–3023. https://doi.org/10.1080/10408398.2019.1674243

Ritchie, H. (2022, December 1). *Dairy vs. plant-based milk: what are the environmental impacts?* Our Word in Data; Elsevier B.V. https://doi.org/10.1016/j.gfs.2018.08.007

Singhal, S., Baker, R. D., & Baker, S. S. (2017). A Comparison of the Nutritional Value of Cow's Milk and Nondairy Beverages. *Journal of Pediatric Gastroenterology and Nutrition*, *64*(5), 799–805. https://doi.org/10.1097/MPG.0000000000001380

Sławińska, N., & Olas, B. (2022). Selected Seeds as Sources of Bioactive Compounds with Diverse Biological Activities. *Nutrients 2023, Vol. 15, Page 187*, *15*(1), 187. https://doi.org/10.3390/NU15010187

Vahanvaty, U. S. (2009). Hemp Seed and Hemp Milk: The New Super Foods? *ICAN: Infant, Child, & Adolescent Nutrition*, *1*(4), 232–234. https://doi.org/10.1177/1941406409342121

Vanga, S. K., Wang, J., Orsat, V., & Raghavan, V. (2020). Effect of pulsed ultrasound, a green food processing technique, on the secondary structure and in-vitro digestibility of almond milk protein. *Food Research International*, *137*(March), 109523. https://doi.org/10.1016/j.foodres.2020.109523

Wang, Q., Jiang, J., & Xiong, Y. L. (2018). High pressure homogenization combined with pH shift treatment : A process to produce physically and oxidatively stable hemp milk. *Food Research International*, *106*(September 2017), 487–494. https://doi.org/10.1016/j.foodres.2018.01.021

Nitric Oxide; Does It Cancer Or Protect?

Fatma Gönül Sezgin

Introduction

Nitric oxide (NO), an endogenous gas and free radical, is an important molecule responsible for vasodilation, wound healing, tumor formation and anti-inflammation (1, 2). It is also responsible for many biological processes such as angiogenesis, cell signaling, and killing of cancerous cells (3). Its molecular weight is 30.006 g/mol and its half-life is 20-30 seconds. Endogenous NO is produced by the nitric oxide synthase enzyme (NOS) converting the amino acid L-arginine to L-citrulline (Figure 1). The oxidation of L-arginine occurs in several steps. First, Nω-hydroxy-Larginine (NOHA) is produced. This is followed by the oxidative cleavage step of the C=N bond in NOHA to NO and L-citrulline. In the next step, there is a return to L-arginine with the citrulline/arginine cycle (4). The physiological concentration of L-arginine in the human body is sufficient for sustained NO production (5) The catalytic activity of NOS (KmL-Arg 1.4 to 32.2 mmol/l) is relatively low. However, L-arginine supplementation may partially increase NO production (6). NO can also be produced without the direct action of NOS, the best example being the release of NO by interaction of NOHA with cytochrome P-450 (7).

NOS has three isoforms in the human body. Neuronal NOS (nNOS) is found in the nonadrenergic, noncholinergic nervous system (NANC), airway nerves, and epithelium, while endothelial NOS (eNOS) is mainly found in the endothelial cells of the pulmonary vasculature. Inductive NOS (iNOS) is responsible for pro- and anti-inflammatory responses. All isoforms contain a domain homologous to tetrahydrobiopterin, heme and cytochrome P450 reductase and are flavoprotein in nature. (8).

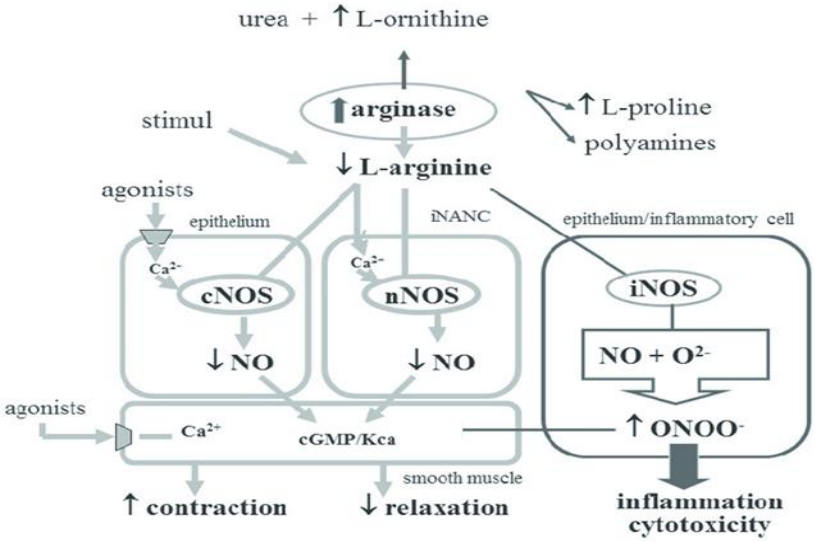

Figure 1. Nitric oxide synthesis and basic mechanisms of NO effects (24)

The difference in NOS isoforms is not only structural and positional. There are also characteristic differences in both their transcriptional and post-translational regulation (9). The activities of neuronal and endothelial NOS, which are called constitutive, depend on the amount of intracellular calcium. They are master regulators of homeostasis and produce NO at the

femto- or picomolar level (10). iNOS activity is dependent on calmodulin. Unlike other isoforms, binding to calmodulin is Cai 2+ independent. This situation causes the release of NO in higher amounts than the physiological way. NO production by iNOS can increase up to 1000 times in pathological conditions. NO, which is regulatory and protective, turns into a cytotoxic agent in this case. The very high levels of NO formed lead to smooth muscle relaxation, increasing vascular permeability and mucus secretion. As a result, it causes mucosal damage (11).

High concentrations of NO react with other reactive oxygen intermediates (ROI) such as superoxide (O2 -) oxygen to produce significant levels of reactive nitrogen species (RNT) that cause cell damage by free radical-mediated Lipid peroxidation, thiol and amine nitration, tyrosine nitration (12, 13). When the formation of these molecules cannot be suppressed, nitrosative stress occurs due to the formation of excessively reactive nitrogen. (13), this situation also creates an imbalance in redox. In the case of unbalanced redox, DNA, various proteins, carbonditrates and lipids are damaged (15), and as a result, cancer may develop (14). NO-induced genotoxicity in the cell activates the DNA repair mechanism by stimulating the G1/S, intra-S and G2/M checkpoints between cell cycle phases (16).

NO, which plays a role in many intracellular or intercellular pathways, becomes very stable and water-soluble at high concentrations in an oxygen-deprived environment. If it is at low concentrations, it can maintain its stability even in the presence of oxygen.

At low concentrations, NO can promote tumor growth in ways such as promoting angiogenesis. At high concentrations, it becomes very toxic to cancer cells and suppresses tumor growth. The potentially toxic nature of cancer cells makes NO the subject of much research in medicine (3).

NO and Cancer.

NO has a high potential in cancer treatment due to its biocompatibility and tumor cell specific cytotoxicity. However, despite this feature, clinical applications have been limited due to the variability and target specificity of available NO donors and distribution network. However, in recent years, researchers have focused on the tumor microenvironment and aimed to benefit from NO toxicity by affecting the physiological conditions there. In a study, it has been reported that NO donor is formed by using free thiol groups with which NO can be easily conjugated, and NO is produced with its correct release. As a result of the same study, it was stated that the conjugate induces cytotoxicity in tumor cells and thus inhibits metastasis (17).

Ions necessary for the body have also been evaluated as microenvironmental targets. Because ions can sometimes turn into agents that destroy cells without creating toxicity and drug resistance. The mediation of NO to Ca2+ release inspired a new study. In the study, nanoparticle NO nano donors coated with zeolitic nitro-/nitrile-imidazole framework-82 with high photoreactivity and stability and berbamine (BER) release were formed.

While these NO nano donors release NO, the released NO causes a sudden increase in Ca2+. On the other hand, BER turns off the Ca2+ excretion pumps and the amount of intracellular Ca2+ increases excessively. This induces apoptosis. Thus, cell killing with endogenous ions has taken place (18).

It has also been observed that the antitumor response of CD8+ lymphocytes is regulated by NO in an experimental strategy in which iNOS and NO are overproduced by gene transfer (19). In another study with colorectal cancer cells, it was reported that sepiapterin treatment increased the tetrahydrobiopterin:dihydrobiopterin ratio and reduced tumor growth by activating nitric oxide synthase (20). In some studies, it has been stated that tumor cells exposed to NO donors show antitumor capacity. It has been reported that the antitumor capacity mechanisms of NO are reduction of COX-2 expression and inhibition of PI3K and MAPK pathways (21, 22).

Other mechanisms showing the anticancer properties of NO have also been suggested. These are that high NO concentrations (>200 nM) can cause cell death through disruption of anti-Apoptotic mediators, p53 upregulation, cytochrome release induction, cytostasis and

cytotoxicity, and cell cycle arrest. (H) In a study investigating the ability of hyaluronic acid (HA) to scavenge nitric oxide, they showed that NO breaks down HA. It was concluded that the nitric oxide-induced degradation of HA inhibits the migration of cancer cells in the tumor environment. And the potential use of HA in different biomedical applications has been suggested.(23).

CONCLUSION

According to the results obtained from the literature review, NO may have beneficial or harmful effects for the cell depending on the environment and its concentration in that environment. The damage it causes to the cell turns into a desired situation in the fight against cancer cells. But its lack of specificity makes its controllability difficult. In addition, the evidence that NO can be used in cancer treatment is quite clear. As seen in the review, studies in recent years have focused on specific mechanisms that can create specificity. In this direction, by targeting the tumor microenvironment, key molecules that can interact with NO in this microenvironment should be well identified. Studies are needed to reveal these molecules and their tumor suppression mechanisms.

REFERENCES

Kim T., Suh J., Kim W.J., (2021) *Adv. Mater*., 33, 2008793**.**

Sung Y. C., Jin P. R., Chu L. A., Hsu F. F., Wang M. R., Chang C. C., Chiou S. J., Qiu J. T.,. Gao D. Y, Lin C. C., Chen Y. S., Hsu Y. C., Wang J., Wang F. N., Yu P. L., Chiang A. S., Wu A. Y. T, Ko J. J. S., Lai C. P. K., Lu T. T, Chen Y. C. Nat. 2019. *Nanotechnol.*, 14, 1160

Kumar A., Radzievski R., Xie J. (2018) Free Radical: Nitric Oxide in Cancer Therapy. *Int J Anal Medicinal Chem*. 1(1): 1-4.

Wu G, Morrıs SM: (1998) Arginine metabolism: nitric oxide and beyond. *Biochem J* 336: 1-17,

Sajeev C, Srıdhar N, Veeranjaneyulu A. (1998) Nitric oxide: concepts, current perspectives and future therapeutic implications. *Indian J Pharmacol* 30: 351

Su Y, Couch M, Block ER: (1997) Substrate inhibition of nitric oxide synthase in pulmonary artery endothelial cells in culture. *Nitric Oxide Biol Chem* 1: 469-475

Jia Y, Zacour M, Tolloczko B, Martin JG. (1998) Nitric oxide synthesis by tracheal smooth muscle cells by a nitric oxide synthase-independent pathway. *Am J Physiol* 275: L895-L901

Förstermann U, Sessa WC. (2012) Nitric oxide synthases: regulation and function. *Eur Heart J*. Apr;33(7):829-37, 837a-837d. doi: 10.1093/eurheartj/ehr304.

Lacza Z, Snipes JA, Zhang J, Horváth EM, Figueroa JP, Szabó C, Busija DW. (2003) Mitochondrial nitric oxide synthase is not eNOS, nNOS or iNOS. *Free Radic Biol Med* 35: 1217-1228.

Ricciardolo FLM, Sterk PJ, Gaston B, Folkerts G. (2004). Nitric oxide in health and disease of the respiratory system. *Physiol Rev* 84: 731-765,

Meurs H, Maarsingh H, Zaagsma J. (2003). Arginase and asthma: novel insights into nitric oxide homeostasis and airway hyperresponsiveness. *Trends Pharmacol Sci* 24: 450-455

Eiserich, J.P., Patel, R.P., O'Donnell, V.B. 1998. Pathophysiology of nitric oxide and related species: Free radical reactions and modification of biomolecules. *Mol. Asp. Med*., 19, 221–357.

Tamer, T. M. (2014) In Engineering of Polymers and Chemical Complexity, Volume II; Focke, W. W., Radusch, H.-J., Eds.; Apple Academic Press,

Juan, C. A.; Pérez de la Lastra, J. M.; Plou, F. J.; Pérez-Lebeña, E. (2021) The Chemistry of Reactive Oxygen Species (ROS) Revisited: Outlining Their Role in Biological Macromolecules (DNA, Lipids and Proteins) and Induced Pathologies. *Int. J. Mol. Sci.* 22, 4642.

Strzelczyk, J. K.; Wiczkowski, A. (2012) Oxidative Damage and Carcinogenesis. *Wspolczesna Onkol*., 3, 230−233

Visconti, R.; Della Monica, R.; Grieco, D. (2016) Cell cycle checkpoint in cancer: A therapeutically targetable double-edged sword. *J. Exp. Clin. Cancer Res*., 35, 153.

Kim T, Suh J, Kim J, Kim WJ. (2022) Lymph-Directed Self-Immolative Nitric Oxide Prodrug for Inhibition of Intractable Metastatic Cancer. *Adv Sci (Weinh).* Jan 5;9(8):2101935. doi: 10.1002/advs.202101935.

X. Chu, X. Jiang, Y. Liu, S. Zhai, Y. Jiang, Y. Chen, J. Wu, Y. Wang, Y. Wu, X. Tao, X. He, W. Bu. 2021. Nitric oxide modulating calcium store for Ca^{2+}-initiated cancer therapy *Adv. Funct. Mater.*, 31 p. 2008507 doi: 10.1002/adfm.202008507

Navasardyan I and Bonavida B. (2021) Regulation of t cells in cancer by nitric oxide. *Cells* 10(10): 26–55

Alam A, Smith SC, Gobalakrishnan S, McGinn M, Yakovlev VA, Rabender CS. (2023) Uncoupled nitric oxide synthase activity promotes colorectal cancer progression. *Front Oncol.* 14;13:1165326. doi: 10.3389/fonc.2023.1165326.

Bocca C, Bozzo F, Bassignana A, et al. (2010) Antiproliferative effect of a novel nitro-oxy derivative of celecoxib in human colon cancer cells: role of COX-2 and nitric oxide. *Anticancer Res* 30(7): 2659–2666.

Bechmann N, Calsina B and Susan Richter JP (2022) Therapeutic potential of nitric oxide–releasing selective estrogen receptor modulators in malignant melanoma. *J Invest Dermatol* 142(8): 2217–2227

Alsharabasy AM, Glynn S, Farràs P, Pandit A. (2022) Interactions between Nitric Oxide and Hyaluronan Implicate the Migration of Breast Cancer Cells. *Biomacromolecules*. 12;23(9):3621-3647. doi: 10.1021/acs.biomac.2c00545

Antosova, M.; Mokra, D.; Pepucha, L.; Plevkova, J.; Buday, T.; Sterusky, M.; Bencova, A. (2017) Physiology of nitric oxide in the respiratory system. *Physiol. Res*. 66, S159–S172

In Silico Identification of Possible Mutation-Prone Regions of the GRIA3 Protein

Zeynep Nur KESKİN[1]
Emre AKTAŞ[2]
Nehir ÖZDEMİR ÖZGENTÜRK[3]

1. Introduction

Schizophrenia is characterized by positive psychotic symptoms, including hallucinations and delusions, and negative symptoms including emotional limitation and social impairment (Smeland., 2020). There are three symptom groups in schizophrenia; positive, negative and cognitive (Stepnicki P., et al. 2018). It is a chronic disease triggered by the interaction of genetic, epigenetic, developmental and environmental factors that interfere with normal brain development and maturation (Millan M. et al., 2016). Although genetic linkage and association studies have targeted a large number of candidate loci and genes, no specific gene variant or gene combination is sufficient to be shown to cause schizophrenia (Jablensky A., 2022). Currently, schizophrenia cannot be diagnosed with genetic risk factors, but further genetic studies will contribute to the diagnosis of the disease (Smeland., 2020).

1.1. Schizophrenia and GRIA3 Protein

Abnormalities in the expression of iontropic glutamate receptor subunits in the temporal lobe of the brain have been detected in schizophrenia and mood disorders (Beneyto M. et al. 2007). In studies conducted with the brains of patients who died of schizophrenia, it has been reported that the expression of the AMPA receptor is abnormal, but inconsistencies exist as in other theories to schizophrenia (Yonezawa K., et al., 2022). In a comprehensive study investigating rare encoded variants in genes that carry a significant risk for schizophrenia, it was stated that NMDA receptor subunit GRIN2A and AMPA receptor GRIA3 play a role in the pathogenesis of schizophrenia together with the disorder of the glutamatergic system (Singh T., et al, 2022).

1.2. Glutamate Receptors

One of the primary excitatory neurotransmitters and the most prevalent neurotransmitter in mammalian brains is glutamate (Moghaddam B., et al, 2012). Most glutamate receptors are ionotropic receptors with ligand-gated ion channels, but a few metabotropic glutamate receptors are also found. Ionotropic glutamate receptors are divided into three subtypes; NMDA (N-methyl-D-aspartate), AMPA (α-amino-3-hydroxy-5-methylisoxaole-4-propionate), and Kainate receptors (Uno Y., et al., 2019 , García-Gaytán AC., et al., 2022). The ionotropic

[1] Yıldız Technical University, Molecular Biology and Genetics, Orcid: https://orcid.org/0009-0009-4782-3016
[2] Res. Asst., Yıldız Technical University, Molecular Biology and Genetics, Orcid: https://orcid.org/:0000-0002-9422-3402
[3] Prof. Dr., Yıldız Technical University, Molecular Biology and Genetics, Orcid: https://orcid.org/0000-0003-3809-6303

glutamate receptors in the brain play a major role in mediating fast excitatory neurotransmission (Beneyto M. et al.,2007).

1.2.1 NMDA receptors.

NMDA receptors are ligand-gated ion channels that conducts excitatory transmission through a Ca2+ permeable component in the central nervous system. It has important physiological roles such as learning, memory and synaptic flexibility (Hansen KB., et al., 2018). NMDA receptors have 7 subunits; GRIN1, GRIN2 A-D and GRIN3 A-B (García-Gaytán AC., et al., 2022).

1.2.2 AMPA receptors.

Together with the NMDA and Kainat receptors, AMPA receptors are tetrameric ion channels that mediate most of the excitatory transmission in the central nervous system. They are the main fast transmission elements in synapses (Greger IH., et al., 2017). The activity of AMPA receptors is critical not only for neuronal development and synaptic plasticity in physiological conditions, but also because it can induce neuronal death in neuropathological conditions (Guo C., et al., 2021). They are transmembrane proteins that combine as a tetrameric complex consisting of 4 subunits, GRIA 1-4 (Kamalova A., et al., 2021). Disorders of the GRIA3 protein have been associated with disorders such as intellectual developmental disorder, bipolar disorder, schizophrenia, epilepsy, autism, and spasticity (MalaCards).

1.3. Detection of Mutations

Single nucleotide polymorphisms, SNPs, are the most common genetic mutation (Ou L., et al., 2017). SNPs that change the amino acid sequence are called nonsynonymous single nucleotide polymorphisms (nsSNPs). The translation product is affected by the change in the amino acid sequence (Soremekun OS, et al., 2021). Some SNPs can cause disease, predispose a person to disease, or impact how well they respond to medicine, while others are phenotypically neutral. (Ou L., et al., 2017). Single amino acid changes are the most common cause of many diseases. Examining single point mutations of a protein is of great importance for understanding disease mechanisms (Ng PC., et al., 2006). The development of databases and web-based algorithms that calculate the probability of mutations to be/ being harmful to see the effect of these mutations on proteins has facilitated and expanded research in this area (Choudjury A., et al., 2022). In silico studies are an important method used in drug discovery and development. Such studies provide advantages in terms of cost as they replace human and animal experiments (Saldanha L., et al., 2023).

In this study, DisEMBL, I-Mutant 2.0 and PhD-SNP bioinformatics tools will be used to detect various mutation-prone regions of the AMPA receptor subunit GRIA3 protein, a protein identified in the literature that may be a possible cause of schizophrenia, and to examine the pathogenic effects of these mutations.

2.Methods & Results

The NCBI-National Center for Biotechnology, the National Center for Biotechnology Information, is a platform established to provide access to biomedical and genomic information (NCBI-National Center for Biotechnology). In order to reach the GRIA3 protein via NCBI, "Glutamate Receptor 3" was searched in "Homo sapiens" was selected from the species filter for sequence information in humans.

The code representing the protein is P42263.2 (NCBI, UniProtKB). The FASTA format is a text format representing nucleotide or peptide sequences with the code in which base pairs

or amino acids are represented by single letters (NCBI-National Center for Biotechnology). The FASTA sequence of the protein at the amino acid level obtained is as follows.

>sp|P42263.2|GRIA3_HUMAN RecName: Full=Glutamate receptor 3; Short=GluR-3; AltName: Full=AMPA-selective glutamate receptor 3; AltName: Full=GluR-C; AltName: Full=GluR-K3; AltName: Full=Glutamate receptor ionotropic, AMPA 3; Short=GluA3; Flags: Precursor

MARQKKMGQSVLRAVFFLVLGLLGHSHGGFPNTISIGGLFMRNTVQEHSAFRFAVQLYNTNQNTTEKPFHL
NYHVDHLDSSNSFSVTNAFCSQFSRGVYAIFGFYDQMSMNTLTSFCGALHTSFVTPSFPTDADVQFVIQMRPALKGA
ILSLLGHYKWEKFVYLYDTERGFSILQAIMEAAVQNNWQVTARSVGNIKDVQEFRRIIEEMDRRQEKRYLIDCEVER
INTILEQVVILGKHSRGYHYMLANLGFTDILLERVMHGGANITGFQIVNNENPMVQQFIQRWVRLDEREFPEAKNAP
LKYTSALTHDAILVIAEAFRYLRRQRVDVSRRGSAGDCLANPAVPWSQGIDIERALKMVQVQGMTGNIQFDTYGRR
TNYTIDVYEMKVSGSRKAGYWNEYERFVPFSDQQISNDSASSENRTIVVTTILESPYVMYKKNHEQLEGNERYEGY
CVDLAYEIAKHVRIKYKLSIVGDGKYGARDPETKIWNGMVGELVYGRADIAVAPLTITLVREEVIDFSKPFMSLGISI
MIKKPQKSKPGVFSFLDPLAYEIWMCIVFAYIGVSVVLFLVSRFSPYEWHLEDNNEEPRDPQSPPDPPNEFGIFNSLW
FSLGAFMQQGCDISPRSLSGRIVGGVWWFFTLIIISSYTANLAAFLTVERMVSPIESAEDLAKQTEIAYGTLDSGSTKE
FFRRSKIAVYEKMWSYMKSAEPSVFTKTTADGVARVRKSKGKFAFLLESTMNEYIEQRKPCDTMKVGGNLDSKGY
GVATPKGSALRNAVNLAVLKLNEQGLLDKLKNKWWYDKGECGSGGGDSKDKTSALSLSNVAGVFYILVGGLGLA
MMVALIEFCYKSRAESKRMKLTKNTQNFKPAPATNTQNYATYREGYNVYGTESVKI

2.1.Identification of Mutation-Prone Regions of the GRIA3 Protein

Mutation-prone regions in the GRIA3 protein were investigated by estimating the irregular/unstructured regions, then stability changes in these regions, evolutionary analysis, and SNP estimation.

2.3.Prediction of disordered/unstructured regions of the GRIA3 protein

The tool DisEMBL (http://dis.embl.de) was used to predict the disordered/unstructured regions in the sequence of the GRIA3 protein. With the DisEMBL tool, irregular regions can be examined for Loop and Coil, Hot-loops and Remark-465 (Linding R., et al., 2003).

Estimations were obtained by loading the amino acid sequence of the GRIA3 protein into the DisEMBL tool and converted into a table as in Table 1. In terms of loops/coils, the irregular/unstructured regions were estimated as 1-8, 390-422, 793-817. Irregular/unstructured regions in terms of hot cycles were estimated as 1-10, 409-424, 805-813. In terms of Remark-465, irregular/unstructured regions were estimated as 1-8, 412-421, 806-815. When the regions common in all results were combined, MARQKKMG between regions 1 and 8, QISNDSASSE between regions 412 and 421, and GSGGGDSK between regions 806 and 813 were determined as common. These detected regions will be used in the next stages of the study. Regions and amino acids determined to be common in the results obtained in Table 1 are highlighted in bold.

Table 1. Results of disordered/unstructured regions of the GRIA3 protein predicted by the DisEMBL tool.

Estimation tool DisEMBL	**Estimated Locations**	**Common Predicted Results**
Disordered by Loops/coils definition	**1-8**, 24-44, 59-86, 119-134, 262-278, 290-308, 329-352, 366-381, **390-422**, 442-453, 472-491, 500-507, 534-549, 575-606, 617-634, 661-668, 678-691, 707-718, 744-773, **793-817**, 852-894	**MARQKKMG: 1-8** **QISNDSASSE: 412-421** **GSGGGDSK: 806-813**
Disordered by Hot-loops definition	**1-10**, 190-200, 270-278, 298-310, 330-349, 367-378, **409-424**, 429-437, 470-489, 534-542, 678-691, 705-726, 791-800**, 805-813**, 859-882	
Disordered by Remark-465 definition	**1-8, 412-421**, 585-597, **806-815**	

2.4.Estimation of stability changes of the GRIA3 protein

The I-Mutant 2.0 (https://folding.biofold.org/cgi-bin/i-mutant2.0.cgi) tool was used to examine the effect of single point mutations on protein stability in the construct and sequence. The I-Mutant 2.0 tool can predict whether mutations stabilize the protein with an accuracy of 80% if the protein structure is known, and 77% if the protein structure is unknown. (Capriotti E., et al., 2005).

After loading the amino acid sequence of the protein to the site, the position of the single point mutations was written and the new residue part was left blank, and the stability change of all 19 amino acid changes was obtained. The temperature in degrees Celsius was adjusted to 37 and the pH (-log[H+]) to 7.4 (Capriotti E., et al., 2005). Protein stability, which is changed by a single point mutation, is given by the score obtained from the protein's structure information and sequence information. In the result format, "Increase" is written if the stability increases according to the free energy change, and "Decrease" if it decreases. The RI value is the reliability index. Of the 475 results obtained by performing 19 single point mutations of 25 amino acids, only those with a confidence index above 8 are selected and shown in Table 2. The RI value of 35 results is 8, and the RI value of 22 results is 9. In the I413S mutation, the RI value is 10. This result indicates that stability has been proven to be reduced in this mutation (in bold in Table 2). Of the 57 stability change analyzes with an RI value of 8 and above, 50 results showed a decrease in stability, while 7 results showed an increase in stability.

Table 2. Effect of GRIA3 mutations predicted by the I-Mutant 2.0 tool on protein stability

Estimation tool	**Variant**	**Results**	**RI**	**Variant**	**Results**	**RI**	**Variant**	**Results**	**RI**
I-Mutant	R3K	Decrease	9	A418Y	Decrease	8	I413G	Decrease	9
	R3H	Decrease	8	A418S	Decrease	9	I413V	Decrease	9
	R3G	Decrease	8	A418K	Decrease	8	I413F	Decrease	9
	K5P	Increase	8	A418Q	Decrease	9	I413T	Decrease	9
	K5L	Increase	8	E421K	Decrease	8	I413Y	Decrease	9
	K5V	Increase	9	E421Q	Decrease	8	I413E	Decrease	8
	K6L	Increase	8	E421A	Decrease	8	I413H	Decrease	9
	K6V	Increase	8	G806K	Decrease	8	I413M	Decrease	9
	K6P	Increase	8	G806Q	Decrease	8	**I413P**	**Decrease**	**9**
	K6F	Increase	8	G806D	Decrease	8	**N415Q**	**Decrease**	**9**
	M7H	Decrease	8	G809R	Decrease	8	**N415G**	**Decrease**	**8**
	M7G	Decrease	9	S812A	Decrease	8	**N415A**	**Decrease**	**8**
	G8K	Decrease	8	G808R	Decrease	8	N415S	Decrease	9
	I413A	Decrease	9	G808K	Decrease	8	A418T	Decrease	8
	I413D	Decrease	9	G808Q	Decrease	9	A418Y	Decrease	8
	I413Q	Decrease	9	G809K	Decrease	8	I413W	Decrease	9
	I413K	Decrease	9	G809Q	Decrease	8	I413R	Decrease	9
	I413S	Decrease	10	G809D	Decrease	8	I413C	Decrease	8
	G810Q	Decrease	8	K813A	Decrease	8			

pH.:7.4, Temperature:37

2.5.Prediction of SNPs of GRIA3 protein

PhD-SNP (http://snps.biofold.org/phd-snp/phd-snp.html) is an optimized tool to predict whether a given single point protein mutation can be classified as a disease-associated or neutral polymorphism (Capriotti E., et al., 2006). The analysis was performed by entering the protein sequence, the location of the mutation, and the symbol of the new amino acid in the tool, replacing all 19 amino acids for 25 positions. As a result of the analysis, the disease effect of

the mutation and the Relativity Index(RI) value was obtained. Disease results among the results obtained are given in Table 3. All mutations are neutral except for the mutations given in Table 3.

Table 3. Disease effect of GRIA3 mutations estimated by the PhD-SNP tool

Estimation Tool	**Variant**	**Results**	**RI**	**Variant**	**Results**	**RI**	**Variant**	**Results**	**RI**
PhD -SNP	M7P	Disease	1	N415E	Disease	5	G808C	Disease	3
	M7K	Disease	1	D416Y	Disease	2	G808P	Disease	1
	Q412P	Disease	4	D416P	Disease	4	G809C	Disease	2
	I413P	**Disease**	**2**	D416C	Disease	3	G810C	Disease	1
	S414P	Disease	2	D416H	Disease	2	D811V	Disease	1
	N415V	Disease	1	D416K	Disease	1	D811F	Disease	2
	N415L	Disease	2	S417I	Disease	3	D811W	Disease	1
	N415I	Disease	7	S417F	Disease	0	D811Y	Disease	5
	N415F	Disease	3	S417W	Disease	2	D811A	Disease	3
	N415W	Disease	3	S417P	Disease	5	D811P	Disease	5
	N415Y	Disease	5	S417K	Disease	2	D811C	Disease	3
	N415G	**Disease**	**4**	S417E	Disease	0	D811H	Disease	1
	N415A	**Disease**	**1**	S419P	Disease	1	D811R	Disease	2
	N415P	Disease	7	G806Y	Disease	0	D811Q	Disease	1
	N415T	Disease	2	G806C	Disease	2	S812W	Disease	0
	N415C	Disease	5	S807W	Disease	0	S812P	Disease	5
	N415H	Disease	5	S807Y	Disease	2	S807R	Disease	2
	N415R	Disease	3	S807P	Disease	5			
	N415K	Disease	2	**N415Q**	**Disease**	**1**			

3.Discussion

The disease effect and stability changes of possible single amino acid changes of the GRIA3 protein associated with schizophrenia were investigated using bioinformatics tools such as DisEMBL, I-Mutant 2.0, and PhD-SNP. With the PhD-SNP tool, 62 mutations were estimated to have a disease effect. It was estimated that 15 out of 19 mutations in the N415 region can cause disease, highlighting this region's importance. The stability of the I413P, N415Q, N415A, and N415G mutations, which are predicted to cause disease by PhD-SNP, were determined by the I-Mutant 2.0 tool with a score above 8. The results obtained enabled the identification of potential variants that may cause schizophrenia. The results of this study can be supported by different in silico studies to be done later.

Acknowledgments

This project was supported by TUBITAK 2209-A University Students Research Projects Support Program.

References

Beneyto, M., Kristiansen, L., Oni-Orisan, A. et al. (2007). Abnormal glutamate receptor expression in the medial temporal lobe in schizophrenia and mood disorders. *Neuropsychopharmacol*. 32,1888–1902 doi: 10.1038/sj.npp.1301312

Capriotti E, Calabrese R, Casadio R. (2006). Predicting the insurgence of human genetic diseases associated to single point protein mutations with support vector machines and evolutionary information. *Bioinformatics*. 22, 2729-2734. doi: 10.1093/bioinformatics/btl423

Capriotti E, Fariselli P and Casadio R (2005). I-Mutant2.0: predicting stability changes upon mutation from the protein sequence or structure.,*Nucl. Acids Res*. 33: W306-W310

García-Gaytán AC, Hernández-Abrego A, Díaz-Muñoz M, Méndez I. (2022 Nov). Glutamatergic system components as potential biomarkers and therapeutic targets in cancer in non-neural organs. *Front Endocrinol (Lausanne)*. 13:1029210. doi: 10.3389/fendo.2022.1029210

Greger IH, Watson JF, Cull-Candy SG. (2017 May). Structural and functional architecture of AMPA-Type glutamate receptors and their auxiliary proteins. *Neuron*. 94(4):713-730. doi: 10.1016/j.neuron.2017.04.009

Guo C, Ma YY. (2021 Aug). Calcium permeable-AMPA receptors and excitotoxicity in neurological disorders. *Front Neural Circuits*. 15:711564. doi: 10.3389/fncir.2021.711564

Hansen KB, Yi F, Perszyk RE, Furukawa H, Wollmuth LP, Gibb AJ, Traynelis SF. (2018 Aug). Structure, function, and allosteric modulation of NMDA receptors. *J Gen Physiol*. 150(8):1081-1105. doi: 10.1085/jgp.201812032

Jablensky A. (2010). The diagnostic concept of schizophrenia: its history, evolution, and future prospects. *Dialogues Clin Neurosci*. 12(3):271-87. doi: 10.31887/DCNS.2010.12.3/ajablensky

Kamalova A, Nakagawa T. (2021 Jan). AMPA receptor structure and auxiliary subunits. *J Physiol*. 599(2):453-469. doi: 10.1113/JP278701

Linding R, Jensen LJ, Diella F, Bork P, Gibson TJ, Russell RB. (2003 Nov). Protein disorder prediction: implications for structural proteomics. *Structure*. 11(11):1453-9. doi: 10.1016/j.str.2003.10.002

Malacards. (2023 May). GRIA3. Malacards: Human Disease Database. Date of Access: 21.05.2023, URL: https://www.malacards.org/search/results/GRIA3?startPage=0

Millan MJ, Andrieux A, et al., (2016 Jul). Altering the course of schizophrenia: progress and perspectives. *Nat Rev Drug Discov*. 15(7):485-515. doi: 10.1038/nrd.2016.28

Moghaddam B, Javitt D. (2012 Jan). From revolution to evolution: the glutamate hypothesis of schizophrenia and its implication for treatment. *Neuropsychopharmacology*. 37(1):4-15. doi: 10.1038/npp.2011.181

NCBI-National Center for Biotechnology. (2023). Home Page. Date of Access: May 6, 2023, from https://www.ncbi.nlm.nih.gov/

Ng PC, Henikoff S. (2006). Predicting the effects of amino acid substitutions on protein function. *Annu Rev Genomics Hum Genet*. 7:61-80. doi: 10.1146/annurev.genom.7.080505.115630.

Ou L, Przybilla MJ, Whitley CB. (2017 Jul). Phenotype prediction for mucopolysaccharidosis type I by in silico analysis. *Orphanet J Rare Dis*. 12(1):125. doi: 10.1186/s13023-017-0678-1

Rizzato F, Rodriguez A, Biarnés X, Laio A. (2017 Oct) Predicting amino acid substitution probabilities using single nucleotide polymorphisms. *Genetics.* 207(2):643-652. doi: 10.1534/genetics.117.300078

Saldanha L, Langel Ü, Vale N. (2023 Feb). In silico studies to support vaccine development. *Pharmaceutics*. 15(2):654. doi: 10.3390/pharmaceutics15020654.

Singh T, et al. (2022 Apr). Rare coding variants in ten genes confer substantial risk for schizophrenia. *Nature*. 604(7906):509-516. doi: 10.1038/s41586-022-04556-w

Smeland, O.B., Frei, O., Dale, A.M. et al. (2020). The polygenic architecture of schizophrenia — rethinking pathogenesis and nosology. *Nat Rev Neurol* 16, 366–379. doi: 10.1038/s41582-020-0364-0

Soremekun OS, Ezenwa C, et al., (2021) Transcription-translation error: In-silico investigation of the structural and functional impact of deleterious single nucleotide polymorphisms in GULP1 gene. *Inform Med Unlocked*. 22:100503. doi: 10.1016/j.imu.2020.100503.

Stępnicki P, Kondej M, Kaczor AA.(2018 Aug). Current concepts and treatments of schizophrenia. *Molecules*. 23(8):2087. doi: 10.3390/molecules23082087

Uno Y, Coyle JT. (2019 May). Glutamate hypothesis in schizophrenia. *Psychiatry Clin Neurosci*. 73(5):204-215. doi: 10.1111/pcn.12823

Yonezawa K, Tani H, et al., (2022 May). AMPA receptors in schizophrenia: A systematic review of postmortem studies on receptor subunit expression and binding. *Schizophr Res*. 243:98-109. doi: 10.1016/j.schres.2022.02.033

Choudhury A, Mohammad T, et al., (2022 May). Comparative analysis of web-based programs for single amino acid substitutions in proteins. *PLoS One*. 17(5):e0267084. doi: 10.1371/journal.pone.0267084.

Axicon Metalens Design with Gold Aperture-Based Nanoantennas

Büşra Ersoy[1]
Ekin Aslan[2]
Erdem Aslan[3]

Introduction

By constructing an electromagnetic phase discontinuity across an interface where light undergoes a change of medium, it is possible to manipulate abnormal reflections and refractions as defined by the generalized Snell's law, and thus fully control the propagation of light(Kildishev et al., 2013; N. Yu et al., 2011):

$$\sin(\theta_t)\, n_t - \sin(\theta_i)\, n_i = \lambda_0 \nabla\Phi / 2\pi \tag{1a}$$

$$\cos(\theta_t)\sin(\psi_t)\, n_t = \lambda_0 \nabla\Phi / 2\pi \tag{1b}$$

$$\sin(\theta_r) n_i - \sin(\theta_i) n_i = \lambda_0 \nabla\Phi / 2\pi \tag{2a}$$

$$\cos(\theta_r)\sin(\psi_r)\, n_i = \lambda_0 \nabla\Phi / 2\pi \tag{2b}$$

In Equation 1a,b and Equation 2a,b, the generalized Snell's law, the angles θ_t, θ_i, and θ_r represent the in-plane refraction, incidence, and reflection angles, respectively. Furthermore, n_t and n_i represent the refractive indices of the transmitting and incident media, respectively, and λ_0 is the wavelength in free space. $\nabla\Phi$ represents the gradient of the phase discontinuity provided by the meta-atoms at the interface. The phase gradient on the incidence plane leads to in-plane reflection and refraction events, while phase gradients off the incidence plane result in out-of-plane behavior. The ψ_t and ψ_r in the equations represent the respective out-of-plane refraction and reflection angles. All of these expressions indicate that they can be achieved in a very thin layer that can provide a phase gradient across an interface (Kildishev et al., 2013).

In addition to standard reflection and refraction, phenomena such as birefringence and negative refraction can occur. These events are caused by the variation of the electromagnetic phase, denoted by Φ, across the interface, which depends on the coordinates of the interface. The specific functionality that the phase profile needs to exhibit is dictated by the desired application. The positional variation of the phase can be obtained by dividing the relevant plane into unit cells. Different nanoantenna designs can be utilized to create unit cells with distinct unit phase profiles. For instance, V-shaped nanoantennas, which have been described in the literature as cells of a gradient metasurface, can generate abrupt phase shifts from 0 to 2π for cross-polarized light due to their different geometries. To achieve full phase control, it is important for the phase shift range to be larger than the 2π phase coverage domain.

[1] Büşra Ersoy, Student, Kayseri University, Department of Electrical and Electronics Engineering, ORCID: 0000-0003-1383-3311
[2] Ekin Aslan, Assoc. Prof, Kayseri University, Department of Electrical and Electronics Engineering, ORCID: 0000-0003-0933-7796
[3] Erdem Aslan, Assoc. Prof, Erciyes University, Department of Electrical and Electronics Engineering, ORCID: 0000-0001-6829-9000

In the work of Yu et al.(N. Yu et al., 2011), it has been demonstrated that the 90° rotation of V-shaped antennas enables phase transitions in the range of 0 to π for cross-polarized incident light. This finding applies specifically to linearly polarized incoming light (Ni et al., 2012; N. Yu et al., 2013). To achieve focusing functionality, these nanoantennas can be arranged in concentric rings. This arrangement allows the nanoantennas to create abrupt phase shifts, distributing the propagating waves across the interface in a way that leads to constructive interference at a distance of f, causing the outgoing cross-polarized light to be focused at a focal distance. This results in lensing functionality being achieved(Kildishev et al., 2013; Ni et al., 2013). Indeed, these types of ultra-thin designed metalenses offer crucial designs for applications such as laser processing, high-precision position alignment, sensing, and the generation of non-diffracting Bessel beams(Aieta et al., 2012). Their unique properties and capabilities make them valuable tools in various fields where precise control and manipulation of light are required (Kildishev et al., 2013).
For flat lenses to achieve focusing, the phase change on their surface must be

$$\Phi(x,y) = \frac{2\pi}{\lambda}\ (\sqrt{(x^2+y^2)+f^2} - f) \tag{3}$$

with the surface plane being the xy −plane. In this equation, f represents the focal length, λ denotes the operating wavelength, and x and y represent the coordinates on the interface. The surface phase gradient arranged according to this equation enables focusing at a desired focal length (Aieta et al., 2012).

In plasmonic applications, noble metals such as gold (Au) and silver (Ag) are typically employed. The frequency-dependent dielectric permittivity in plasmonic materials is crucially defined by the plasma frequency ω_p. For instance, the complex and real relative permittivities are expressed as follows depending on ω_p:

$$\varepsilon_r' = 1 - \frac{\omega_p^2}{\omega^2+\gamma^2} \tag{1}$$

$$\varepsilon_r'' = 1 - \frac{\omega_p^2\gamma}{\omega(\omega^2+\gamma^2)} \tag{2}$$

Here, γ is the damping rate, which is usually in the terahertz range and specific to the material. When operating at optical frequencies ($\omega \ll \gamma$), Equation 2 can be turn into to Equation 3:

$$\varepsilon_r'' = \frac{\omega_p^2}{\omega^3} \tag{3}$$

This equation indicates that in order to reduce optical losses in plasmonic materials, it is necessary to decrease the plasma frequency or damping rate. The damping rate is temperature-dependent and is related to the scattering mechanisms of electrons in the metal (Kesim et al., 2014).

The objective of this study is to design metalenses utilizing plasmonic-based nanostructures through the creation of phase gradients. Circular aperiodic arrays of these structures are utilized. By inducing radial phase variations ranging from 0 to 2π via the resonant behavior of individual meta molecules, a distinctive metalens design with multiple focal centers is accomplished. Numerical analysis is employed to derive theoretical focusing parameters, including numerical aperture (NA) and focusing efficiency.

Method

Our study includes the design of equilateral-shaped antennas based on aperture structures, taking inspiration from the phase transition generated by antenna geometries presented in Yu

et al(N. Yu et al., 2011). The study by Yu et al. (N. Yu et al., 2011) includes the phase shifts and scattering amplitudes in cross-polarization for eight types of V-shaped nanostructures. The desired phase steps and high scattering characteristics are achieved by manipulating the arm angle and rotation difference in the meta-atoms. The unit cell images of the eight types utilized in our design are presented in Figure 1. The angles of the antennas obtained using various angles, as shown in Figure 1, are sequentially 2α = 30°,68°, 79°, and 104°. The other geometric dimensions of the employed meta-cells are as follows: arm length d = 1000 nm, arm width w = 200 nm, and interarm spacing c = 200 nm.

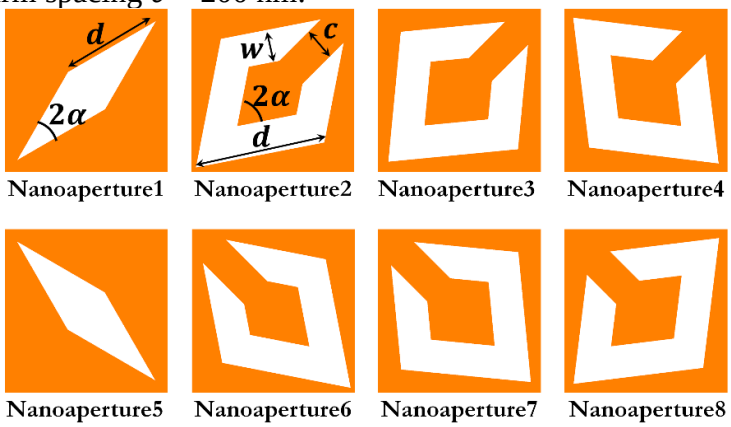

Figure 1- Top views of metacells in each arrangement.

The proposed nanostructures are designed as longitudinally opened nanoapertures on a silicon nitride (SiN) membrane coated with a subwavelength-thick layer of gold (Au). The thicknesses of the Au layer t_{Au} and the SiN membrane t_{SiN} are set to t_{Au}= 50 nm and t_{SiN}= 100 nm, respectively, for all analyses. The source wavelength is λ = 850 nm. The design of the nanostructures is accomplished through simulations using the finite-difference time-domain (FDTD) method. The analyzed structures are illuminated with vertically incident x −polarized light in the visible and near-infrared (NIR) wavelengths.

Results and Discussion

In the initial analyses, the transmittance of the structures is measured in the far field to investigate their resonant behavior, and the results are presented in Figure 2. As observed, the designed structures and their symmetries exhibit resonant behavior at 850 nm in all four angle values.

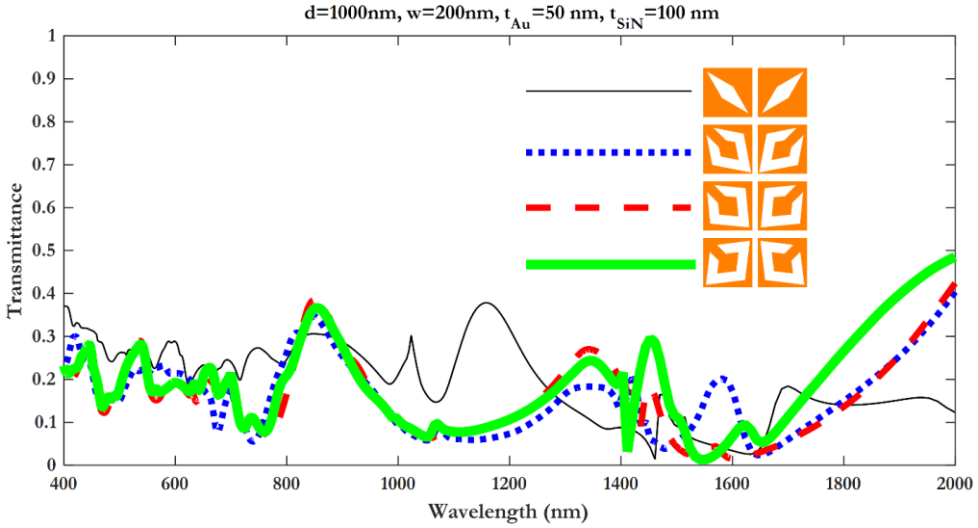

Figure 2- The transmittance analysis results of the antennas used in the arrangement.

One of the conditions for efficient focusing is the resonant behavior of the antennas used at the desired wavelength (Ding et al., 2015; Lee et al., 2011). The designed metalens consists of plasmonic nanoapertures that exhibit resonant behavior at the targeted operating wavelength, as depicted in Figure 3. The antennas are arranged in aperiodic fashion, with equal spacing, along the radial direction to achieve a uniform phase change within the range of [0,2π]. This represents a flat axicon lens approach, which results in a greater focal depth, thereby enabling long focal spots along the focusing direction. (Chang et al., 2023; Mohtashami et al., 2021). The focal performance is analyzed for the designed aperiodic arrangement, which consists of nanoapertures on a SiN membrane coated with a layer of Au.

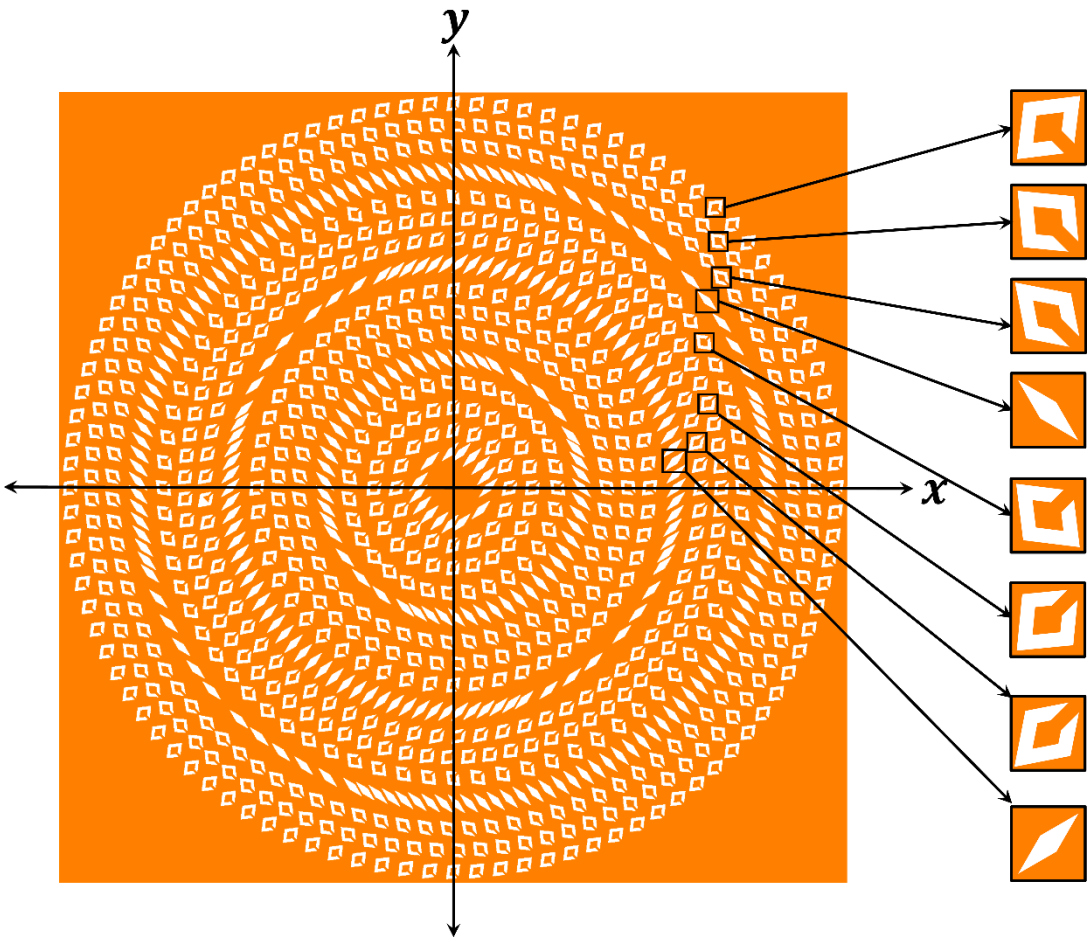

Figure 3- Top view of the antenna arrangement.

In order to demonstrate the focal points exhibited by the antenna array shown in Figure 3, two vertical monitors are placed in the $xz-$ plane and $xy-$ plane. The results obtained from the monitors are presented in Figure 4. The panels of the figure provide the normalized light intensity distributions with respect to the source in the propagation plane (Figure 4a) and perpendicular to both the propagation plane and the metalens (Figure 4b). According to this, in the designed structure, at focal distances of f_1 = 2.88 μm, f_2 = 4.07 μm, f_3 = 8.14 μm, f_4 = 9.75 μm, ve f_5 = 16.79 μm, multiple focal spots with a spot count of five and normalized light intensity greater than 1 have been determined. The focal distances of the identified spots are presented in Table 1.

Theoretical focusing parameters are determined through analysis by placing horizontal field monitors at the center of these identified focal spots. The light intensity distributions of each monitor at the f_1, f_2, f_3, f_4, and f_5 locations are shown in Figure 5.

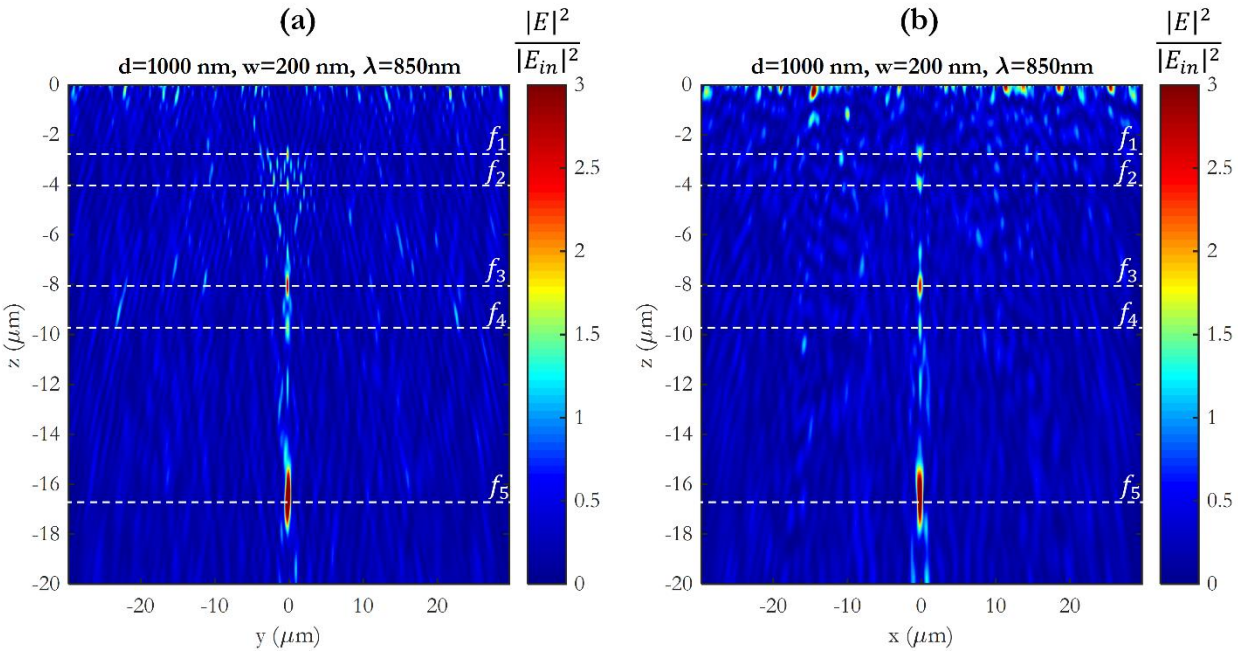

Figure 4- Light intensity distributions normalized to incident light intensity on vertical monitors.

Table 1- *Focal distance values for multiple focal points.*

Focal Spot	Focal Lenght (μm)
f_1	2.88 μm
f_2	4.07 μm
f_3	8.14 μm
f_4	9.75 μm
f_5	16.79 μm

Table 2 presents the theoretical focusing parameters of the proposed metalens, which determine its maximum resolution. These parameters are crucial factors in determining the performance of the metalens. NA is one of the focusing parameters, representing the ratio between the metalens diameter and the focal length. It plays a significant role in optical systems. NA of a metalenses expresses the resolution level determined by the design of metal or dielectric structures at the nano scale and the operating frequency. The NA is calculated using the formula $NA = n * sin\theta$, where n represents refractive index of the environment in which the metastructure is located and θ denotes the half-angle of the maximum cone of light accepted by the metalens (Aieta et al., 2012). This value determines how light will be reflected in traditional lenses, thus affecting the resolution of the lens. The second parameter to be calculated is the full width at half maximum (FWHM), which represents the width of the light intensity distribution at half of its maximum value. In microlenses, FWHM represents the distance between two points that intersect half of the light intensity, and it is calculated as $FWHM = \frac{\lambda_0}{2NA}$. This distance determines the width of the light beam and represents the midpoint of the light intensity during the transition from one point to another (Ali & Aksu, 2021; Aslan & Aslan, 2020; X. Yu et al., 2021). Another parameter we have is the depth of focus (DOF). The DOF for a regular lens with a diameter of D and a focal length of f is calculated as $DOF = 4\lambda_0 \frac{f^2}{D^2}$. It represents the distance in which objects can still be seen clearly in a region beyond the focal point (Ali & Aksu, 2021; Bayati et al., 2020). The final important parameter is the focal efficiency $\eta.\eta$ represents the proportion of light energy collected in the

optical system that is concentrated at the focal point. It is calculated by dividing the average light intensity at the focal point by the incoming average light intensity. The formulated expression is $\eta = \frac{\langle I_f \rangle}{\langle I_i \rangle}$, where η represents the calculated value as the ratio of the average light intensity at the focal point $\langle I_f \rangle$ to the incoming average light intensity $\langle I_i \rangle$ (Aslan, 2021).

Table 2- *The focusing parameter values for the proposed metalens arrangement.*

Lens Properties	Focal Points	Values
NA	f_1=2.88 μm	0.99
	f_2=4.07 μm	0.99
	f_3=8.14 μm	0.96
	f_4=9.752 μm	0.95
	f_5=16.79 μm	0.87
FWHM (μm)	f_1=2.88 μm	0,.3
	f_2=4.07 μm	0.43
	f_3=8.14 μm	0.44
	f_4=9.752 μm	0.45
	f_5=16.79 μm	0.49
DOF (μm)	f_1=2.88 μm	0.008
	f_2=4.07 μm	0.016
	f_3=8.14 μm	0.064
	f_4=9.752 μm	0.092
	f_5=16.79 μm	0.272
η (%)	f_1=2.88 μm	0.4
	f_2=4.07 μm	0.3
	f_3=8.14 μm	0.7
	f_4=9.752 μm	0.5
	f_5=16.79 μm	2

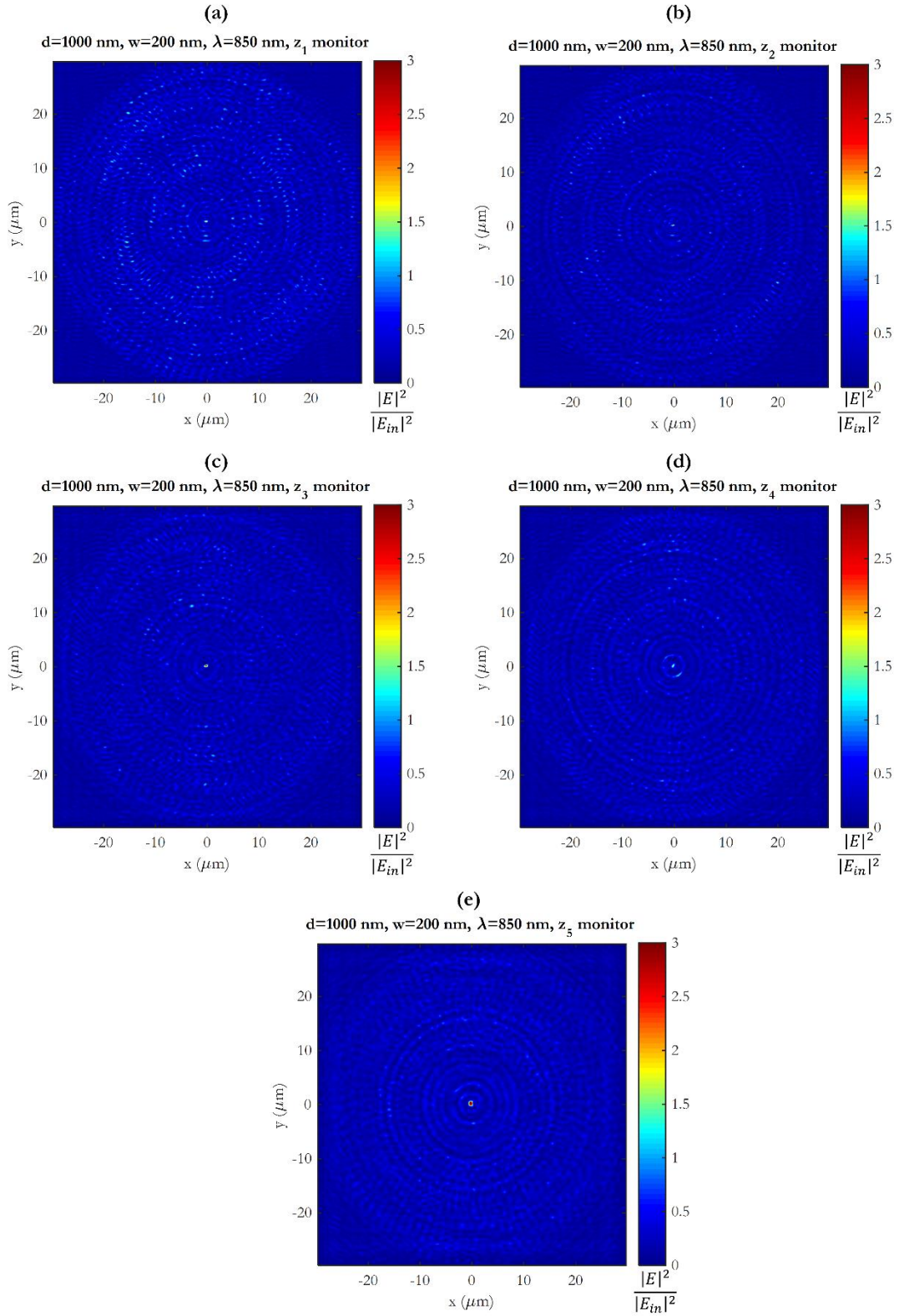

Figure* 5-** *Normalized light intensity distributions obtained from horizontal monitors placed at the centers of focal spots.* ***(a) $z = f_1$, ***(b)*** $z = f_2$, ***(c)*** $z = f_3$, ***(d)*** $z = f_4$, *and* ***(d)*** $z = f_5$.

Conclusion

Plasmonic metalenses are phase-modulated metasurfaces constituting specific phase distributions due to plasmonic nanostructures in their content. The desired phase response on the cells of plasmonic metalenses relies on various factors including the dielectric substrate and

size, shape, and rotational mode of metallic nanostructures. In the present study, we designed eight plasmonic unit cells for the metalens, enabling phase manipulation across the entire phase range necessary for achieving axicon focusing functionality. These unit cells consist of aperture-based nanoantennas embedded in a nanoscaled layer of gold film on a silicon nitride membrane with subwavelength-thickness. Simulations are conducted at a wavelength of 850 nm. The unit cells are arranged in a circular pattern at equal radial distances, forming circular phase rings that induce complete phase transition at the metalens interface. Taking into account the limitations of the analytical analiz infrastructure, our proposed plasmonic metalens design enabled the identification of multifocal points. Theoretical calculations are performed to determine key focusing parameters for each focal point, including focal length, NA, DOF, FWHM, and η.

Acknowledgement

This study acknowledges the support provided by The Scientific and Technological Research Council of Turkey (TUBITAK− Project ID: 121E518).

References

Aieta, F., Genevet, P., Kats, M. A., Yu, N., Blanchard, R., Gaburro, Z., & Capasso, F. (2012). Aberration-free ultrathin flat lenses and axicons at telecom wavelengths based on plasmonic metasurfaces. *Nano Letters*, *12*(9), 4932–4936. https://doi.org/10.1021/NL302516V/SUPPL_FILE/NL302516V_SI_001.PDF

Ali, F., & Aksu, S. (2021). A hybrid broadband metalens operating at ultraviolet frequencies. *Scientific Reports*, *11*(1), 1–8. https://doi.org/10.1038/s41598-021-81956-4

Aslan, E. (2021). Lensing for optical communication by diffraction from Peano curve-based fractal with alternative plasmonic material. *Optik*, *242*, 167072. https://doi.org/10.1016/J.IJLEO.2021.167072

Aslan, E., & Aslan, E. (2020). A Microlens by Gallium Doped Zinc Oxide-Nanoantenna. *Mühendislik Bilimleri ve Tasarım Dergisi*, *8*(3), 931–942. https://doi.org/10.21923/JESD.784056

Bayati, E., Pestourie, R., Colburn, S., Lin, Z., Johnson, S. G., & Majumdar, A. (2020). Inverse Designed Metalenses with Extended Depth of Focus. *ACS Photonics*, *7*(4), 873–878. https://doi.org/10.1021/ACSPHOTONICS.9B01703/ASSET/IMAGES/LARGE/PH9B01703_0004.JPEG

Chang, K. H., Chen, Y. C., Huang, Y. S., Hsu, W. L., Lu, G. H., Liu, C. F., Weng, C. J., Lin, Y. H., Chen, C. C., Lee, C. C., Chang, Y. C., Wang, P. H., & Wang, C. M. (2023). Axicon metalens for broadband light harvesting. *Nanophotonics*, *12*(7), 1309–1315. https://doi.org/10.1515/NANOPH-2023-0017/MACHINEREADABLECITATION/RIS

Ding, F., Wang, Z., He, S., Shalaev, V. M., & Kildishev, A. V. (2015). Broadband high-efficiency half-wave plate: A supercell-based plasmonic metasurface approach. *ACS Nano*, *9*(4), 4111–4119. https://doi.org/10.1021/ACSNANO.5B00218/SUPPL_FILE/NN5B00218_SI_001.PDF

Kesim, Y. E., Battal, E., & Okyay, A. K. (2014). Plasmonic materials based on ZnO films and their potential for developing broadband middle-infrared absorbers. *AIP Advances*, *4*(7). https://doi.org/10.1063/1.4887520/20698

Kildishev, A. V., Boltasseva, A., & Shalaev, V. M. (2013). Planar photonics with metasurfaces. *Science (New York, N.Y.)*, *339*(6125), 12320091–12320096. https://doi.org/10.1126/SCIENCE.1232009

Lee, Y., Zhang, J. X. J., & Alu, A. (2011). Efficient apertureless scanning probes using patterned plasmonic surfaces. *Optics Express*, *19*(27), 25990–25999. https://doi.org/10.1364/OE.19.025990

Mohtashami, Y., DeCrescent, R. A., Heki, L. K., Iyer, P. P., Butakov, N. A., Wong, M. S., Alhassan, A., Mitchell, W. J., Nakamura, S., DenBaars, S. P., & Schuller, J. A. (2021). Light-emitting metalenses and meta-axicons for focusing and beaming of spontaneous emission. *Nature Communications*, *12*(1), 1–7. https://doi.org/10.1038/s41467-021-23433-0

Ni, X., Emani, N. K., Kildishev, A. V., Boltasseva, A., & Shalaev, V. M. (2012). Broadband light bending with plasmonic nanoantennas. *Science*, *335*(6067), 427. https://doi.org/10.1126/SCIENCE.1214686/SUPPL_FILE/NI.SOM.PDF

Ni, X., Ishii, S., Kildishev, A. V., & Shalaev, V. M. (2013). Ultra-thin, planar, Babinet-inverted plasmonic metalenses. *Light: Science and Applications*, *2*(APRIL), e72. https://doi.org/10.1038/LSA.2013.28

Yu, N., Genevet, P., Aieta, F., Kats, M. A., Blanchard, R., Aoust, G., Tetienne, J. P., Gaburro, Z., & Capasso, F. (2013). Flat Optics: Controlling Wavefronts with Optical Antenna Metasurfaces. *IEEE Journal of Selected Topics in Quantum Electronics*, *19*(3). https://doi.org/10.1109/JSTQE.2013.2241399

Yu, N., Genevet, P., Kats, M. A., Aieta, F., Tetienne, J. P., Capasso, F., & Gaburro, Z. (2011). Light propagation with phase discontinuities: generalized laws of reflection and

refraction. *Science (New York, N.Y.)*, *334*(6054), 333–337. https://doi.org/10.1126/SCIENCE.1210713

Yu, X., Shen, Y., Dai, G., Zou, L., Zhang, T., & Deng, X. (2021). Phase-Controlled Planar Metalenses for High-Resolution Terahertz Focusing. *Photonics*, *8*(5), 143. https://doi.org/10.3390/PHOTONICS8050143

Multifocal Metalens with Titanium Nitride Aperiodic Nanoapertures for Fiber Optical Wavelengths

Büşra ERSOY[1]
Ekin ASLAN[2]
Erdem ASLAN[3]

Introduction

Plasmonic metasurfaces are nanotechnological structures that have been intensively studied and attracted significant interest in recent years. These structures are obtained by applying uniquely designed nano-scale patterns onto the surfaces of metals. Plasmonic metasurfaces enable efficient manipulation and control of electromagnetic waves called surface plasmon polaritons (SPPs). They are considered important materials and devices that offer various applications in terms of their optical, electronic, and magnetic properties (Ding et al., 2018). For instance, the manipulation of SPPs can be utilized in photonics circuits and optical communication systems to enable efficient signal transmission and processing. Moreover, plasmonic metasurfaces can play a significant role in the design of highly sensitive sensors, advanced imaging techniques, and enhanced absorptive or reflective surfaces(Kildishev et al., 2013; Yu & Capasso, 2014). Therefore, plasmonic metasurfaces offer significant potential in the development of future optoelectronic and nanophotonic devices.

Metalenses, on the other hand, have emerged as a new technology with the potential to replace traditional optical lenses. Metalenses perform focusing and imaging operations by manipulating light through nanostructures created by combining thin metal films and dielectric materials. These structures enable smaller sizes and higher resolutions compared to conventional lenses (Yu & Capasso, 2014). The potential of metalenses has sparked significant interest in various fields such as optical communications, biomedical imaging, artificial intelligence, and virtual reality (Khorasaninejad & Capasso, 2017).

In plasmonic applications, noble metals such as gold (Au) and silver (Ag) are commonly used. However, these designs are susceptible to high levels of optical losses due to a large number of free electrons and interband transitions. As a result, recent research has focused on alternative plasmonic materials such as doped silicon (Si), doped germanium (Ge), III-nitrides, and transparent conductive oxides. Most of these alternative plasmonic materials are semiconductors, and their main advantage lies in having fewer free electrons compared to metals, resulting in lower losses, particularly in the infrared (IR) wavelength range. These alternative plasmonic materials offer additional advantages over metals, including lower cost

[1] Büşra Ersoy, Student, Kayseri University, Department of Electrical and Electronics Engineering, ORCID: 0000-0003-1383-3311
[2]Ekin Aslan, Assoc. Prof, Kayseri University, Department of Electrical and Electronics Engineering, ORCID: 0000-0003-0933-7796
[3]Erdem Aslan, Assoc. Prof, Erciyes University, Department of Electrical and Electronics Engineering, ORCID: 0000-0001-6829-9000

and the ability to control plasma frequency through adjustable electron density (effective doping concentration) (Kesim, 2014).

Transition metal nitrides such as titanium nitride (TiN), zirconium nitride (ZrN), hafnium nitride (HfN), and tantalum nitride (TaN) also exhibit metallic properties and are classified as alternative plasmonic materials in the visible and IR (Naik et al., 2011). The primary advantage of these materials is their compatibility with Complementary Metal-Oxide-Semiconductor (CMOS) procedures. Additionally, they can be grown under nitrogen- or metal-rich conditions, resulting in films exhibiting metallic properties. Consequently, their plasma frequencies can be tuned.(Kesim, 2014).

The most advantageous characteristic of transition metal nitrides compared to noble metals is their non-refractory nature, which explains their thermal stability at temperatures above 2000°C. (Guler et al., 2014; Naik et al., 2013; Shaltout et al., 2016). Due to the low melting points and soft structures of traditional plasmonic metals, they can pose challenges in demanding operating conditions. As a solution, transition metal nitrides can be employed to realize nanophotonic devices that require operation at high temperatures. The optical properties of TiN are very similar to Au, exhibiting zero-crossing wavelengths in the visible range. This makes TiN plasmonic in the visible and near-infrared range.

The plasmonic properties of TiN have been experimentally demonstrated through the excitation of surface plasmon polaritons (SPPs) on TiN films in the literature. In a comparative study conducted in 2012 on the near-field distribution of TiN and Au spherical particles (Guler et al., 2012), the significance of TiN resonant nanostructures is highlighted. The local field enhancement of TiN particles is spectrally present in the important region known as the biological transparency window (650-950 nm). A lithographically fabricated array of TiN nanoparticles has been studied to demonstrate its potential for providing better heating efficiency compared to Au nanoparticles with the same geometries in the biological transparency window (Guler et al., 2013; Shaltout et al., 2016). In 2014, it is demonstrated that a TiN-based metasurface, consisting of patterned rectangular rings, achieved broad absorption in the visible and near-IR regions due to impedance matching and reduced reflection (Li et al., 2014). In this study, the effectiveness of TiN nanostructures is tested, and both absorbers exhibited high absorption when illuminated with a 5-second pulsed laser at 550 nm, compared to Au. Following laser illumination, TiN nanostructures are able to withstand high-intensity pulses where Au nanostructures failed. Beyond absorptivity, the refractory properties of TiN can provide highly efficient thermal emitters. Thermal emission from one-dimensional grating metamaterials based on TiN is investigated at working temperatures of approximately 540°C, resulting in mid-IR radiation centered around 3 μm (Liu et al., 2015). This study experimentally demonstrates that the thermal excitation of plasmon polaritons on the grating surface produces a well-collimated beam with a spatial coherence length of 32λ (angular divergence of 1.8°) and a maximum full width of 70 nm, which is quasi-monochromatic (Shaltout et al., 2016).

In this study, we are created various metamolecules by taking into account the geometric structure and angular arrangement of V-shaped metamolecules in the work of N. Yu et al., (2011) in order to generate phase gradients in the range of $[0,2\pi]$. In this context, alternative plasmonic based eight unit cells that provide phase manipulation in the full phase range are designed. The resonative behaviors of this nanoapertures in TiN layer on silicon nitride (SiN) membrane are numerically obtained. Simulations are carried out at a fiber optical wavelength

of 850 nm at which each cell is resonant. Then an aperiodic arrangement of the cells is numerically analyzed to create an interface phase profile required for the axicon focusing function. Given the constraints imposed by the technical infrastructure of the analyses, this proposed alternative plasmonic metalens design has led to the identification of multifocal points. Theoretical calculations have been employed to determine various focusing parameters for each focal point, including focal length, numerical aperture, depth of focus, focal spot width, and focal efficiency.

Method

The unit cells used to create the electromagnetic model of the proposed metasurface lens are presented in Figure 1. All analyses are performed for a operating wavelength of 850 nm. Each unit cell shares common geometric parameters, including the interior angle α of an equilateral geometry, the length d of the equilateral quadrilateral, the antenna width w, and the distance c between the open arms of the antennas. The geometric parameters for each nanoantenna in the Type 1 and Type 2 arrangements are provided in Table 1. Simulations are performed using the Finite-Difference Time-Domain (FDTD) method for the design of nanostructures. The dielectric function of TiN as an alternative plasmonic layer is obtained from (Naik et al., 2013) , which utilized the work of Boltasseva's team. The refractive index data for SiN membrane, on the other hand, is obtained from Vogt (2015). In the electromagnetic modeling of TiN, a Lorentz-Drude model is employed, which accounts for both the effects of free electrons and bound charges Drude-Lorentz parameters involve the characterization of optical properties of materials, such as refractive index, dielectric function, and dispersion behavior. These parameters are determined through the analysis of ellipsometry data, which provides information about the material's response to electromagnetic waves and plasmonic behavior. The specific values of Drude-Lorentz parameters can vary for each material and are typically reported in scientific research papers or technical literature. In the study by (Naik et al., 2013), Drude-Lorentz parameters for several alternative plasmonic materials, including TiN, are calculated. The dielectric function of the materials is approximately calculated using Equation 1 in the wavelength range of 350-2000 nm.

$$\varepsilon(\omega) = \varepsilon_b - \frac{\omega_p^2}{\omega(\omega + i\gamma_p)} + \frac{f_1\omega_1^2}{(\omega_1^2 - \omega^2 - i\omega\gamma_1)} \quad (1)$$

Here, while the second term stands for Drude model, the third one represents Lorentz oscillator.Here ε_b is the polarization response from the core electrons (background permittivity), ω_p is the plasma frequency, γ_p is the carrier relaxation rate, f_1 is the strength of the Lorentz oscillator, ω_1 the center frequency of the Lorentz oscillator, and γ_1 is the damping of the Lorentz oscillator. Thus, the optical properties of TiN (deposited at 500 °C) are taken as ε_b= 2.485, ω_p = 5.953 eV, γ_p= 0.5142 eV, f_1= 2.0376, ω_1= 3.9545 eV, γ_1=2.4852 eV (Naik et al., 2013).

The real and imaginary dielectric permittivities of TiN and similar materials, defined using the Lorentz-Drude model, are provided in Naik et al. (2011) and Naik et al. (2013). The wavelengths at which the real part of TiN's dielectric permittivity becomes negative are in the visible and infrared ranges. Therefore, TiN can be utilized as an alternative plasmonic material.

Unless otherwise specified, the thicknesses of the TiN and SiN layers are 50 nm and 100 nm, respectively.

Results and Discussion

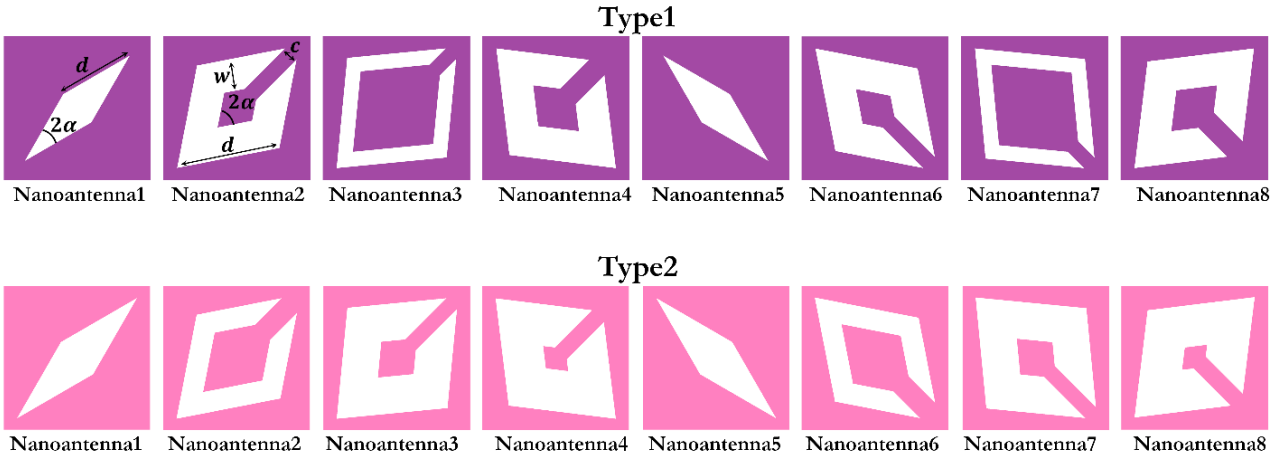

Figure 1- *Top views of metacells in each arrangement*

Table 1- *Geometrical parameters of Type1 and Type2 nanoantennas*

	Geometrical parameters	
	Type1	**Type2**
Nanoantenna1,5	d = 1000 nm, α = 15°	d = 1300 nm, α = 15°
Nanoantenna2,6	d = 1300 nm, w = 400 nm, c = 200 nm, α = 34°	d = 1000 nm, w = 200 nm, c = 200 nm, α = 34°
Nanoantenna3,7	d = 1500 nm, w = 200 nm, c = 200 nm, α = 39.5°	d = 1500 nm, w = 500 nm, c = 200 nm, α = 39.5°
Nanoantenna4,8	d = 1000 nm, w = 300 nm, c = 200 nm, α = 52°	d = 1300 nm, w = 500 nm, c = 200 nm, α = 52°

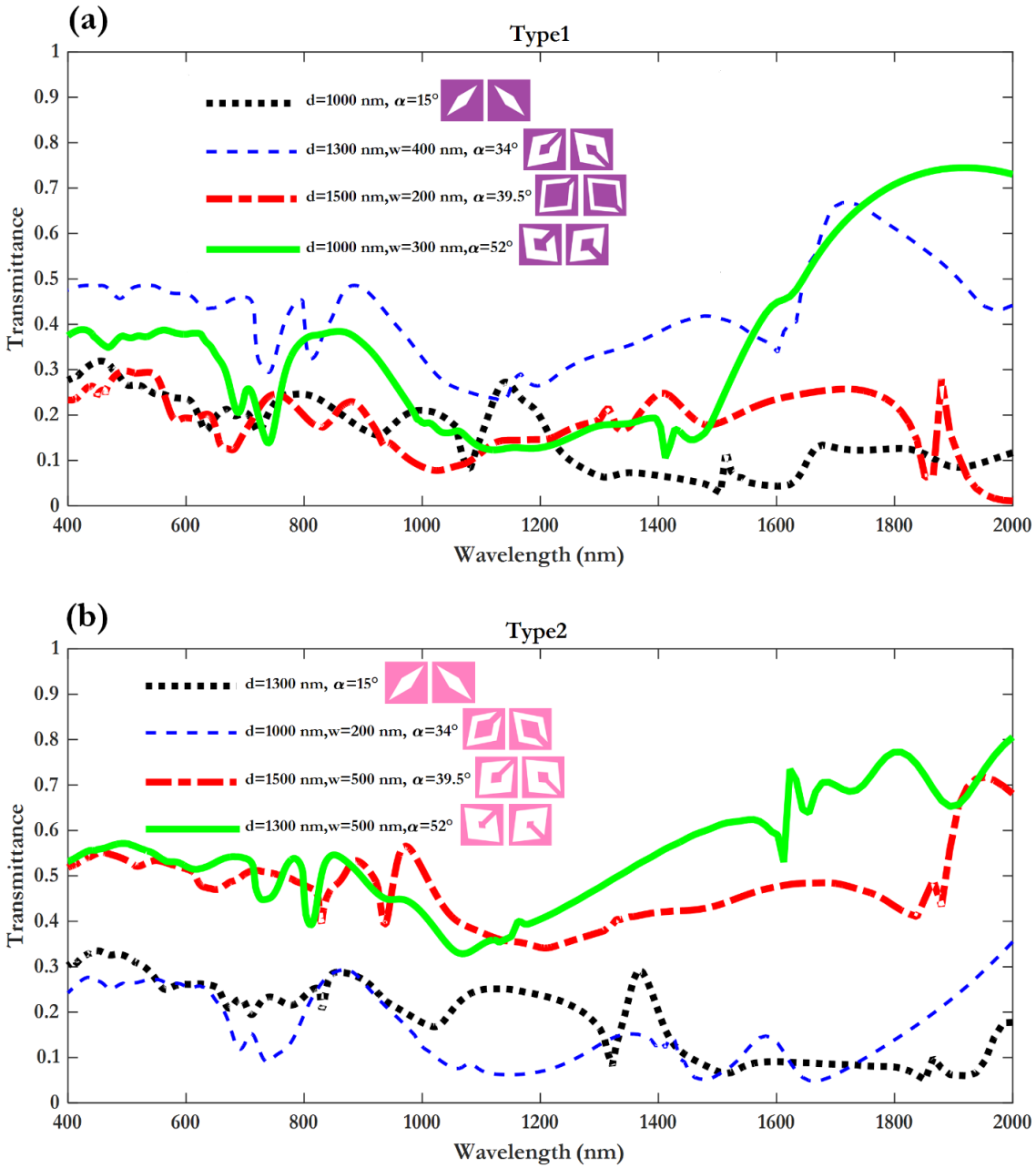

***Figure 2**. The transmittance analysis results of the antennas used in **(a)** Type1 arrangement and **(b)** Type2 arrangement.*

In the initial analyses, the transmittance of the structures is measured in the far field to investigate their resonant behavior at a wavelength of 850 nm. To determine the resonant behavior of the metamolecules, the periodic arrays of each metamolecule are analyzed. The periodicities, which are the repeating dimensions of the metamolecules in the x and y directions, were selected as P_x and P_y. The unit cell is illuminated with a plane wave of $x-$ polarized light propagating in the $z-$ direction, using a plane wave source positioned along the $z-$ axis of the system. Power meter transmittance monitors are placed to measure the power transmitted to the far-field regions of the structure. In the simulations, periodic boundary conditions along the $x-$ and $y-$ axes and perfectly matched layers along the $z-$ axis are employed. Figure 2 illustrates the transmittance monitor results for all nanocells belonging to the targeted array types. As shown in Figure 2, each unit cell exhibits resonance at a wavelength of 850 nm.

Two circular arrangements of the designed cells given in Figure 1, at equal radial distances are designed. In this way, circular phase rings in both arrangements that provide full phase transition on the metalens interface are formed. The arrangement images are provided in

Figure 3. To ensure physical interference between the cells, the distance between each arrangement trajectory is set to 100 nm, corresponding to the distance between the antennas. For better visual clarity, different colorings are presented for the Type 1 arrangement (Figure 3a) and the Type 2 arrangement (Figure 3b).

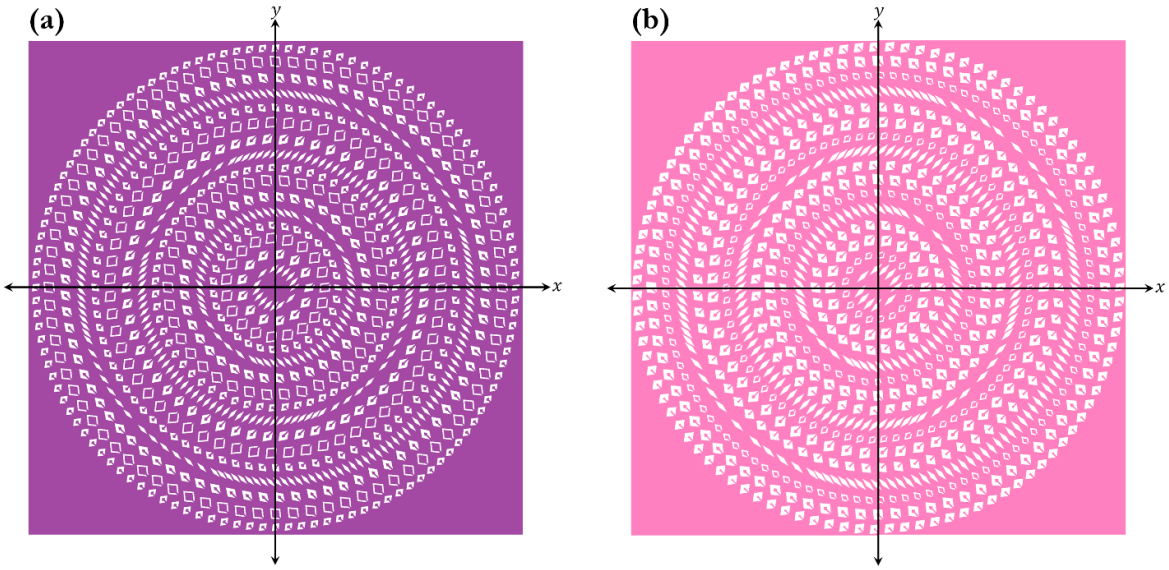

***Figure 3**- The arrangement of the antennas for **(a)** Type1 and **(b)** Type2*

In order to demonstrate the focusing performance of the structures in Figure 3, vertical monitors are placed along the $xz-$ axis. The distributions of normalized light intensity $\frac{|E|^2}{|E_{in}|^2}$, determined through the field distributions obtained from the monitors, are shown in Figure 4. The white dashed lines shown in the figure indicate the positions of the focal points determined as z_{1-10} for Type 1 and z_{1-7} for Type 2 along the $z-$axis. These analyses on the focusing performance demonstrate that both circular designs exhibit multiple focal points along the direction of light transmission. The focal distances for both designs are provided in Table 2 and Table 3. The focal points are determined as the most intense spots where the normalized light intensity exceeds 1.

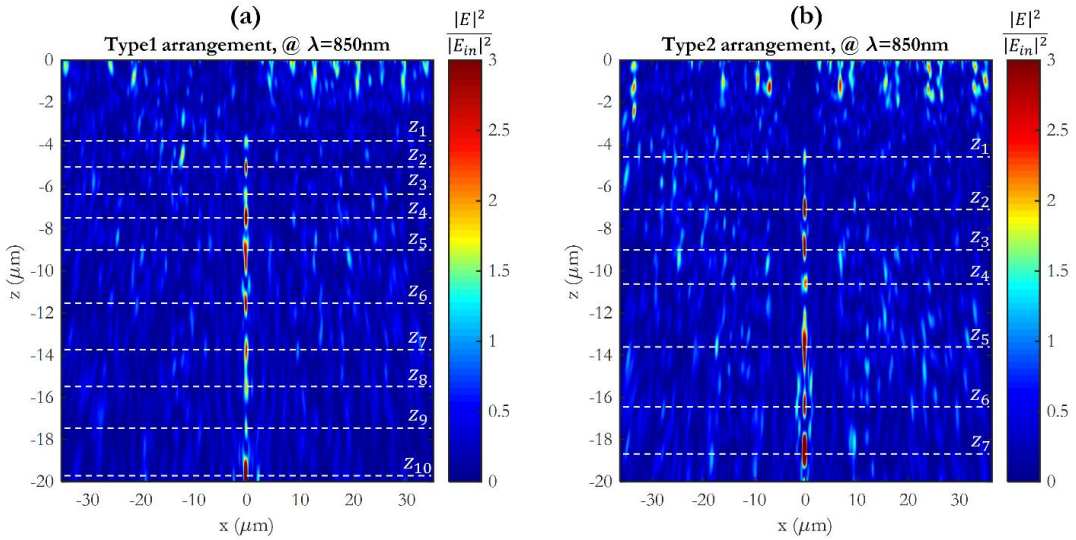

***Figure 4**- The normalized light intensity distributions along the focusing axis and polarization direction, for **(a)** Type1 and **(b)** Type2*

Table 2- *Focal lengths for Type1 arrangement*

Type1	
f_1	3.934 μm
f_2	5.15 μm
f_3	6.448 μm
f_4	7.516 μm
f_5	9.156 μm
f_6	11.6 μm
f_7	13.8 μm
f_8	15.61 μm
f_9	17.54 μm
f_{10}	19.79 μm

Table 3- *Focal lengths for Type2 arrangement*

Type2	
f_1	4.666 μm
f_2	7.082 μm
f_3	8.904 μm
f_4	10.65 μm
f_5	13.74 μm
f_6	16.45 μm
f_7	18.57 μm

To determine the other mentioned parameters related to the focusing performance, simulations are repeated by placing horizontal monitors extending along the xy −plane at the determined focal points. Through these types of analyses, the focal spot size and intensity distribution, apart from the focal distance, are intended to be determined. The normalized light intensity distributions at the focal points obtained from these monitors for Type 1 and Type 2 are shown in Figure 5 and Figure 6, respectively. Each panel in the figures represents the distribution at different focal points corresponding to the respective arrangement, and as observed, each axicon exhibits a highly narrow focal spot.

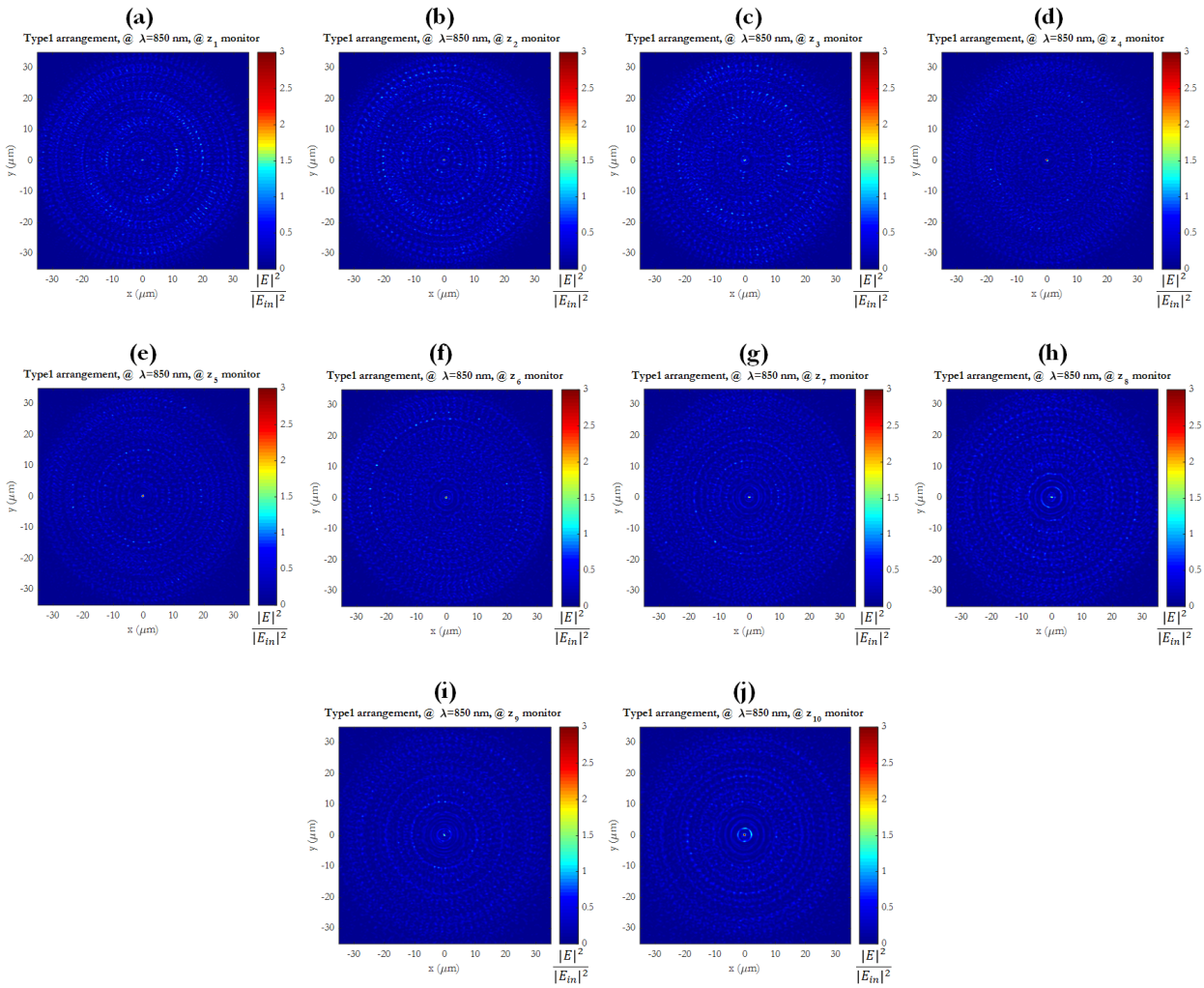

Figure 5- *The normalized light intensity distributions obtained from the focal planes for the Type1 arrangement: At* ***(a)*** $f_1 = 3.934\ \mu m$, ***(b)*** $f_2 = 5.15\ \mu m$, ***(c)*** $f_3 = 6.448\ \mu m$, ***(d)*** $f_4 = 7.516\ \mu m$, ***(e)*** $f_5 = 9.156\ \mu m$, ***(f)*** $f_6 = 11.6\ \mu m$, ***(g)*** $f_7 = 13.8\ \mu m$, ***(h)*** $f_8 = 15.61\ \mu m$, ***(i)*** $f_9 = 17.54\ \mu m$, *and* ***(j)*** $f_{10} = 19.79\ \mu m$.

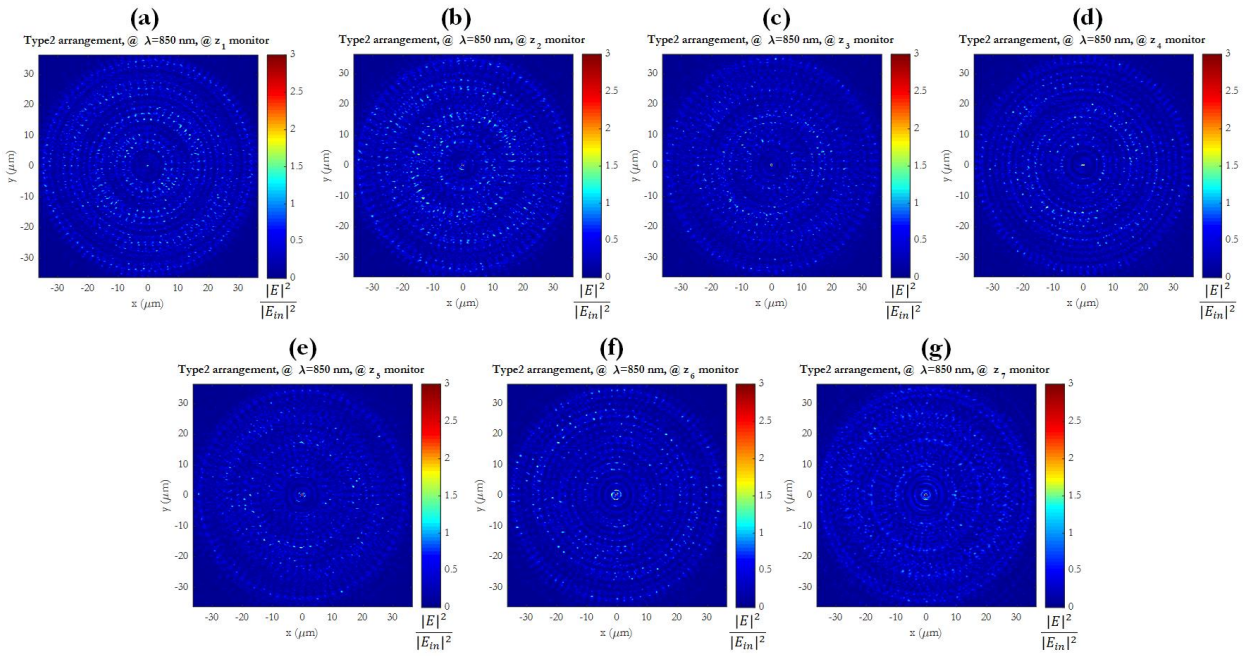

Figure 6. *The normalized light intensity distributions obtained from the focal planes for the Type2 arrangement: At* ***(a)*** $f_1 = 4.666\ \mu m$, ***(b)*** $f_2 = 7.082\ \mu m$, ***(c)*** $f_3 = 8.904\ \mu m$, ***(d)*** $f_4 = 10.65\ \mu m$, ***(e)*** $f_5 = 13.74\ \mu m$, ***(f)*** $f_6 = 16.45\ \mu m$, *and* ***(g)*** $f_7 = 18.57\ \mu m$.

The focusing parameters obtained from the simulations are described below, and the calculated values are presented in Table 4 and Table 5. The first focusing parameter is the numerical aperture (NA). NA is a parameter that determines the maximum resolution of the metalens and is calculated as follows:

$$NA = n * sin(\theta) \quad (2)$$

Here, n is the refractive index of the medium, and θ is the half-angle of the objective. This value determines how light will be refracted in the lens and influences the resolution of the lens (Aieta et al., 2012). The second parameter to be calculated is the Full Width at Half Maximum (FWHM). FWHM is the distance between two points that intersect half of the light intensity during the transition from one point to another. This distance determines the width of the light beam. FWHM is calculated as follows (Aslan & Aslan, 2020):

$$FWHM = \frac{\lambda}{2NA} \quad (3)$$

Here, λ represents the operation wavelength.

Table 4- *The focusing parameter values for the Type1 arrangement*

Lens Properties	Focusing Spot	Results
NA	f_1= 3.934μm	0.99
	f_2= 5.15 μm	0.99
	f_3=6.448 μm	0.98
	f_4=7.516 μm	0.98
	f_5=9.156 μm	0.97
	f_6=11.6 μm	0.95
	f_7=13.8 μm	0.93
	f_8=15.61 μm	0.91
	f_9=17.54 μm	0.89

	f_{10}=19.79 μm	0.87
FWHM	f_1= 3.934μm	0.43
	f_2= 5.15 μm	0.43
	f_3=6.448 μm	0.43
	f_4=7.516 μm	0.44
	f_5=9.156 μm	0.44
	f_6=11.6 μm	0.45
	f_7=13.8 μm	0.46
	f_8=15.61 μm	0.47
	f_9=17.54 μm	0.48
	f_{10}=19.79 μm	0.49
DOF	f_1= 3.934μm	0.01
	f_2= 5.15 μm	0.02
	f_3=6.448 μm	0.03
	f_4=7.516 μm	0.04
	f_5=9.156 μm	0.06
	f_6=11.6 μm	0.09
	f_7=13.8 μm	0.13
	f_8=15.61 μm	0.17
	f_9=17.54 μm	0.21
	f_{10}=19.79 μm	0.27
η(%)	f_1= 3.934μm	0.3
	f_2= 5.15 μm	0.6
	f_3=6.448 μm	0.4
	f_4=7.516 μm	0.8
	f_5=9.156 μm	0.7
	f_6=11.6 μm	0.6
	f_7=13.8 μm	0.5
	f_8=15.61 μm	0.4
	f_9=17.54 μm	0.2
	f_{10}=19.79 μm	1.5

Another important parameter is the depth of focus (DOF). DOF represents the distance over which objects can still be seen clearly beyond the focal point and is calculated as follows (Ali & Aksu, 2021):

$$DOF = 4\lambda \frac{f^2}{D^2} \tag{4}$$

Here, f represents the focal length, and D represents the diameter of the lens. (Bayati et al., 2020). The final important parameter is the focal efficiency η. Focal efficiency refers to how much of the collected light energy in the optical system is concentrated at the focal point. It is calculated by dividing the average light intensity in the focal spot by the average incident light intensity (Aslan, 2021):

$$\eta = \frac{\langle I_f \rangle}{\langle I_i \rangle} \tag{4}$$

Table 5- *The focusing parameter values for the Type2 arrangement*

Lens Properties	Focusing Spot	Results
NA	f_1=4.666 μm	0.99
	f_2=7.082 μm	0.98
	f_3=8.904 μm	0.97
	f_4=10.65 μm	0.96
	f_5=13.74 μm	0.94
	f_6=16.45 μm	0.91
	f_7=18.57 μm	0.89
FWHM	f_1=4.666 μm	0.43
	f_2=7.082 μm	0.43
	f_3=8.904 μm	0.44
	f_4=10.65 μm	0.44
	f_5=13.74 μm	0.45
	f_6=16.45 μm	0.47
	f_7=18.57 μm	0.48
DOF (μm)	f_1=4.666 μm	0.01
	f_2=7.082 μm	0.03
	f_3=8.904 μm	0.05
	f_4=10.65 μm	0.07
	f_5=13.74 μm	0.12
	f_6=16.45 μm	0.17
	f_7=18.57 μm	0.22
η(%)	f_1=4.666 μm	0.3
	f_2=7.082 μm	0.7
	f_3=8.904 μm	0.8
	f_4=10.65 μm	0.3
	f_5=13.74 μm	0.7
	f_6=16.45 μm	0.6
	f_7=18.57 μm	2.3

Conclusion

In this study including metalens designs as two different arrangements of split rhombus shaped metacells, multifocal behaviours are shown via numerical analyses. First the theoritical spectral transmittance of the cells are presented. Then, lensing performances of this flat-lens structures in two-type-arrangements are presented at a fiber optical wavelength 850 nm via ligth intensity distributions at focal points. The low efficiency values in multi-foci can be attributed to the absence of significantly high resonant transition values at 850nm. However, the sharing of light energy among multiple foci can also explain the lower focal efficiencies compared to single-focus studies in the literature. The obtained multi-foci are characterized by elongated elliptical focal spots in the direction of focusing, resembling axicon-like focal quality. This imparts light trapping capability to the metalens design.

Acknowledge

The work described in this study is supported by The Scientific and Technological Research Council of Turkey (TUBITAK− Project ID: 121E518).

References

Aieta, F., Genevet, P., Kats, M. A., Yu, N., Blanchard, R., Gaburro, Z., & Capasso, F. (2012). Aberration-free ultrathin flat lenses and axicons at telecom wavelengths based on plasmonic metasurfaces. *Nano Letters*, *12*(9), 4932–4936. https://doi.org/10.1021/NL302516V/SUPPL_FILE/NL302516V_SI_001.PDF

Ali, F., & Aksu, S. (2021). A hybrid broadband metalens operating at ultraviolet frequencies. *Scientific Reports 2021 11:1*, *11*(1), 1–8. https://doi.org/10.1038/s41598-021-81956-4

Aslan, E. (2021). Lensing for optical communication by diffraction from Peano curve-based fractal with alternative plasmonic material. *Optik*, *242*, 167072. https://doi.org/10.1016/J.IJLEO.2021.167072

Aslan, E., & Aslan, E. (2020). A Microlens by Gallium Doped Zinc Oxide-Nanoantenna. *Mühendislik Bilimleri ve Tasarım Dergisi*, *8*(3), 931–942. https://doi.org/10.21923/JESD.784056

Bayati, E., Pestourie, R., Colburn, S., Lin, Z., Johnson, S. G., & Majumdar, A. (2020). Inverse Designed Metalenses with Extended Depth of Focus. *ACS Photonics*, *7*(4), 873–878. https://doi.org/10.1021/ACSPHOTONICS.9B01703/ASSET/IMAGES/LARGE/PH9B01703_0004.JPEG

Ding, F., Yang, Y., Deshpande, R. A., & Bozhevolnyi, S. I. (2018). A review of gap-surface plasmon metasurfaces: Fundamentals and applications. *Nanophotonics*, *7*(6), 1129–1156. https://doi.org/10.1515/NANOPH-2017-0125/ASSET/GRAPHIC/J_NANOPH-2017-0125_FIG_005.JPG

Guler, U., Boltasseva, A., & Shalaev, V. M. (2014). Refractory Plasmonics. *Science*, *344*(6181), 263–264. https://doi.org/10.1126/SCIENCE.1252722

Guler, U., Naik, G. V., Boltasseva, A., Shalaev, V. M., & Kildishev, A. V. (2012). Performance analysis of nitride alternative plasmonic materials for localized surface plasmon applications. *Applied Physics B: Lasers and Optics*, *107*(2), 285–291. https://doi.org/10.1007/S00340-012-4955-3

Guler, U., Ndukaife, J. C., Naik, G. V., Nnanna, A. G. A., Kildishev, A. V., Shalaev, V. M., & Boltasseva, A. (2013). Local heating with lithographically fabricated plasmonic titanium nitride nanoparticles. *Nano Letters*, *13*(12), 6078–6083. https://doi.org/10.1021/NL4033457

Kesim, Y. E. (2014). *Ald grown zno as an alternative material for plasmonic and uncooled infrared imaging applications* [Bilkent University]. https://core.ac.uk/display/52926405?source=1&algorithmId=15&similarToDoc=52923596&similarToDocKey=CORE&recSetID=80bf561f-4d80-4a6e-beb8-58278a16672c&position=4&recommendation_type=same_repo&otherRecs=480563030,154803930,52936873,52926405,52926415

Khorasaninejad, M., & Capasso, F. (2017). Metalenses: Versatile multifunctional photonic components. *Science (New York, N.Y.)*, *358*(6367). https://doi.org/10.1126/SCIENCE.AAM8100

Kildishev, A. V., Boltasseva, A., & Shalaev, V. M. (2013). Planar photonics with metasurfaces. *Science (New York, N.Y.)*, *339*(6125), 12320091–12320096. https://doi.org/10.1126/SCIENCE.1232009

Liu, J., Guler, U., Lagutchev, A., Kildishev, A., Malis, O., Boltasseva, A., Shalaev, V. M., S Tigran, M. I., Shahbazyan, V., Springer, A., Greffet, J. J., Carminati, R., Joulain, K., Mulet, J. P., Mainguy, S., & Chen, Y. (2015). Quasi-coherent thermal emitter based on refractory plasmonic materials. *Optical Materials Express*, *5*(12), 2721–2728. https://doi.org/10.1364/OME.5.002721

Li, W., Guler, U., Kinsey, N., Naik, G. V., Boltasseva, A., Guan, J., Shalaev, V. M., & Kildishev, A. V. (2014). Refractory Plasmonics with Titanium Nitride: Broadband

Metamaterial Absorber. *Advanced Materials*, *26*(47), 7959–7965. https://doi.org/10.1002/ADMA.201401874

Naik, G. V., Kim, J., & Boltasseva, A. (2011). Oxides and nitrides as alternative plasmonic materials in the optical range. *Optical Materials Express*, *1*(6). http://arxiv.org/abs/1108.0993

Naik, G. V., Shalaev, V. M., & Boltasseva, A. (2013). Alternative plasmonic materials: beyond gold and silver. *Advanced Materials (Deerfield Beach, Fla.)*, *25*(24), 3264–3294. https://doi.org/10.1002/ADMA.201205076

Shaltout, A. M., Kinsey, N., Kim, J., Chandrasekar, R., Ndukaife, J. C., Boltasseva, A., & Shalaev, V. M. (2016). Development of Optical Metasurfaces: Emerging Concepts and New Materials. *Proceedings of the IEEE*, *104*(12), 2270–2287. https://doi.org/10.1109/JPROC.2016.2590882

Vogt, M. R. (2015). Development of physical models for the simulation of optical properties of solar cell modules [Gottfried Wilhelm Leibniz Universität Hannover]. In *Gottfried Wilhelm Leibniz Universität Hannover*. https://doi.org/10.15488/8592

Yu, N., & Capasso, F. (2014). Flat optics with designer metasurfaces. *Nature Materials 2014 13:2*, *13*(2), 139–150. https://doi.org/10.1038/nmat3839

Yu, N., Genevet, P., Kats, M. A., Aieta, F., Tetienne, J. P., Capasso, F., & Gaburro, Z. (2011). Light propagation with phase discontinuities: generalized laws of reflection and refraction. *Science (New York, N.Y.)*, *334*(6054), 333–337. https://doi.org/10.1126/SCIENCE.1210713

Using Artificial Intelligence Methods in Performance Evaluation of Sales Personnel Working in the Savings Finance Sector

Cengiz SERTKAYA[1]
Zekeriya KÖSE[2]

Introduction

The relationships that companies establish with their customers are one of the most important factors that increase the competitiveness of the company in the competitive conditions of the market. Good relations ensure growth and increase in the share obtained in the market. At the same time, as the trust and loyalty of the customers to the company increase, the loyalty between them causes the formation of permanent customer groups over time (Özdağoğlu et al., 2010). In this process, sales personnel are at the forefront of the groups that work closely with the customers.

Sales personnel are in the middle layer between the company and the customer, who can communicate directly with the customer due to their duties. New campaigns and products created by companies can be delivered to customers quickly through sales personnel. During this communication, with the question-answer method, the customer asks the questions that come to his mind directly, and due to the acceleration of the decision-making process, it is ensured that he is quickly included in the campaigns or the sale of the products.

The role of sales personnel is very important for companies working in the savings finance sector. Targets are set several times a year for the expected performance of sales personnel. Both performance targets and processes related to the course of performance are followed by customer relationship management systems (CRM) or resource planning systems (ERP) (Calixto & Ferreira, 2020). It is extremely important to determine whether the targets set will be achieved through data analysis checks carried out at intervals before the end of the year, and to take the necessary measures in order to achieve the year-end targets. Considering the different sales targets, different qualifications and the large number of sales personnel working in the company, the diversity of analysis makes the solution of the problem difficult and becomes a process that is too complex and time-consuming to be solved with human skills. In such cases, artificial intelligence-based computer systems with human-like decision-making capabilities but higher processing capacity and long-term performance are needed.

It is known that the number of studies in the literature on the prediction of the performance of sales personnel is quite low (Sohrabpour et al., 2021; Verstraete et al., 2020). It has been observed that the existing studies are generally focused on data mining processes and finding the most suitable classification model for the business structure in a way that will maximize the profitability level in the examined area (Cheriyan et al., 2019).

In a study, a probabilistic latent semantic indexing model (SPLSA), which can make an emotion-based evaluation based on customer feedback, was created for the prediction of sales performance (Yu et al., 2012).

In another study, data obtained between October 2013 and March 2014 were used for the performance analysis of 53 employees. It has been stated that the features that affect performance focus on training, bonuses and promotions.

[1] Cengiz SERTKAYA, Istanbul Topkapi University, Computer Engineering Department,
[2] Zekeriya KÖSE, Eminevim, IT Application Solutions Department,

In a study, criteria other than classical features such as weekly sales, air temperature, fuel price were used to estimate the sales performance of 99 different departments. According to the results obtained, it was stated that the long-short-term memory (LSTM) deep learning model was the most successful model.

In another study, three different regression models, namely multiple linear, elastic-net and polynomial, were created for the performance prediction of sales personnel working in Wallmart. The performance of the models was evaluated by R2 and RMSE calculations. Since the multiple linear regression model obtained 0.93 R2 and the smallest RMSE values, it was determined as the best estimation model (Chen, 2023).

In another study, decision tree (DCT), gradient reinforcement tree (GBT), k-nearest neighbor (KNN) and random forest (RF) artificial intelligence models were created to examine the number of assets that a company will have in the future from growth indicators. In the study using 1224 data, the most successful model was GBT with an accuracy value of 96.67% (Chaising et al., 2023).

In another study, sales performances for the next 5 years were estimated over the sales data collected between 2015-2017 for sales performance forecasting. Generalized linear model (GLM), decision tree and gradient strengthening tree methods from machine learning algorithms were used. The GBT model was the most successful model with an accuracy rate of 98% (Cheriyan et al., 2019).

In this study, analyzes were made on the sales data of Eminevim, which is the leader in the savings finance sector, using data mining methods, and an artificial intelligence-based model that can make forward-looking sales forecasts is proposed.

Method

In the model development processes of the study, a process such as data acquisition, preparation, analysis and model establishment was followed.

A.Data Collection

The dataset used in the study was examined by bringing together various tables from the CRM application database of the sales data of Eminevim company for the January 2021-December 2022 time interval. In the selection of the criteria to be used in the performance evaluation of the sales personnel, the literature suggests that the sources should be examined in two groups as qualitative and quantitative (Dinçer et al., 2012). While the qualitative criteria cover features such as the technical competencies of the person and the success in communication with the customer, the quantitative criteria consist of the extra-task efforts and activities he has shown, such as the trainings he received to improve himself, the customer visit plans, with the features containing numerical data on his performance in the first place. The criteria examined in this study are shown in Table 1.

Table 1 – Dataset Attributes

#	Attribute	Description
1	Education level	Education level of personnel
2	Promotion count	Total promotion count
3	Comment count	Total comment count
4	Visit count	Total visit count
5	Bonus count	Total bonus count
6	Customer count	Number of customers in portfolio
7	Training count	Total training count
8	Sales volume	Total sales volume in a month

Here, features 1-7 show the input feature, and feature 8 shows the output feature to be predicted. On the dataset, due to the data privacy policy of the institution, the sales information of some sales personnel was randomly removed from the dataset and the sales volume data, which is the output information, was anonymized by normalizing the remaining data between 0-1. Here, the formula used for the normalization process is given in Equation 1 (Aksu et al., 2019).

$$X_{nor} = \left(\frac{X_i - X_{min}}{X_{max} - X_{min}}\right) \quad (1)$$

B.Data Analysis

One of the important steps in the analysis of the collected data is to examine their distribution over time. Ensuring the correct distribution is among the important information that shows the quality and data diversity of the dataset. For this reason, the percentages of the number of data per year and quarters in the year are calculated and given in Table 2.

Table 2 – Dataset Distribution by Quarters

	Year	
Quarter	2021	2022
1	%12	%10
2	%14	%12
3	%12	%10
4	%10	%10

When the distribution of the data was examined, it was seen that a homogeneous distribution was achieved between the periods. In the next process, the analysis of the relationship levels of the input and output features planned to be used in the learning process of the models was made. This analysis method, which is called principal component analysis (PCA) in the literature, is important in order to see the connection levels and aspects of the output feature and input features (Oliveira-Esquerre et al., 2002a). For this purpose, many analysis methods are suggested in the literature (Sertkaya & Yurtay, 2018), one of the methods proposed within the scope of this study, the correlation matrix whose formula is given in Equation 2 was used (Everitt & Dunn, 2001).

$$K(X,Y) = \frac{E[(X-\mu_x)\times(Y-\mu_y)]}{\sigma_x \sigma_y} \quad (2)$$

Here, X is the input, Y is the output property, E is the expected value operator, μ_x and μ_y are the expected values, and σ_x and σ_y are the standard deviation values.

The TBA value varies between -1 and 1, decreases as it approaches 0, and increases as it approaches -1 and 1. The obtained correlation matrix results between input and output properties are given in Table 3.

Table 3 – Correlation Results

	Output
Inputs	Sales volume
Education level	-0.25
Promotion count	0.56
Comment count	0.42
Visit count	0.35
Bonus count	0.37
Customer count	0.40
Training count	-0.15

According to the TBA results, it is seen that the number of promotions, comment score, number of interviews, number of premiums and number of customers are positively related to sales volume, while education level and number of education attributes have a negative relationship. The relationship level of the number of promotions and comment score features is quite high.

PCA is also known as the feature reduction procedure (Oliveira-Esquerre et al., 2002b). This process is performed by removing the features whose PCA values are below a determined level from the dataset. In this way, training of models with fewer features can be achieved more quickly. At this stage, the features with a PCA value of 0.25 and above recommended in the literature were selected to be applied to the model in the next stage (TDS, n.d.). In this case, the number of training feature is removed from the dataset.

After the dataset was finalized, the dataset was divided into two sub-datasets, 80% training and 20% testing, in order to establish the artificial intelligence model to be developed and conduct real tests, and the dataset processes were completed.

C. Gradient Boost Tree Model

Collective learning is one of the features inherent in decision trees that combine multiple sub-learners and allow many simultaneous predictions. With this feature, the probability of finding a successful result is quite high. Gradient strengthening decision trees (GBT), on the other hand, increase the number of branches that produce successful results by improving the bad result branches produced by classical decision trees. When the results produced by the branches are brought together, the overall result of the system is formed by the combination of many successful results, and a system response is produced in which the problem is addressed and comprehended from many perspectives. Figure 1 shows the general structure of GBT trees (Shoaran et al., 2018).

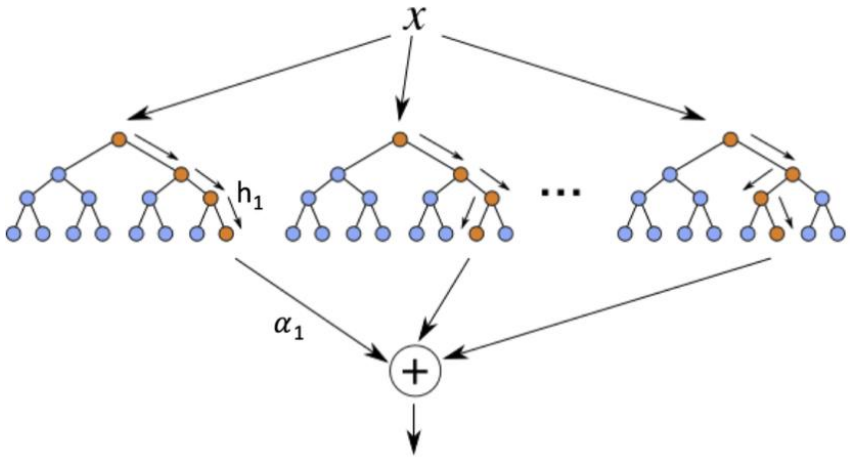

Figure 1 – General structure of GBT tree(Shoaran et al., 2018)

XGBoost library in Python language was used in the implementation of the GBT algorithm. It is extremely important to set the parameter values required for the algorithm to work efficiently (XG, n.d.). This ensures the optimization of the model, prevents memorization problems and shortens the learning time (ABG, n.d.). The values given in Table 4, which gave the best results in the simulation trials after the model was set up, were selected for the GBT model.

Table 4 – Parameter Values of GBT Model

Parameter	Value
Base score	0.5
Colsample by node	1
Colsample by tree	1
Importance type	gain
Learning rate	0.3
N estimators	500
Num parallel tree	1
Sub sample	0.8
Gamma	0

Results

As a result of the simulation of the GBT model trained to predict the performance of the sales personnel with the test data, the prediction values were obtained for each test data as shown in Figure 2.

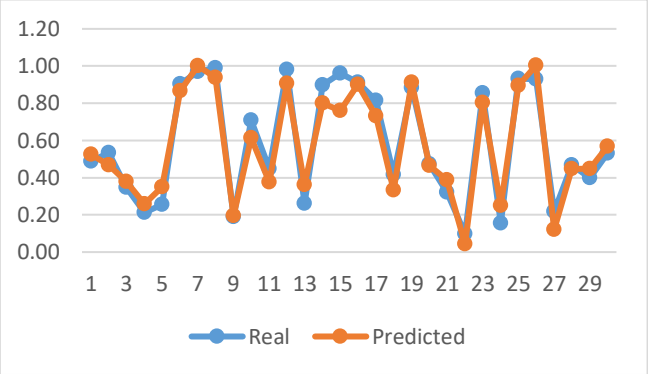

Figure 2 – Real and Predicted Values of GBT Model

As can be seen from the figure, it is understood that the actual value and the predicted values produced by the model are compatible with each other and the proposed model gives consistent results for the problem.

In order to evaluate the overall system success of the GBT model, the accuracy calculations commonly used in the literature were made according to the formula in Equation 3 (Sertkaya et al., 2023).

$$D = \left(\frac{O_i - E_{ort}}{O_i}\right) * 100 \quad (3)$$

Here, D is the accuracy value, O_i is the expected range of the predicted and true value, and E_{ort} is the mean of their differences.

After the accuracy calculation, the success of the proposed model was obtained as 92%.

Conclusion

Within the scope of this study, important criteria have been revealed to be used in the evaluation of the performance of sales personnel for companies operating in the field of savings finance. Sales are extremely important as they are among the primary needs for the growth of companies in this sector. For this purpose, the data of the years 2021 and 2022 belonging to Eminevim, which is the leader of the sector, was used. Considering the up-to-dateness of the selected data and the company's extensive branch infrastructure in Turkey, a very important dataset in terms of sampling the sector has been used within the scope of the study.

In the study, the steps applied in order to be ready for artificial intelligence models on the dataset are explained in detail.

The gradient reinforced decision tree model, which is one of the successful models in the literature on sales performance, was used in this study. It is stated with which parameters the model should be constructed for this kind of problem.

In order to measure the success of the GBT model, the accuracy values were calculated and according to the results obtained, it was shown that the proposed model is a successful model that can be used in the performance estimation of sales personnel for companies operating in the savings finance sector.

In future studies, different datasets and artificial intelligence methods can be used. Evaluations can be made by comparing the results obtained from the studies with the results of this study.

References

ABG. (n.d.). *A Beginner's guide to XGBoost. This article will have trees…. lots of… | by George Seif | Towards Data Science*. Retrieved May 24, 2023, from https://towardsdatascience.com/a-beginners-guide-to-xgboost-87f5d4c30ed7

Aksu, G., Güzeller, C. O., & Eser, M. T. (2019). The Effect of the Normalization Method Used in Different Sample Sizes on the Success of Artificial Neural Network Model. *International Journal of Assessment Tools in Education*, *6*(2), 170–192. https://doi.org/10.21449/IJATE.479404

Calixto, N., & Ferreira, J. (2020). Salespeople Performance Evaluation with Predictive Analytics in B2B. *Applied Sciences 2020, Vol. 10, Page 4036*, *10*(11), 4036. https://doi.org/10.3390/APP10114036

Chaising, S., Syukur, M., & Nithibandanseree, P. (2023). Comparison of Machine Learning Algorithms for Prediction of Total Assets. *2023 International Conference on Cyber Management and Engineering, CyMaEn 2023*, 255–259. https://doi.org/10.1109/CYMAEN57228.2023.10051085

Chen, Z. (2023). Sales Forecast of Walmart on Account of Multivariate Regression and Machine Learning Methods. *Proceedings of the International Conference on Financial Innovation, FinTech and Information Technology, FFIT 2022, October 28-30, 2022, Shenzhen, China*. https://doi.org/10.4108/EAI.28-10-2022.2328455

Cheriyan, S., Ibrahim, S., Mohanan, S., & Treesa, S. (2019). Intelligent Sales Prediction Using Machine Learning Techniques. *Proceedings - 2018 International Conference on Computing, Electronics and Communications Engineering, ICCECE 2018*, 53–58. https://doi.org/10.1109/ICCECOME.2018.8659115

Dinçer, B., Dinçer, C., Üniversitesi, G., İdari, İ., Fakültesi, B., Bölümü, İ., & Görevlisi, A. (2012). Satış Elemanı Performans Değerlemesinde Bir Öneri: Üçgensel Performans Değerleme Yöntemi. *Öneri Dergisi*, *9*(35), 163–171. https://doi.org/10.14783/OD.V9I35.1012000268

Everitt, Brian., & Dunn, Graham. (2001). *Applied multivariate data analysis*. https://www.wiley.com/en-us/Applied+Multivariate+Data+Analysis%2C+2nd+Edition-p-9780470711170

Oliveira-Esquerre, K. P., Mori, M., & Bruns, R. E. (2002a). Simulation of an industrial wastewater treatment plant using artificial neural networks and principal components analysis. *Brazilian Journal of Chemical Engineering*, *19*(4), 365–370. https://doi.org/10.1590/S0104-66322002000400002

Oliveira-Esquerre, K. P., Mori, M., & Bruns, R. E. (2002b). Simulation of an industrial wastewater treatment plant using artificial neural networks and principal components analysis. *Brazilian Journal of Chemical Engineering*, *19*(4), 365–370. https://doi.org/10.1590/S0104-66322002000400002

Özdağoğlu, A., Özdağoğlu, G., & Öz, E. (2010). Müşteri Sadakatinin Sağlanmasında Müşteri Ilişkileri Yönetiminin Önemi: Izmir'de Bir Hipermarket Araştırması. In *Atatürk Üniversitesi İktisadi ve İdari Bilimler Dergisi* (Vol. 22, Issue 1, pp. 367–388). Atatürk Üniversitesi. https://dergipark.org.tr/tr/pub/atauniiibd/issue/2693/35450

Sertkaya, C., Köse, Z., Mühendisliği Bölümü, B., Fakültesi, M., Topkapı Üniversitesi, İ., & Uygulama Çözümleri Bölümü, B. (2023). Yapay Zeka ile Tasarruf Finansmanı Sektörü Firmalarının Sosyal Medya Etkinliklerinin Tahmin Edilmesi. *International Journal of Advanced Natural Sciences and Engineering Researches*, *7*(3), 109–114. https://doi.org/10.59287/IJANSER.377

Sertkaya, C., & Yurtay, N. (2018). Artificial immune system based wastewater parameter estimation. *Turkish Journal of Electrical Engineering and Computer Sciences*, *26*(6), 3356–3366. https://doi.org/10.3906/elk-1503-206

Shoaran, M., Haghi, B. A., Taghavi, M., Farivar, M., & Emami-Neyestanak, A. (2018). Energy-efficient classification for resource-constrained biomedical applications. *IEEE Journal on Emerging and Selected Topics in Circuits and Systems*, *8*(4), 693–707. https://doi.org/10.1109/JETCAS.2018.2844733

Sohrabpour, V., Oghazi, P., Toorajipour, R., & Nazarpour, A. (2021). Export sales forecasting using artificial intelligence. *Technological Forecasting and Social Change*, *163*, 120480. https://doi.org/10.1016/J.TECHFORE.2020.120480

TDS. (n.d.). *Understanding Principal Component Analysis | by Trist'n Joseph | Towards Data Science*. Retrieved May 24, 2023, from https://towardsdatascience.com/understanding-principal-component-analysis-ddaf350a363a

Verstraete, G., Aghezzaf, E. H., & Desmet, B. (2020). A leading macroeconomic indicators' based framework to automatically generate tactical sales forecasts. *Computers & Industrial Engineering*, *139*, 106169. https://doi.org/10.1016/J.CIE.2019.106169

XG. (n.d.). *XGBoost Nasıl Çalışır? Neden İyi Performans Gösterir? - Veri Bilimi Okulu - Veri Bilimi Okulu*. Retrieved May 24, 2023, from https://www.veribilimiokulu.com/xgboost-nasil-calisir/

Yu, X., Liu, Y., Huang, X., & An, A. (2012). Mining online reviews for predicting sales performance: A case study in the movie domain. *IEEE Transactions on Knowledge and Data Engineering*, *24*(4), 720–734. https://doi.org/10.1109/TKDE.2010.269

Data Prıvacy İn Bıg Data: Federed Learnıng

Büşra BÜYÜKTANIR [1]
Buket DOĞAN[2]

INTRODUCTION

In today's world, with internet-based evolving technologies, both the users utilizing these technologies and the objects resulting from these technologies are constantly generating data [1]. These big data produced are utilized in numerous sectors such as security, education, healthcare, research, and development, as well as the institutions and organizations associated with these sectors. Governments, institutions, and organizations that witness improvements in various aspects such as speeding up business processes, reducing costs, and providing benefits in terms of analysis and statistical significance invest more in the field of big data. Data, when in piles, become more meaningful after processing unpredictable situations. Thus, governments, institutions, and organizations utilizing meaningful data can conduct a situation analysis and make more accurate predictions for the future. The correct utilization of data in this manner leads to increased revenue and enrichment of business sectors [2].

On the other hand, the privacy of personal data contained within the generated data is of great importance [3]. Data stored on servers or shared for processing brings along security issues in order to ensure data privacy. Countries have taken precautionary measures in the form of laws to ensure security. The General Data Protection Regulation (GDPR) and the Personal Data Protection Law (KVKK) restrict the processing of personal information by others without the individual's consent. However, relying solely on legal measures is insufficient to ensure security [4]. Technological solutions are needed in practical terms to achieve security.

Big data is the raw material for artificial intelligence, machine learning, and deep learning [5]. In recent years, these fields have been rapidly developing and still evolving [6]. The quantity and diversity of data that influence decision-making processes are of great importance in order to produce results that are closest to the truth [7]. These technological methods used to process and make data meaningful contribute to the development of applications concerning the security of personal data. Federated learning, a new-generation artificial intelligence approach, ensures data privacy and enables the generation and sharing of big data [8].

In this study, the federated learning architecture, which has been developed to ensure data privacy and security in big data, is examined. Federated learning allows the models to be trained on the data where they are generated, without the need to send the data to a central server. Instead, the models are sent to the server after training and then distributed back to each participant. In other words, the machine learning model is executed at the location where the data is generated, and the data is not transferred to another location. Processing the data where it resides eliminates concerns regarding data privacy.

The remainder of the study is organized as follows: Detailed explanations of big data and federated learning concepts are provided, along with a comprehensive examination of the

[1] Büşra Büyüktanır, RA, Marmara University, Computer Engineering
[2] Buket Doğan, Assoc. Prof., Marmara University, Computer Engineering

use of federated learning for big data. Relevant studies from the literature on the subject are discussed. Finally, the obtained results are evaluated.

BIG DATA and FEDERED LEARNING

A.Big Data

With the development of information and communication technologies, internet technologies such as social media applications, web pages, blogs, sensors, etc., provide the opportunity to collect big data. The diversity and volume of rapidly collected data have led to the emergence of the concept of big data [9]. Big data refers to large-scale, diverse, and abundant datasets that are collected at high speed from various sources. The term "3V" is commonly used to describe the three main characteristics of big data: volume, velocity, and variety. Volume represents the size of large data sets, variety encompasses the use of different data types such as images, text, videos, and velocity denotes the rapid collection and processing of data.

Big datasets collected through internet websites, web-based applications, social media, sensors, etc. can be utilized in various fields such as banking, healthcare, education, marketing, public relations, security, logistics, agriculture, and more. Different techniques such as data mining, machine learning, artificial intelligence, and other advanced analytical technologies are employed for data collection, processing, preparation, accessibility, storage, and analysis. These techniques enable businesses, organizations, and researchers to extract valuable information from big data sets, offering a deeper understanding and a competitive advantage. They facilitate making better decisions, identifying trends, analyzing customer behavior, making predictions, discovering relationships, and developing innovative solutions.

Institutions and individuals that fail to adapt to big data find themselves at a disadvantage in the face of rapid data growth and advancing technologies. Those who can effectively harness big data, however, gain a competitive advantage by improving their business processes and conducting more efficient research, development, and implementation activities [10].

Big data is utilized by following the stages of data collection, storage, cleansing, analysis, interpretation, and decision-making and implementation. Throughout these stages, ensuring the security and confidentiality of data plays a significant role. Federated learning technology has emerged to preserve data privacy in big data by safeguarding data security and confidentiality [11].

B.Federated Learning

Federated learning is a technology developed for client-server systems [12]. With this technology, data is not sent from clients/users/edges to the server, but rather analyzed here. Data is not shared with clients; instead, local model training is performed. The weights of each model trained by the clients are combined and sent to the server. By combining the model weights sent to the server, a final model is created [13]. Thus, by performing local model training and not sharing data, data privacy is ensured. Additionally, sending models from clients to the server instead of data reduces network traffic and communication costs, enabling fast communication with low energy consumption. Figure 1 illustrates the functioning of the federated learning architecture.

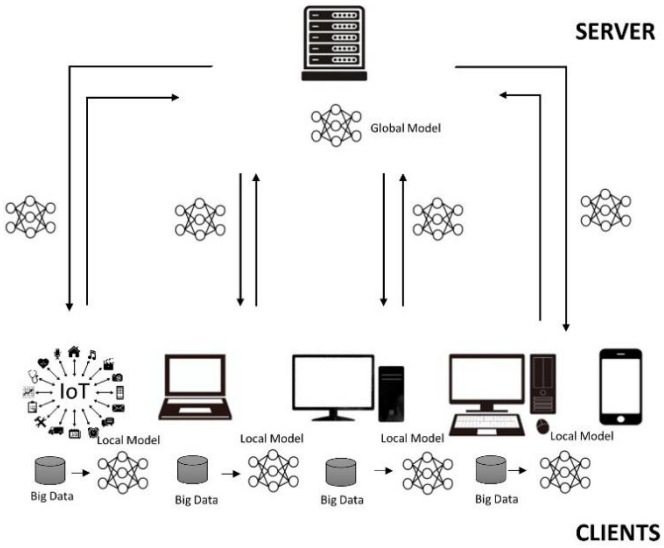

Figure 1. The functioning of the federated learning architecture.

When it comes to the data sources generated and utilized during model training, the federated learning method is divided into two types based on the number of clients involved: cross-device federated learning and cross-silo federated learning [14].

Cross-device federated learning enables the use of smartphones, wearable devices, and similar devices as clients, where the data generated by these devices are used for model training. Since the data produced by each individual client may be limited, a large number of clients is required for successful model training. Therefore, the number of clients, i.e., users utilizing these devices, can reach millions. Mobile device applications can be given as an example.

Cross-silo federated learning is employed by data-generating organizations or companies, whereby participating clients are typically companies or institutions such as hospitals and banks. As a result, the number of clients is generally limited. This method is frequently used in cases where data is sensitive and not easily shareable among different clients.

1.1 Federated Learning Types

Data sets in the dataset are matrices consisting of rows and columns. Each row represents a sample of data, while each column represents its attribute. Federated learning employs three different methods to solve federated learning problems: Horizontal Federated Learning, Vertical Federated Learning, and Federated Transfer Learning [15].

a. Horizontal Federated Learning

In cases where the same field is shared as an attribute among different datasets, but the examples are different, the Horizontal Federated Learning method is utilized. An application example for the Horizontal Federated Learning method is presented in Figure 2. As an illustration in the figure, patient data in three hospitals located in different geographical locations are available. There might be minimal patient overlap among the three hospitals, but the attributes in the patient data are similar. In this scenario, a horizontal federation learning model can be constructed using the patient data from the three hospitals [16].

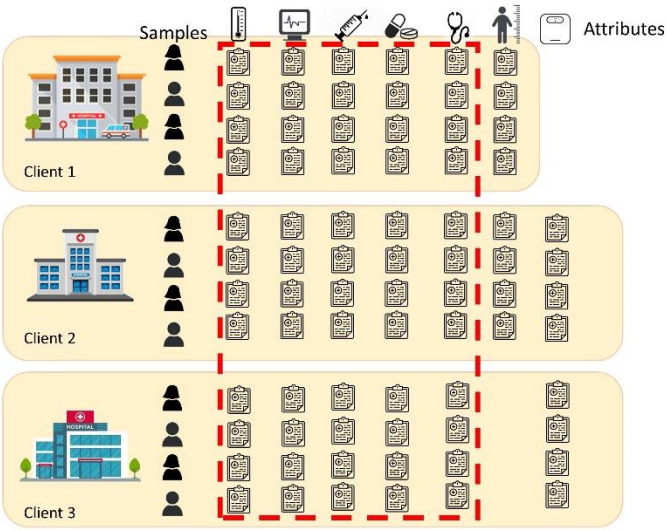

Figure 2. Horizontal federated learning application example [16].

b. Vertical Federated Learning

In cases where the same examples exist in datasets but with different attribute domains, the Vertical Federated Learning method is employed [16]. Figure 3 presents an application example of the Vertical Federated Learning method. According to the figure, there is a hospital and a health application that have the same patients. In other words, the same patients are registered at the hospital and are users of the same application. The hospital collects data obtained from patients' health check-ups, while the application records information about patients' height, weight, nutrition, and step history. Consequently, user attributes differ between the two sources. While the number of users may be small in this method, the dimensionality of the training data can be large. Therefore, the size of the dataset generated by patients is significantly large.

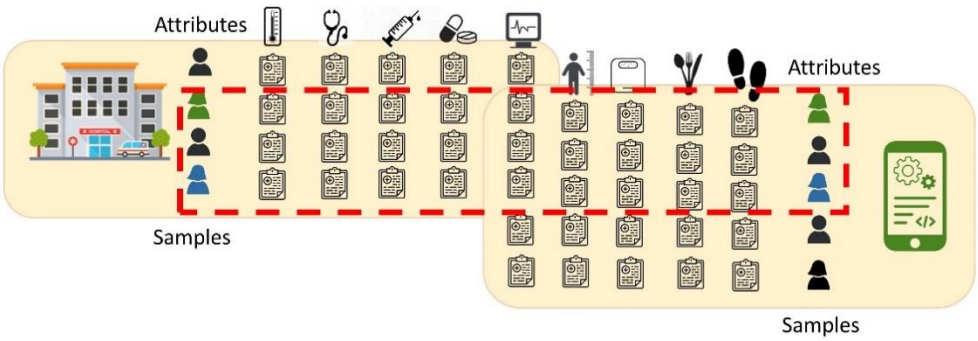

Figure 3. Vertical federated learning application example [16].

c. Federated Transfer Learning

In cases where both the features and the samples in the datasets are different, Federated Transfer Learning method is utilized [16]. An application example for the Federated Transfer Learning method is presented in Figure 4. In many machine learning algorithms, the development of applications assumes that the training and test data have the same features and follow the same distribution. However, this assumption is often not valid in real-life environments. The Federated Transfer Learning method provides a solution to this problem.

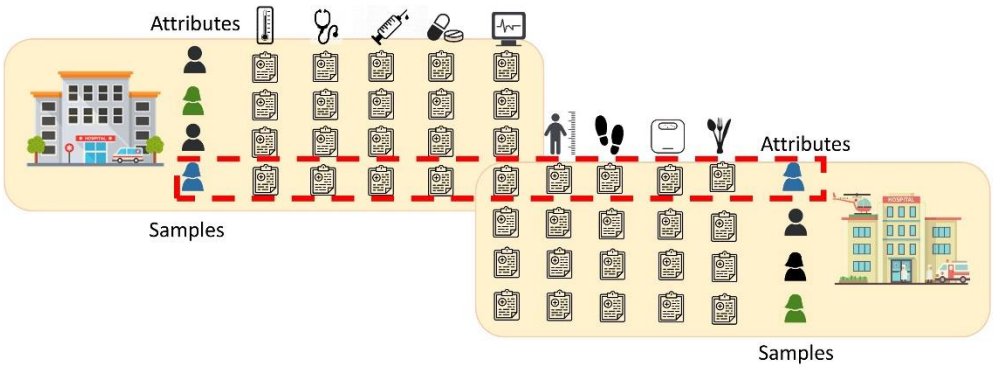

Figure 4. Federated transfer learning application example [16].

1.2 Developing Models with Federated Learning

Federated learning begins with the creation and training of a machine learning model on the server in a client-server architecture. Then, selected clients download the current model weights and training program from the server. Subsequently, each client trains the model using the locally generated data associated with the machine learning application. The information of the trained models on the clients is sent to the server, usually on a periodic basis within a specific program. Various privacy protocol techniques are employed during the transfer from clients to the server. The existing model on the server is updated using the collected models. The updated centralized model on the server is then shared with the clients, and the models held by the clients are updated accordingly. Figure 5 illustrates the steps of model formation in the federated learning architecture, with numbers for visual representation.

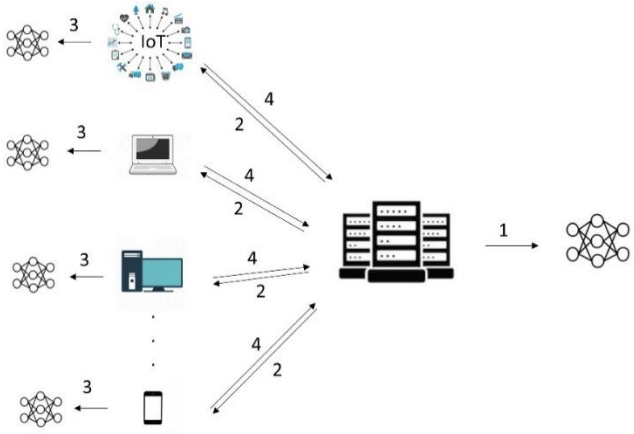

Figure 5. Federated learning model formation.

1.3 Privacy in Federated Learning

In developing applications, particularly in sectors such as healthcare, education, and banking, using federated learning architecture, ensuring the privacy and security of both server-side and client-side model parameters is crucial. Although the data remains local, it is believed that data can be reconstructed from the updates sent from the server to the client and vice versa. Therefore, various privacy algorithms are available for this purpose.

a. Safe Collection

A cryptographic set that enables multiple parties on servers and clients to perform computations collectively while ensuring that the input information from clients or servers remains unknown to other parties is referred to as [17].

b. Differential Privacy

The security of data is ensured in crowded data sets through this commonly used type of privacy, where noise is added to the data and the information about its source is concealed [18].

c. Homomorphic Encryption

Homomorphic encryption is an optional encryption method used to add additional security and privacy to applications in federated learning, allowing users to perform computations on encrypted data. The results of the computations remain in encrypted form, and when decrypted, the output matches the output generated by computations performed on unencrypted data. It employs a public key for encryption and a private key for decryption [19].

1.4 Federated Learning Platforms

In federated learning architecture, there are multiple platforms available for processing data generated from multiple edges to be used in model training. These platforms ensure the preservation of data privacy, enable the creation of a collaborative learning model, and facilitate the sharing of models. The names and descriptions of the federated learning platforms most preferred by researchers in the scope of this study are presented in Table 1.

Table 1. Federated learning platform names and descriptions.

Platform Name	Description
TensorFlow Federated (TFF)	It is an open source federated learning platform based on TensorFlow developed by Google [20].
PySyft	It is an open source federated learning library based on PyTorch that provides data privacy developed for deep learning by OpenMined [21].
Federated AI Technology Enabler (FATE)	It is an industrial-grade open source unified learning platform developed by Webank that offers horizontal, vertical and transfer learning methods between different organizations [21].
PaddleFL (PFL)	It is an open source federated learning framework that supports differential privacy based on PaddlePaddle, developed by the Chinese search engine Baidu for deep learning [21].
IBM Federated Learning (IBM FL)	IBM Federation Learning: It is a federated learning platform developed by IBM, available in both licensed and free versions [22].

C. Federated Learning for Big Data

Federated learning is utilized as a solution for the challenges encountered in the collection, storage, analysis, and privacy preservation of big data services. Figure 6 illustrates the federated learning architecture for big data services [23].

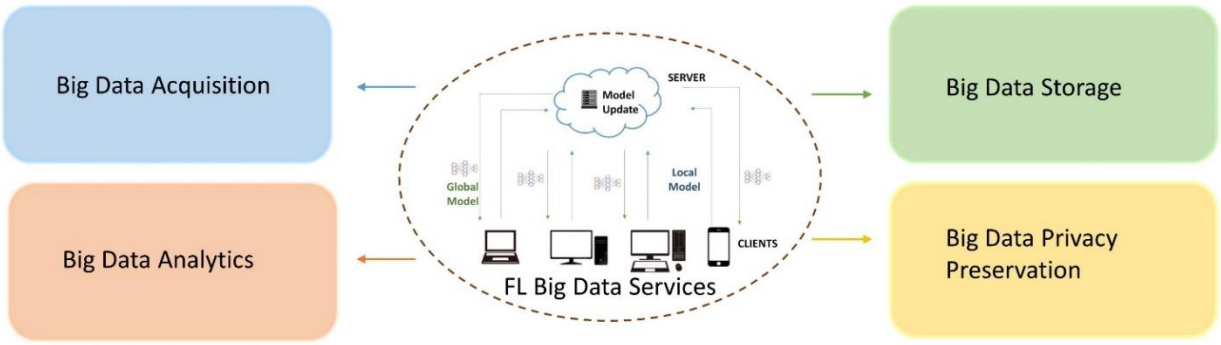

Figure 6. Federated learning for big data services [23].

Machine learning used for systems where clients and servers work together causes network traffic, communication delays, and fast energy consumption for devices due to the collection of large data generated by clients and sharing it with the server in artificial intelligence applications. In addition to these problems, sharing data compromises data security by making it accessible to attackers.

With federated learning architecture, data is not transmitted outside the area where it is generated, and model training is performed locally. This ensures data security. The size of the generated large data is larger than the size of the model trained on this data. Since a smaller-sized model is sent to the server instead of data, there is no traffic on the network, and communication delays are eliminated.

Big Data Acquisition: Instead of collecting data from each client and sharing it with the server, locally trained models with this data are shared with the server.

Big Data Storage: If the number of clients is high, storing the data sent to the server incurs additional costs. With federated learning architecture, data is not shared outside of where it is generated. The trained model is updated and circulated between the server and clients without the need for storage.

Big Data Analytics: Sending data to the server for analysis results in a long training time for the model trained on the collected large data. In the proposed approach with federated learning architecture, models are trained on clients and combined on the server. The training time on clients and the sharing time with the server are shorter than the model training time applied in traditional methods. However, sharing patient and customer information by certain institutions such as hospitals and banks raises concerns about data privacy. Not sharing such data will result in inadequate training of the model and a compromise in accuracy as it won't be exposed to different types of data.

Big Data Privacy Preservation: The main purpose of federated learning technology is to secure data privacy. By not transmitting data from clients to the server and applying methods such as homomorphic encryption and differential privacy to the models trained on clients, both data privacy and data security are ensured. The problem of data insufficiency in model training is eliminated due to the non-disclosure of personal information. Additionally, the final model obtained through the combination of models on the server is shared back with the clients. This allows continuously learning updated models to be used by clients.

D. Related Works

First introduced by Google in 2016, Federated Learning [24] has emerged as a solution to issues such as data accessibility and privacy, and has found applications in various domains such as finance, healthcare, education, smart cities, wearable devices, blockchain, and the Internet of Things [25-26].

Nowadays, artificial intelligence and machine learning methods are being utilized in numerous fields. The accuracy of a model trained using these methods is directly proportional to the amount of data available. However, training models with limited data in domains where data sharing raises concerns about privacy may introduce a certain level of bias. Therefore, for collaborative frameworks involving clients and servers, data sharing among organizations and devices can be achieved through federated learning, ensuring data privacy is maintained. In the literature, studies have been conducted in the healthcare domain using federated learning architecture for tasks such as the detection of diseases like Covid-19 based on chest X-rays using deep learning algorithms [27-30], autoencoder models [31], and electronic health records [32-33]. Sharing customer information between organizations, such as in banks, poses risks. Federated learning can be a good approach to mitigate this risk [34-35]. Federated learning has also been employed in the transportation domain, as evident from studies on intelligent transportation systems [36] and autonomous driving [37].

Furthermore, federated learning has been successfully applied in various areas such as identity authentication using drones [38], text recognition [39], energy prediction in smart buildings [40], violence prediction in simulated environments [41], network intrusion detection [42-43], and speech recognition [44].

When examining the studies conducted and included in the literature, federated learning technology has demonstrated successful results in multiple domains, ranging from healthcare to transportation. It has been particularly utilized in research focusing on data privacy. Given that federated learning is a current technology capable of processing large datasets and generating value-added outputs, it is considered crucial for researchers to delve into this field.

CONCLUSION

Big data production is increasing and can be beneficial in various fields when processed correctly. However, traditional machine learning approaches are not compliant with data protection laws as they are based on centralized data collection. Therefore, innovative solutions that can preserve data privacy are needed for advancements in the field of artificial intelligence. Additionally, organizations collect and analyze data in centralized systems for their own business processes. However, this poses a risk to data security. Data privacy is of utmost importance and should be handled with great care.

Federated learning is a current technology that ensures data privacy. With this technology, the need for data centers decreases, and it enables the training of new models among similar or different institutions without data exchange through horizontal, vertical, and transfer learning types. It also complies with legal measures taken to ensure data security.

In conclusion, the volume and diversity of generated data are increasing. Ensuring the security and privacy of this data through automated systems is crucial. Federated learning technology allows data to be processed where it is generated, thereby stopping data sharing among different devices/institutions and ensuring data security and privacy. Studies in the literature indicate that this technology, which is utilized in many fields, should be implemented in numerous public institutions.

References

[1] Lee, J., Bagheri, B., & Kao, H. A. (2015). A cyber-physical systems architecture for industry 4.0-based manufacturing systems. Manufacturing letters, 3, 18-23.

[2] Atalay, M., & Çelik, E. (2017). Büyük veri analizinde yapay zekâ ve makine öğrenmesi uygulamalari-artificial intelligence and machine learning applications in big data analysis. Mehmet Akif Ersoy Üniversitesi Sosyal Bilimler Enstitüsü Dergisi, 9(22), 155-172.

[3] Zhou, K., Liu, T., & Zhou, L. (2015, August). Industry 4.0: Towards future industrial opportunities and challenges. In 2015 12th International conference on fuzzy systems and knowledge discovery (FSKD) (pp. 2147-2152). IEEE.

[4] Gökçay, B., & Arda, B. (2019). Kişisel sağlık verilerinin korunması kapsamında sağlık araştırmalarında etik bakış. Türk Kardiyoloji Derneği Arşivi, 47(3), 218-227.

[5] Kayaalp, K., & Süzen, A. A. (2018). Derin öğrenme ve Türkiye'deki uygulamaları. Yayın Yeri: IKSAD International Publishing House, Basım sayısı, 1.

[6] Abadi, M., Barham, P., Chen, J., Chen, Z., Davis, A., Dean, J., ... & Zheng, X. (2016, November). Tensorflow: a system for large-scale machine learning. In Osdi (Vol. 16, No. 2016, pp. 265-283).

[7] Aktan, E. (2018). Büyük veri: Uygulama alanları, analitiği ve güvenlik boyutu. Bilgi Yönetimi, 1(1), 1-22.

[8] Bagdasaryan, E., Veit, A., Hua, Y., Estrin, D., & Shmatikov, V. (2020, June). How to backdoor federated learning. In International Conference on Artificial Intelligence and Statistics (pp. 2938-2948). PMLR.

[9] Sagiroglu, S., & Sinanc, D. (2013, May). Big data: A review. In 2013 international conference on collaboration technologies and systems (CTS) (pp. 42-47). IEEE.

[10] Özdemir, İ., & SAĞIROĞLU, Ş. (2018). Denetimlerde büyük veri kullanımı ve üzerine bir değerlendirme. Gazi University Journal of Science Part C: Design and Technology, 6(2), 470-480.

[11] Zhang, K., Song, X., Zhang, C., & Yu, S. (2022). Challenges and future directions of secure federated learning: a survey. Frontiers of computer science, 16, 1-8.

[12] Kairouz, P., McMahan, H. B., Avent, B., Bellet, A., Bennis, M., Bhagoji, A. N., ... & Zhao, S. (2021). Advances and open problems in federated learning. Foundations and Trends® in Machine Learning, 14(1–2), 1-210.

[13] Süzen, A.A. and K. Kayaalp, Büyük Verilerde Gizlilik Tabanlı Yaklaşım: Federe Öğrenme. International Journal of 3D Printing Technologies and Digital Industry. 3(3): P. 297-304.

[14] Huang, C., Huang, J., & Liu, X. (2022). Cross-Silo Federated Learning: Challenges and Opportunities. arXiv preprint arXiv:2206.12949.

[15] Y. Chen, X. Qin, J. Wang, C. Yu, and W. Gao, "Fedhealth: A Federated Transfer Learning Framework For Wearable Healthcare," IEEE Intelligent Systems, vol. 35, no. 4, pp. 83-93, 2020.

[16] L. Li, Y. Fan, M. Tse, and K.-Y. Lin, "A Review Of Applications In Federated Learning,"

Computers & Industrial Engineering, p. 106854, 2020.

[17] Pettai, M., & Laud, P., Combining differential privacy and secure multiparty computation. In Proceedings of the 31st Annual Computer Security Applications Conference, Pages 421-430, 2015. ACM.

[18] Choudhury, O., Gkoulalas-Divanis, A., Salonidis, T., Sylla, I., Park, Y., Hsu, G., & Das, A., Differential Privacy-enabled Federated Learning for Sensitive Health Data. arXiv preprint arXiv:1910.02578. 2019.

[19] Aslett, L. J., Esperança, P. M., & Holmes, C. C., A review of homomorphic encryption and software tools for encrypted statistical machine learning. arXiv preprint arXiv:1508.06574, 2015.

[20] Lim, W. Y. B., Luong, N. C., Hoang, D. T., Jiao, Y., Liang, Y. C., Yang, Q., ... & Miao, C. (2020). Federated learning in mobile edge networks: A comprehensive survey. IEEE Communications Surveys & Tutorials, 22(3), 2031-2063.

[21] N. Rodríguez-Barroso et al., "Federated Learning and Differential Privacy: Software Tools

Analysis, The Sherpa. AI FL Framework and Methodological Guidelines For Preserving Data Privacy," Information Fusion, vol. 64, pp. 270-292, 2020.

[22] Büyüknacar, Y. C. Y. FEDERE ÖĞRENME VE VERİ MAHREMİYETİ.

[23] Gadekallu, T. R., Pham, Q. V., Huynh-The, T., Bhattacharya, S., Maddikunta, P. K. R., & Liyanage, M. (2021). Federated learning for big data: A survey on opportunities, applications, and future directions. arXiv preprint arXiv:2110.04160.

[24] Jiang, J.C., et al., Federated learning in smart city sensing: Challenges and opportunities.Sensors, 20(21): p. 6230, 2020.

[25] Liu, Y., et al., A systematic literature review on federated learning: From a model quality perspective. arXiv preprint arXiv:2012.01973, 2020.

[26] Yang, Q., et al., Federated learning. Synthesis Lectures on Artificial Intelligence and Machine Learning, 13(3): p. 1-207, 2019.

[27] Cetinkaya, A. E., Akin, M., & Sagiroglu, S. (2021, September). A communication efficient federated learning approach to multi chest diseases classification. In 2021 6th International Conference on Computer Science and Engineering (UBMK) (pp. 429-434). IEEE.

[28] Zhang, L., Shen, B., Barnawi, A., Xi, S., Kumar, N., & Wu, Y. (2021). FedDPGAN: federated differentially private generative adversarial networks framework for the detection of COVID-19 pneumonia. Information Systems Frontiers, 23(6), 1403-1415.

[29] Makkar, A., & Santosh, K. C. (2023). SecureFed: federated learning empowered medical imaging technique to analyze lung abnormalities in chest X-rays. International Journal of Machine Learning and Cybernetics, 1-12.

[30] Kandati, D. R., & Gadekallu, T. R. (2022). Genetic clustered federated learning for COVID-19 detection. Electronics, 11(17), 2714.

[31] L. Huang, A. L. Shea, H. Qian, A. Masurkar, H. Deng, and D. Liu, "Patient clustering improves efficiency of federated machine learning to predict mortality and hospital stay time using distributed electronic medical records," J. Biomed. Inform., vol. 99, no. September, p. 103291, 2019, doi: 10.1016/j.jbi.2019.103291.

[32] Boughorbel, S., Jarray, F., Venugopal, N., Moosa, S., Elhadi, H., & Makhlouf, M. (2019). Federated uncertainty-aware learning for distributed hospital ehr data. arXiv preprint arXiv:1910.12191.

[33] Liu, D., Dligach, D., & Miller, T. (2019, August). Two-stage federated phenotyping and patient representation learning. In Proceedings of the conference. Association for Computational Linguistics. Meeting (Vol. 2019, p. 283). NIH Public Access.

[34] A. Imteaj and M. H. Amini, "Leveraging asynchronous federated learning to predict customers financial distress," Intell. Syst. with Appl., vol. 14, 2022, doi: 10.1016/j.iswa.2022.200064.

[35] G. Long, "Federated Learning for Open Banking."

[36] Elbir, A. M., Soner, B., Çöleri, S., Gündüz, D., & Bennis, M. (2022, September). Federated learning in vehicular networks. In 2022 IEEE International Mediterranean Conference on Communications and Networking (MeditCom) (pp. 72-77). IEEE.

[37] Nguyen, A., Do, T., Tran, M., Nguyen, B. X., Duong, C., Phan, T., ... & Tran, Q. D. (2022, June). Deep federated learning for autonomous driving. In 2022 IEEE Intelligent Vehicles Symposium (IV) (pp. 1824-1830). IEEE.

[38] Yazdinejad, A., Parizi, R. M., Dehghantanha, A., & Karimipour, H. (2021). Federated learning for drone authentication. Ad Hoc Networks, 120, 102574.

[39] Zhu, X., Wang, J., Hong, Z., Xia, T., & Xiao, J. (2019, November). Federated learning of unsegmented chinese text recognition model. In 2019 IEEE 31st International Conference on Tools with Artificial Intelligence (ICTAI) (pp. 1341-1345). IEEE.

[40] Dasari, S. V., Mittal, K., Sasirekha, G. V. K., Bapat, J., & Das, D. (2021, April). Privacy enhanced energy prediction in smart building using federated learning. In 2021 IEEE International IOT, Electronics and Mechatronics Conference (IEMTRONICS) (pp. 1-6). IEEE.

[41] Borger, T., Mosteiro, P., Kaya, H., Rijcken, E., Salah, A. A., Scheepers, F., & Spruit, M. (2022). Federated learning for violence incident prediction in a simulated cross-institutional psychiatric setting. Expert Systems with Applications, 199, 116720.

[42] Tang, Z., Hu, H., & Xu, C. (2022). A federated learning method for network intrusion detection. Concurrency and Computation: Practice and Experience, 34(10), e6812.

[43] Doriguzzi-Corin, R., & Siracusa, D. (2022). FLAD: adaptive federated learning for DDoS attack detection. arXiv preprint arXiv:2205.06661.

[44] D. Guliani, F. Beaufays, and G. Motta, “Training Speech Recognition Models With Federated Learning: A Quality/Cost Framework,” in ICASSP 2021-2021 IEEE International Conference on Acoustics, Speech and Signal Processing (ICASSP), 2021, pp. 3080-3084: IEEE.

The Effect of Micro Fiber Type and Fiber Combination on the Elastic Modulus of Hybrid Fiber Reinforced Self-Compacting Concrete

Mahmut Başsürücü[1]
Kazım Türk[2]

Introduction

The elastic modulus, one of the most important mechanical properties of concrete, shows the capacity of concrete to resist deformation. Materials exhibit linear elastic behavior up to a certain stress value under load effects. However, if this stress value is exceeded, the materials show plastic behavior. In the design of concrete or reinforced concrete structural elements, the maximum stress value obtained within the elastic limit has a very important role in terms of structural safety and human comfort.

Currently, hybrid fiber reinforced self-compacting concrete (HFRSCC) is preferred as a novelty material for civil engineering applications. Self-compacting concrete (SCC), which was developed in Japan at the end of the 1980s, is defined as concrete that can easily spread under its weight, pass between rebar, and fill the mold without bleeding or segregation, regardless of any compaction process, even in very densely reinforced structural elements (Okamura, 1997; Ozawa et al., 1989). In the design of SCC, superplasticizer chemical admixtures, large amounts of powder materials and/or viscosity enhancers are used to prevent segregation and bleeding of the concrete during transportation and placement (Valcuende et al., 2005). On the other hand, the influence of steel fiber reinforcement on the engineering properties of concrete was first studied in the 1950s and 1960s (Hannant, 1987). Fiber combinations having different types (steel, polypropylene, glass, carbon, etc.), sizes (macro and micro), and aspect ratios are widely used today to enhance the tensile strength, toughness, and ductility properties of concrete. Fiber reinforced concrete obtained by including more than one type of fiber in concrete is called hybrid fiber reinforced concrete. The hybrid fiber idea of using macro and micro fibers together in a concrete mixture was first proposed by Rossi et al. (1987). It was stated that micro fibers controlled and bridged the growth of micro cracks and caused high tensile strength in concrete, and in the next stage, macro fibers controlled macro cracks by increasing both the ductility and load carrying capacity of structural elements (Mobasher & Li, 1996). The studies have been conducted by many authors (Banthia & Sappakittipakorn, 2007; Bassurucu & Turk, 2023; Turk et al., 2021), it has been concluded that the better performance of hybrid fiber reinforced concrete is largely due to the synergistic effect. Moreover, it was emphasized that hybrid fiber reinforcement caused important enhancements in the flexural, shear, and bond behavior of reinforced concrete structural elements compared to control without fiber reinforcement and single fiber reinforced concrete specimens (Katlav et al., 2022;

[1] Mahmut Başsürücü, Dr., Malatya Turgut Ozal University, Department of Construction Technology
[2] Kazım Türk, Prof. Dr., Inonu University, Civil Engineering

Turk et al., 2020; Turk & Bassurucu, 2021, 2022). In conclusion, the elastic modulus of reinforced concrete structural elements produced from HFRSCC has very important in terms of the design and the performance evaluation when it is considered the use of hybrid fiber reinforced composite, commonly.

In this research, the influence of fiber combination and micro fiber type on the elastic modulus values of HFRSCC mixtures was investigated experimentally and statistically. For this purpose, the elastic modulus tests of SCC mixtures with different fiber hybridizations were carried out. Besides, empirical equations were developed to predict the elastic modulus values of HFRSCC mixtures, and graphs were drawn to guide designers in determining the most appropriate micro fiber types and quantity.

Materials and Method

Materials

In this study, pozzolanic cement (CEM IV 32.5 R) manufactured by the Elazig Cimentas factory was used. Moreover, Class F fly ash waste from Isken Sugozu Thermal Power Station was added as a mineral additive to contribute to the amount of fine powder material (<0.125 mm) in the SCC mixtures. The oxide compounds of pozzolanic cement and fly ash were presented in Table 1.

Table 1. Oxide compounds of pozzolanic cement and fly ash (%).

Compound	Pozzolanic cement	Fly ash
SiO_2	29	63.04
Al_2O_3	9.5	21.63
Fe_2O_3	5.5	6.77
CaO	41	1.07
MgO	1	-
SO_3	2.86	0.10
K_2O	0.68	-
Na_2O	0.60	-
LOI	-	2.6
Specific gravity	2.95	2.3
Surface area (cm^2/g)	4380	2690

Two types of aggregates, fine (0-5 mm) and coarse (5-15 mm) were used in the production of SCC mixtures. The saturated surface dry specific gravity of fine and coarse aggregates was obtained as 2.39 and 2.68, respectively. In fresh SCC mixtures, 80% fine and 20% coarse aggregate were used of the total aggregates to obtain the highest compactness, reduce segregation and ensure homogeneous distribution of fibers in the concrete. The gradation of the total aggregate was presented in Table 2. Moreover, it was aimed to produce concrete according to SCC workability conditions without increasing the amount of mixing water in SCC mixtures by using a superplasticizer with a specific gravity of 1.08 produced by Sika Construction Chemicals.

Table 2. The gradation of total aggregate.

Sieve size (mm)	Aggregate (% passing)
16	100
8	88.7
4	78.4
2	49.3
1	30.2
0.5	18.4
0.25	10.7
0.125	7.4

As for the fiber types preferred in the study, a total of three different fiber types were used: double-hooked macro steel and two different micro types (steel and polypropylene). The properties and pictures of fibers were shown in Table 3 and Figure 1, respectively.

Table 3. The properties of fibers.

Fiber type	Length (mm)	Diameter (mm)	Aspect Ratio	Tensile Strength (MPa)	Elastic Modulus (GPa)	Density (g/cm3)
Macro steel	60	0.90	66	1150	210	7.8
Micro steel	13	0.15	87	3000	200	7.2
Polypropylene	6	0.025	240	350	-	0.91

Figure 1. The pictures of macro and micro fibers.

SCC Mixture Proportions

In this research, a total of five self-compacting concrete mixtures were designed as the control without fiber reinforcement, single macro steel, binary hybrid (macro/micro steel and macro steel/micro polypropylene), and ternary hybrid (macro steel/micro steel/polypropylene) fiber reinforced. In all SCC mixtures, the mixture proportions were determined by trial and error method to provide the workability limits recommended by EFNARC (2005) and to prevent the balling effect of micro fibers. For the designed SCC mixtures, the water/binder ratio, pozzolanic cement, fly ash, and water components were kept constant and were determined as 0.28, 500 kg/m^3, 400 kg/m^3, and 250 kg/m^3, respectively. Moreover, fine (0-5

mm) and coarse (5-15 mm) aggregates were used as 80% and 20% of the total aggregate amount, respectively, for all SCC mixtures. On the other hand, the total steel fiber volume was selected at 1% for the single and HFRSCC mixtures while the total fiber volume was 1.25% for the SCC mixtures including micro polypropylene fiber. Besides, the amount of superplasticizer was varied between 0.5% and 1% by weight of the binder. The proportions of SCC mixtures were given in Table 4. In the naming of SCC mixtures, MACSF, MICSF, and PPF stand for macro steel, micro steel, and micro polypropylene fiber, respectively. For example, MACSF1_PPF0.25 indicates that 1% macro steel and 0.25% polypropylene fiber by volume were included in the SCC mixture.

Table 4. The proportions (kg/m^3) and fresh properties of SCC.

Components	**SCC Mixtures**				
	CONTROL	**MACSF 1**	**MACSF0.8-MICSF0.2**	**MACSF 1-PPF0.25**	**MACSF0.8-MICSF0.2-PPF0.25**
Pozzolanic cement	500	500	500	500	500
Fly ash	400	400	400	400	400
Fine aggregate	799	778	778	768	766
Coarse aggregate	200	194	194	192	192
Superplasticizer	4.5	5	5	8.5	9
Water	250	250	250	250	250
Macro steel fiber	-	78.5	62.8	78.5	62.8
Micro steel fiber	-	-	14.4	-	14.4
Micro polypropylene fiber	-	-	-	2.28	2.28
Slump-flow diameter (mm)	790	775	765	750	740
t_{500} (s)	4.2	5.3	5.8	6.5	6.8
J-ring value (mm)	1.7	3.3	3.4	7	8

The production of SCC mixtures consists of two stages. In the first stage, coarse aggregate, fine aggregate, macro/micro fiber, and two-thirds of the mixing water were added to the mixer and mixed for 3 minutes. In the second stage, cement, fly ash, and the remaining one-third of the mixing water with the superplasticizer were added to the mixer and mixed for 7 minutes, and thus SCC mixtures were prepared by applying a total mixing process for 10 minutes.

In addition to all these, as can be seen from Table 4, it was determined that all SCC mixtures ensured the workability conditions recommended by EFNARC (2005) except for the t_{500} values of the polypropylene fiber reinforced SCC mixtures, and thus the designed SCC mixtures had good flowability, excellent passing ability, and stability.

Preparation and Testing of SCC Specimens

In this study, the produced specimens were cured in water for 28-days to obtain the engineering properties (the compressive, the splitting tensile, the flexural tensile strength, and the elastic modulus) for all designed SCC mixtures. On the other hand, elastic modulus tests were performed on Ø100x200 mm cylindrical specimens according to ASTM C469 (2002). Finally, elastic modulus values were obtained by averaging the test results of three SCC specimens produced for each SCC mixture. For the elastic modulus tests, as seen in Figure 2(a), sulfur capping was cast so that the load to be applied to the cylindrical specimens could be uniformly distributed across the specimens of the cross-section. Moreover, before cylindrical specimens were subjected to uniaxial compressive loading, a compressometer with LVDTs was mounted on the specimen to measure horizontal and vertical deformation (Figure 2 (b)). Then,

the cylindrical specimens were placed in the press and subjected to loading. After the experiment started, the horizontal and vertical deformation values of the cylindrical specimens under loading were instantly transferred to the computer by the data acquisition system. Finally, the elastic modulus values of the SCC specimens were calculated based on 40% of the maximum stress using the method specified in the ASTM C469 (2002) standard.

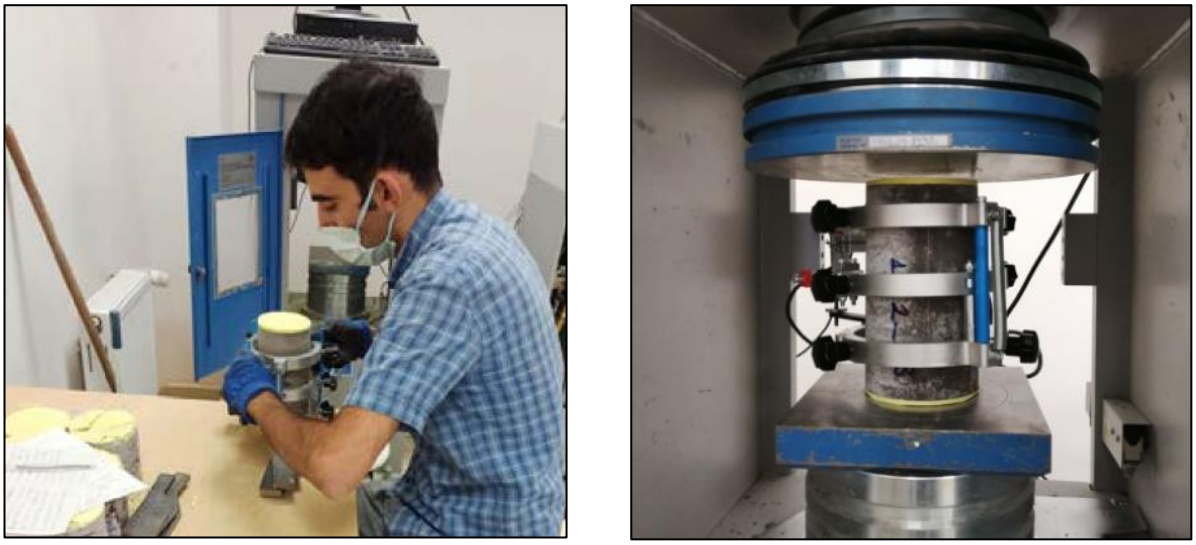

(a) **(b)**

Figure 2. The elastic modulus test for SCC specimens; (a) Compressometer installation, (b) Testing of SCC specimens.

Results and Discussion

Experimental Evaluation of Elastic Modulus Values of HFRSCC

Determining the deformations that occur in the concrete under load effects was very important in terms of building safety for the design of reinforced concrete structural elements and the evaluation of the performance of existing structures. The average elastic modulus values of non-fiber control and single/binary/ternary fiber reinforced SCC mixtures were presented in Table 5 and Figure 3. For the elastic modulus values of SCC specimens with different fiber hybridizations, the age of 28 days was preferred. Because it was emphasized in the literature that the increase in the elastic modulus values of concrete after 28 days was very low and the elastic modulus values for this curing age could be estimated by some models (Zhou et al., 1995).

As can be seen from Table 5, the elastic modulus value of the control SCC specimens without fiber was determined as 34662 MPa. Moreover, the elastic modulus values of the single macro and binary HFRSCC specimens increased with 7.02% and 7.84%, respectively, compared to the control specimens without fiber. From this here, it can be addressed that single or binary hybrid steel fiber reinforcement with a total fiber volume of 1% increased the elastic modulus value, but binary hybrid steel fiber reinforcement had a slightly more positive effect. This may be attributed to the high elastic modulus of the steel fibers the replaced by aggregates and the homogeneous distribution of fibers in the matrix for single/binary hybrid steel fiber reinforced SCC mixtures (see Figure 4(a-b)). In the study conducted by Yagmur (2020) in the literature, it was emphasized that the elastic modulus value increased for concrete containing 1% or less steel fiber by volume while the elastic modulus value decreased for concretes containing more than 1% steel fiber by volume.

Table 5. The engineering properties of SCC mixtures for 28 curing days.

SCC Mixtures	Elastic Modulus (MPa)	Compressive Strength (MPa)	Splitting Tensile Strength (MPa)	Flexural Tensile Strength (MPa)
CONTROL	34662	49.6	4.1	6.27
MACSF1	37097	48.4	5.6	10.88
MACSF0.8_MICSF0.2	37378	53.85	6.2	10.02
MACSF1_PPF0.25	34207	48.2	6.35	11.58
MACSF0.8_MICSF0.2_PPF0.25	34241	59.1	7.49	12.45

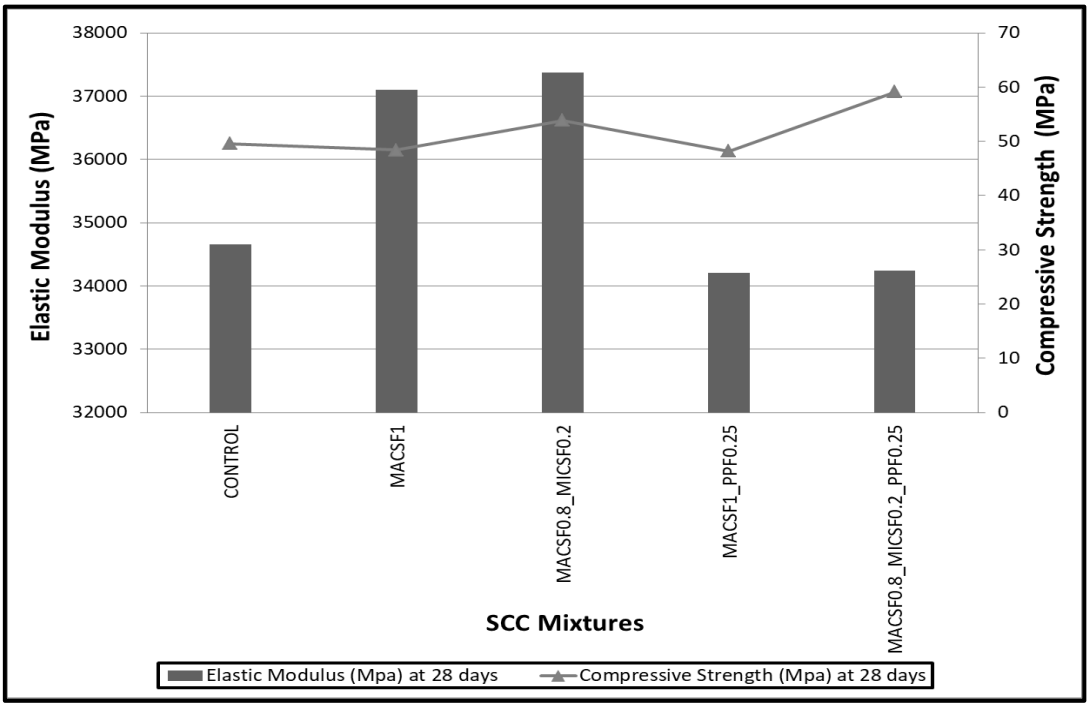

Figure 3. The elastic modulus and compressive strength values of SCC mixtures.

(a) MACSF1

(b) MACSF0.8_MICSF0.2

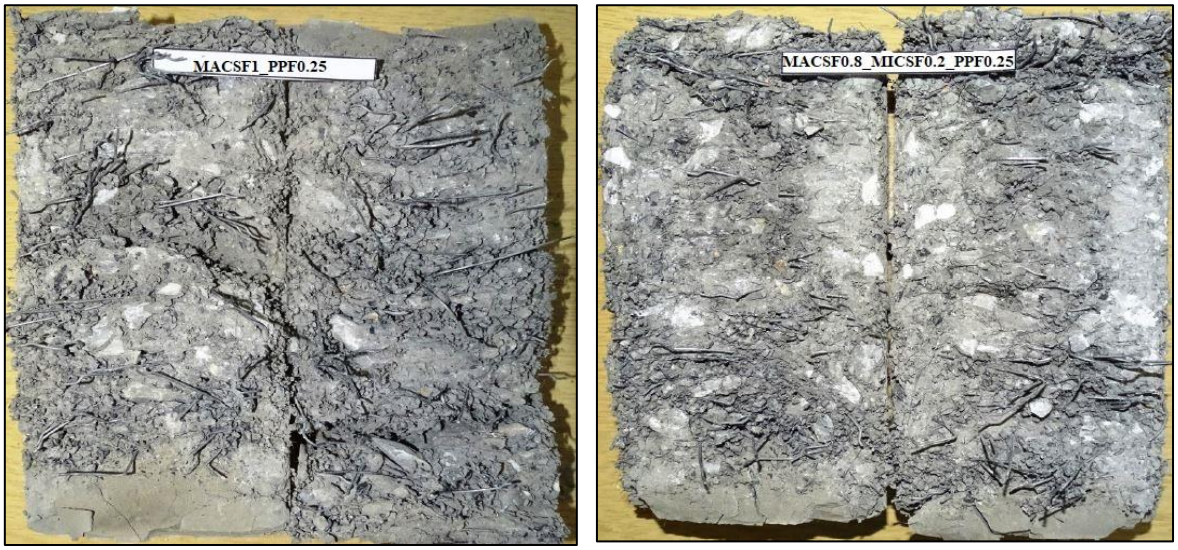

(c) MACSF1_PPF0.25 (d) MACSF0.8_MICSF0.2_PPF0.25

Figure 4. Fiber distribution pictures of single/hybrid fiber reinforced SCC specimens.

On the other hand, it was determined that the elastic modulus values of the binary HFRSCC specimens containing polypropylene fiber decreased with 7.79% compared to the specimens containing only 1% macro steel fiber. Moreover, it was found that the elastic modulus value of ternary HFRSCC specimens reduced with 8.39% compared to the binary hybrid steel fiber reinforced specimens. In conclusion, it can be stated that polypropylene fiber reinforcement as micro fiber in HFRSCC mixtures negatively affected the elastic modulus values. The decrease in elastic modulus of HFRSCC samples containing polypropylene fibers may be attributed to the low elastic modulus of polypropylene fibers compared to steel fibers and the inhomogeneous distribution of the fibers in the matrix due to negative influence of polypropylene fiber on the workability ((see Table 4 and Figure 4(c-d)). In the studies performed in the literature (Singh & Rai, 2021; Topçu et al., 2017), it was emphasized that polypropylene fiber reinforcement had a negative effect on the elastic modulus of the concrete.

In addition to all these, it can be said that macro and micro fibers bridged the cracks formed in the specimens under the effect of axial compressive load during the test and prevented the propagation of cracks up to a certain load level. Therefore, it was thought that the integrity of the HFRSCC specimens was maintained for a longer time compared to the control specimens without fiber, allowing the specimens to carry more load (Figure (5)).

Figure 5. Pictures of SCC specimens after elastic modulus test.

Statistical Evaluation of Experimental Results

The elastic modulus values of binary and ternary HFRSCC was predicted with the help of multiple linear regression analysis (MLR). In the statistical analysis, the variables were the volume fractions of macro, micro steel, and polypropylene fibers. The summary outputs of the statistical analysis using the elastic modulus values were shown in Table 6. It was obtained from this analysis that R^2 values of elastic modulus were 0.998. From this here, it can be concluded that there was a good correlation between the test results and the predicted values obtained. Besides, as can be seen from Table 7, it was determined that the efficient ratio values of the elastic modulus values obtained by MLR analysis were approximately 1.

Table 6. The summary output of MLR analysis for the elastic modulus.

	Coefficients	**Standard Error**	**t stat**	**P-value**
Intercept	34662	123.5	280.66	0.002
MACSF	249675	16337.51	15.28	0.042
MICSF	328425	57596.57	5.7	0.111
PPF	-1205400	49400	-24.4	0.026

Table 7. The experimental and predicted values for the elastic modulus.

SCC Mixtures	**Test**	**Predicted**	**EM_T/EM_{Pr}**
CONTROL	34662	34662	1.000
MACSF1	37097	37159	0.998
MACSF0.8_MICSF0.2	37378	37316	1.002
MACSF1_PPF0.25	34207	34145	1.002
MACSF0.8_MICSF0.2_PPF0.25	34241	34303	0.998

On the other hand, the graph was drawn based on MLR analysis considering three different variables (the volume fraction of macro, micro steel, and polypropylene fiber). Also, the graph will be guide for designers to obtain the most suitable micro fiber type and the volume fraction of fiber (Figure (6)).

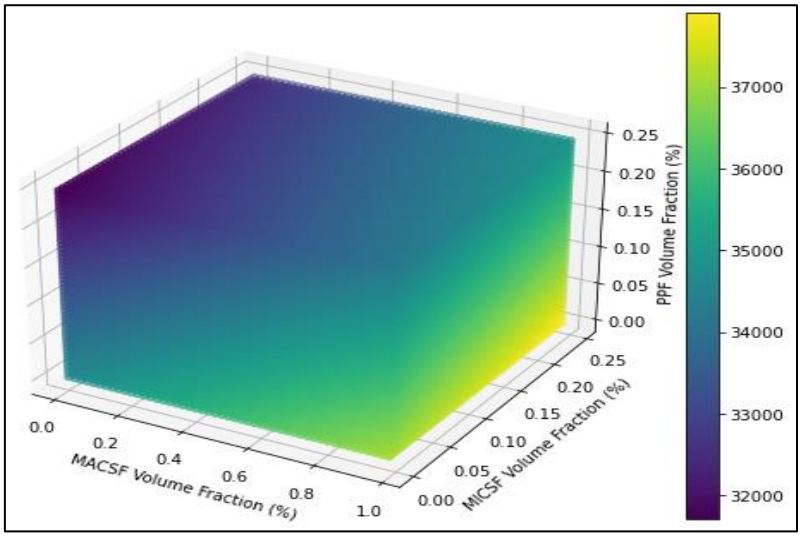

Figure 6. The influence of total fiber amount and micro fiber types on elastic modulus values for binary and ternary HFRSCC.

In addition to all these, the empirical equation was developed to estimate the elastic modulus values of hybrid fiber reinforced SCC specimens (Equation 1). In this equation, the effect of fiber reinforcement on the elasticity modulus was determined based on the fiber reinforcement index and the flexural tensile strength of fiber reinforced concrete. In many studies in the literature, fiber reinforcement index was used to interpret the performance of fiber reinforced concrete elements (Harajli et al., 1995; Turk et al., 2021). As can be seen from Figure 7, there was a high correlation between the normalized elastic modulus and fiber reinforcement index.

$$EM = (1287.4\left(\frac{V_f L_f}{d_f}\right)^2 - 3732.9\left(\frac{V_f L_f}{d_f}\right) + 5519.7)f_{tf} \quad (1)$$

where, EM was the elastic modulus value of fiber reinforced SCC specimens, V_f was the fiber volume fraction (%), L_f was the fiber length (mm), d_f was the fiber diameter (mm) and f_{tf} was the flexural tensile strength of SCC (MPa).

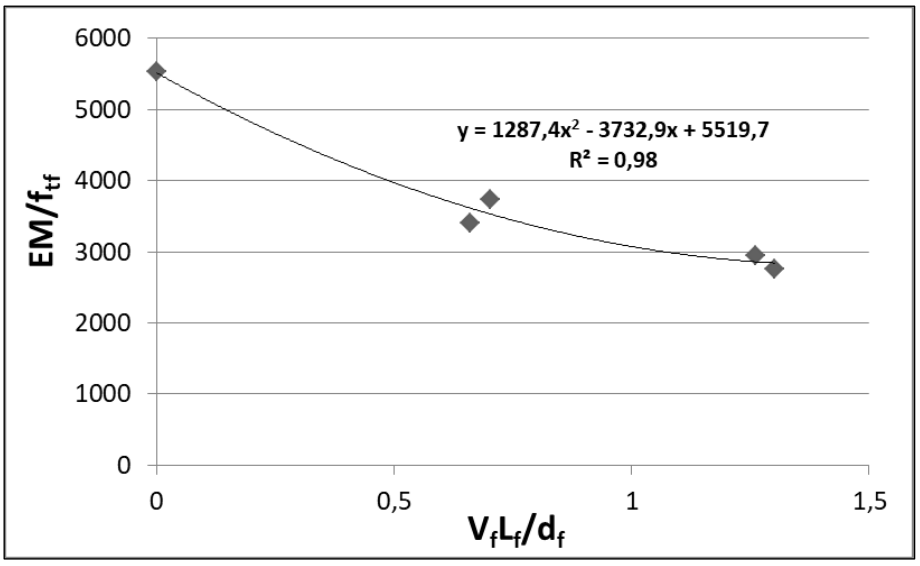

Figure 7. The variation of normalized elastic modulus and fiber reinforcement index.

Conclusions

In this research, the influence of fiber combination and micro fiber type on the elastic modulus values of HFRSCC mixtures was investigated experimentally and statistically. The conclusions can be drawn as follows:

- The single or binary hybrid steel fiber reinforcement with a total fiber volume of 1% increased the elastic modulus value compared to control test specimens without fiber.
- A total of 1% binary blends of hybrid steel fiber increased the elastic modulus more than single steel fiber reinforcement.
- The inclusion of polypropylene fiber as micro fiber to HFRSCC mixtures negatively influenced the elastic modulus values.
- The use of micro steel fiber together with macro steel fiber as hybrid had a more positive effect on the elastic modulus values compared to micro polypropylene fiber.
- The empirical equation was developed to predict the elastic modulus values of HFRSCC mixtures.
- The graph drawn will guide for designers to use the most suitable micro fiber type and volume fraction of fibers in production of HFRSCC mixtures.

Acknowledgement

The financial support for this study was provided by Scientific Research Projects Committee of Inonu University, Türkiye (Project No: FDK-2019-1974). Their support was gratefully acknowledged.

References

ASTM C469-02. (2002). Standard Test Method for Static Modulus of Elasticity and Poisson's Ratio of Concrete in Compression. In *ASTM Standard Book* (Vol. 04).

Banthia, N., & Sappakittipakorn, M. (2007). Toughness enhancement in steel fiber reinforced concrete through fiber hybridization. *Cement and Concrete Research*, *37*(9), 1366–1372. https://doi.org/10.1016/j.cemconres.2007.05.005

Bassurucu, M., & Turk, K. (2023). An experimental and statistical investigation on the fresh and hardened properties of HFR-SCC: the effect of micro fibre type and fibre hybridization. *European Journal of Environmental and Civil Engineering*, *27*(1), 263–287. https://doi.org/10.1080/19648189.2022.2042396

EFNARC. (2005). The European Guidelines for Self-Compacting Concrete. *The European Guidelines for Self Compacting Concrete*.

Hannant, D. (1987). *Fiber Cements and Fiber Concrete*. Wiley.

Harajli, M. H., Maalouf, D., & Khatib, H. (1995). Effect of fibers on the punching shear strength of slab-column connections. *Cement and Concrete Composites*, *17*(2), 161–170. https://doi.org/10.1016/0958-9465(94)00031-S

Katlav, M., Turk, K., & Turgut, P. (2022). Research into effect of hybrid steel fibers on the V-shaped RC folded plate thickness. *Structures*, *44*(August), 665–679. https://doi.org/10.1016/j.istruc.2022.08.046

Mobasher, B., & Li, C. Y. (1996). Mechanical properties of hybrid cement-based composites. *ACI Materials Journal*, *93*(3), 284–292. https://doi.org/10.14359/9813

Okamura, H. (1997). Self-Compacting High-Performance Concrete. *Concrete International*, *19*(7).

Ozawa, K., Maekawa, K., Kunishima, M., & Okamura, H. (1989). Development of high performance concrete based on the durability design of concrete structures. *Proceeding of the Second East - Asia and Pacific Conference on Structural Engineering and Construction (EASEC - 2)*, *1*, 445–450.

Rossi, P., Acker, P., & Malier, Y. (1987). Effect of steel fibres at two different stages: The material and the structure. *Materials and Structures*, *20*(6), 436–439. https://doi.org/10.1007/BF02472494

Singh, N. K., & Rai, B. (2021). Assessment of synergetic effect on microscopic and mechanical properties of steel-polypropylene hybrid fiber reinforced concrete. *Structural Concrete*, *22*(1), 516–534. https://doi.org/10.1002/suco.201900166

Topçu, İ. B., Enes Demirel, O., & Uygunoğlu, T. (2017). Polipropilen Lif Katkılı Harçların Fiziksel ve Mekanik Özelikleri. *Journal of Polytechnic*, *20*(1), 91–96.

Turk, K., & Bassurucu, M. (2021). Bond strength of full-scale beams with blended short and long steel fiber. *Pamukkale University Journal of Engineering Sciences*, *27*(3), 274–280. https://doi.org/10.5505/pajes.2020.34846

Turk, K., & Bassurucu, M. (2022). An investigation on the effect of hybrid fiber reinforced on the flexural behavior of RC beams having different lap-spliced lengths. *Structural Concrete*, *January*, 1–13. https://doi.org/10.1002/suco.202200106

Turk, K., Bassurucu, M., & Bitkin, R. E. (2021). Workability, strength and flexural toughness properties of hybrid steel fiber reinforced SCC with high-volume fiber. *Construction and Building Materials*, *266*, 120944. https://doi.org/10.1016/j.conbuildmat.2020.120944

Turk, K., Kina, C., & Oztekin, E. (2020). Effect of macro and micro fiber volume on the flexural performance of hybrid fiber reinforced SCC. *Advances in Concrete Construction*, *10*(3), 257–269. https://doi.org/10.12989/acc.2020.10.3.257

Valcuende, M., Parra, C., & Benlloch, J. (2005). Permeability, porosity and compressive strength of self-compacting concretes. *Mater Construcc*, *55*(280), 17–25.

Yağmur, E. (2020). Elastic Modulus Prediction for Fiber-Reinforced Concretes. *Pamukkale University Journal of Engineering Sciences*, *26*(6), 1098–1109. https://doi.org/10.5505/pajes.2019.34017

Zhou, F. P., Lydon, F. D., & Barr, B. I. G. (1995). Effect of coarse aggregate on elastic modulus and compressive strength of high performance concrete. *Cement and Concrete Research*, *25*(1), 177–186. https://doi.org/10.1016/0008-8846(94)00125-I

GIS Analysis for Topographic Effects of Landfill: A Case Study of Istanbul-Odayeri Landfill

Hüseyin YURTSEVEN[1]
Mehmet Can SARIKAP[2]
Miraç Nur CİNER[3]
Emine ELMASLAR ÖZBAŞ[4]
H. Kurtuluş ÖZCAN[5]
Sinan GÜNEYSU[6]
Atakan ÖNGEN[7]
Serdar AYDIN[8]

INTRODUCTION

A significant amount of municipal solid waste (MSW) is produced globally as a result of modern life. Because it directly affects people, especially those who live in cities, MSW is a significant source of pollution if it is not properly disposed of. MSW is made up of a variety of different material categories. Along with changes in people's consumption habits, the amount of organic materials, plastics, glass, and similar components in solid waste is increasing (Ozcan, 2016). As a result, appropriate MSW disposal has become critical for reasons such as conservation of natural resources, pollution prevention, energy savings, and economic concerns.

In a hierarchical system, waste prevention and reducing waste generation at the source are given the highest priority. The recommended technology application should follow prevention and avoidance principles, with the goal of minimizing negative consequences on energy, the environment, and human health. Furthermore, the technology selected may differ depending on the geographical location of the implementation region (Güvenç, 2016).

The final option in waste management hierarchy is proper MSW disposal. Sanitary landfills receive a major part of solid waste. Because of the economic benefits, the disposal of solid waste in sanitary landfills is the most often utilized approach among various alternative waste disposal methods such as incineration and composting. The process of disposing of solid waste in large, impermeable areas, compacting it, and covering it in order to make a natural biological reactor is known as sanitary landfilling (Tchobanoglous et al, 1993). To qualify as

[1] Assoc. Prof. Dr., Istanbul University-Cerrahpaşa, Surveying and Cadastre Department, Orcıd: 0000-0003-2469-9365
[2] Lec., Istanbul University-Cerrahpaşa, Project and Technology Office, Orcıd: 0000-0002-5044-1184
[3] Res. Asst., Istanbul University-Cerrahpaşa, Environmental Engineering Department, Orcıd: 0000-0002-9920-928X
[4] Assoc. Prof. Dr., Istanbul University-Cerrahpaşa, Environmental Engineering Department, Orcıd: 0000-0001-9065-6684
[5] Prof. Dr., Istanbul University-Cerrahpaşa, Environmental Engineering Department, Orcıd: 0000-0002-9810-3985
[6] Assoc. Prof. Dr., Istanbul University-Cerrahpaşa, Environmental Engineering Department, Orcıd: 0000-0002-4875-101X
[7] Assoc. Prof. Dr., Istanbul University-Cerrahpaşa, Environmental Engineering Department, Orcıd: 0000-0002-9043-7382
[8] Prof. Dr., Istanbul University-Cerrahpaşa, Environmental Engineering Department, Orcıd: 0000-0002-0626-5224

sanitary landfilling, the essential procedures must be followed for the collection, removal, and treatment/utilization of the produced leachate and landfill gas.

The selection of a landfill site is the most important stage in MSW management. The examination of places with the lowest cost and minimal environmental impact is critical in site selection (Kuru et al, 2021). The selection of sanitary landfill sites includes taking into account a number of factors, which may be divided into two categories: non-environmental factors and environmental ones. Non-environmental variables such as present land usage, economic concerns or limits, legal procedures, and so on are examples of non-environmental factors. Environmental factors, on the other hand, include waste type and characterization, permeability of the site soil (geological factors), depth of the groundwater table from the soil surface (hydrological factors), and meteorological factors such as annual precipitation (Beskese et al, 2015). Considerations are given to factors such as the impact on air transportation safety, distance to specially protected areas with specific purposes such as forest areas, afforestation areas, wildlife and vegetation conservation, the condition of groundwater and surface water sources, as well as their protection zones, groundwater levels, and groundwater flow directions, in the selection of a sanitary landfill site. Topographic, geological, geomorphological, geotechnical, and hydrogeological conditions of the site, risks of flooding, landslides, avalanches, erosion, and high seismic activity, prevailing wind direction and precipitation patterns, and the status of natural or cultural heritage are also considered (MEU 2014). To make the most of the volume and space available, there are a number of methods to manage MSW within the landfill area. These methods vary depending on the topography (presence of slopes, bumps or hole) of the landfill site, the characteristics of the soil, the kind of soil cover used to cover the waste, the equipment available for landfilling operations, and the operational characteristics differs to the landfill site.

The purpose of this study is to examine how the Odayeri landfill site and its surroundings, where Istanbul's MSW is stored, have changed spatially over time using GIS-enabled satellite images.

MATERİALS AND METHODS

Study Area

Istanbul is a city located between the continents of Europe and Asia, between the longitudes of 28^{o} 10' and 29^{o} 55' East and the latitudes of 41^{o} 33' and 40^{o} 28' North. The city is bounded in Europe by Çatalca and in Asia by Kocaeli, with the Marmara Sea and Bursa to the south, Tekirdağ to the southwest, and Kırklareli to the northwest. Istanbul is Turkey's most populated metropolis, with a population of over 16 million people living on an area of approximately 5.750 km^2 (TURKSTAT 2022).

Istanbul and its surroundings are made up of the Thrace and Kocaeli plateaus. The sea surrounds these plateaus from the north and south, and the Istanbul Strait separates them. While Istanbul and its surrounding areas do not have a single dominating regional climatic type, there are numerous climate types that differ from one another due to differences in terrain, elevation, relative position, aspect, and flora. Istanbul's climate is unique in that it is affected by both the Black Sea and the continental climate of the Balkans and Anatolia. Marmara climate prevails throughout the city. Except for the Black Sea shore, this climatic type affects the whole Marmara area. In July, the average temperature is between 23°C and 24°C. The average temperature in January, the coldest month, is around 3-5°C. There are no significant

temperature changes in Istanbul between summer and winter, or between day and night. The most rain falls throughout the winter. The yearly precipitation averages 500 mm to 700 mm, with snowfall being typical. When compared to the Mediterranean climate, freezing occurrences are more often (Apak and Ubay, 2007).

Maquis is the most frequent plant species found in Istanbul's area. These plants have adapted to a hot, dry summer. The slopes, however, are not naked due to features of the climate. The Belgrade Forest, located 20 kilometers north of the city, is the most substantial forested region visible in certain areas. The Belgrade Forest is home to several diverse species, the most common of which are oak trees (Yaltırık, 1966).

In Istanbul province, there are no significant rivers. The Riva River is the major river and the main source of water on the Kocaeli Peninsula. The two most important streams that pour into the Bosphorus are the Küçüksu and Göksu. Other significant rivers that run into the Golden Horn are the Kağıthane and Alibey streams, Sazlıdere stream, which flows into Küçükçekmece Lake, Karasu stream, which flows into Büyükçekmece Lake, and Trança stream, which flows into Terkos Lake. These are Istanbul's major waterways. The province has three small but significant lakes, all of which are located on the European side. Terkos Lake, which is separated from the sea, has freshwater. The Terkos basin is an important supply of water for the city. Because of its proximity to the Marmara Sea, Küçükçekmece Lake (11 km^2) and Büyükçekmece Lake (16 km^2) contain saltwater.

Landfill Site

Landfilling is the last option for disposing of MSW. Like in many major cities, solid waste management has been a major priority for Istanbul's authorities.

Since 1995, MSW from Istanbul's European side has been stored in the Odayeri Landfill Site. The 125-hectare dispose of site is located in a gently sloping valley and is covered with layers of clay, sand, gravel, and coal in certain areas (Akkaya et al., 2011). The Odayeri Sanitary Landfill Site, which opened in 1995, is located near Kemerburgaz (Figure 1). The landfill site no longer accepts organic waste as of January 1, 2018. MSW on the European side of Istanbul’s has been placed in the Odayeri Sanitary Landfill for the past 23 years. According to the Turkish Statistical Institute's Environmental Status Report issued in 2020, the average daily MSW amount per capita is 1.13 kg (TURKSTAT 2020).

Currently, MSW that does not include organic substance is being placed in Class II landfill areas. The average daily waste volume in the Odayeri sanitary landfill is 11154 tons (Korkutan et al., 2018).

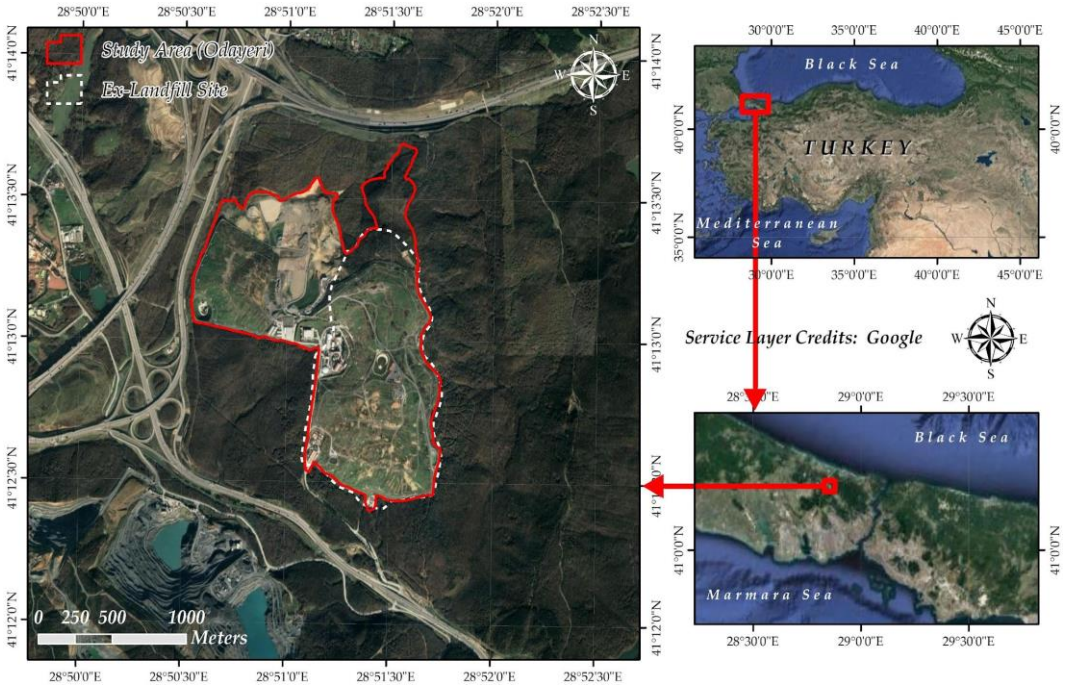

Figure 1. Location of Odayeri Landfill Site

MSW, which do not have a uniform property, are classified into three types. The first group includes organic components that can be separated, such as food waste, fruit and vegetable waste, and garden waste (grass, leaves, and so on); the second group includes flammable materials that decompose slowly or cannot decompose, such as paper, cardboard, textiles, plastics, and other synthetics; and the third group includes inert components, such as stone, sand, glass, and metals. The variety and quantity of MSW increase as the population of the community grows. The changes in Istanbul's MSW composition throughout time are shown in Table 1. Improvements in living conditions, scientific and technological advancements, and the development of modern packing materials all have a significant influence on both the volume of MSW produced per person and the composition of the MSW. This trend may also be seen in Table 1's changing MSW composition over time.

Tablo 1. Changes in the composition of Istanbul's MSW throughout time

Parameter	CH2M Hill, (1992) (%weight)	Arıkan, (1996) (%weight)	Özkaya, (2004) (%weight)	Yıldız et al, (2013) (%weight)
Ash	15	13,2	9	0,63
Organic Matter	45	48	44	54,09
Paper	14,5	8,4	8	15,57
Plastic	9,5	11	5	2,62
Glass	3,8	4,6	6	3,03
Textile	5,6	2,9	5	3,42
Metal	2,2	2,3	6	1,12
Other substances	4,4	6,3	9	2,03
Diaper	-	3,2	8	5,45

GIS Analysis of Landfill Site

The current part of the study looked at the impact of MSW storage activities on the surrounding surface and environment in the organized landfill region of Odayeri. Assessments

were performed for this purpose based on data accessible since the site's inception in 1995. In this context, spatial changes on orthophoto data (Table 2) and satellite images for the years 1996, 2002, 2005, 2010, 2013, 2014, 2017, 2018, 2021 and 2022 were made through the Geographic Information System (GIS).

Table 2. Imagery Data

Year	Data
1996	Orthophoto
2002	Hi-Resolution Satellite Imagery
2005	Hi-Resolution Satellite Imagery
2010	Hi-Resolution Satellite Imagery
2013	Orthophoto
2014	Hi-Resolution Satellite Imagery
2017	Hi-Resolution Satellite Imagery
2018	Hi-Resolution Satellite Imagery
2021	Hi-Resolution Satellite Imagery
2022	Hi-Resolution Satellite Imagery

The data on plant types provided by the General Directorate of Forestry in 2003 were utilized at the stage of identifying changes in land use caused by spatial changes. When these statistics are examined, it is discovered that places within the existing limits of the Odayeri Landfill Site consist of stone pine stands, mixed broadleaf (mainly oak) stands, oak-hornbeam mixed stands, glades, open-pit mines, and lakes.

Evaluations were carried out utilizing digital elevation models (DEM) to identify the fillings carried out in the region. Digital elevation models (DEMs) are recognized as crucial data sources for environmental modeling (Hutchinson et al., 2011; Wilson and Fotheringham, 2008). In this study, we utilized DEMs generated from two specific sources. The Shuttle Radar Topography Mission (SRTM) DEM is the first source. The photogrammetrically produced National Topographic DEM is the second source.

The National Aeronautics and Space Administration (NASA), the National Geospatial-Intelligence Agency (NGA) of the United States Department of Defense (DOD), the German Aerospace Center (DLR), and the Italian Space Agency (ASI) collaborated on the Shuttle Radar Topography Mission (SRTM) in 2000. It is worth noting that the SRTM data only includes topographic information from the year 2000. Until 2015, the highest resolution SRTM data was confined to the area of the United States. However, on September 23, 2014, the US government stated its intention to make the highest resolution SRTM data (1 arc second, or 30 meters) available globally by late 2015 (JPL NASA, 2014). As a result, SRTM data with a resolution of 1 arc second, or about 30 meters, was used for this investigation.

Topographic Digital Elevation Models (Topo-DEMs) with a 5-meter grid interval are produced nationally by the General Directorate of Mapping (GDM), which serves as the National Mapping Agency of Turkey. These Topo-DEMs are generated using automatic matching techniques and rely on 30-centimeter resolution stereo aerial photographs. They provide comprehensive coverage of the terrain, capturing intricate details such as human-made structures and vegetation. The Topo-DEM was produced in the year 2013 (GDM, 2023). Thus, the aim was to calculate the topographic changes and volumetric differences between the years 2000 (SRTM-DEM) and 2013 (Topo-DEM). All processing and analysis of the entire dataset were performed using the ArcGIS Desktop 10.8 GIS software (ArcGIS Desktop, 2023).

RESULTS

In the methods of creating orthophoto data from various sources, high-resolution satellite imagery, DEM data, and vector forest stand data spatially assessable in geographic information system (GIS) databases were carried out within the scope of the study. In this context, coordinate transformations were used to collect data from various sources into a single database, and coordinate and projection transformations were performed using the World Geodetic System 1984 (WGS84) and Universal Transverse Mercator (UTM) Zone 35 North (EPSG: 32635).

The major goal after compiling the data was to determine spatial changes in the Odayeri Landfill Site by digitizing the boundaries of each year using the appropriate photographs. Following that, the boundary data for each year were analyzed in conjunction with the forest stand data to discover changes in land use cover. Since it was available, the General Directorate of Forestry's oldest available forest stand data from 2003 was used at this stage. These data were utilized in the overlay analysis to determine changes in land use cover. These figures are based on forest inventory data collected using photogrammetric and ground surveys. Because there was no digital (vector) data accessible prior to 2003, an assessment was carried out using the oldest known aerial photograph from 1970. As shown in Figure 2, the evaluation found that there was no activity on the site at the time.

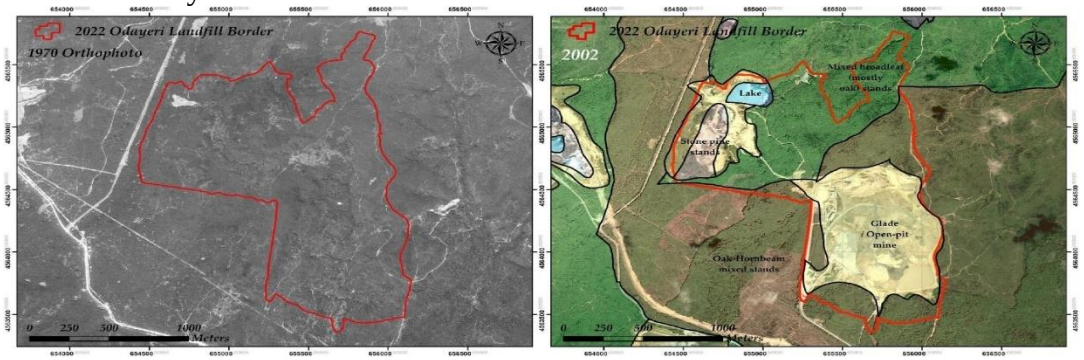

Figure 2. Condition of Odayeri Landfill in 1970 (Left), Stand Types Data (Right)

As previously stated, the Odayeri Landfill Site began operations in 1995. Spatial extents from 1996 to the present have been established using photos from the developed database. The results of the overlay analysis with forest stand data are shown in Figure 3, Figure 4, and Table 3.

Table 3. Land cover changes throughout time

	1996	**2002**	**2005**	**2010**	**2013**	**2014**	**2017**	**2018**	**2021**	**2022**
Stone pine stands	0	0.357	0.357	0.357	0.357	3.687	10.452	10.452	10.452	10.452
Mixed broadleaf (mostly oak) stands	0	0.825	4.183	6.206	7.302	19.270	25.656	34.725	50.399	62.048
Oak-Hornbeam mixed stands	0.035	2.197	9.176	40.294	42.301	43.093	43.390	43.390	47.591	47.751
Glade / Open-pit mine	30.627	73.719	75.186	76.505	76.505	78.553	91.563	91.697	91.697	91.697
Lake	0	0	0	0	0	0	4.383	4.385	4.385	4.385
Total Area (ha)	30.662	77.098	88.903	123.362	126.464	144.602	175.444	184.649	204.523	216.332

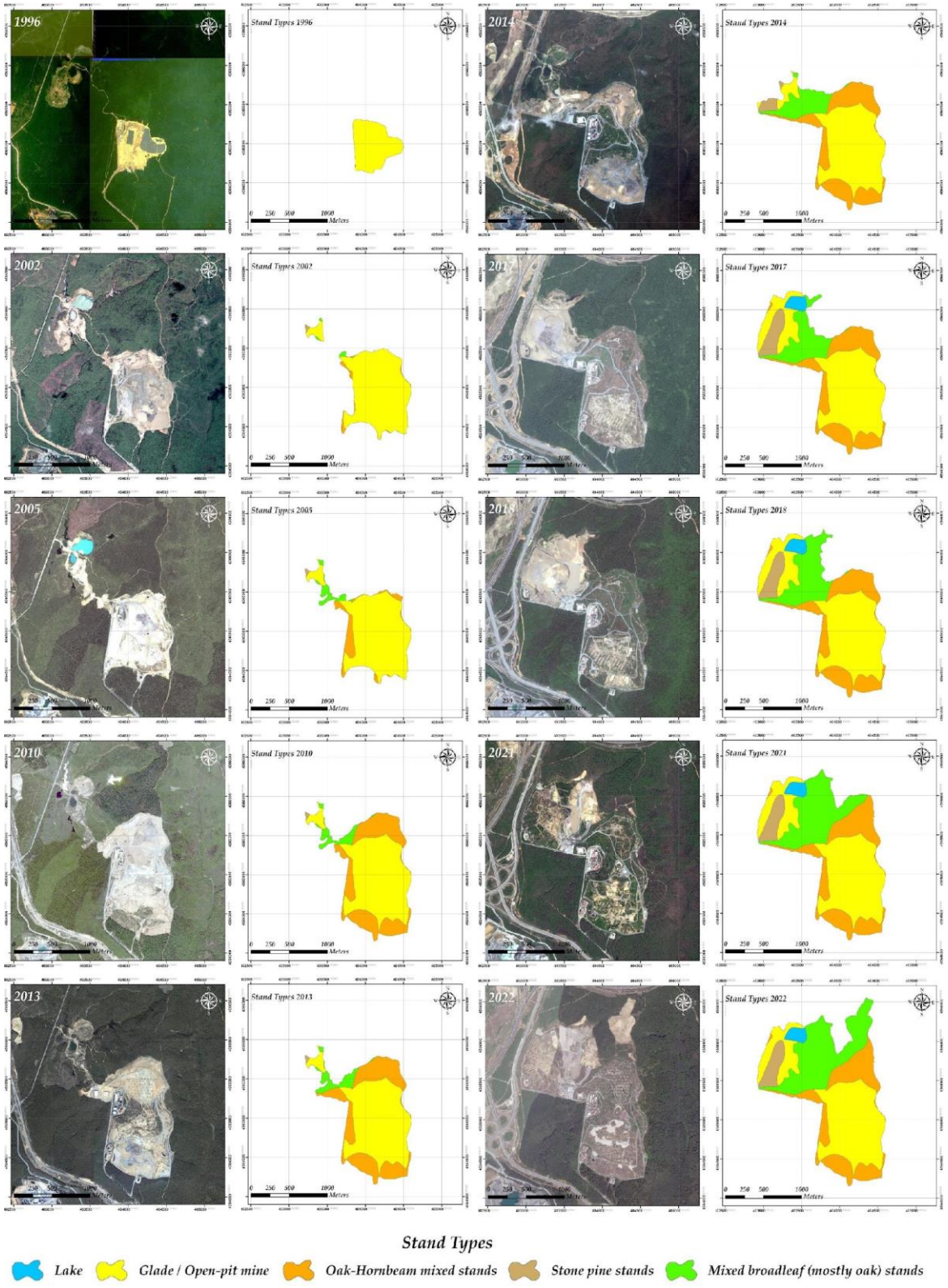

Figure 3. Situation of Odayeri Landfill in 1996, 2002, 2005, 2010, 2013, 2014, 2017, 2018, 2021 and 2022 and the stands it cover.

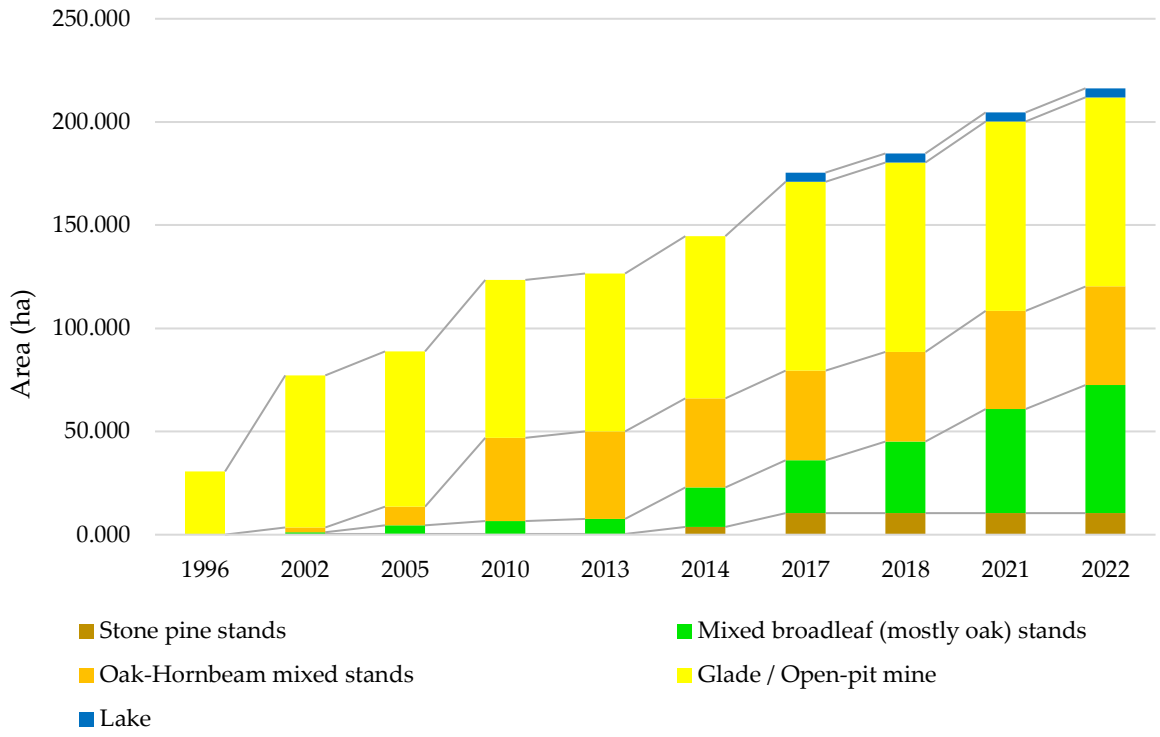

Figure 4. Temporal changes in land cover

Storage activities were carried out in an area of roughly 30 hectares in the Odayeri Landfill Site during the first year after its formation in 1995 until 1996. A linear trend has been detected when assessing spatial variations over time (Figure 5). Within this framework, it has been determined that forest areas provide spatial improvements based on needs.

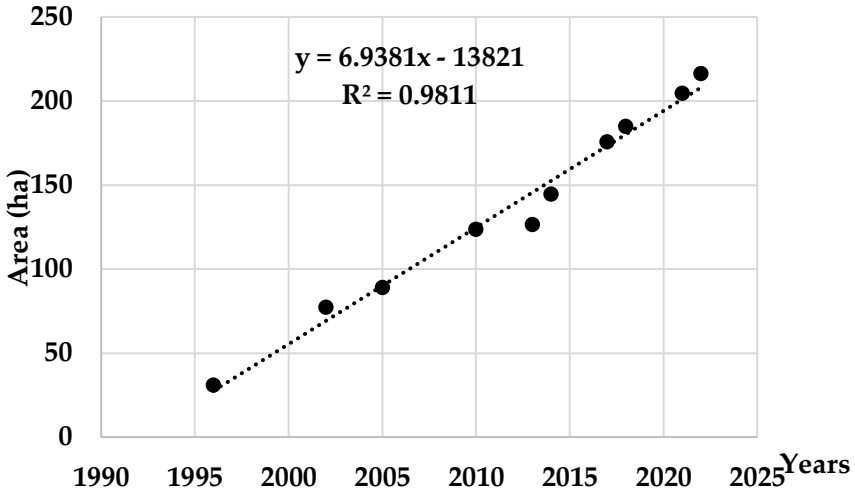

Figure 5. Total area change trend

Another study conducted in the study area focuses on determining the topographic changes. In this stage, the 2000 SRTM-DEM and 2013 Topo-DEM (Turkish GDM-DEM) data were used. The aim was to identify the topographic changes in the area that were closed off for storage by reaching the storage threshold boundary in the southern part of the study area (Figure 1. Ex-Landfill Area). In line with this objective, the changes occurring in the three-dimensional aspect were initially identified. By subtracting one terrain model from the other in a GIS environment, a Difference Surface Model was obtained. The analysis revealed differences of

up to 65 meters between the two terrain models. Additionally, excavations of up to 12 meters were identified within this area (Figure 6). At this stage, it was determined that the removal of trees from the area during soil preparation in the forest area was the cause of this difference.

DEM data was used to assess the volumetric changes occurring in the landfill site. A total storage volume of roughly 24 million cubic meters was accomplished within the closed-off storage region, which has a breadth of around 120 hectares, according to analyses conducted in a GIS environment. Volumetric losses were recorded at this stage in locations where excavation occurred or where the forest cover was removed due to the aforementioned topographical adjustments in the landfill site (Figure 6) (Table 4).

Table 4. Volumetric difference in landfill area

	Volume (m^3)	Area (m^2)
Net Gain	-24,397,192.4	1,073,433.0
Unchanged	0.0	0.0
Net Loss	449,709.6	151,631.8
Total	-23,947,482.8	1,225,064.8

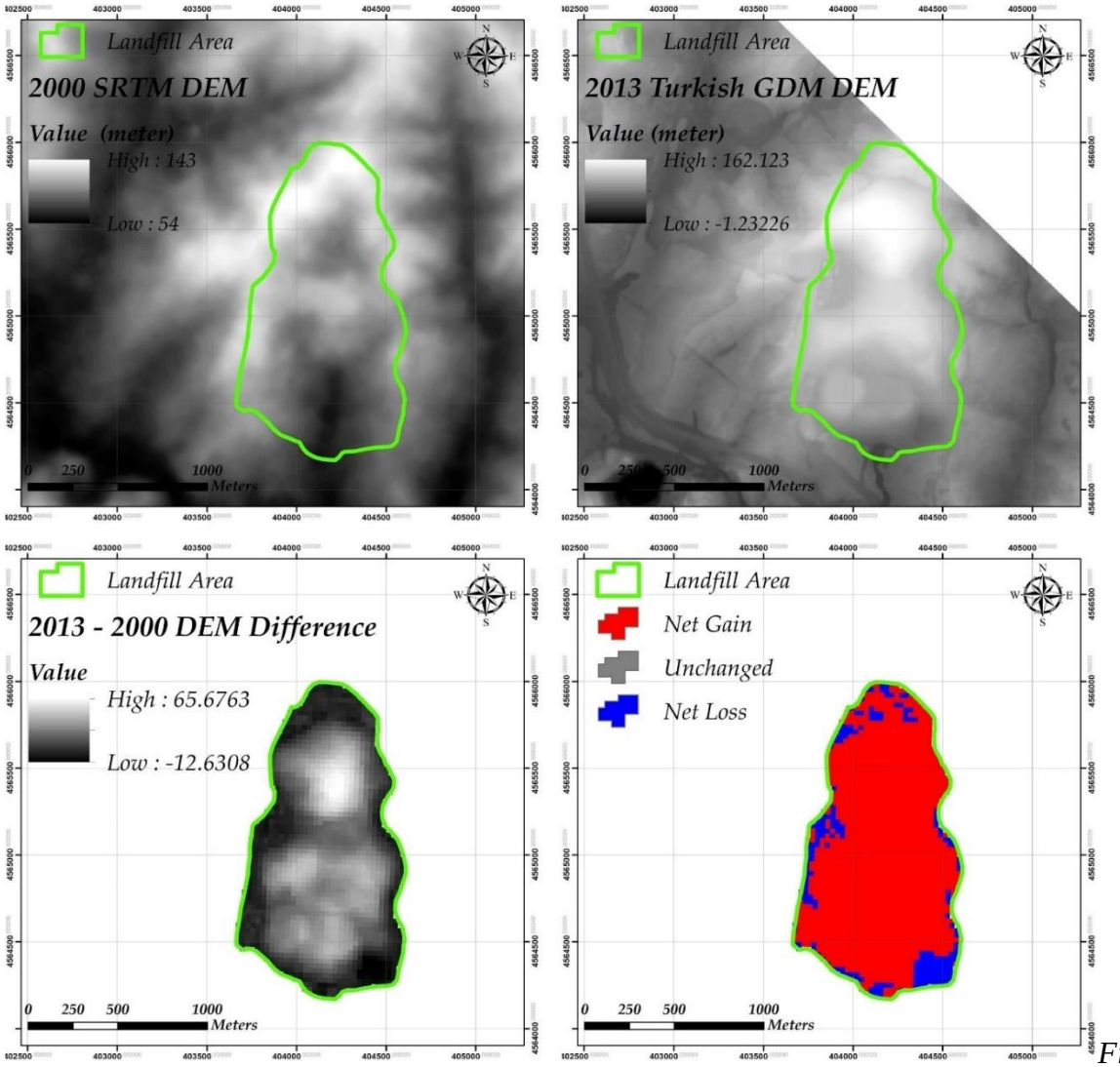

Figure 6. 2000 SRTM-DEM, 2013 Topo-DEM (Turkish GDM-DEM), 2013-2000 DEM Difference Map, 2013-2000 Cut-Fill Map

CONCLUSİONS

The final stage in the management of MSW, known as landfilling, ensures the minimization of environmental impacts caused by MSW. Sanitary landfilling is an integral part of every waste management system. Due to the fact that processes such as biological treatment and incineration themselves generate waste by-products, the disposal of a certain amount of waste in a sanitary landfill sites is always necessary in all cases. Due to its economic advantages; landfilling, also known as "sanitary landfilling," is frequently preferred for the disposal of MSW. Sanitary landfilling is the most widely used MSW disposal method globally due to its low cost of disposal and operational convenience.

The storage of MSW in sanitary landfills is a long-term activity. Landfill areas are typically designed to provide service for an average of 25 years. Therefore, during the waste disposal process, certain changes occur in the topography and vegetation of the landfill area and its surrounding environment. It is crucial to have a good understanding of the land conditions and land use in the areas where landfill sites are established. Agricultural land classifications and the current land use of the area play a significant role in site selection. In this study, the aim was to determine the topographic changes caused by MSW disposal activities in the Odayeri Sanitary Landfill Site located in Istanbul, Turkey.

According to the findings of the study, it was determined that storage was conducted in an area of approximately 120 ha. When examining the spatial changes over the years, a linear change is observed. During the storage period, it was observed that there were spatial gains from forest areas, depending on the needs. To determine the topographic changes in the area, changes occurring in the third dimension were identified. Based on the results obtained from the Difference Surface Model, variations of up to 65 m were found between the two land models. Additionally, it was determined that excavations of up to 12 m, believed to be due to surface leveling during the preparation stage of the landfill area, were carried out within this region (Figure 6).

The construction and operation technology implemented in a modern sanitary landfill site ensures the protection of public health and the environment. In this respect, important considerations include the appropriate design of the landfill site and the effective implementation of post-closure monitoring. These measures are essential to guarantee the long-term effectiveness and safety of the landfill, as well as to minimize potential risks to the surrounding environment and public health. The re-vegetation of closed sanitary landfill sites is carried out with the aim of adapting the surrounding environment to the site, ensuring public acceptance, and minimizing erosion on slopes. Additionally, the utilization of closed landfill areas for purposes such as parks, golf courses, or grass skiing areas is also common. Therefore, it is expected that the changes in land use structure occurring during the operation of sanitary landfill site will not be permanent.

REFERENCES

Akkaya, E., Demir, A., & Varank, G. (2011). Characterisation of Odayeri Sanitary Landfill Leachate. *Sigma, 3*, 238-251.

Apak, G., & Ubay, B. (2007). Türkiye iklim değişikliği birinci ulusal bildirimi. *Republic of Turkey Ministry of Environment and Forestry*. Ankara, Turkey. *(In Turkish)*

ArcGIS Desktop, (2023). Date of access: 02.05.2023, Available: http://desktop.arcgis.com/

Arikan, O.A. (1996). *İstanbul katı atıklarının karakterizasyonu ve havasız kompostlaşabilirliği üzerine bir çalışma*, Yüksek Lisans Tezi, İstanbul Teknik Üniversitesi / Fen Bilimleri Enstitüsü, Istanbul. *(In Turkish)*

Beskese, A., Demir, H.H., Ozcan, H.K., & Okten, H.E. (2015). Landfill site selection using fuzzy AHP and fuzzy TOPSIS: a case study for Istanbul, *Environmental Earth Science*, *73*, 3513-3521.Doi: 10.1007/s12665-014-3635-5

CH2M Hill International Ltd.-Antel Arıtma A.Ş. (1992). İstanbul anakenti katı atık yönetimi etüdü projesi raporu. İstanbul/ Turkey. *(In Turkish)*

GDM (General Directorate of Mapping), (2023). Date of access: 02.05.2023, Available: https://www.harita.gov.tr.

Güvenç, L. (2016). *Kartal belediyesi sınırları içerisinde oluşan ambalaj atıklarının belirlenmesi ve ekonomik analizi*, Yüksek Lisans Tezi. İstanbul Üniversitesi Fen Bilimleri Enstitüsü, İstanbul. *(In Turkish)*

Hutchinson, M. F., Xu, T. & Stein, J. A. (2011). Recent progress in the ANUDEM elevation gridding procedure. *Geomorphometry*, 19-22.

Korkutan, M., Doğru, A. Ö., & Göksel, C. (2018). Impact analysis of sanitary landfill based odour in Istanbul using GIS. *International Journal of Environment and Geoinformatics*, *5*(2), 169-177. Doi: https://doi.org/10.30897/ijegeo.421545

Kuru, A., Tok, E., Agdas, G.M., Demir, H.H., Ozcan, H.K., & Demir, G. (2021). GIS and multicriteria decision analysis for landfill site selection in Edirne Province, Turkey. *Journal of the Institute of Science and Technology, 11*(2): 969-981. Doi: 10.21597/jist.792249

MEU (Republic of Turkey Ministry of Environment and Urbanisation), (2014). Düzenli depolama tesisleri saha yönetimi ve işletme kılavuzu. Ankara, Turkey. *(In Turkish)*

Ozcan, H. K., Guvenc, S. Y., Guvenc, L., & Demir, G. (2016). Municipal solid waste characterization according to different income levels: A case study. *Sustainability*, *8*(10), 1044. Doi: 10.3390/su8101044

Özkaya, B. (2004). *Katı atık depo sahalarında sızıntı suyu geri devrinin atıkların ayrışması ve sızıntı suyu üzerindeki etkilerinin incelenmesi*, Doktora Tezi, Yıldız Teknik Üniversitesi Fen Bilimleri Enstitüsü, Istanbul. *(In Turkish)*

Tchobanoglous, G., Theisen, H., & Vigil, S. (1993). *Integrated solid waste management-engineering principles and management issues*. McGraw-Hill, Inc. ISNB 0070632375.

TURKSTAT (Turkish Statistical Institute), (2020). Atık istatistikleri. Newsletter; Number: 37198. Ankara, Turkey. *(In Turkish)*

TURKSTAT (Turkish Statistical Institute), (2022). Adrese dayalı nüfus kayıt sistemi sonuçları. Ankara, Turkey. *(In Turkish)*

Wilson, J. P., & Fotheringham, A. S. (Eds.). (2008). *The handbook of geographic information science*. Blackwell Pub.

Yaltırak., F. (1966). Belgrad Ormanı vejetasyonunun floristik analizi ve ana mescere tiplerinin kompozisyonu üzerinde arastırmalar. *General Directorate of Forestry Publication*. *(In Turkish)*

Yildiz, S., Yaman, C., Demir, G., Ozcan, H. K., Coban, A., Okten, H. E., Sezer, K., & Goren, S. (2013). Characterization of municipal solid waste in Istanbul, Turkey. *Environmental Progress Sustainable Energy, 32*(3), 734-739. Doi: https://doi.org/10.1002/ep.11640

Comparison of K-means and Fuzzy C-means Clustering Algorithms on Water Quality Parameters: Case Study of Ergene Basin for 17 Stations

Gülay ARSLAN ÇENE[1]
Coşkun PARİM[2]
Erhan ÇENE[3]

Introduction

Surface water quality plays a critical role in safeguarding human health and ecological systems, particularly in urban areas where rivers and tributaries pass through industrial, domestic/sewage, and agricultural areas, posing significant challenges (Qadir et al., 2008). The deterioration of surface water quality is influenced by various anthropogenic factors, such as urbanization, industrial and agricultural practices, chemical spills, dam construction, as well as natural processes like erosion and climatic conditions. These factors contribute to the presence of macro pollutants and micropollutants, which include complex organic compounds and nutrients, leading to environmental consequences such as oxygen depletion and algal blooms in aquatic ecosystems (Emadian et al., 2020).

To effectively control and manage water pollution, it is necessary to evaluate multiple limnological parameters in streams and rivers, as they are particularly vulnerable to pollution (Singh et al., 2005 and Köse et al., 2014). However, accurately determining the specific contribution of each factor to water quality remains uncertain, highlighting the need to reduce this uncertainty by examining temporal and spatial variations in water quality and identifying hidden sources of pollution (Zhang Y et al., 2009). This knowledge is crucial for guiding decision-making processes and prioritizing actions aimed at improving water quality (Wang et al., 2008; Zhang Q et al., 2009).

Previous research has shown that deterministic water quality models based on simulations often yield inaccurate results, as they fail to capture the intricate nature of water quality influenced by multiple factors and struggle to address imperfections and uncertainties in the underlying data. In contrast, multivariate statistical methods have frequently been utilized in the existing literature to assess surface water quality, offering a more comprehensive approach (Orak et al., 2020; İşçen et al., 2009; Bilgin and Konanç, 2016).

In 1988, the Water Pollution Control Regulation was published, establishing a framework for comprehensive water quality management. This regulation implemented a classification system for surface waters, dividing them into four classes based on their quality levels. The classification system aims to assess and monitor the pollution status of surface waters. The four classes are defined as follows: (Akın and Akın 2007)

Class I: High Quality Water: This class represents surface waters with excellent water quality, indicating minimal pollution and high ecological integrity. Class I waters are considered pristine and suitable for various purposes, including drinking water supply and conservation of aquatic ecosystems.

[1]Research Assistant, Marmara University, Departmant of Environmental Engineering, Orcıd: 0000-0003-1983-266X
[2]Research Assistant PhD., Yildiz Technical University, Departmant of Statistics, Orcıd: 0000-0002-6412-1325
[3] Assistant Professor, Yildiz Technical University, Departmant of Statistics, Orcıd: 0000-0001-5336-6004

Class II: Slightly Polluted Water: Class II waters indicate a slightly higher level of pollution compared to Class I. Although they may exhibit slight impairments in water quality, they are still relatively clean and suitable for most water uses, including recreational activities and irrigation.

Class III: Polluted Water: Class III waters denote a higher degree of pollution compared to the previous classes. These waters may exhibit noticeable impairments in quality, potentially resulting from various pollution sources such as industrial discharges or agricultural runoff. Special attention and management practices are required to mitigate pollution in Class III waters.

Class IV: Highly Polluted Water: Class IV represents surface waters with a significantly high level of pollution. These waters exhibit severe impairments in quality and may pose risks to both human health and the environment. Class IV waters typically require intensive pollution control measures and restoration efforts to improve their quality.

The Ergene River, situated in the European part of Turkey, serves as a crucial water source for 1.7 million people in the region, catering to recreational, industrial, and agricultural needs. However, due to intense industrial and agricultural activities and inadequate regulations regarding wastewater discharge quality in Turkey, the Ergene River has become one of the most polluted rivers in both Turkey and Europe. Moreover, as the Ergene River converges with the Maritsa River, an international transboundary river that flows into the Aegean Sea, the water quality of the Ergene River carries international significance. Currently, macro pollutant levels in the Ergene River are regularly monitored. This study aims to assess the status of macro pollutants in the Ergene River, examine the impact of seasonal variations on macro pollutant concentrations, and evaluate the compliance of macro pollutant levels with surface water quality standards established by the European Union and Turkey. The study is based on a dataset comprising 15 water-related variables from 17 water stations within the period of 1985-2013.

This study aims to employ k-means and fuzzy c-means cluster analysis on water stations on the Ergene basin and compare the results with the water quality classification of Water Pollution Control Regulation.

Methodology

Mean and standard deviation, for each parameter among each station is reported (Table 2). To reveal the similarities and differences among water stations k-means cluster analysis and fuzzy c-means cluster analysis are employed (Landau, Leese, Stahl, & Everitt, 2011). In addition, multidimensional scaling maps the variables on a two-dimensional coordinate system according to their similarities and differences (Kruskal, 1964) and can be used to support CA (Kruskal, 1977). MDS and CA are employed to visualize the performance metrics of water quality indicators and how they spread through a two-dimensional space. Two MDS maps are used in this study, one for k-means cluster analysis results and one for fuzzy c-means cluster analysis results. All the statistical analyses are performed with the R programming language (R Core Team, 2022).

k-means cluster analysis

K-means cluster analysis is a widely used method for partitioning data into k clusters based on similarity metrics such as Euclidean distance or cosine similarity (MacQueen, 1967). The algorithm works by iteratively assigning each data point to one of k clusters based on the similarity between the data point and the centroid of each cluster. The centroid of each cluster is calculated as the mean of the data points in that cluster, and the similarity between a data point and a cluster centroid is often measured by the squared Euclidean distance between the two.

The k-means algorithm can be formalized as follows:

1. Initialize k cluster centroids randomly.
2. Assign each data point to the nearest cluster centroid.
3. Recalculate the centroids of each cluster as the average of the data points in that cluster.
4. Repeat steps 2 and 3 until convergence is reached.

The resulting clusters can be used to identify patterns in the data and to gain insights into the relationships between variables. A drawback of k-means is that it can be sensitive to the initial random initialization of the cluster centroids and can converge to suboptimal solutions. Several variants of k-means have been proposed to address this issue (Arthur & Vassilvitskii, 2007).

Fuzzy c-means cluster analysis

Fuzzy c-means (FCM) is a generalization of k-means that allows for overlapping clusters and degrees of membership. In FCM, each data point is assigned a degree of membership in each cluster, rather than being assigned to a single cluster. The algorithm works by iteratively updating the degrees of membership of each data point based on the distance to each cluster centroid and a fuzziness parameter that controls the degree of overlap between clusters. The cluster centroids are then updated based on the weighted average of the data points, where the weights are the degrees of membership.

The FCM algorithm can be formalized as follows:

1. Initialize k cluster centroids randomly.
2. Calculate the degree of membership of each data point to each cluster.
3. Update the cluster centroids based on the weighted average of the data points, where the weights are the degrees of membership.
4. Repeat steps 2 and 3 until convergence is reached.

FCM can handle noisy data and outliers better than k-means and can be used in applications such as image segmentation and pattern recognition (Bezdek et al., 1981).

Multidimensional Scaling

Multidimensional scaling (MDS) is a technique used to visualize the similarities and differences between objects or observations in high-dimensional space. MDS works by reducing the dimensionality of the data while preserving the pairwise distances between the objects. The result is a two- or three-dimensional representation of the data that allows for easy visualization and interpretation.

MDS can be formalized as follows:

Given a dissimilarity matrix D of size n x n, where n is the number of objects, the goal of MDS is to find a set of points X in m-dimensional space (usually m = 2 or 3) such that the pairwise Euclidean distances between the points approximate the dissimilarity matrix D:

$$d_{ij} = \|x_i - x_j\|_2$$

for all $i, j = 1,2, \ldots, n$

The solution to this problem can be obtained by optimizing an objective function such as stress or Kruskal's stress (Kruskal, 1964).

MDS can be used to explore relationships between variables, to identify patterns in the data, and to identify outliers or unusual observations. MDS is a useful technique for exploratory data analysis and can help to generate hypotheses for further investigation.

Data

The Ergene River Basin, located in northwestern Turkey, is an important water resource for the region, providing water for irrigation, drinking, and industrial purposes. The basin covers an area of approximately 10,000 km² and is home to over two million people. However, due to the high level of pollution in the Ergene River, the quality of the water has been deteriorating, leading to serious environmental and health problems. According to a study conducted by Dokmeci, A. H. (2017), the Ergene River is contaminated with heavy metals, organic pollutants, and pathogens, posing a threat to both human health and the ecosystem. Therefore, protecting and restoring the water quality in the Ergene River Basin is crucial for ensuring the sustainable use of this vital resource for the region. Thus, investigating similarities and differences among water stations inside the Ergene Basin has great importance.

The Ergene Basin dataset consists of 15 water related variables from 17 water stations within the period of 1985-2013. The study area is denoted in Figure 1.

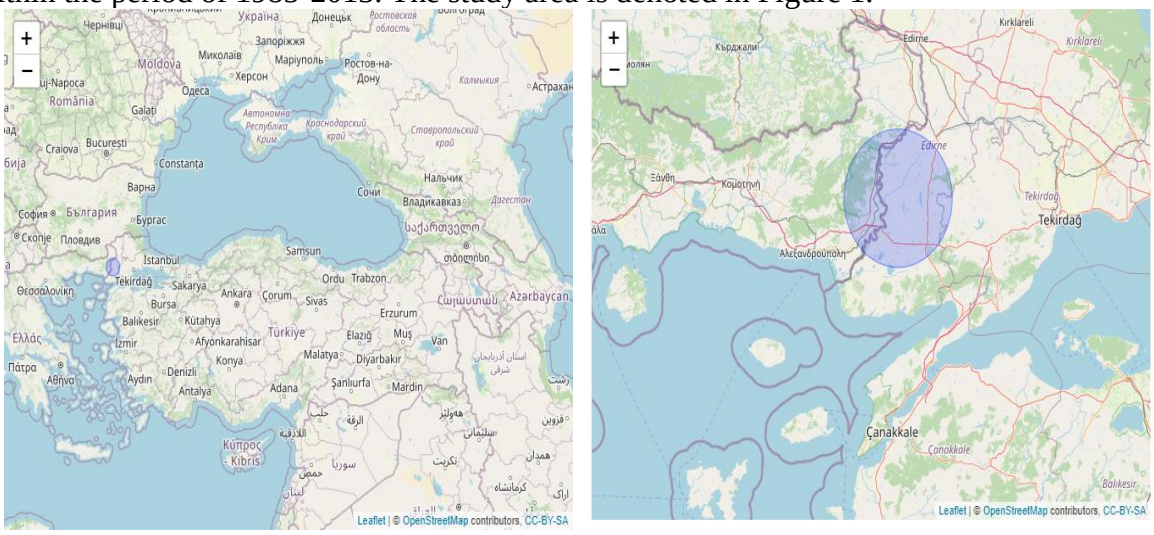

Figure 1: *The study area Ergene Basin, Turkiye*

The water parameters are in yearly format so for each station there are 420 observations and in the entire dataset there are 7140 observations. The list of the stations and variables is given in Table 1.

Table 1. Description of Stations and water quality parameters

Station	Station No	Station Name	Parameter	Description
S1	01-11-00-001	MERIC NEHRI KAPIKULE	**BOD5**	Biochemical oxygen demand
S2	01-11-00-002	TUNCA NEHRI SU AKACAGI	**Cl-**	Chloride
S3	01-11-00-003	ARDA NEHRI ESKI DEMIRYOLU KOPRUSU	**DO**	Dissolved oxygen
S4	01-11-00-008	MERIC NEHRI ESKIKOY	**EC**	Escherichia coli
S5	01-11-00-009	MERIC NEHRI IPSALA	**Al**	Aluminum
S6	01-11-00-013	ERGENE NEHRI CORLU KOPRUSU	**NH4-N**	Ammonium–nitrogen
S7	01-11-00-014	ERGENE NEHRI INANLI	**NO2-N**	Nitrite–nitrogen
S8	01-11-00-015	ERGENE NEHRI LULEBURGAZ	**NO3-N**	Nitrate–nitrogen
S9	01-11-00-016	ERGENE NEHRI ALPULLU	**o-PO4**	Orthophosphate
S10	01-11-00-017	ERGENE NEHRI UZUNKOPRU	**pH**	Potential of Hydrogen
S11	01-11-00-018	SAZLIDERE OLMUK GIRISI	**pV**	Photovoltaics
S12	01-11-00-019	SAZLIDERE OLMUK CIKISI	**SS**	Suspended Solid
S13	01-11-00-022	GALA GOLU CIKISI	**T**	Temperature
S14	01-11-00-023	MERIC NEHRI FERREKUPURU	**TDS**	Total Dissolved Solid
S15	01-11-00-024	MERIC NEHRI EDIRNE CIKISI BOSNA	**Turb**	Turbidity
S16	01-11-00-025	MERIC NEHRI_KARASAZ SU ALMA AGZI		
S17	01-11-01-020	SULOGLU DERESI SULOGLU BARAJI		

Water quality parameters are important measures of the health and safety of water sources, which can be affected by various natural and human-induced factors. Biochemical Oxygen Demand (BOD5) is a measure of the amount of oxygen required by microorganisms to decompose organic matter in water. High BOD5 levels indicate high levels of organic pollution, which can cause a decrease in dissolved oxygen (DO) levels, leading to the death of aquatic organisms. Chloride (Cl-) is an important indicator of salinity in water, which can affect the taste, quality, and suitability of water for different uses. High chloride levels can be harmful to aquatic life and can cause corrosion in pipelines and other infrastructure.

Dissolved oxygen (DO) is a measure of the amount of oxygen present in water and is essential for the survival of aquatic organisms. Low DO levels can lead to the death of fish and other aquatic organisms, as well as contribute to the growth of harmful algal blooms. Escherichia coli (EC) is a bacterium found in the intestines of humans and animals, and its presence in water can indicate fecal contamination, which can pose a significant risk to human health. Aluminum (Al) is a toxic metal that can cause a range of health effects in humans and aquatic organisms, including neurological damage and respiratory problems.

Ammonium-nitrogen (NH4-N), Nitrite-nitrogen (NO2-N), Nitrate-nitrogen (NO3-N), and Orthophosphate (o-PO4) are important indicators of nutrient pollution in water, which can lead to the growth of harmful algae and other aquatic plants, deplete dissolved oxygen, and cause fish kills. The potential of Hydrogen (pH) is a measure of the acidity or basicity of water, which can affect the solubility and toxicity of different substances in water. Photovoltaics (pV) is a measure of the light intensity in water, which can affect the growth and reproduction of aquatic organisms. Suspended solids (SS) and Turbidity (Turb) are measures of the amount of particulate matter in water, which can affect the clarity, taste, and quality of water, as well as affect aquatic habitats.

Water quality parameters are essential tools for monitoring and managing the health and safety of water sources. Understanding the effects of different water quality parameters, such as BOD5, Cl-, DO, EC, Al, NH4-N, NO2-N, NO3-N, o-PO4, pH, pV, SS, and Turb, can help identify potential water quality issues and implement appropriate management strategies to protect and improve water quality.

The averages and standard deviations of water quality parameters for each observation point (station) are given in Table 2. Among stations, the average BOD5 values varies from 2.38 to 77.91, the average CL- values varies from 17.16 to 727.98, the average DO values varies from 2.94 to 10.29, the average EC values varies from 332.28 to 4455.74, the average Al values varies from 107.05 to 865.92, the average NH4-N values varies from 0.13 to 15.37, the average NO2-N values varies from 0.01 to 0.37, the average NO3-N values varies from 0.37 to 3.88, the average O-PO4 values varies from 0.1 to 8.83, the average pH values varies from 7.29 to 8.43, the average pV values varies from 2.06 to 56.4, the average SS values varies from 29.52 to 301.57, the average T values varies 15.03 to 17.97, the average TDS values varies from 245.94 to 2523.93, and the average Turb values varies from 24.86 to 449.87.

Table 2. Averages and standard deviations of water quality parameters in observation points.

Station	BOD_5	Cl^-	DO	EC	Al
S1: 01-11-00-001	4.32 (1.79)	25.70 (8.66)	9.59 (1.38)	600.21 (97.93)	165.50 (21.32)
S2: 01-11-00-002	4.49 (2.04)	51.61 (16.63)	10.29 (1.64)	837.85 (602.03)	241.62 (27.09)
S3: 01-11-00-003	2.38 (1.76)	17.16 (6.73)	10.09 (1.47)	332.28 (38.44)	107.05 (14.70)
S4: 01-11-00-008	4.34 (1.33)	27.62 (5.83)	9.35 (1.34)	539.67 (64.47)	156.21 (21.68)
S5: 01-11-00-009	5.67 (2.50)	55.50 (18.08)	9.82 (1.74)	660.12 (106.33)	181.50 (37.06)
S6: 01-11-00-013	8.54 (7.81)	78.08 (26.38)	8.52 (2.46)	715.39 (164.04)	187.65 (32.34)
S7: 01-11-00-014	55.31 (34.94)	618.58 (376.46)	3.52 (2.46)	3062.97(1515.61)	469.79 (145.59)
S8: 01-11-00-015	54.97 (35.29)	475.56 (252.23)	2.94 (2.41)	4455.74 (9590.90)	490.94 (146.38)
S9: 01-11-00-016	54.08 (29.35)	424.75 (232.64)	3.22 (2.24)	2394.71 (1023.98)	485.64 (121.30)
S10: 01-11-00-017	32.39 (18.27)	295.92 (174.23)	3.82 (2.06)	1848.89 (829.60)	865.92 (2563.77)
S11: 01-11-00-018	5.43 (4.59)	166.39 (433.84)	8.18 (1.90)	833.84 (92.97)	285.90 (26.93)

S12: 01-11-00-019	77.91 (79.68)	82.61 (8.28)	3.38 (1.34)	1081.50 (149.18)	432.81 (123.28)
S13: 01-11-00-022	5.70 (2.59)	727.98 (922.49)	9.12 (1.34)	3857.04 (6736.50)	245.98 (64.29)
S14: 01-11-00-023	5.45 (1.48)	238.14 (568.08)	9.65 (1.57)	1083.25 (1203.49)	180.06 (29.61)
S15: 01-11-00-024	4.81 (1.25)	31.57 (8.03)	9.75 (1.30)	1085.36 (2676.61)	172.44 (18.22)
S16: 01-11-00-025	9.85 (6.11)	113.02 (48.51)	8.26 (1.61)	954.58 (246.75)	239.10 (59.13)
S17: 01-11-01-020	3.57 (1.92)	30.71 (6.70)	10.09 (1.63)	597.72 (1177.50)	132.85 (71.19)
Station	**NH_4-N**	**NO_2-N**	**NO_3-N**	**O-PO_4**	**pH**
S1: 01-11-00-001	1.00 (1.25)	0.02 (0.02)	2.83 (1.98)	1.35 (0.88)	7.92 (0.28)
S2: 01-11-00-002	0.68 (0.57)	0.04 (0.05)	2.11 (1.15)	1.55 (1.11)	8.17 (0.26)
S3: 01-11-00-003	0.13 (0.10)	0.01 (0.01)	0.94 (0.94)	0.13 (0.10)	8.01 (0.24)
S4: 01-11-00-008	0.50 (0.45)	0.01 (0.02)	1.80 (1.04)	1.06 (0.68)	7.90 (0.25)
S5: 01-11-00-009	0.80 (0.27)	0.03 (0.08)	1.52 (0.90)	0.97 (0.40)	7.93 (0.24)
S6: 01-11-00-013	1.19 (1.14)	0.09 (0.23)	1.98 (2.05)	2.34 (1.59)	7.72 (0.24)
S7: 01-11-00-014	15.37 (11.65)	0.04 (0.05)	0.46 (0.41)	8.83 (21.09)	7.71 (0.20)
S8: 01-11-00-015	10.78 (5.46)	0.04 (0.03)	0.73 (1.35)	4.67 (1.98)	7.80 (0.22)
S9: 01-11-00-016	10.93 (4.81)	0.08 (0.16)	0.57 (0.50)	4.26 (1.94)	7.76 (0.35)
S10: 01-11-00-017	7.23 (4.18)	0.34 (1.61)	1.16 (2.14)	3.31 (1.68)	7.83 (0.27)
S11: 01-11-00-018	0.50 (0.29)	0.10 (0.06)	3.88 (2.82)	0.61 (0.37)	7.93 (0.19)
S12: 01-11-00-019	6.10 (5.89)	0.13 (0.28)	0.87 (0.68)	0.36 (0.27)	7.29 (0.21)
S13: 01-11-00-022	0.68 (0.21)	0.03 (0.07)	0.37 (0.56)	0.28 (0.18)	8.43 (1.95)
S14: 01-11-00-023	0.75 (0.37)	0.03 (0.07)	1.77 (1.19)	1.02 (0.46)	7.93 (0.26)
S15: 01-11-00-024	0.95 (0.92)	0.02 (0.02)	2.18 (1.57)	1.33 (0.86)	8.00 (0.26)
S16: 01-11-00-025	1.84 (0.99)	0.37 (1.62)	1.35 (1.37)	1.29 (0.50)	7.84 (0.25)
S17: 01-11-01-020	0.35 (0.14)	0.01 (0.01)	0.82 (1.07)	0.10 (0.07)	8.29 (0.31)
Station	**pV**	**SS**	**T**	**TDS**	**Turb**
S1: 01-11-00-001	3.57 (1.12)	61.76 (34.06)	16.60 (3.37)	399.92 (76.76)	56.13 (34.39)
S2: 01-11-00-002	3.79 (0.91)	67.88 (68.37)	16.98 (3.20)	466.01 (72.52)	47.65 (27.13)
S3: 01-11-00-003	2.06 (0.52)	29.52 (19.60)	15.68 (3.72)	278.67 (364.50)	24.86 (21.44)
S4: 01-11-00-008	3.44 (0.63)	59.06 (27.67)	16.40 (3.52)	366.39 (60.22)	49.70 (25.43)
S5: 01-11-00-009	3.95 (0.48)	75.18 (43.92)	17.78 (3.31)	444.28 (66.43)	75.13 (69.51)
S6: 01-11-00-013	4.33 (2.75)	81.28 (66.24)	17.05 (3.85)	459.50 (101.52)	89.55 (83.27)
S7: 01-11-00-014	35.77 (15.15)	174.00 (88.30)	17.75 (4.26)	2192.21 (1438.90)	152.15 (84.97)
S8: 01-11-00-015	32.79 (19.86)	111.38 (83.46)	17.33 (4.09)	1837.40 (1006.43)	112.79 (98.69)
S9: 01-11-00-016	30.32 (15.34)	301.57 (274.03)	17.96 (3.56)	1530.11 (673.24)	323.70 (322.75)
S10: 01-11-00-017	17.78 (9.31)	182.93 (220.51)	17.45 (3.48)	1169.02 (535.32)	214.73 (327.79)
S11: 01-11-00-018	2.86 (0.82)	43.27 (27.12)	15.03 (3.86)	535.54 (86.41)	35.34 (23.07)
S12: 01-11-00-019	56.40 (59.02)	262.75 (270.34)	16.56 (3.06)	986.33 (753.63)	449.87 (622.92)
S13: 01-11-00-022	6.59 (0.95)	67.68 (45.18)	17.09 (2.87)	2523.93 (4021.10)	52.96 (36.58)
S14: 01-11-00-023	4.08 (0.58)	67.67 (47.45)	17.50 (3.07)	812.34 (1179.22)	62.26 (66.04)
S15: 01-11-00-024	3.65 (0.73)	57.43 (23.71)	16.44 (3.46)	570.35 (991.11)	54.70 (29.32)
S16: 01-11-00-025	5.583 (1.17)	68.52 (30.42)	16.87 (2.91)	622.99 (170.90)	67.16 (53.39)
S17: 01-11-01-020	4.45 (0.76)	48.14 (83.85)	17.97 (3.74)	245.94 (32.28)	27.44 (16.22)

Results

Two cluster analysis methods are conducted among water stations: K-means clustering and Fuzzy c-means clustering. Both clustering methods suggest using 4 clusters. Based on the clustering results cluster 1 is named as Slightly Polluted Water Cluster, cluster 2 is named as High-Quality Water Cluster, cluster 3 is named as Highly Polluted Water Cluster, and cluster 4 is named as Polluted Water Cluster. The center of the clusters is provided in Table 3.

Table 3. Centers of Clusters based on K-means and Fuzzy C-means Clustering.

K-Means Clustering						Fuzzy C-means Clusters					
Cluster	**BOD_5**	**Cl^-**	**DO**	**EC**	**Al**	**Cluster**	**BOD_5**	**Cl^-**	**DO**	**EC**	**Al**
1	5.82	140.82	9.56	1102.87	188.11	**1**	4.69	132.56	10.07	1128.54	182.91
2	6.73	98.93	8.83	723.38	214.77	**2**	6.45	135.95	9.27	808.34	210.45
3	52.60	458.31	2.64	3020.92	598.56	**3**	69.54	506.89	2.20	3414.14	693.37
4	86.27	123.59	3.99	1214.66	444.58	**4**	23.85	152.69	5.06	1129.16	278.78
Cluster	**NH_4-N**	**NO_2-N**	**NO_3-N**	**o-PO_4**	**pH**	**Cluster**	**NH_4-N**	**NO_2-N**	**NO_3-N**	**o-PO_4**	**pH**
1	0.99	0.06	1.54	1.14	7.98	**1**	0.89	0.07	1.62	1.15	8.00
2	0.64	0.07	2.17	0.71	8.03	**2**	0.60	0.06	1.99	0.69	8.07
3	10.84	0.13	0.93	5.07	7.73	**3**	13.54	0.16	0.73	5.44	7.70
4	9.91	0.12	0.67	1.67	7.36	**4**	3.43	0.05	1.32	2.01	7.70
Cluster	**pV**	**SS**	**T**	**TDS**	**Turb**	**Cluster**	**pV**	**SS**	**T**	**TDS**	**Turb**
1	4.52	72.72	14.95	697.28	68.63	**1**	3.97	75.62	14.58	706.43	73.18
2	4.35	44.55	21.46	484.22	30.59	**2**	4.31	44.18	20.93	545.98	31.69
3	29.53	125.58	18.38	1729.00	116.96	**3**	46.26	224.40	18.88	2021.20	278.47
4	72.81	642.67	15.09	1151.27	990.73	**4**	12.28	123.04	15.97	718.03	135.35

The center of the clusters can be used to identify the characteristics of stations. For the k-means clustering results, the center of the first cluster has the lowest BOD5, Al, NO2-N, T average, has the second lowest EC, NH4-N, o-PO4, pV, SS, TDS and Turb average, has the second highest Cl-, NO3-N and pH average, and the highest DO average. The center of the second cluster has the lowest Cl-, EC, NH4-N, o-PO4, pV, SS, TDS and Turb average, has the second lowest BOD5, Al, and NO2-N, has the second highest DO average, and the highest NO3-N, pH and T average. The center of the third cluster has the lowest DO average, has the second lowest NO3-N, pH average, has the second highest BOD5, pV, SS, T and Turb average, and has the highest Cl-, EC, Al, NH4-N, NO2-N, o-PO4 and TDS average. The center of the fourth cluster has the lowest NO3-N and pH average, has the second lowest Cl-, DO and T average, has the second highest EC, Al, NH4-N, NO2-N, o-PO4 and TDS average, and has the highest BOD5, pV, SS and Turb average.

For the fuzzy c-means clustering results, the center of the first cluster has the lowest BOD5, Cl-, Al, pV and T average, has the second lowest EC, NH4-N, o-PO4, SS, TDS and Turb average, has the second highest NO2-N, NO3-N and pH average, and the highest DO average. The center of the second cluster has the lowest EC, NH4-N, o-PO4, SS, TDS and Turb average, has the second lowest BOD5, Cl-, Al, NO2-N, and pV average, has the second highest DO average, and the highest NO3-N, pH and T average. The center of the third cluster has the lowest DO, NO3-N, and pH average, has the second highest T average, and has the highest BOD5, Cl-, EC, Al, NH4-N, NO2-N, o-PO4, pV, SS, TDS and Turb average. The center of the fourth cluster has the lowest NO2-N and pH average, has the second lowest, DO, NO3-N and T average, has the second highest BOD5, Cl-, EC, Al, NH4-N, o-PO4, pV, SS, TDS and Turb average.

Figure 2 and Figure 3 visualize the k-means clustering results and fuzzy c-means clustering results of water quality classes for each station-year combination.

	Stations																
Year	S1	S2	S3	S4	S5	S6	S7	S8	S9	S10	S11	S12	S13	S14	S15	S16	S17
1985	1	1	1	1	1	1	1	1	4	1	1	4	1	1	1	1	1
1986	1	1	1	1	1	1	1	1	4	1	1	4	1	2	1	1	2
1987	1	1	1	1	1	1	1	1	4	1	1	4	1	1	1	1	1
1988	1	1	1	1	1	1	1	1	4	4	1	4	1	1	1	1	1
1989	1	1	1	1	1	1	1	1	1	1	1	4	1	1	1	1	1
1990	1	1	1	1	1	1	3	3	4	3	1	4	1	1	1	1	1
1991	1	1	1	1	1	1	3	1	4	4	1	4	1	1	1	1	1
1992	1	1	1	1	1	1	3	3	4	3	1	4	1	1	1	1	1
1993	1	1	1	1	1	1	3	3	4	3	1	4	1	1	1	1	1
1994	1	1	1	1	1	1	3	3	3	3	1	4	1	1	1	1	1

1995	1	1	1	1	1	1	3	3	3	3	1	4	1	1	1	1	1
1996	1	1	1	1	1	1	3	3	3	3	1	3	1	1	1	1	2
1997	1	1	1	1	1	1	3	3	3	3	1	3	1	1	1	1	1
1998	2	1	1	1	1	1	3	3	3	3	1	3	1	2	1	1	1
1999	1	1	1	1	1	1	3	3	3	3	1	1	1	1	1	1	1
2000	1	1	1	1	1	1	3	3	3	3	1	1	1	1	1	1	1
2001	1	1	1	1	2	2	3	3	3	3	1	3	1	2	1	2	2
2002	1	1	1	1	1	2	3	3	3	3	1	3	1	1	1	1	2
2003	1	1	1	1	2	1	3	3	3	3	1	1	1	1	1	1	1
2004	1	1	1	1	2	1	3	3	3	3	1	3	1	1	1	1	1
2005	1	1	1	1	3	3	3	3	3	3	3	3	1	1	1	3	2
2006	2	2	1	1	2	3	3	3	3	3	3	3	2	2	2	3	2
2007	2	1	1	2	2	2	3	3	3	3	2	3	1	2	2	2	2
2008	2	2	2	2	2	3	3	3	3	3	2	3	2	2	1	2	2
2009	1	1	1	1	2	1	3	3	3	3	1	1	1	2	1	2	2
2010	2	2	2	2	2	2	3	3	3	3	2	3	2	2	2	2	2
2011	2	2	2	2	2	2	3	3	3	3	2	3	2	2	2	2	2
2012	2	2	2	2	2	2	3	3	3	3	2	3	2	2	2	2	2
2013	2	2	2	2	2	2	3	3	3	3	2	2	2	2	2	2	2

Figure 2*. Water quality classes with K-means clustering*

According to Figure 2, the analysis of water quality clusters acquired by k-means clustering across stations and years reveals intriguing variations and notable trends. Several stations exhibit consistent water quality characteristics throughout the study period. For instance, stations S1 to S6 consistently belong to the Slightly Polluted Water Cluster until the 2000s. However, a significant shift occurs during subsequent years, as these stations transition to the High-Quality Water Cluster. This change suggests notable improvements in water quality in these locations, possibly attributed to effective pollution control measures or natural processes that have positively influenced the aquatic ecosystems.

Other stations, such as S7 to S10, consistently fall into the Highly Polluted Water Cluster, indicating persistent pollution challenges throughout the study period. This highlights the need for targeted pollution control strategies and continuous monitoring to address the underlying sources of contamination in these areas.

Furthermore, stations S11 to S13 demonstrate interesting changes over time. These stations initially exhibit mixed water quality clusters, with occasional presence in the Slightly Polluted Water Cluster and the Polluted Water Cluster. However, starting from the early 2000s, these stations consistently belong to the High-Quality Water Cluster. This transformation reflects substantial improvements in water quality in these particular locations, indicating the effectiveness of pollution reduction efforts or changes in environmental factors that positively influenced water conditions.

	Stations																
Year	S1	S2	S3	S4	S5	S6	S7	S8	S9	S10	S11	S12	S13	S14	S15	S16	S17
1985	1	1	1	1	1	1	1	1	4	4	1	3	2	1	1	1	1
1986	1	1	1	1	1	1	1	1	4	4	1	3	1	2	1	2	2
1987	1	1	1	1	1	1	4	4	4	1	1	3	1	1	1	1	1
1988	1	1	1	1	1	1	4	4	1	4	1	3	1	1	1	1	1
1989	1	1	1	1	1	1	4	4	4	4	1	3	1	1	1	2	1
1990	1	1	1	1	1	1	3	4	3	4	1	3	1	1	1	1	1
1991	1	1	1	1	1	1	3	4	4	4	1	3	1	1	1	1	1
1992	1	1	1	1	1	1	3	4	3	4	1	3	1	1	1	1	1
1993	1	1	1	1	1	1	3	4	3	4	1	3	1	1	1	1	1
1994	1	1	1	1	1	1	3	3	3	3	1	3	1	1	1	1	1
1995	1	1	1	1	1	1	3	3	3	4	1	3	1	1	1	1	1
1996	1	1	1	1	1	1	3	3	3	4	1	4	1	1	1	1	2

1997	1	1	1	1	1	1	3	3	3	4	1	3	1	1	1	1	1
1998	2	1	1	1	2	1	4	4	4	4	1	4	2	2	1	4	1
1999	1	1	1	1	1	1	4	3	4	4	1	4	2	1	1	1	1
2000	1	1	1	1	1	1	4	3	3	4	1	4	1	1	1	4	1
2001	2	2	1	2	2	2	3	3	3	3	2	4	2	2	2	4	2
2002	1	1	1	1	1	2	3	3	3	3	1	4	1	1	1	1	2
2003	1	1	2	1	2	1	3	3	3	4	1	4	1	1	1	1	2
2004	1	1	1	1	2	4	3	3	3	3	4	4	4	2	1	4	4
2005	4	4	4	4	4	4	3	3	3	3	4	4	4	4	4	4	4
2006	4	4	4	4	4	4	3	3	3	3	4	4	4	4	4	4	2
2007	2	2	2	2	2	2	3	3	3	3	4	4	2	2	2	2	2
2008	2	2	2	2	2	4	3	3	3	3	4	4	2	2	2	2	2
2009	2	1	2	2	2	1	3	3	3	3	4	4	2	2	1	2	2
2010	2	2	2	2	2	2	3	3	3	3	2	4	2	2	2	2	2
2011	2	2	2	2	2	2	3	3	3	3	2	3	2	2	2	2	2
2012	2	2	2	2	2	2	3	3	3	3	2	3	2	2	2	2	2
2013	2	2	2	2	2	2	3	3	3	3	2	2	2	2	2	2	2

Figure 3. *Water quality classes with fuzzy C-means clustering.*

The analysis of the water quality clusters across stations and years in the fuzzy C-means clustering reveals interesting patterns and notable changes. Stations S1 to S6, which were initially classified as belonging to the Slightly Polluted Water Cluster until the 2000s, show a remarkable improvement in water quality. Starting from the 2000s, these stations consistently transition to the High-Quality Water Cluster, indicating successful efforts to mitigate pollution and enhance water conditions in these areas.

Stations S7 to S10, on the other hand, persistently fall within the Highly Polluted Water Cluster throughout the study period, indicating ongoing pollution challenges in these locations. These stations require focused interventions and continued monitoring to address the sources of contamination and improve water quality.

Furthermore, stations S11 to S13 demonstrate interesting dynamics over time. Initially showing mixed water quality clusters, with occasional presence in the Slightly Polluted Water Cluster and the Polluted Water Cluster, these stations experience a positive shift in the early 2000s. They consistently join the High-Quality Water Cluster, suggesting significant improvements in water quality. These changes may be attributed to pollution reduction measures, changes in land use practices, or other environmental factors that positively impacted water conditions in these specific locations.

Overall, the analysis highlights both positive and persistent challenges in water quality across the studied stations. The shift of several stations to the High-Quality Water Cluster indicates successful pollution control efforts, while the presence of highly polluted water in other stations underscores the need for targeted interventions. Understanding these patterns and trends is crucial for effective water management strategies, continuous monitoring, and ongoing efforts to protect and improve the health of the aquatic ecosystems in the region.

MDS is also used to visualize both the k-means cluster analysis (Figure 4) and fuzzy c-means cluster analysis in a two-dimensional graph (Figure 5). The graphs also visualize the findings of Figure 2 and Figure 3 with a different approach.

MDS visualization for the k-means cluster analysis reveals how year and station combination behave (Figure 4). For cluster 1 which is labeled as Slightly Polluted Water we can identify most of the station year combinations belong to pre 2000s with stations S1 to S6, S11, S13, S14 and S15 noteworthy. For the cluster 2 which is labeled as High-Quality Water mostly contains stations from post 2000s with stations S1, S4, S5, S11, S13, S14 and S17. For the cluster 3 which is labeled as Highly Polluted Water contains both pre 2000 and post 2000 era. This cluster mostly contains stations S7, S8, S9, and S10. For the cluster 4 labeled as Polluted Water Cluster contains stations S9, S10 and S12 for the years period before 1995.

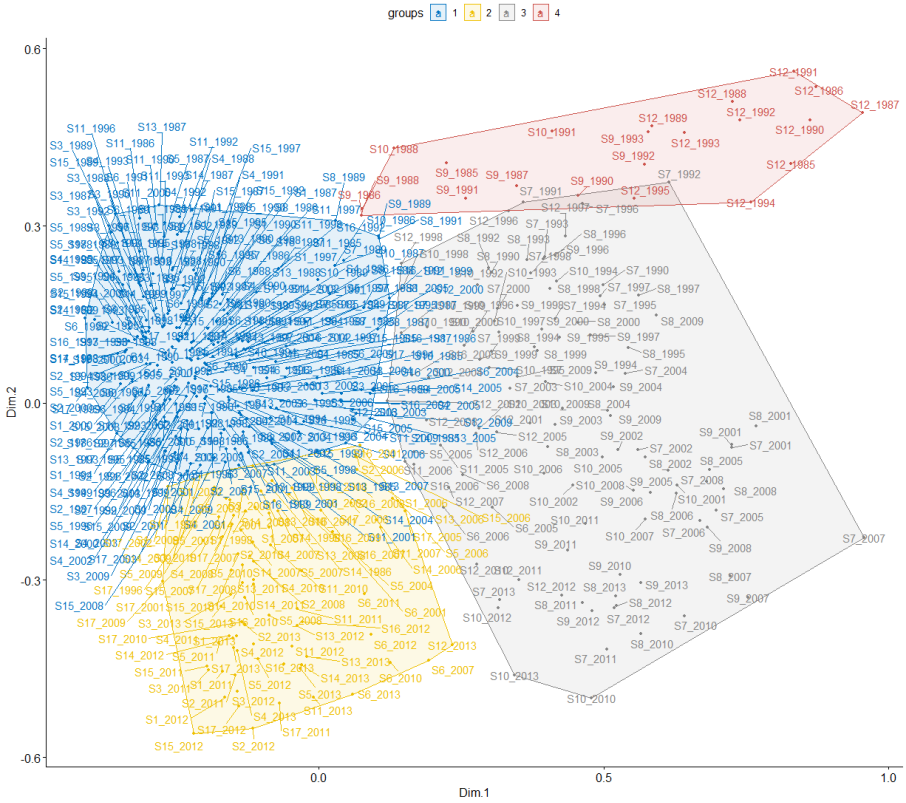

Figure 4. *MDS maps for K-means clustering.*

MDS visualization for the fuzzy c-means cluster analysis reveals how year and station combination behave (Figure 5). For cluster 1 which is labeled as Slightly Polluted Water we can identify most of the station year combinations belong to pre 2000s with stations S1 to S6, S11, S13, S14, S15, S16 and S17 noteworthy. For the cluster 2 which is labeled as High-Quality Water mostly contains stations from post 2000s with stations S1 to S6 and S13 to S17. For the cluster 3 which is labeled as Highly Polluted Water contains both pre 2000 and post 2000 era. This cluster mostly contains stations S7, S8, S9, S10 and S12. For the cluster 4 labeled as Polluted Water Cluster contains S7, S8, S9, S10 for the years period before 2000 and S11 and S12 after 2004.

Discussion and Conclusion

River water quality assessment plays a crucial role in monitoring and managing freshwater resources. Clustering analysis techniques, such as k-means and fuzzy clustering, offer valuable insights by grouping river segments or monitoring locations based on shared characteristics. This study aims to compare the effectiveness and applicability of k-means and fuzzy clustering methods in analyzing river water quality data.

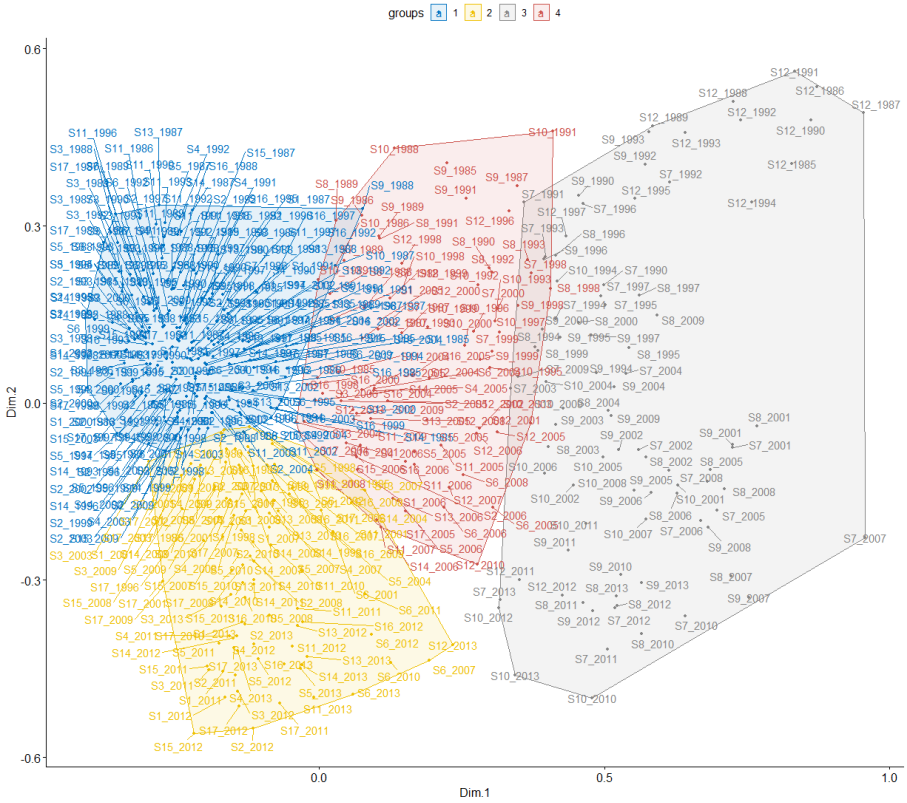

Figure 5. *MDS maps for Fuzzy C-means clustering.*

Through a comparative analysis of the two clustering methods, we provide insights into their strengths and limitations for river water quality assessment. We discuss the implications of each method's outcomes for decision-making, water resource management, and the identification of pollution sources as well as their comparison with Water Pollution Control Regulations.

The classification system outlined in the Water Pollution Control Regulation serves as a crucial tool for assessing and managing water quality across different regions. It provides a basis for developing appropriate pollution control strategies, monitoring programs, and environmental policies to safeguard water resources and promote sustainable water management practices.

This study contributes to the advancement of clustering techniques in the field of river water quality analysis and provides a foundation for further research and refinement of these methods. It underscores the importance of selecting appropriate clustering algorithms based on the specific objectives and characteristics of the water quality dataset.

Table 3 presents the physicochemical and microbiological water quality data obtained from multiple stations located within the Ergene River Basin, spanning the years 1983 to 2013. The data within the table encompass a diverse set of parameters that pertain to the physical, chemical, and biological attributes of water samples collected from distinct monitoring stations within the basin over the specified time.

The analysis of aluminum as an inorganic pollution parameter indicates that it serves as an indicator of Class IV water quality, and its measured values significantly exceed the threshold limit (>1).

In basin waters, Biological Oxygen Demand (BOD) values are generally observed to be significantly high. BOD serves as an important indicator of biological activity and organic matter content in aquatic systems. When comparing the BOD5 (Biological Oxygen Demand over 5 days) values according to the Turkish Standards Institute's regulations, it was observed that the first and second K-means cluster models corresponded to Class II water quality, while

the third and fourth K-means cluster models corresponded to Class IV water quality. Similarly, using the Fuzzy C-means cluster model, it was determined that the first and second Fuzzy C-means models corresponded to Class II water quality, while the third and fourth Fuzzy C-means models corresponded to Class IV water quality. These results indicate variations in water quality within the studied area based on BOD5 levels, as defined by the respective classification criteria.

Dissolved oxygen serves as a crucial parameter for monitoring changes in water quality. In accordance with the Water Pollution Control Regulation, the first and second K-means cluster models classify the water as Class I in terms of quality, while the third K-means cluster model indicates Class IV water quality based on the dissolved oxygen threshold value. Similarly, the fourth K-means cluster model is associated with Class II water quality. Notably, the findings obtained from the Fuzzy C-means cluster model analysis corroborated the water quality classifications derived from the dissolved oxygen values, demonstrating concurrence between the clustering approaches.

Significant regional variations have been observed in the electrical conductivity (EC) values detected in the waters, and based on the Water Pollution Control Regulation, it has been determined that the EC values identified in the first and fourth cluster models correspond to Class III water quality, the EC values in the second cluster model correspond to Class II water quality, and the third cluster model represents Class IV water quality (Turkish Regulations, 2015). Additionally, it has been found that the range of 150-500 μS/cm specified for electrical conductivity in the protocol on standards for aquatic products and the protection of surface water sources against pollution is exceeded throughout almost the entire basin (Uslu and Türkman, 1987).

The nitrate levels measured in the basin stations have been determined to comply with the Class I water quality standards set by the Water Pollution Control Regulation. Regarding nitrite concentrations, the first K-means cluster model corresponds to Class I threshold, the second K-means cluster model corresponds to Class II, the third K-means cluster model corresponds to Class IV, and the fourth K-means cluster model corresponds to Class III threshold. Similarly, when comparing nitrite values using the Fuzzy C-means cluster model, it has been established that the first Fuzzy C-means model corresponds to Class III threshold, the second and fourth Fuzzy C-means models correspond to Class II, and the third Fuzzy C-means model corresponds to Class IV water quality (Turkish Regulations, 2015). These findings provide scientific evidence of the nitrate and nitrite levels in accordance with the water quality classifications established by the respective clustering methods and regulatory guidelines.

Nitrite is an intermediate product in the biological oxidation process that converts ammonium to nitrate, and it can reach high levels, particularly in oxygen-deficient environments and in waters contaminated with organic matter (Egemen and Sunlu, 1996). According to the drinking water standards reported by the World Health Organization, the nitrite value in water is expected to not exceed the limit of 0.2 mg/L (WHO, 2011).

According to the Surface Water Quality Regulation (SWQR) in our country, the orthophosphate phosphorus value is reported as <0.05 mg/L for Class I waters and 0.65 mg/L for Class IV waters. Considering these criteria, both models indicate Class IV water quality. This observation aligns with the regulations set by the SWQR and confirms the classification of the water samples according to their orthophosphate phosphorus levels.

The geological composition of the region is a significant factor influencing the pH of water, and natural waters typically exhibit a slightly alkaline nature due to their carbonate and bicarbonate content. The optimal pH range for aquatic organisms is 6.5 to 8.5, while fish generally thrive within a range of 6.4 to 8.6 (Tanyolaç, 2009). Deviations from these pH ranges can have adverse effects on the survival of aquatic organisms as they move further away from the acceptable intervals. In the Ergene River Basin, the stations demonstrate a mildly alkaline character in terms of pH. According to the Water Pollution Control Regulation, all stations within the basin possess Class 1-2 water quality based on their pH values. Furthermore, it has

been determined that the pH values of the waters do not exceed the range of 6.5 to 9.5, as specified in the Turkish Standards Institute's regulation for water intended for human consumption (TS266, 2005).

Total dissolved solids (TDS) primarily comprise inorganic minerals and organic substances, including a wide range of salts (Miranda and Krishnakumar, 2015). High TDS concentration in water can result in aesthetic issues such as discoloration, unpleasant taste, or precipitation (Sibanda et al., 2014). The levels of TDS, in a general sense, serve as an indicator of the overall pollutant load. According to the Water Quality Control Regulation, when comparing TDS values, the first and fourth K-means cluster models represent Class II water quality, while the second K-means cluster model represents Class I, and the third K-means cluster model represents Class III. Similar results were observed when evaluating the same values using the Fuzzy C-means cluster model. Specifically, the first, second, and fourth Fuzzy C-means models correspond to Class II water quality, the third Fuzzy C-means model corresponds to Class II, and the third Fuzzy C-means model corresponds to Class III (Turkish Regulations, 2015).

Suspended solids (SS) are natural pollutants and cause turbidity in the river water (Mahvi & Razazi, 2005). The excess amount of SS in water can also be an indicator of land erosion in the river catchment.

High turbidity levels limit the amount of light able to penetrate the water’s surface. This affects plant growth by reducing their ability to photosynthesis. Reduced plant growth leads to decreased amounts of oxygen in the water and the loss of vital habitat for aquatic animals. Fine particles settle on surfaces, smothering plants, rocks, logs and fish eggs and larvae. Fish can also suffer from clogged gills. The turbidity level results in the Ergene Basin vary between 30.59 and 990.73 NTU, indicating a high degree of turbidity in the water.

The importance of assessing water quality accurately has been amplified due to the diminishing availability of water resources on both national and global scales, coupled with the rapid growth of the world population (Evsahibioğlu et al., 2010). Anthropogenic activities have further exacerbated the deterioration of water quality, underscoring the significance of employing various methods, including mathematical modeling, statistical techniques, and soft computing methods, to evaluate water quality (Bilgin and Konanç, 2016). Based on the surface water data obtained in our study, it has been determined that the Ergene River, which is significantly exposed to industrial pollution, exerts considerable pressures on the ecosystem. The data obtained from statistical analyses clearly demonstrate the adverse effects of environmental and industrial pollution on the system.

References

Akın, M., & Akın, G. (2007). Suyun önemi, Türkiye'de Su Potansiyeli, Su Havzaları ve Su Kirliliği, Ankara ˘ Üniversitesi Dil ve Tarih-Coğrafya Fakültesi Dergisi.

Arthur, D., & Vassilvitskii, S. (2007, January). K-means++ the advantages of careful seeding. In Proceedings of the eighteenth annual ACM-SIAM symposium on Discrete algorithms (pp. 1027-1035).

Bezdek, J. C., Coray, C., Gunderson, R., & Watson, J. (1981). Detection and characterization of cluster substructure i. linear structure: Fuzzy c-lines. SIAM Journal on Applied Mathematics, 40(2), 339-357.

Bilgin, A., & Konanç, M U. (2016). Evaluation of surface water quality and heavy metal pollution of Coruh River basin Turkey by multivariate statistical methods. Environmental Earth Sciences, 75(12), 1029. https://doi.org/10.1007/s12665-016-5821-0.

Dokmeci, A. H. (2017). Evaluation of heavy metal pollution in the Ergene River Basin from a public health perspective. Turkish Journal of Public Health, 15(3), 212.

EC (European Communities), (2006). EC of the European Parliament and of the council of 6 September 2006 on the quality of fresh waters needing protection or improvement in order to support fish life. Directive 2006/44

Egemen Ö, Sunlu U. (1996). Su kalitesi. İzmir: Ege Üniversitesi Su Ürünleri Fakültesi Yayınları Yayın No:14. Ege Üniversitesi Basımevi 153s.

Emadian S.M Sefiloglu F.O., Akmehmet Balcioglu I., Tezel. (2020). Identification of core micropollutants of Ergene River and their categorization based on spatiotemporal distribution. Science of the Total Environment

Evsahibioğlu, A N, Çakmak, B, & Aküzüm, A. (2010). Su Yönetimi, Su Kullanım Stratejileri ve Sınırı Aşan Sular. TMMOB Ziraat Mühendisleri Odası Türkiye Ziraat Mühendisliği VII. Teknik Kongresi, 1, 119–134.

İşçen, C F, Altın, A, Şenoğlu, B, & Yavuz, H S. (2009). Evaluation of surface water quality characteristics by using multivariate statistical techniques: a case study of the Euphrates river basin, Turkey. Environmental Monitoring and Assessment, 151 (1), 259–264. https://doi.org/10.1007/s10661-008-0267-9.

Köse, E., Tokatlı, C., Çiçek, A. (2014). Monitoring Stream Water Quality: A Statistical Evaluation. Polish Journal of Environmental Studies, 23 (5): 1637-1647.

Kruskal, J. (1977). The relationship between multidimensional scaling and clustering. In Classification and clustering (pp. 17-44). Academic Press.

Kruskal, J. B. (1964). Multidimensional scaling by optimizing goodness of fit to a nonmetric hypothesis. Psychometrika, 29(1), 1-27.

Landau, S., Leese, M., Stahl, D., & Everitt, B. S. (2011). Cluster analysis. John Wiley & Sons.

MacQueen, J. (1967, June). Classification and analysis of multivariate observations. In 5th Berkeley Symp. Math. Statist. Probability (pp. 281-297). Los Angeles LA USA: University of California.

Mahvi A.H., Razazi M. (2005) Application of polyelectrolyte in turbidity removal from surface water, Am. J. Appl. Sci. 2, 397

Miranda, J. & Krishnakumar, G. (2015) Microalgal diversity in relation to the physicochemical parameters of some Industrial sites in Mangalore, South India. Environ Monit Assess 187(11)

Orak E., Akkoyunlu A., Can Z.S. (2020). Assessment of water quality classes using self-organizing map and fuzzy C-means clustering methods in Ergene River, Turkey. Springer

Qadir, A., Malik, R.N., Husain, S.Z. (2008). Spatio-temporal variations in water quality of Nullah Aik-tributary of the river Chenab, Pakistan. Environ. Monit. Assess. 140, 43e59.

R Core Team (2022). R: A language and environment for statistical computing. R Foundation for Statistical Computing, Vienna, Austria. URL https://www.R-project.org/.

Sibanda T, Chigor VN, Koba S, Obi CL, Okoh AI (2014) Characterisation of the physicochemical qualities of a typical ruralbased river: ecological and public health implications. Int J Environ Sci Technol 11(6):1771–1780

Singh K. P., Malık A., Sınha S. (2005). Water Quality Assessment and Apportionment of Pollution Sources of Gomti River (India) Using Multivariate Statistical Techniques - A Case Study. Anal Chim Acta, 538; 355–374.

Tanyolaç J. (2009). Limnoloji. Ankara: Hatiboğlu Yayınevi 294s.

Tokatlı C., Çiçek A., Emiroğlu Öç., Köse E. (2019). Water Quality Monitoring of Meriç, Tunca and Ergene Rivers (Edirne, Turkey) in Rainy Season. Research Journal of Biology Sciences, 1308-0261, 12(1): 13-17, 2019

Turkish Water Pollution Control Regulation Regulations (2015) Su kirliliği kontrolü yönetmeliği (SKKY). Yayımlandığı Resmi Gazete: Tarih 15 Nisan Çarşamba 2015, Sayı :259327 https://www.resmigazete.gov.tr/eskiler/2015/04/20150415-18.htm

Uslu, O., Türkman, A. (1987). Su Kirliliği ve Kontrolü. T.C. Başbakanlık Çevre Genel Müdürlüğü Yayınları, Eğitim Dizisi I, Ankara.

Wang, J.Y., Da, L.J., Song, K., Li, B.L. (2008). Temporal variations of surface water quality in urban, suburban and rural areas during rapid urbanization in Shanghai, China. Environ. Pollut. 152, 387e393

WHO (World Health Organization). (2011). Guidelines for drinking-water quality. World Health Organization Library Cataloguing-in-Publication Data, NLM classification: WA 675.

Zhang, Q., Li, Z.W., Zeng, G.M., Li, J.B., Fang, Y., Yuan, Q.S., Wang, Y.M., Ye, F.Y. (2009). Assessment of surface water quality using multivariate statistical techniques in red soil hilly region: a case study of Xiangjiang watershed, China. Environ. Monit. Assess. 152, 123e131.

Zhang, Y., Guo, F., Meng, W., Wang, X.Q. (2009). Water quality assessment and source identification of Daliao river basin using multivariate statistical methods. Environ. Monit. Assess. 152, 105e121.

Effects of Na-Humate and Ca-Humate Application on Cold Hardiness of Wheat and Corn

Vedat BEDİRHANOĞLU[1]
Metin TURAN[2]
Adem GÜNEŞ[3]
Müdahir ÖZGÜL[4]

Introduction

This study was carried out to determine the effects of Na-humate and Ca-humate applications on the cold resistance of wheat and corn plants. Wheat and corn are strategic plants that rank first both in the world and our country in terms of cultivation area and production among the cultivated plants used in human nutrition, and they play an essential role as the basic energy and protein source of people. Wheat and corn yields in our country show significant differences depending on seasonal and year-to-year differences in climatic conditions, especially cold damage. Changes in the temperature regime due to global climate changes, especially low temperatures and cold damage, can affect the region and cause significant yield losses in these plants. Therefore, effective fertilizer formulations should be used to reduce yield and quality losses caused by low temperature and cold stress in wheat and corn, important income sources for farmers in that region.

Humic substances are chemically stable, dark colored, and have a high molecular weight structure, contains 44-58% Carbon, 42-46% Oxygen, 6-8% Hydrogen, and 0.5-4% Nitrogen (Larcher, 2003). Humic substances are divided into three groups humic acid, fulvic acid, and humin according to their solubility in acids and bases (Sparks, 2003:82). Humic acid has a large molecular weight and takes a long time to break down. Therefore, humic acids are generally used as soil promoters (Chen and Avnimelech, 1986:161-186; Yılmaz, 2007:74).

Humic substances increase soil fertility by affecting the physical, chemical, and biological properties of soils. It has been reported that humic compounds have a positive effect on plant, root, and shoot development growth through several mechanisms, increase the availability of nutrients in the soil, and provide resistance against different stress conditions (Nardi et al. 2002:1527-1536). The cation exchange power of humic substances is considerably higher than that of clay minerals, so they significantly increase the CECs of soils (Stevenson,

[1] Dr. Vedat BEDİRHANOĞLU, International Agricultural Research and Training Center, Orcıd: 0000-0003-4642-715X
[2] Prof. Dr. Metin TURAN, Yeditepe University, Agricultural Trade and Management, Orcıd: 0000-0002-4849-7680
[3] Doç. Dr. Adem GÜNEŞ, Erciyes University, Soil Science And Plant Nutrition, Orcıd: 0000-0003-0411-6134
[4] Prof. Dr. Müdahir ÖZGÜL, Atatürk University, Soil Science And Plant Nutrition, Orcıd: 0000-0002-5855-0086

1994:367-372). Due to this feature, all the necessary metals in the soil can chelate with humic acids.

Humic substances bond with calcium carbonate forming weak, soluble calcium humates. Calcium protects plant tissues against freeze-thaw stress and prevents cold damage by reducing the outflow of substances from the plant cell. Accumulating calcium in cell vacuoles plays an important role in maintaining anion-cation balance (Kacar and Katkat, 2009a:351-374). Sodium plays an important role in enzyme activities, reduces the freezing point of plant sap, and reduces cold damage in winter and early spring (Kacar and Katkat, 2009b:593-602).

This study aimed to reduce the effects of cold damage caused by unexpected temperature changes by applying Ca-humate and Na-humate fertilizer formulations.

Materials and Methods

The experiment was carried out on the farm of Atatürk University Agricultural Management Directorate in Erzurum. The trial was conducted at the field with 2 plants (Wheat, Corn), 3 different fertilizer applications (Control, Ca-Humat, Na-Humat), 5 different application levels (0, 1, 3, 9, 12 kg/ha), 3 replications as a factorial experiment under complete randomized design. Before the applications, soil samples were collected from each plot, and physical, chemical, and biological analyzes were performed. Ca-humate and Na-humate were applied to the plants with soil and foliar at the beginning of the growth period, in the middle of the growing period, and during the ripening period.

The pH of the soil samples was measured potentiometrically in a 1:2.5 soil-water suspension with a Glass Electrode pH meter (McLean, 1982). The lime content of the soils was determined volumetrically by using Scheibler Klasimeter (Nelson and Sommer 1982). The organic matter contents of the soils were determined by the Smith-Weldon method (Nelson and Sommer, 1982). Nitrogen content of soil samples was determined using Dumas Nitrogen Analyzer. Phosphorus contents of soils were determined with an ICP-OES Inductively Coupled Plasma spectrophotometer (Perkin-Elmer, Optima 2100 DV, ICP/OES, Shelton, CT 064844794, USA) (Olsen and Sommer, 1982).

At the end of the experiment, cold damage on the leaves of the plants was determined by the electrical conduction technique (Griffith et al. 1992). In order to determine the cell permeability, the plant leaves were thoroughly washed with distilled water, and shaken in 10 ml of deionized water at 25^{o}C for 24 hours, and the electrical conductivity (EC_1) of the solution was measured. Afterward, the samples were left in an autoclave at 120^{o}C for 20 minutes. The samples were removed from the autoclave and the electrical conductivity (EC_2) values were measured again when the temperature dropped to 25^{o}C. From the obtained electrical conductivity values; cell permeability was determined from the formula (%)=(EC_1/EC_2)x100 (Lutts et al. 1996). Analysis of variance and multiple comparison tests were performed on the results obtained from the experiment (SPSS, 2004).

Results and Discussion

Wheat

The Effect of Applications on the Chemical Properties of Soils

The effects of Na and Ca-humate treatments on some chemical properties of wheat-planted soils were evaluated (Table 1). pH level increased from 7.60 to 7.85 and 7.65, respectively, due to increasing amounts of Na and Ca-humate applications. Stevenson (1994), found that the accumulation of humic substances in soils contributes to the increase of pH. The lime contents of the soils did not change significantly depending on the increasing levels of Na and Ca-humate applications ($p<0.01$).

Table 1 *- Some chemical analysis results of Na and Ca-humate applied to wheat-planted soils*

Treatments		pH (1:2,5)	$CaCO_3$	Organic Matter (%)	N mg/kg	P
	Initially	**7 .60**	**0.55**	**1.40**	**7.35**	**4.26**
Na-Humat (kg/ha)	**0**	7.65c	0.52	1.36c	6.80c	3.36c
	1	7.68bc	0.54	1.42b	7.10b	3.45c
	3	7.72b	0.56	1.38c	6.75c	3.65bc
	9	7.70b	0.53	1.40b	7.00b	3.85b
	12	7.85a	0.55	1.48a	7.40a	4.02a
Ca-Humat (kg/ha)	**0**	7.64	0.53	1.34	6.65d	3.42a
	1	7.72	0.55	1.36	7.40ab	3.35ab
	3	7.68	0.51	1.38	7.54a	3.22b
	9	7.71	0.56	1.40	7.36b	3.14b
	12	7.65	0.58	1.36	7.28c	3.01c

The organic matter content of the soils increased depending on the Na and Ca-humate applications. The highest amount of organic matter was obtained with Na-humate application at the level of 12 kg/ha, and with Ca-humate application at the level of 9 kg/ha. The amount of N was 6.80 and 6.65 mg/kg in the control groups and increased with increasing Na and Ca-humate application doses. The amount of N available to the plant reached the highest value at 12 kg/ha Na-humate level and 3 kg/ha Ca-humate application level with 7.40 and 7.54 mg/kg, respectively. The amount of available P to the plant in the soil generally increased with Na-humate application and reached 4.02 mg/kg with 12 kg/ha Na-humate application. The amount of P decreased in general with Ca-humate application and reduced to the lowest value (3.01 mg/kg) with 12 kg/ha Ca-humate application (Table 1). David et al. (1994) reported that applying humic acid compounds obtained from different sources to the tomato plant increases the uptake of plant nutrients, especially for N and P.

The Effect of Applications on the Yield and Yield Parameters of Wheat

Spike weight, average grain yield, and cell permeability values of the wheat plant significantly increased depending on the increasing Na and Ca-humate applications ($p<0.01$). Spike weight and average grain yield reached the highest levels with 9 kg/ha Na and Ca-humate applications. With 9 kg/ha Na and Ca-humate applications, the spike weight increased by 23.29% and 28.74%, respectively, while the average grain yield increased by 24.40% and 28.89%, respectively, compared to the control group (Table 2). Nardi et al. (2002) found that humic compounds increase plant nutrient availability and have a positive effect on plant growth in their study of different plants.

Table 2 - *The Effect of Na and Ca-humat on the Yield and Yield Parameters of Wheat*

Treatments		**Spike Weight**	**Average Grain Yield**	**Cell Permeability**
		kg/ha		**%**
Na-Humat (kg/ha)	0	28.563e	22.035d	15.62d
	1	29.653d	24.123c	16.55c
	3	32.460b	25.689b	20.32b
	9	35.214a	27.411a	22.14a
	12	30.569c	25.236b	16.98c
Ca-Humat (kg/ha)	0	29.251e	22.236e	16.11d
	1	30.562d	25.163d	16.88d
	3	34.026b	27.015b	19.52b
	9	37.659a	28.659a	20.16a
	12	32.514c	26.511c	18.63c

Cell permeability increased depending on Na and Cahumate applications. While cell permeability was 15.62% to 16.11% in the control group, it reached the highest value in 9 kg/ha Na and Ca-humate applications. With 9 kg/ha Na and Ca-humate applications, it was determined that there was an increase of 41.74% and 25.14%, respectively, compared to the control group (Table 2). Waldrighi et al. (1996) determined in their study that humic acid increased the uptake of plant nutrients by increasing cell permeability.

As a result of Na and Ca-humate applications, the spike weight and average grain yield values of the wheat plant were subjected to regression analysis. As a result of the analysis, the spike weight reached the optimum value at the application doses of 6.5 kg/ha and 6.8 kg/ha, depending on the Na and Ca-humate application, respectively. The average grain yield was obtained with 7.2 kg/ha Na-humate and 7.4 kg/ha Ca-humate application doses (Figure 1).

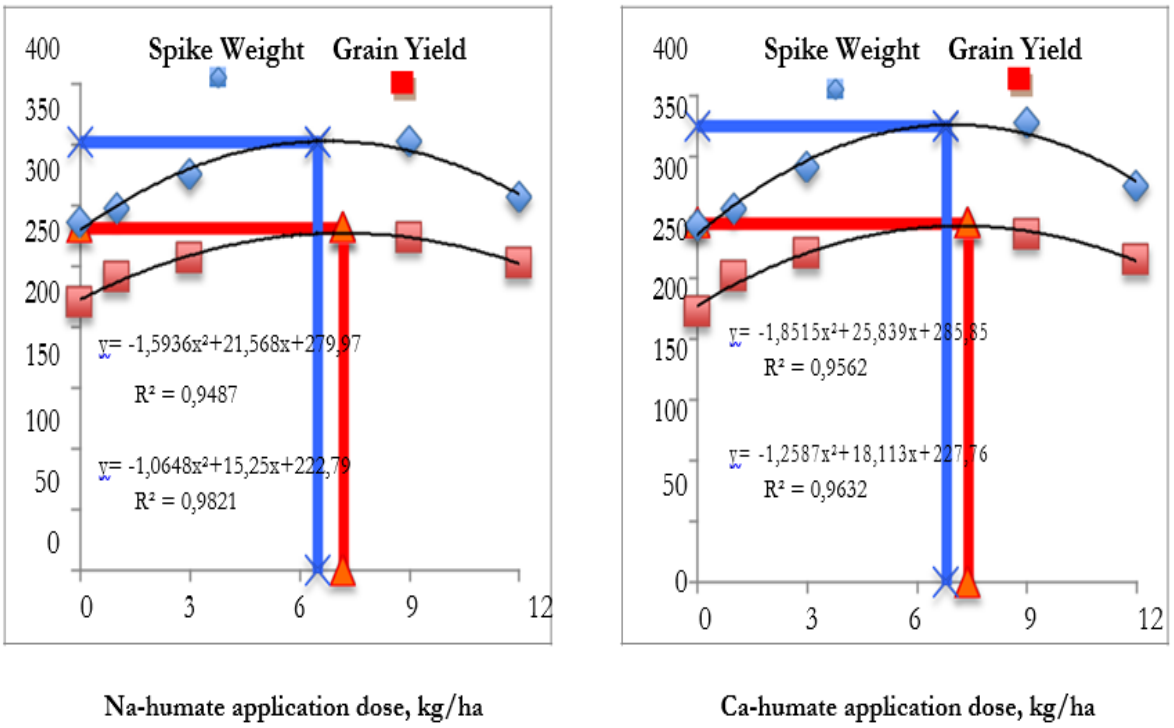

Figure 1. *Changes in spike weight and average grain yield of the wheat plants depending on Na and Ca-humate applications.*

The Effect of Applications on the Cold Resistance of Wheat

As a result of the statistical analysis, it was determined that the effects of Na and Ca-humate applications on the cold damage rate of the plant were very significant ($p<0.05$).

While the cold damage rate at 0 °C was 52.16% in the control group, it decreased to 34.26% at the highest Na-humate application dose (12 kg/ha). The cold damage rate decreased by 34.32% at 12 kg/ha Na-humate application dose compared to the control. While the cold damage rate was 60.07% in the control group at -5 °C, it decreased to 42.76% at the highest Na-humate application dose of 12 kg/ha. Cold damage rate decreased by 28.82% at 12 kg/ha application dose compared to the control. While the cold damage rate was 73.91% in the control group at -10 °C, it decreased to 53.19% at the highest Na-humate application dose of 12 kg/ha. The cold damage rate decreased by 28.03% at 12 kg/ha application dose compared to the control. While the cold damage rate was 85.46% in the control group at -15 °C, it decreased to 65.35% at the highest Na-humate application dose of 12 kg/ha. The cold damage rate decreased by 23.53% at 12 kg/ha application dose compared to the control. While the cold damage rate was 92.27% in the control group at -20 °C, it decreased to 69.88% at the highest Na-humate application dose of 12 kg/ha. The cold damage rate decreased by 24.27% at 12 kg/ha application dose compared to the control (Table 3).

Tablo 3 - The effect of Na and Ca-humate applications on the cold damage rate of wheat plants.

Treatments		Cold Damage Rate (%)				
		0 °C	**-5 °C**	**-10 °C**	**-15 °C**	**-20 °C**
Na-Humat (kg/ha)	0	52.16a	60.07b	73.91a	85.46a	92.27a
	1	48.69b	62.18a	70.42b	81.73b	89.97b
	3	41.25c	55.86c	66.11c	75.73c	79.78c
	9	38.59d	50.06d	62.52d	71.52d	72.36d
	12	34.26e	42.76e	53.19e	65.35e	69.88e
Ca-Humat (kg/ha)	0	54.15a	62.53a	72.11a	86.41a	93.22a
	1	52.36a	60.25ab	65.59b	80.19b	86.52b
	3	45.26b	58.41b	62.33c	72.17c	72.15c
	9	40.11c	55.12c	59.23d	68.53d	71.11c
	12	36.59d	45.36d	52.17e	62.11e	67.48d

While the cold damage rate at 0 °C was 54.15% in the control group, it decreased to 36.59% at the highest Ca-humate application dose of 12 kg/ha. The cold damage rate decreased by 33.17% at 12 kg/ha application dose compared to the control. While the cold damage rate was 62.53% in the control group at -5 oC, it decreased to 45.36% at the highest Ca-humate application dose of 12 kg/ha. The cold damage rate decreased by 27.46% at 12 kg/ha application dose compared to the control. While the cold damage rate was 72.11% in the control group at -10 oC, it decreased to 52.17% at the highest Ca-humate application dose of 12 kg/ha. The cold damage rate decreased by 27.65% at 12 kg/ha application dose compared to the control. While the cold damage rate was 86.41% in the control group at -15 oC, it decreased to 62.11% at the highest Ca-humate application dose of 12 kg/ha. The cold damage rate decreased by 28.12% at 12 kg/ha application dose compared to the control. While the cold damage rate was 93.22% in the control group at -20 oC, it decreased to 67.48% at the highest Ca-humate application dose of 12 kg/ha. The cold damage rate decreased by 27.61% at 12 kg/ha application dose compared to the control (Table 3). Nardi et al. (2002) reported that humic compounds provide resistance against different stress conditions.

Corn

The Effect of Applications on the Chemical Properties of Soils

The effects of different levels of Na and Ca-humate applications on some chemical properties of the corn-planted soils were evaluated (Table 4). While the initial soil pH was 7.53, depending on the increasing Na and Ca-Humate application doses, the pH value reached 7.63 and 7.59, respectively. While the lime content of the soils did not show a significant change depending on the application of Na-humate, a significant increase was determined due to the application of Ca-humate compared to the control group ($p<0.01$).

Table 4 -Some chemical analysis results of Na and Ca-humate applied to corn-planted soils

Treatments		pH	$CaCO_3$	Organic Matter	N	P
		(1:2,5)		(%)	mg/kg	
	Initial	**7.53**	**0.60**	**1.25**	**8.12**	**3.26**
Na-Humat (kg/ha)	**0**	7.51d	0.58	1.22	7.52	3.02d
	1	7.54c	0.62	1.26	7.41	3.11d
	3	7.59b	0.58	1.25	7.40	3.24c
	9	7.52d	0.61	1.22	7.35	3.36b
	12	7.63a	0.62	1.24	7.38	3.59a
Ca-Humat (kg/ha)	**0**	7.52	0.59c	1.20	7.48c	3.00a
	1	7.55	0.62bc	1.21	7.51c	2.96a
	3	7.56	0.64b	1.18	7.62b	2.95a
	9	7.59	0.66a	1.16	7.60b	2.86b
	12	7.55	0.67a	1.19	7.85a	2.75c

The organic matter content of the soils did not show a statistically significant change depending on the applied Na and Ca-humate application. The highest amount of organic matter was obtained from the 1 kg/ha dose of Na and Ca-Humate applications. While the amount of N in the soil decreased depending on the increasing Na-humate application doses, it increased due to the increasing Ca-humate application doses. At the highest Ca-Humat application dose, the amount of N reached 7.85 mg/kg. The amount of P available to the plant in the soil generally increased with Na-humate application and reached 3.59 mg/kg with 12 kg/ha Na-humate application. However, the amount of P in the soil decreased with increasing Ca-humate application doses (Table 4). Brannon and Sommers (1985) determined that humic substances physically increase the structure and water-holding capacity of the soil, biologically increase the usefulness of inorganic plant nutrients, and beneficial to soil microorganisms effective in plant growth.

The Effect of Applications on the Yield and Yield Parameters of Corn

The effects of Na and Ca-humate applications on yield and yield parameters of corn plant were evaluated. Yield and cell permeability values of corn plants increased due to increasing Na and Ca-humate applications, and this increase was found to be statistically significant ($p<0.01$).

The highest corn yield was obtained at 9 kg/ha levels of Na and Ca-humate applications. It was determined that with 9 kg/ha Na and C-humate applications, there was an increase of 33.68% and 33.76%, respectively, compared to the control group. Ayaş et al. (2005) determined that increasing amounts of humic acid applied to the spinach plant increased the total yield, nitrogen, and phosphorus content of the plant. While the cell permeability reached the highest value (17.11%) at the level of 9 kg/ha of Na-humate application, it reached the highest value (15.86%) at the level of 3 kg/ha of Ca-humate application (Table 5). Chen and Avaid (1990) reported that humic acids increase cell permeability and positively affect plant growth.

Table 5 - The Effect of Na and Ca-humat on the Yield and Cell Permeability of Corn

Treatments		Plant Weight	Cell Permeability
		kg/ha	%
Na-Humat (kg/ha)	0	521.1c	15.26c
	1	632.6b	15.63c
	3	685.1a	16.24b
	9	696.6a	17.11a
	12	625.8b	16.59b
Ca-Humat (kg/ha)	0	532.6d	14.15b
	1	645.1c	15.24a
	3	692.5b	15.86a
	9	712.4a	15.42a
	12	652.8c	15.11a

As a result of Na and Ca-humate applications, the plant weight values of the corn were subjected to regression analysis. As a result of the analysis, the optimum plant weight was determined with 6.5 kg/ha Na-humate and 6.8 kg/ha Ca-humate application doses (Figure 2).

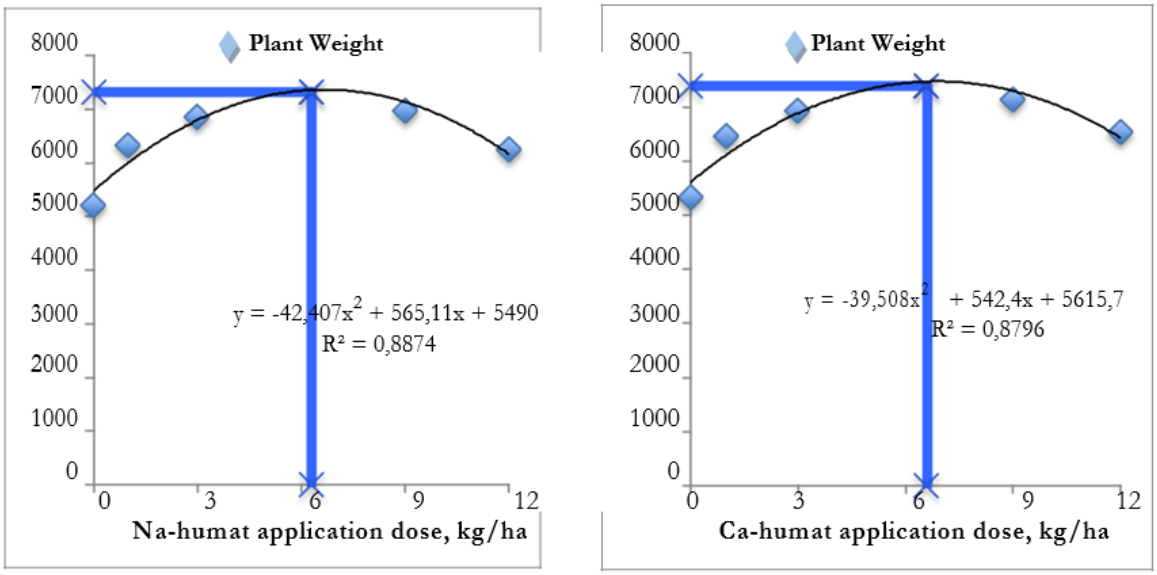

Figure 2. Changes in plant weight of the corn depending on Na and Ca-humate applications.

The Effect of Applications on the Cold Resistance of Wheat

The effects of applying different doses of Na and Ca-humate to corn plants on the cold damage rate were evaluated. As a result of the statistical analysis, it was determined that the effects of Na and Ca-humate applications on the cold damage rate of the plant were very important ($p<0.05$).

While the cold damage rate at 0°C was 60.12% in the control group, it decreased to 44.29% at the highest Na-humate application dose (12 kg/ha). Cold damage rate decreased by 26.33% at 12 kg/ha application dose compared to the control. While the cold damage rate was 68.52% in the control group at -5°C, it decreased to 47.53% at the highest Na-humate application dose (12 kg/ha). Cold damage rate decreased by 30.63% at 12 kg/ha application dose compared to the control. While the cold damage rate was 73.63% in the control group at -

10ºC, it decreased to 58.63% at the highest Na-humate application dose (12 kg/ha). The cold damage rate decreased by 19.83% at 12 kg/ha application dose compared to the control. While the cold damage rate was 96.53% in the control group at -15ºC, it decreased to 80.06% at the highest Na-humate application dose (12 kg/ha). Cold damage rate decreased by 17.09% at 12 kg/ha application dose compared to the control. While the cold damage rate was 98.66% in the control group at -20ºC, it decreased to 85.62% at the highest Na-humate application dose (12 kg/ha). The cold damage rate was decreased by 13.22 % at 12 kg/ha application dose compared to the control (Table 6).

Table 6 – *The effect of Na and Ca-humate applications on the cold damage rate of corn plants.*

Treatments		**Cold Damage Rate (%)**				
		0⁰C	**-5⁰C**	**-10⁰C**	**-15⁰C**	**-20⁰C**
Na-Humat (kg/ha)	0	60.12a	68.52a	75.63a	96.53a	98.66a
	1	56.23b	62.13b	71.42b	91.52b	94.52b
	3	51.24c	57.42c	65.25c	88.53c	92.11c
	9	46.53d	51.22d	61.22d	83.17d	90.24d
	12	44.29e	47.53e	58.63e	80.06e	85.62e
Ca-Humat (kg/ha)	0	61.25a	67.52a	72.45a	95.68a	98.11a
	1	58.41b	64.59b	70.15b	92.36b	95.42b
	3	52.36c	55.28c	66.26c	89.52c	94.16b
	9	50.14d	54.11c	58.42d	85.46d	92.33c
	12	46.59e	49.53d	54.26e	82.11e	88.71d

While the cold damage rate at 0ºC was 61.25% in the control group, it decreased to 46.59% at the highest Ca-Humat application dose (12 kg/ha). Cold damage rate decreased by 23.93% at 12 kg/ha application dose compared to the control. While the cold damage rate was 67.52% in the control group at -5ºC, it decreased to 49.53% at the highest Ca-Humat application dose (12 kg/ha). The cold damage rate decreased by 26.21% at 12 kg/ha application dose compared to the control. While the cold damage rate was 72.45% in the control group at -10ºC, it decreased to 54.26% at the highest Ca-Humate application dose (12 kg/ha). The cold damage rate decreased by 25.11% at 12 kg/ha application dose compared to the control. While the cold damage rate was 95.68% in the control group at -15ºC, it decreased to 82.11% at the highest Ca-Humat application dose (12 kg/ha). The cold damage rate decreased by 14.18% at 12 kg/ha application dose compared to the control. While the cold damage rate was 98.11% in the control group at -20ºC, it decreased to 88.71% at the highest Ca-Humate application dose (12 kg/ha). The cold damage rate decreased by 9.58% at 12 kg/ha application dose compared to the control (Table 6). Kutlu and Gülmezoğlu (2019) stated in their study that humic acid increases the tolerance of the oat plant in winter conditions and can be considered as a useful application against cold stress.

Conclusion

In this study, the effects of Na and Ca-humate applications on some yield components and cold resistance of wheat and corn plants were evaluated.

According to the results, as reported by previous researchers, it was determined that Na and Ca-humate applications improved the physical and chemical properties of the soil, and

increased the uptake of plant nutrients. Depending on the increasing Na and Ca-humate applications, some yield parameters and cell permeability values of wheat and corn plants increased compared to the control groups, and this increase was found to be statistically significant ($p<0.01$). When the cold damage rate of the plants was evaluated, it was determined that the effects of Na and Ca-humate applications on the cold damage rate were very important in wheat and corn plants ($p<0.05$). The results showed that applying Na and Ca-humat can reduce cold damage rates in wheat and corn plants in cold regions.

Acknowledgements

The study was supported by the Scientific Research Projects of Atatürk University. Project number: 2012-276.

References

Ayaş, H., Gülser, F. (2005). The effects of sulphur and humic acid on yield components and micronutrient contents of spinach (Spinacia oleracea var. Spinoza). Journal of Biological Science. Vol.5, number 6. 801-804.

Brannon, C. A., & Sommers, L. E. (1985). Preparation and characterization of model humic polymers containing organic phosphorus. Soil Biology and Biochemistry, 17(2), 213-219.

Chen, Y., Avnimelech, Y. (1986). The Role of Organic Matter in Modern Agricultur. Martinus Nijhoff Publisers, Dordrecht, 80.

Chen, Y., Aviad, T. (1990). Effects of humic substances on plant growth. Humic substances in soil and crop sciences: Selected readings, 161-186.

David, P.P., Nelson, P.V., Sanders, D.C. (1994). Humic Acid Improves Growth of Tomato Seedling in Solution Culture. Journal of Plant Nutrition (USA), 17(1), 173-184.

Griffith, M., Ala, P., Yang, D.S.C., Hon, W., Moffat, B. (1992). Antifreeze protein produced endogenously in winter rye leaves. Plant Physiol. 100, p: 593-596.

Kacar, B. Katkat, V, K. (2009a). Bitki Besleme. Nobel Bilim ve Araştırma Merkezi Yayınları No: 49, 351-374 s, Ankara.

Kacar, B. Katkat, V, K. (2009b). Bitki Besleme. Nobel Bilim ve Araştırma Merkezi Yayınları No: 49, 593-602 s, Ankara.

Kutlu, İ., Gülmezoğlu, N. (2019). Effects of humic acid and zinc applications on yield and agronomic features of oat genotypes sown in winter or spring. ICOFAAS 2019, 62.

Larcher, W. (2003). Physiological Plant Ecology: Ecophysiology and Stress Physiology ofFunctional Groups, 4th. Edition, Springer, New York.

Lutts S., Kinet JM., Bouharmont J. (1996). NaCl-induced senescence in leaves of rice (*Oryza sativa* L.) cultivars differing in salinity resistance. Annals of Botany 78: 389-398.

McLean, E. O. (1982). Soil pH and Lime Requirement. Methods of Soil Analysis Part2. Chemical and Microbiological Properties Second Edition. Agronamy. No: 9 Part 1. Edition P: 199-224

Nardi, S., Pizzeghello, D., Muscolo, A., Vianello, A. (2002). Physiological effects of humic substances on higher plants. Soil Biology and Biochemistry, 34(11), 1527-1536.

Nelson, D. W., Sommers L. E. (1982). Organic Matter. Methods of Soil Analysis Part 2. Chemical and Microbiological Properties Second Edition. Agronamy. No: 9 Part 2. Edition P: 574-579.

Olsen, S.R., Sommers, L.E. (1982). Phosphorus. Methaods of Soil Analysis Part 2. Chemical and Microbiological Properties Second Edition. Agronomy No: 9 Part 2. Edition P: 403-427.

Sparks, D. L. (2003). Environmental Soil Chemistry, Second Edition, Academic Press, San Diego, 82.

SPSS. (2004). SPSS Inc. SPSS® 13.0 Base User's Guide, Prentice Hall. Stevenson, F. J., 1994. Humus Chemistry: Genesis, Composition, Reactions, 2nd. Edition, John Wiley and Sons, Inc, New York 285.

Stevenson, F. J. (1994). Humus chemistry: genesis, composition, reactions. John Wiley & Sons. Page: 367-372

Yılmaz, C. (2007). Hümik ve Fülvik Asit. Hasad Bitkisel Üretim. Ocak, 260, 74.

Waldigri, M., Pera, A., Agnolucci, M., Frassinetti, S., Lunardi, D., Vallini, G. (1996). Effects of compost-derived humic acids on vegetable biomass production and microbial growth within a plant (Cichorium intybus) soil system: a comparative study. Agriculture, Ecosystems and Environment, 58, (2-3), 133-144.

Strucutral Design and Optimization of Bearingless Helicopter Rotor System

Mert Mustafa Tekin[1]
Vahit Mermertaş[2]

1. Introduction

The importance of vertical take-off and landing (VTOL) aircrafts are getting more popular day by day. The biggest member of the VTOL industry is helicopters which is leading that industry for a long time. New developments and advances in the material science, vibration and acoustics, flight dynamics and control, battery and fuel technology are creating a new era for the future designs of these aircrafts, especially the rotor system and blades.

The importance of rotor blades for helicopters cannot be overstated. Designing these blades requires considering factors such as manufacturability, reliability, accessibility, cost-effectiveness, performance and ease of installation. Moreover, rotor blade design entails a joint optimization problem that involves various elements, including aerodynamics, aeroelasticity, flight dynamics and control, structural design, vibration, acoustics, and material science.

Composite materials are a popular choice for solving these issues because of their exceptional fatigue resistance, low weight, high strength, and modulus. Furthermore, composite structures offer the added benefit of being able to be tailored to specific requirements, which is made possible by the anisotropic nature of composite materials. This means that designers can deliberately adjust the strength of the structure in particular directions as desired. This is an enormous advantage for designing such complex structures. Moreover, Mangalgiri indicates that the usage of composite materials reduces the weight of the aircrafts 30% in total (Mangalgiri, 1990: 657-654).

The use of composite materials in the rotor system can be optimized by utilizing finite element modelling software during the design phase. Moreover, computer aided design software can be employed to generate a detailed design of this intricate system in a digital environment. Additionally, multibody dynamic solvers contribute while extracting loads and creating kinematic and dynamic relations. In this study, the advantage of these three continuous engineering loops will be used to design and optimize a tail rotor system effectively.

The most prevalent rotor configuration globally is the single rotor type system, which consists of a main rotor and a tail rotor. The main rotor is placed horizontally, and the tail rotor is placed vertically with respect to the ground. According to Newton's third law and the gyroscopic effect theory, the main rotor produces torque, and the fuselage creates counter-torque during operation. This counter-torque is offset by the tail rotor blades, which produce anti-torque (Johnson, 2013: 271-274). In this study, it is concentrated to develop a comprehensive design for a single rotor configuration tail rotor system.

[1] Mert Mustafa Tekin, Master's Degree Student, Istanbul Technical University, Department of Mechanical Engineering
[2] Vahit Mermertaş, Prof. Dr., Istanbul Technical University, Department of Mechanical Engineering, ORCID: 0000-0001-9441-1502

Determining the suitable rotor type is a significant step following the establishment of the rotor configuration for a helicopter. The four most common rotor types for single rotor configuration are articulated, semi-articulated, hingeless, and bearingless rotors which are widely using in helicopter industry. Articulated rotors feature flap, lag, and pitch hinges to minimize root moments on the rotor blade, resulting in greater flexibility in rotor blade design. Though, this approach also leads to increased rotor hub complexity, maintenance costs, and the requirement for multipart bearings in the system, known as elastomeric bearings or tension links (Johnson, 2013: 273).

Semi articulated rotors comprise feathering and tethering hinge and generally two-sided rotor blades are installed directly to the rotor hub from the blade root region. The hub flaps in relative to the rotor shaft axis, resulting in the complete blade structure flapping according to the rotor hub's position. A pre-cone angle is often comprised in the hub to lessen solid coning loads. Nonetheless, without lag hinges, the blade's in-plane loads must be accommodated by the root structure (Johnson, 2013: 273-274). Semi articulates systems are cost effective and easy to design systems so, it is preferred most of the civil and small-scale helicopters (mostly 1-4 seated helicopters). However, it is inefficient to use in large scale helicopters because of the excessive loads and more complex design relative to the small-scale ones.

Unlike other articulated and semi articulated rotors, hingeless rotor system doesn't have flap or lag hinges, and the rotor blades attach directly to the hub system using only a feathering hinge. The rotor blade design must consider the high moments at the blade root due to the lack of flap and lag hinges. Structural stiffness is less substantial than centrifugal stiffening, leading to mode shapes resembling rigid body rotations (Johnson, 2013: 273-274). Without flap and lag hinges, the rotor system exhibits flap-lag coupling, meaning deflection in one motion affects deflection in the other motion. Hingeless rotor design is an intermediate design step through to the bearingless rotor system. Some of the helicopter models are used that system and saw the advantages of not using any complex hinges and bearings in the rotor system directly.

The design of bearingless rotor systems eliminates the need for flap, lag, and pitch hinges, and instead, the rotor blades are directly attached to the hub. The rotor blades provide the necessary flap, lag, and pitch movements through deflection (Bramwell, 2000: 277-288). With fewer parts in the rotor hub, the system has lower parasite drag, low weight, increased aerodynamic performance, less noise and is easier to maintain. Additionally, the absence of complex bearings and dampers helps to reduce costs.

One of the biggest advantages of the bearingless rotor system is reduced maintenance operations. Aircrafts have to be inspected after a certain flight hour or if the part is primary structure, sometimes it has to be inspected for after every flight. In this study, developed bearingless rotor reduces the number of primary structures and therefore that saves time for a certain inspection after flight. Moreover, the maintenance cost is lower compared to the other types of rotor systems because of the simplicity of the system in terms of design. To conclude, bearingless rotor concepts have the lowest direct operating cost among the all-rotor systems. Not only the direct operating cost, also the manufacturing cost of bearingless rotor systems is quite favourable when the mass and number of components is compared with the other rotor systems (Emmerling, et al., 2019: 3).

Moreover, the reliability of the bearingless rotor system is higher compared to the other rotor systems since there are fewer dynamic parts in the system. This reduces the risk of failure for overall rotor system and increases the reliability. Briefly, bearingless rotor systems mostly

face less incidents during operation when compared to the other rotor systems (Emmerling et al., 2019: 3).

Another big advantage of bearingless rotors is the degradation of noise and vibration during the flight. One of the reasons is coming from that the system has fewer rotating parts compared to the other systems. Moreover, bearingless rotor systems have more rationalised design; the aerodynamic design reduces the amount of turbulence and that leads to less noise generation. Finally, the bearingless rotor system have a stiffer structure compared to the other systems. Increased stiffness helps to reduce noise levels in the structure because of the mitigated deflection levels. Moreover, with the development of active control systems, the pitch, flap and lag motions can be more controlled and allows to avoid in range of high pitch-flap or flap-lag couplings. This also has an effect on reducing noise in overall.

The purpose of this study is to evaluate the advantages of a bearingless tail rotor system through the use of numerical methods and modern technology, as well as to perform an extensive weight optimization on the rotor blade components to reduce the overall weight of the rotor system as well as helicopter.

2. Literature Review

There were lots of studies about bearingless rotor systems that are starting from mid-1970's which also coincides with the developments in composite materials and these advances directly influences the aviation and automotive industries.

Klöppel et al. investigates the bearingless tail rotor concept including the noise generation, weight, reliability, manoeuvrability, structural design and power efficiency aspects. Results shows that articulated rotors provide higher stability and dynamic properties while bearingless rotors requires significantly less power compared to the articulated rotors (Klöppel et al., 1983).

Narayana et al. investigates the four bladed stiff in plane bearingless tail rotor and dynamic validation of that structure. This study mostly covers in the aerodynamic and design parameters. As the parameters; mass distribution, flap, lag and torsional stiffness parameters are extracted for the baseline design. Moreover, Campbell diagrams and stability charts have been extracted to investigate the stability performance. Finally, structural and dynamic parameters are tested in a whirl tower test which is a quite important step to understand the behaviour of the bearingless rotor at those times (Narayana et al., 1998)

Kim et al. developed a bearingless main rotor system and performed some structural test in a whirl tower with KARI (Korea Aerospace Research Institute). The structural design comprises four bladed soft in plane rotor blade without any hinges and bearings. This is an important improvement in terms of proving the bearingless rotor concept could accommodates higher loads unlike the tail rotor system. Crucial form flexbeam and hollow shape torque tube is designed for that study. As a result of that study, it is mandatory to have a quite simplified lead-lag damper (which will call as snubber later) and it is proved that that kind of hingeless and bearingless system can be applicable for the main rotor system with high accuracy on predicting dynamic and static loads (Kim et al., 2014)

Ichihashi et al. released an article which overviews the design, fabrication and testing of composite bearingless rotor system. The aim of the study is to increase the manoeuvrability and stability which is mentioned as a con compared to articulated rotors. Moreover, it is also aimed to reduce the parts that are used in the rotor hub design to decrease parasite drag at root

region. Finally, Ichihashi et al. proved that with flight test that stability and manoeuvrability of the bearingless rotors could be improved and these parameters are not blockers for development of that concept (Ichihashi et al., 1992).

Cheney is tried to develop a bearingless rotor concept even more less complex and cost effective. In this study, Cheney used all of the advantages of the composite materials and tailoring capabilities. The required low torsional stiffness of the rotor blade to reduce control loads is provided by tailoring capabilities of composite materials. Additionally, Cheney performed coupon and material fatigue tests, analytical results of a full-scale model and wind tunnel test results of scaled rotor blade model. Moreover, after these tests, the inertial and stiffness data are extracted and optimized including Campbell diagram. Finally, stability and manoeuvrability concerns are eliminated with performing stable operation up to 180 knots in the wind tunnel tests (Cheney, 1976).

3. Design and Modelling of Bearingless Tail Rotor Components

The design study can be segmented into rotor hub and rotor blade design. Rotor hub design involves rotor hub, pitch link and swashplate assembly whereas rotor blade design includes flexbeam, torque tube, snubber, skins, sandwich structure, and inner stiffeners, such as epoxy moulding compounds and other aerospace grade structural inner foam materials.

The rotor hub is a critical structural component responsible for bearing the various loads and moments generated by the engine and the helicopter's operation. As the rotor blades are attached directly to the hub plate with cantilever beam conditions, the hub must be robust enough to withstand the centrifugal force generated during operation. Typically, materials that require high strength are produced through machining or forging, as welding can weaken the material. The hub plate for most helicopter designs is forged to ensure that grain boundaries are oriented along the material's length, improving strength. In this study, Ti 6Al 4V has been chosen as the rotor hub material.

As an integral part of the rotor hub assembly, the pitch link serves to transmit pitch input from the pilot's controls to each rotor blade. This link is directly connected to the torque tube and the rotor blade, any failure of this component can result in serious consequences can be called as catastrophic. Consequently, the pitch link is designed with durability and strength concerns during the design. For the purposes of this study, the pitch link will be treated as a 2D rigid element in order to simplify some of the calculations since it is not considered for an optimization design space component.

Swashplate assembly is a crucial component that facilitates the transfer of pilot inputs to the rotor blades via spherical bearing motion. It is comprised of two distinct parts: a non-rotating swashplate that is connected to the rotor mast via a spherical bearing and can tilt in multiple directions, and a rotating swashplate that rotates at the same speed as the tail rotor system. The non-rotating swashplate is linked to the rotating swashplate via ball bearings. In this study, the most common swashplate assembly will be used and not targeted to optimize it further.

Before starting rotor blade design, it is quite important to understand the concept; especially the cross-section model of the rotor blades. Hodges proposed a comprehensive study for composite rotor blade modelling (Hodges, 1990: 561-565) and as many of the conventional helicopter rotor blades take that study as basis for cross section modelling, it is also considered as the baseline cross-section of the rotor blade.

One of the most structural part of the rotor blade is called flexbeam. Flexbeam is a flexible structural member that connects directly to the rotor hub plate in bearingless rotor systems, enabling flap, lead, and pitch movements (Brynes et al., 1994a). Flexbeam is generally made from either GFRP or CFRP materials, which provide advantages such as easy maintenance and manufacturing, reduced weight and complexity, and increased fatigue life and damage tolerance. It is attached to the hub plate with four bolts at the root section and is covered by a torque tube structure and snubber bearings at the same section. In this study, a rectangular shaped flexbeam is designed considering simplification of manufacturing and design operations.

The torque tube is an essential component that ensures equal distribution of the pitch link input among the rotor blade. It must bear high torsional stiffness to prevent any deformation during the transfer of torque. The connection between the flexbeam and torque tube is made through four bolts at the 50% rotor radius, along with snubber bearings mounted at the root area. The pitch link is connected to the swashplate crosshead at one end and the pitch lever, which is linked to the root of the torque tube, at the other. Whenever the swashplate assembly receives a control input, it directly affects the torque tube, resulting in a torsional motion that is transferred from the root section with the help of the snubber bearing and bolted joint section at the 50% blade span. Finally, the flexbeam and torque tube work together to produce a combined torsional movement that reproduces the necessary pitch input to the rotor blade. They not only accommodate torsional motion as well as flap and lag motions together (Brynes et al., 1994a).

The snubber bearing is positioned at the root of the blade and connects the flexbeam and torque tube, using a snubber retainer and film adhesives. It comprises of elastomer and metal shims to provide stiffness in different directions, as well as upper and lower plates for interfacing with the flexbeam and torque tube. The snubber provides two main functions: it transfers control inputs between the rotor blade and other components, and it centres the flexbeam with respect to the torque tube while eliminating relative torsional motion differences. Additionally, the snubber provides a path for current in the incident of a lightning strike. Essentially, snubber bearings are similar to elastomeric bearings that exists in articulated rotors, with the main difference being the loads they experience during flight (Brynes et al., 1992).

Skin assembly is divided into three main structures; hexagon honeycomb, upper and lower skin. The assembly is responsible for providing torsional stiffness and creating the airfoil shape. To meet weight and strength requirements, the blade skins are constructed using [45°/0°/-45°] fiberglass lay-up to increase torsional stiffness of skins lay-ups. Hexagonal honeycomb structure fills the gap between the skins, providing out-of-plane stiffness, damage tolerance, and structural integrity. Skins could be manufactured by hand lay-up method with the help of a tool and hexagon honeycombs mostly machined with the help of 5 axis milling machines. Once constructed, the skin and honeycomb structures are bonded together to create the aerodynamically functional region of the rotor blade. Afterwards, these parts are secondarily bonded and forms the skin assembly.

As a results, an overview of the baseline design for a bearingless tail rotor system could be seen in Figure 1.

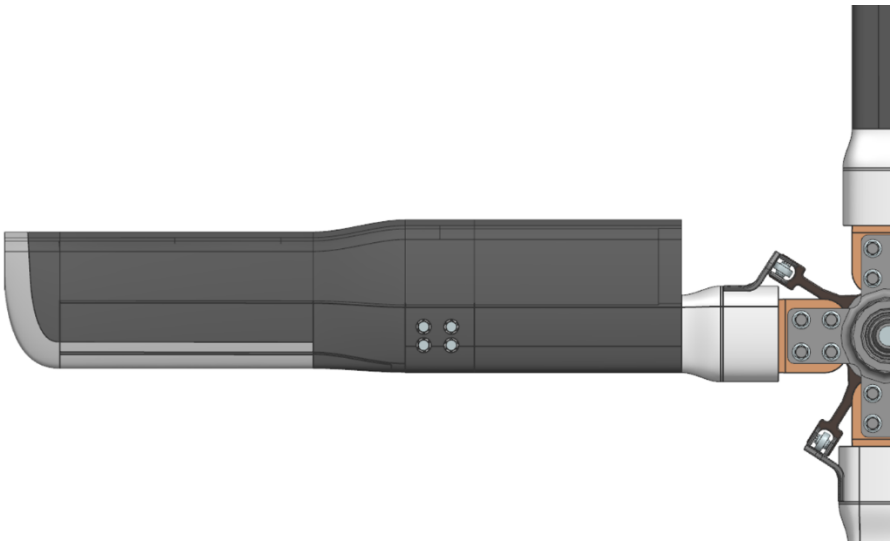

Figure 1. *Overview of the bearingless tail rotor system.*

4. Preparation of Baseline Design of Flexbeam

As mentioned previously, flexbeam is the most important component since it accommodates many principal loads as well as increases the motion spectrum of the entire rotor blade. Moreover, there is no standard design principle is available such as torque tube. The external shape and ply configuration is significantly specific to the designed helicopter model. Therefore, it is quite important to perform an initial sizing for a baseline design before starting optimization process.

In this step, it is aimed to divide flexbeam into several regions in order to assign specific capabilities to each region to accommodate load and motion spectrum in overall. This separation is based on tailoring capabilities of the composite materials, as known as anisotropy. It is aimed to take advantage of that tailoring capability and reflect it to the current design approach. The design of a flexbeam necessitates dividing it into three primary groups and two subgroups, which are known as HAR (Hub Attachment Region), ITR (Inboard Transition Region), PR (Pitch Region), OTR (Outboard Transition Region), and BAR (Blade Attachment Region), respectively (Brynes et al., 1994a).

HAR is responsible for creating an interface for attaching the rotor blade to the rotor hub. After performing some non-linear static analyses for bearing and bypass stresses acting on the holes, it is obtained that the interface should be provided with the help of four bolts in two rows, in total. The HAR is the most heavily loaded region in terms of forces and moments, and it has four Ø28 mm holes that necessitate an increase in the number of plies, particularly off-axis plies, to support bearing loads (Brynes et al., 1994b). During the design, transition fit tolerance range has been selected for hub interface holes in order to provide proper load transfer between flexbeam and rotor hub. The width and thickness of the HAR are uniform along the region as no flexibility is needed based on the design principle of the flexbeam (Brynes et al., 1994a).

ITR region is primarily designed to enhance the structure's flap-bending capacity by properly tapering the width and thickness to handle the flapwise and lagwise moments. Basically, ITR section is divided into two sub regions named as ITR-1 and ITR-2. ITR-1 is characterized by a thickness taper, while ITR-2 features both width and thickness tapering and a necessary width transition across the HAR. Both ITR-1 and ITR-2 utilize a combination of

(UD) unidirectional and off-axis ply configuration. The optimal length of the transition region should be determined based on two factors: the length of the transition region and composite drop-off design principles. During the development of that study, it is aimed to determine and finalize the proper length and width of ITR region to be able to ensure required motion of flap, lead and lag will be achieved (Brynes et al., 1994a).

The main function of the PR is to bear the torsional stresses across the length of the rotor blade. The pitch region plays a crucial role in managing torsional loads, minimizing control input loads, ensuring necessary edgewise buckling stability, and establishing the chordwise frequency of the rotor blade. The edgewise stiffness of the flexbeam is an important factor because it affects the first chordwise frequency of the structure, which is controlled by the PR. Therefore, proper checks should be done during sizing of PR in order to avoid ground resonance issue. Moreover, the outcomes of ground resonance for an articulated rotor system are investigated and validated by many researches that have been made in the past (Eckert, 2007). Therefore, it is quite significant to understand the dynamics of that phenomenon and take actions accordingly. Tuning the first chordwise frequency between 1.5-1.9 cycles/rev is a vital consideration in bearingless tail rotor applications, as it can avoid the requirement for a lag damper and prevent load amplification at the resonant harmonic frequencies of the rotor blade assembly. To avoid aeroelastic instability and load amplification, it is typically necessary to tune the first chordwise frequency between harmonic frequencies, like 1.0, 2.0, or 3.0 cycles/rev (Brynes et al., 1994a).

OTR is basically a transition region between PR and BAR and the only important parameter while designing is to follow the drop off ratio rules in order to avoid any excessive stress concentration at that region. Moreover, it is quite important to extend the PR as could as possible since it leads to reducing of the control loads. However, that extension leads to shortening of ITR and OTR or increasing the total length of the flexbeam. Extension is not an option since it is already finalized at the begging of the study while finalizing rotor radius. Besides, shortening ITR and OTR leads to excessive stresses and strains due to sudden transaction between thicker and thinner regions. For that reason, the optimum value should be calculated between these three regions during design step (Brynes et al., 1994a).

BAR is responsible for creating the required interface between the rotor blade and the flexbeam to ensure proper functioning of the rotor system. Designing of BAR quite critical since it is obviously a transfer region of most dominant load, which is centrifugal load (Brynes et al., 1994a). Double shear connection using two rows of four fasteners is employed in this region to ensure a secure connection between the flexbeam and rotor blade. As a result, Ø20 fastener holes with transition fit tolerance feature is selected. The width and thickness of BAR are consistent throughout the region, and its ply configuration is similar to that of HAR. Nonetheless, HAR is thicker as it is exposed to higher moments than BAR. In Figure 2., the regions of flexbeam could be seen.

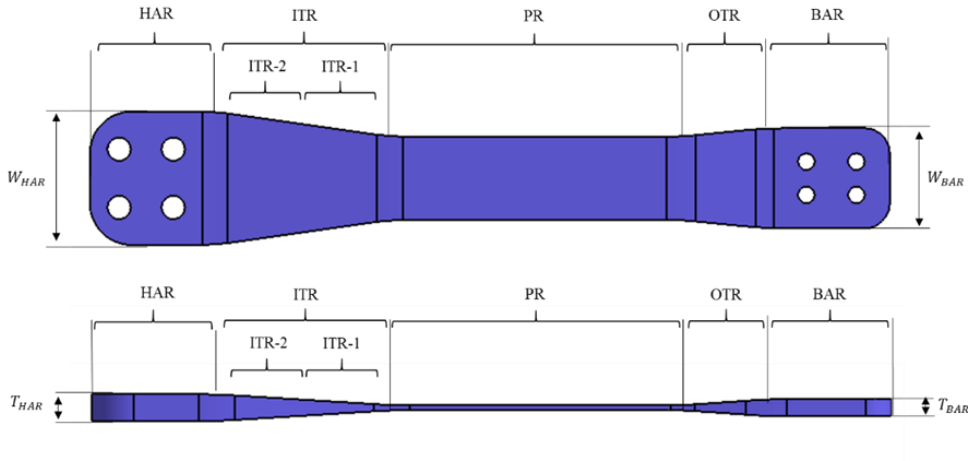

Figure 2. *Definitions of flexbeam regions.*

5. Structural Optimization Method

After finalization of the baseline design for the tail rotor system and blade components, optimization step could be performed. In this optimization, a three-stage special method for composite structures is used. Free-size optimization is the first step of the optimization process and it will be followed by size and shuffling optimizations, respectively.

Free sizing optimization is primarily focused on optimizing composite structures. The aim is to generate design ideas that explore all the possibilities of a composite structure while considering both the structure and the material. To accomplish this, a super-ply concept is implemented where each fiber orientation is assigned a free thickness super-ply. The approach of free-size optimization is distinct from topology optimization in that it doesn't strive to achieve a specific thickness. Rather, it allows thickness to vary between T0 and T for each element within a shell cross-section, as displayed in Figure 3.

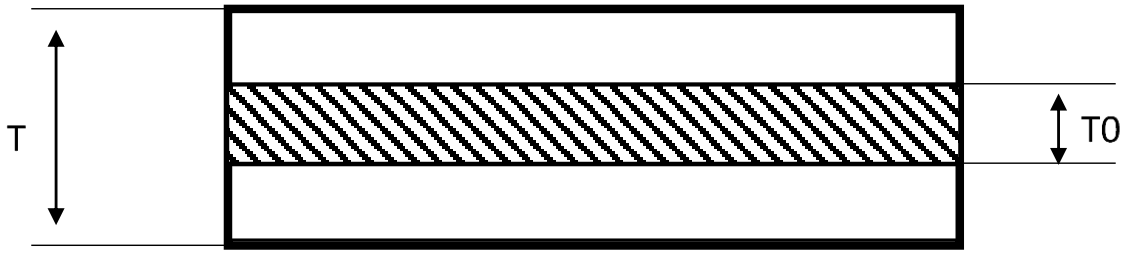

Figure 3. *Minimum and maximum laminate thickness constrain in free size optimization.*

In the design phase of free-sizing, SMEAR option is usually preferred to cancel out the impact of stacking sequence unless the super-ply laminate model follows the stacking preference. Moreover, free-sizing optimization comes with extra manufacturing restrictions. Generally, composite laminates go through a curing process after being stacked, and it has to adhere to certain manufacturing standards to avoid undesirable consequences (Goelke, 2021: 97).

The free size optimization process also provides valuable insights into the load paths within the structure. User could clearly visualize the load flow and could comment on it in post optimization step. This is quite significant since initially there was no idea about the load flow about the design because of complexity of the component interfaces. Although any orientation

can be utilized during the design, common orientations like 0°, ±45 and 90° are recommended to be more practical in terms of availability in markets and lay-up simplicity.

The process of sizing optimization involves adjusting the thickness of each layer within the laminate to achieve optimal results. Sizing optimization allows to check ply continuity across the zones and these zones could be tracked automatically, without the need for manual tracking of numerous zones. Moreover, sizing optimization also involves the refinement of adjusting manufacturable ply thicknesses instead of using super-plies anymore (Goelke, 2021: 98). This stage could be seen in Figure 4.

Free size and sizing optimization are the fundamental steps to perform a proper composite optimization. After these steps, designer will understand the behaviour of the structure that have different ply configurations. This provides visibility and allows designer to check and re-design the baseline design if needed. Additionally, sizing optimization allows to involve the manufacturing constraints to the optimization process to have more realistic results. Even though some manual adjustments are required in size optimization step, it is quite acceptable since the necessary manual operations have minor effect on the optimization process time. Moreover, during the modelling of the structure with using FEM and CAD software, it is quite important to use simplified and adjustable (parametric) features to reduce the time required to finalize the optimization process.

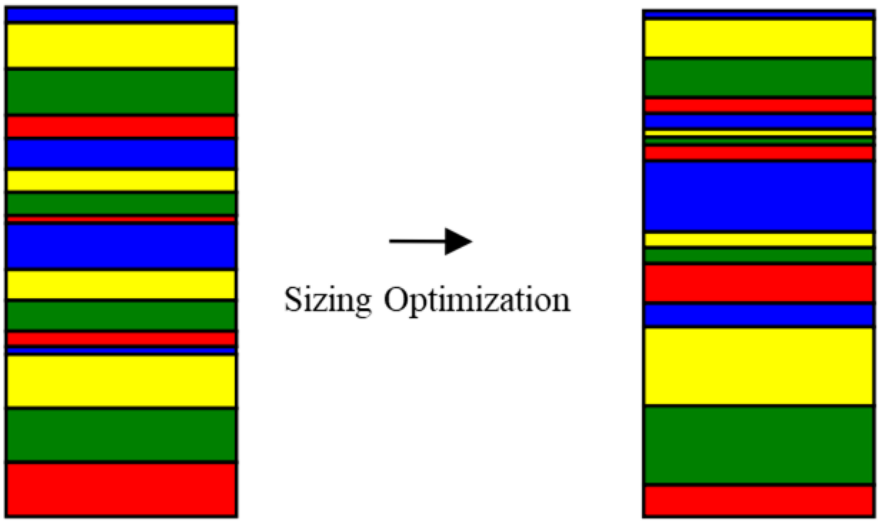

Figure 4. *Graphical representation of sizing optimization (Goelke, 2021: 98).*

Size optimization addresses the question of the exact number of plies needed for each ply outline to meet strength and manufacturing engineering requirements. Mathematical optimization algorithms are employed to optimize the ply thickness, size, and orientation of the structure iteratively, taking into account a variety of engineering constraints, including buckling strength, maximum stresses, composite strains, and deflections (Goelke, 2021: 98).

The free size optimization output model could be directly used as sizing optimization input. This could be done with adding FSTOSZ control card output to the free size optimization step and analysis could be run with that. This allows designer to transfer all required and pre-defined engineering and manufacturing constraints to the new analysis step which is sizing optimization (Goelke, 2021: 112).

Shuffling optimization is a stage in the optimization process of composite design that answers the question of finding feasible stacking sequences that meet the final manufacturing

requirements, taking into account various factors. This information consists of the part's dimensions, the outlines of the plies that create the sections of unchanging thickness, and the specific quantity of plies for each outline. The precise disposition of these plies to meet the manufacturing engineering requirements is yet to be determined and requires the use of composite shuffling optimization (Goelke, 2021: 99).

Shuffling optimization can be performed using the input data obtained from the size optimization phase. Similar to the transition from free-size to size optimization, output parameters from size optimization could be directly transferrable with using SZTOSH control card (Goelke, 2021: 116).

The DSHUFFLE bulk data card includes a MAXSUCC continuation line, which determines the maximum number of plies that can be successively stacked for a specific orientation. A characteristic cover stacking sequence is [-45/0/45/90], and it can be frequent as many times as needed. The plies on the top and bottom shells of the laminate are determined using the cover stacking sequence, which can be established by utilizing the COVER continuation line on the DSHUFFLE bulk data card. Moreover, the plies located in the centre of the laminate can be specified using a core stacking sequence that can be repeated as needed. A core stacking sequence, which establishes the plies on the middle surface of the laminate, can be defined using the DSHUFFLE bulk data card. This sequence can be repeated as many times as necessary and is set using the CORE continuation line (Goelke, 2021: 118). For an overview of the shuffling optimization process, see Figure 5.

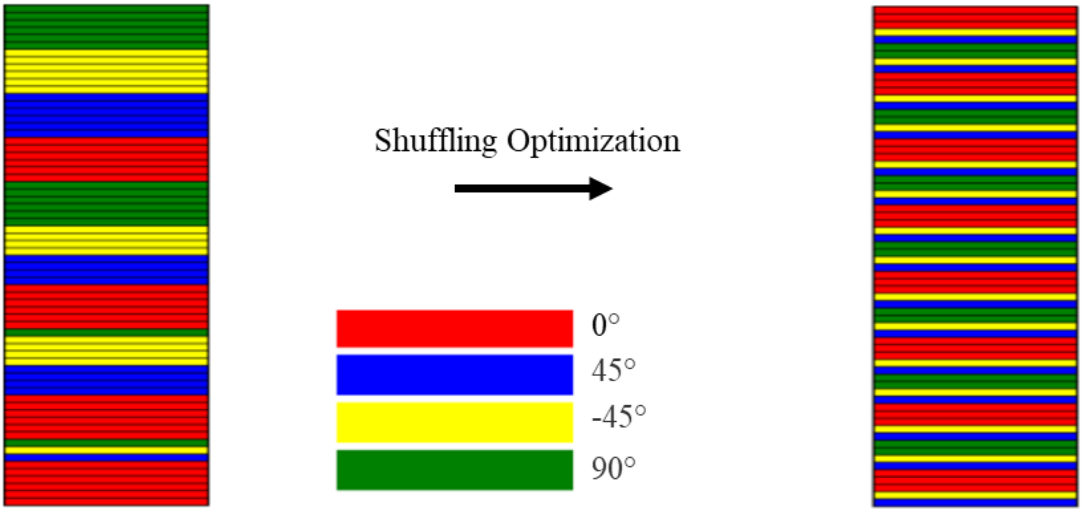

Figure 5: *Graphical representation of shuffling optimization (Goelke, 2021: 118).*

6. Validation of Flexbeam and Torque Tube Baseline Designs

Optimization of rotor blade is concentrated on two main primary components; flexbeam and torque tube. These two parts are selected because they are primary structures for bearingless tail rotor blade design and as weight, they have the biggest pie on weight percentage. It is aimed to first validate the strength of the baseline designs under centrifugal force since this is the most dominant force compared to the flight loads.

The baseline flexbeam design is generated with the help of patents (Brynes et al., 1994a & Brynes et al., 1994b). Optimization process will be constrained by the values obtained from the required motion envelope. The composite strains experienced by the flexbeam will also be

used as another constraint. In the end, the optimized flexbeam should operate properly under the constrains that is given at the beginning. The optimization's objective is to create a flexbeam design that can accommodate the necessary motions while minimizing mass and maximizing stiffness. In order to reduce complexity, the thickness and ply orientation is kept as simple as possible for both flexbeam and torque tube components. Basically, this leads to a flexbeam which has constant thickness along the spanwise and chordwise directions. As a result, the baseline design for the flexbeam can be seen in Figure 6.

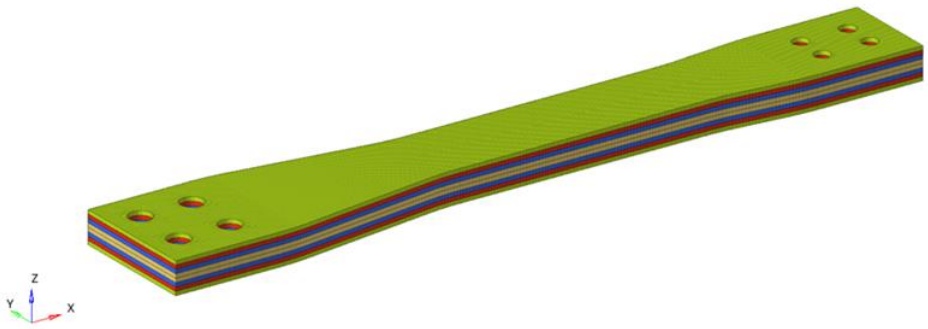

Figure 6. *Baseline design of flexbeam.*

The purpose of the non-linear static analysis with using only centrifugal load is to investigate the behaviour of the flexbeam under most dominant load and also to understand some of its modal characteristics. The laminate is constructed from plies with orientations of 0°, ±45°, and 90°, with each ply having a total thickness of 10mm. Carbon/Epoxy material is selected because of high strength and lower density features. The predominant function of the 0° plies in the laminate is to support the centrifugal load. The +45°/-45° plies are employed to resist in-plane shear forces, while the 90° plies are used to resist transverse loads during operation. After the free size optimization is finalized, the percentage of ply orientations that is required for the flexbeam to withstand flight loads will be determined. Finally, the baseline laminate complies with composite guidelines and is symmetrically balanced, as presented in Figure 7.

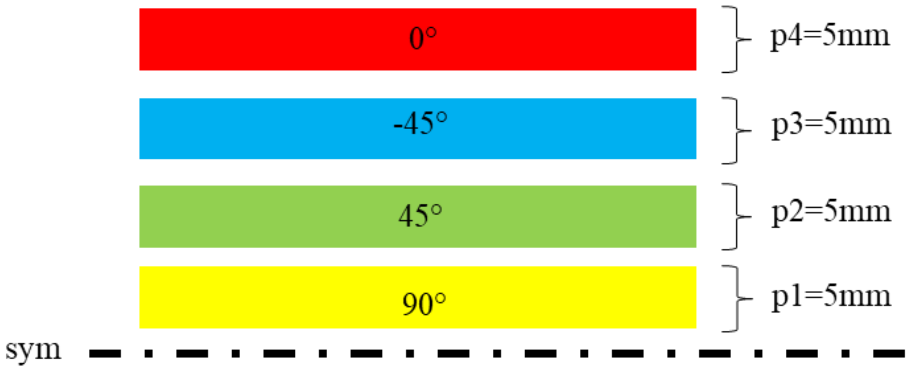

Figure 7. *Baseline ply configuration for flexbeam.*

Two subcases will be carried out during the optimization process: the first subcase entails applying centrifugal force and observing the structure's response under high axial load, while the second subcase involves performing modal analysis to understand the component's modal behaviour. The flexbeam's root region holes are clamped, and force is applied to the tip region holes. Note that other inertial loads are extracted by applying a RESTRAT analysis in NASTRAN solver and importing these SOL103 and SOL106 outputs to ADAM's Multibody

Dynamic Solver software (Xiaocheng, 1999: 2-5). Moreover, the effect of centrifugal stiffening is included during the modal analysis. To make the analysis easier, the calculated centrifugal force is multiplied by a safety factor of 1.5 and distributed equally among four equivalent holes. The analysis setup employs a total of 11,201 nodes and 10,740 quad shell elements, with the Tsai-Wu method chosen as the failure criteria.

The Rigid Body Element (RBE) method is employed for the fixed and force application points in the analysis. RBEs act as a Multi-Point Constraint (MPC) that can connect multiple nodes to one node or vice versa. The two most frequently utilized RBE types are RBE2 and RBE3, which will be used extensively in this study. By linking an independent node to numerous dependent nodes without any degrees of freedom in relation to each other, the RBE2 method introduces extra stiffness to the component, which can result in slightly different outcomes than anticipated. For example, due to the additional rigidity, the modes of the structure may have shifted upwards. Nonetheless, the RBE2 method can be valuable in describing fixed joints because the nodes at these joints are practically rigid to each other.

RBE3 is different from RBE2 in that the reference node is a dependent node and the linked nodes are independent. This allows for relative motion between the independent nodes, which makes load and moment applications more accurate by avoiding additional stiffness generation. The loads or moments applied are distributed among the independent nodes according to their weighting factor. In the flexbeam analysis, RBE2 is used at the clamped end and RBE3 is used at the force application locations.

The first step of the analysis is to perform a linear static analysis with only the centrifugal load, as mentioned previously. The baseline design uses 0°, ±45°, and 90° plies equally, and it is necessary to ensure that the design can tolerate the centrifugal load. A basic approach is used for the analysis; if flexbeam could accommodate centrifugal load with the baseline design, it could be said that flexbeam could also could accommodate other loads because for the baseline design it is intended to create a quasi-isotropic structure.

The decision to perform a non-linear static analysis only is based on the belief that the deflections in the spanwise direction will be negligible however the load-deflection relationship will be non-linear. Furthermore, performing a non-linear static analysis enables a better understanding of the component's behaviour under loads, as the load is incrementally applied and the component has enough time to reach equilibrium. Figure 8 indicates the deflections, composite strains and stresses, respectively.

Additionally, modal analysis is carried out to assess the risk of ground resonance effects and determine the natural frequencies of the structure. The first three modes are examined to identify any critical frequencies that may coincide with the landing gear frequencies and cause resonance issues. This analysis must be performed and confirmed at this stage of the design development otherwise could cause some issues at the latest stages of design. After optimization, it is important to ensure that the natural frequencies of the rotor blade are not significantly altered. Therefore, modal analysis is a crucial step to avoid any unexpected resonance problems. Figure 9 represents the results of the modal analysis.

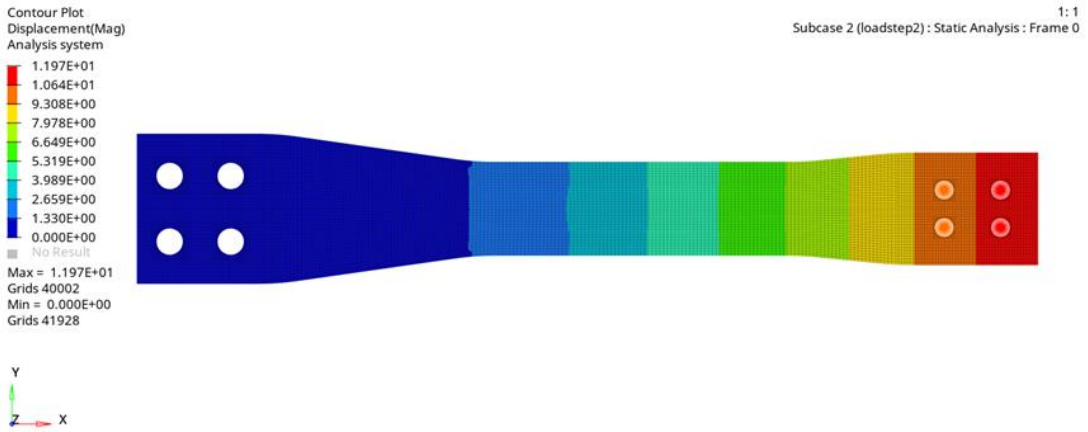

(a) Displacements.

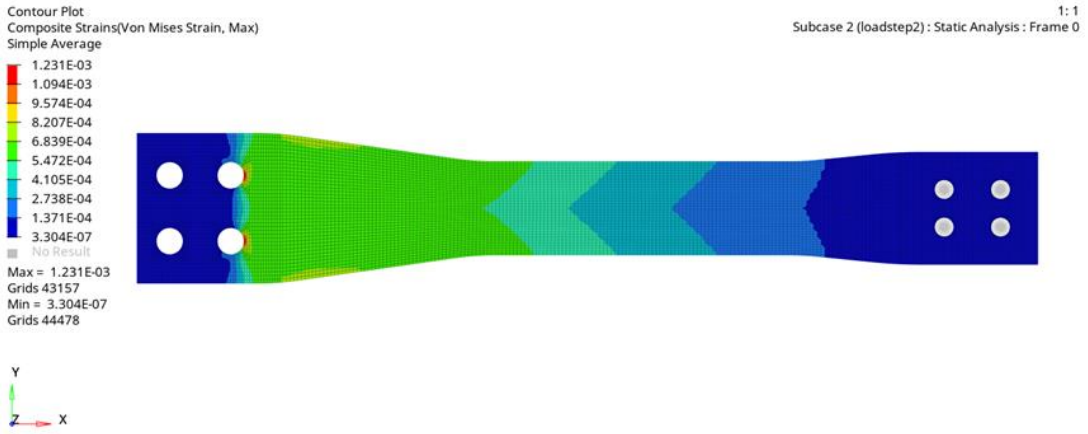

(b) Composite strains.

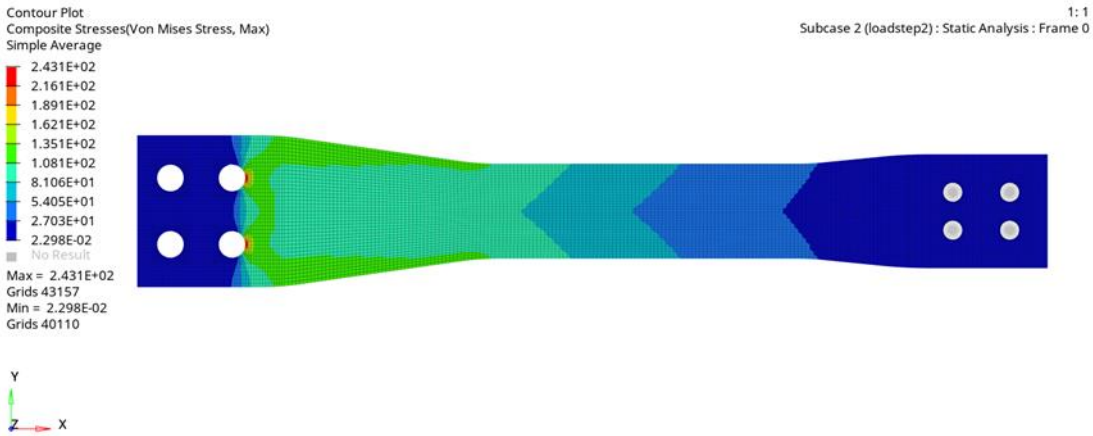

(c) Composite stresses.

Figure 8. *Displacements, strains and stresses on baseline flexbeam under centrifugal load.*

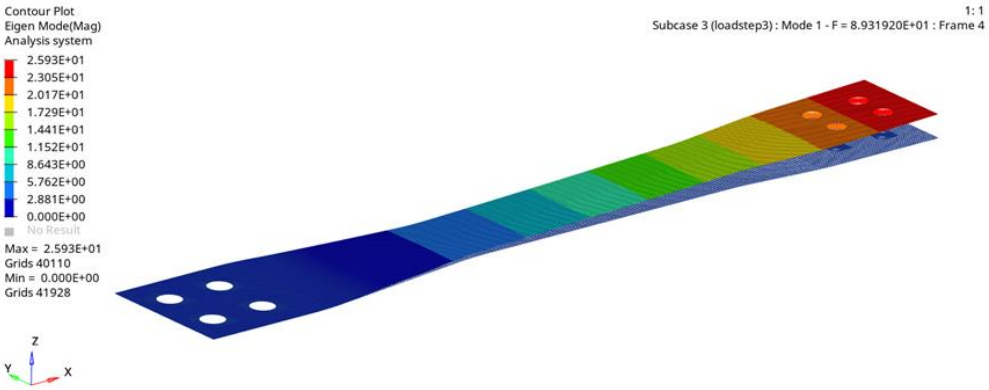

(a) First mode.

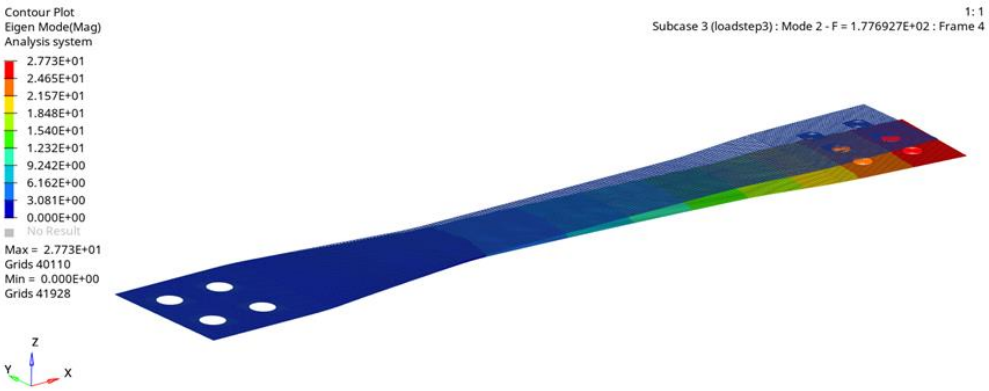

(b) Second mode.

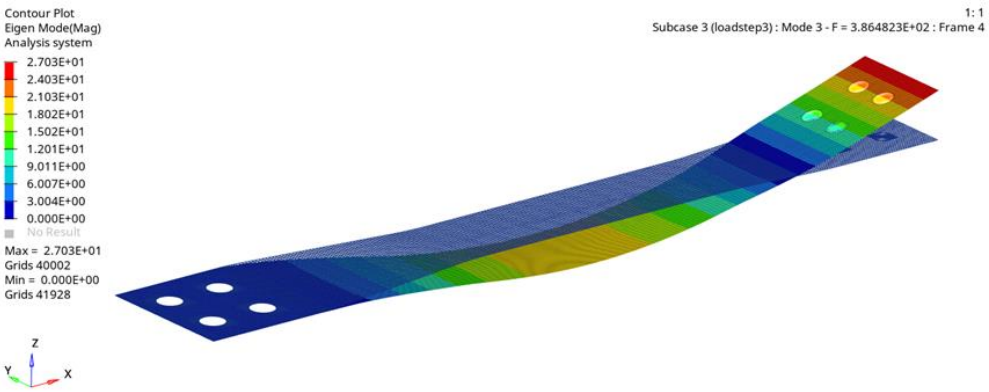

(c) Third mode.

Figure 9. *First three modes of baseline flexbeam with centrifugal load.*

Moreover, a very similar approach will be performed for also another primary structure which is torque tube. The torque tube plays a crucial role in the bearingless rotor system by ensuring that the pitch is distributed equally across the entire length of the rotor blade. It is typically a hollow, cylindrical, or elliptical structure that runs nearly the entire length of the blade tip. Additionally, the pitch input provided by the pilot is initially transmitted to the swashplate assembly and then to the pitch link, pitch lever, and torque tube, respectively. Finally, torque tube provides a bridge between flexbeam and the other rotor blade components. Flapwise and lagwise movements are primarily controlled by the flexbeam, whereas the torque tube is responsible for managing torsional (pitch) loads. The design aims to maximize

compliance and minimize weight while maintaining torsional stiffness. Figure 10 shows the baseline design of the torque tube.

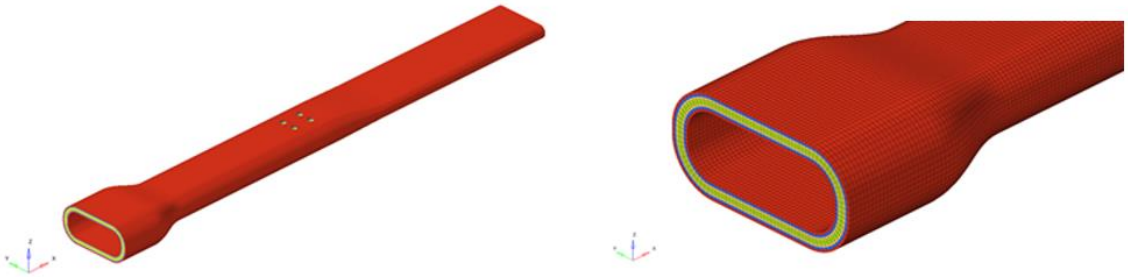

Figure 10. *Baseline torque tube design.*

Torque tube is connected to the flexbeam at two locations, specifically the snubber attachment area (STA300) and the bolted joint connection (STA950 and STA1010). Both the torque tube and the flexbeam are dynamic components that are interconnected, so the analysis of the torque tube is carried out with the flexbeam, and the fasteners are also taken into account. The boundary conditions can be seen in Figure 11.

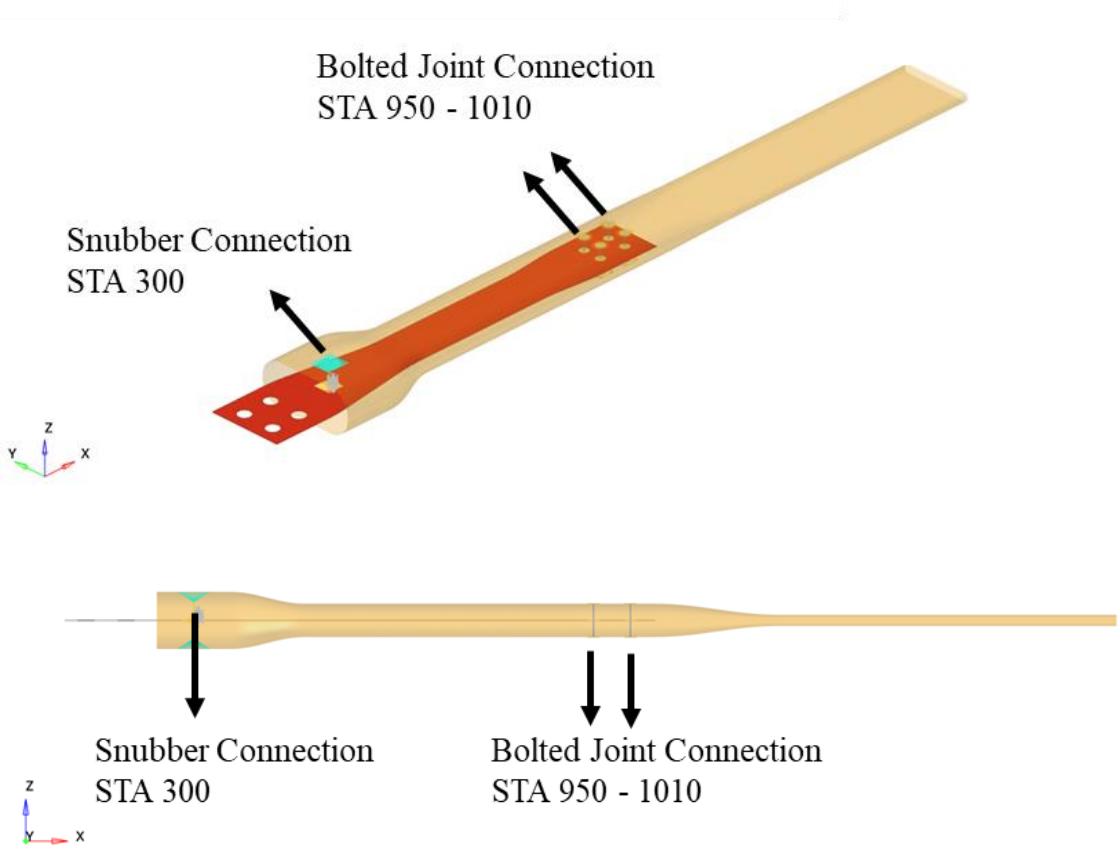

Figure 11. *Boundary conditions of torque tube.*

Definition of torque tube boundary conditions for the inward (root) section starts with definition of contact area with the snubber. For that definition, RBE3 is the best coupling element to describe the relative motion between these two components. Once the contact nodes for flexbeam and torque tube are determined, they are connected to form a dependent node.

Consequently, two dependent nodes have created and these two dependent nodes is connected with CBUSH element type which allows to define stiffness and damping values for each direction. This flexibility of defining antistrophic stiffness values for snubber is the crucial point, otherwise the proper contact between flexbeam and torque tube could not be defined successfully. As in Figure 12, the snubber is modelled as a spring-damper model. Additionally, in the bolted joint region between STA950 and STA1010, fasteners are represented using CBAR element type. CBEAM element type enables the fastener to be depicted with particular stiffness and strength values. Structural steel S450 is chosen as the bolt material based on EN1993-1-1 §3.2.6 standards.

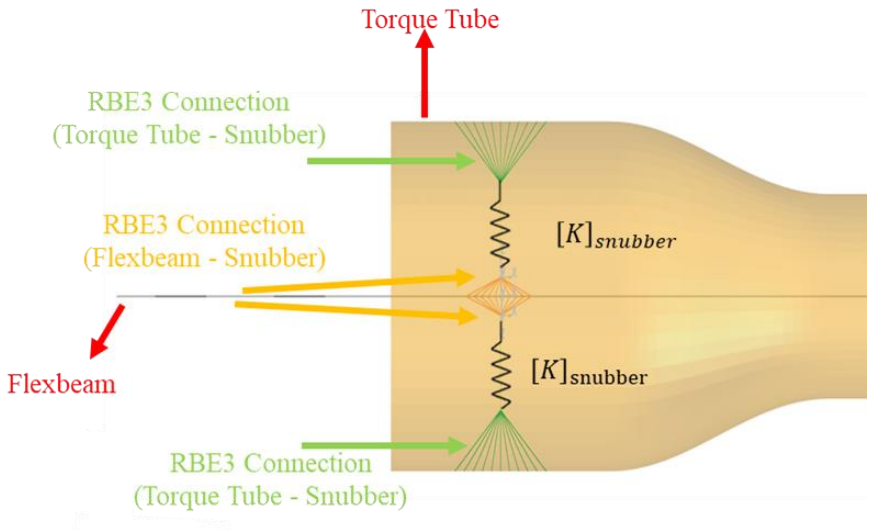

Figure 12. *Root side connection of torque tube.*

Because of the nature of the design, the fasteners are placed perpendicular to their principal axis. This leads to an excessive shear and bending moments on the both root and blade fasteners. As a result, that non-proper positioning leads to enlarging of the root and blade fasteners than it is calculated. For the fasteners that will be used to connect flexbeam and torque tube, Ø20 mm fasteners are planned to use for both flexbeam and torque tube with a transition fit characteristic. In order to evenly distribute the load to separate nodes located in holes, the RBE3 connection type has been chosen over RBE2 as it does not cause any additional stiffness to the structure. The RBE3 method facilitates the clear observation of shear stresses and strains that are present in bolted joints. Therefore, a four-bolt connection, as shown in Figure 13, is used to connect the flexbeam and torque tube at the bolted joint region.

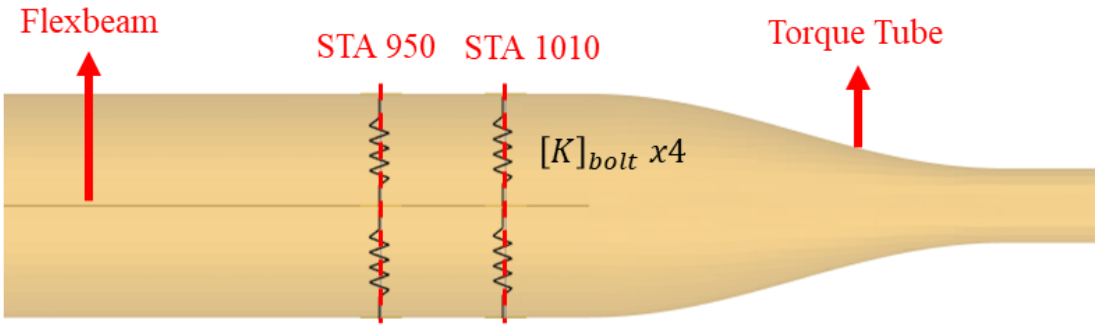

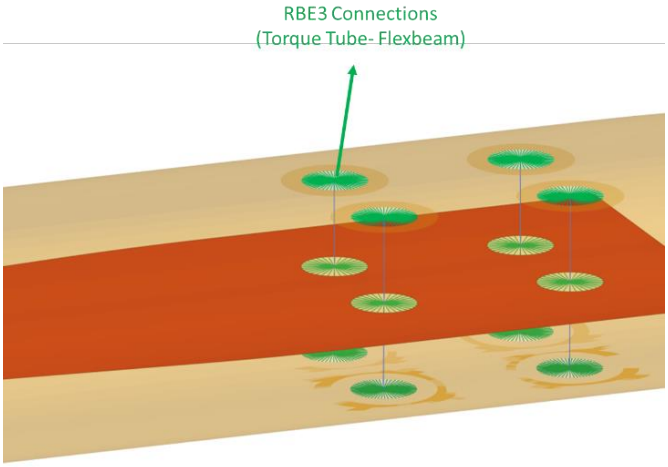

Figure 13. *Torque tube – flexbeam connection at STA 950 and STA 1010.*

The same stack up and orientation are employed for the super ply concept with flexbeam in the baseline design of torque tube, with the only difference being varying thicknesses. The laminate includes plies with orientations of 0°, ±45°, and 90°, and each ply has a total thickness of 5 mm, as shown in Figure 14.

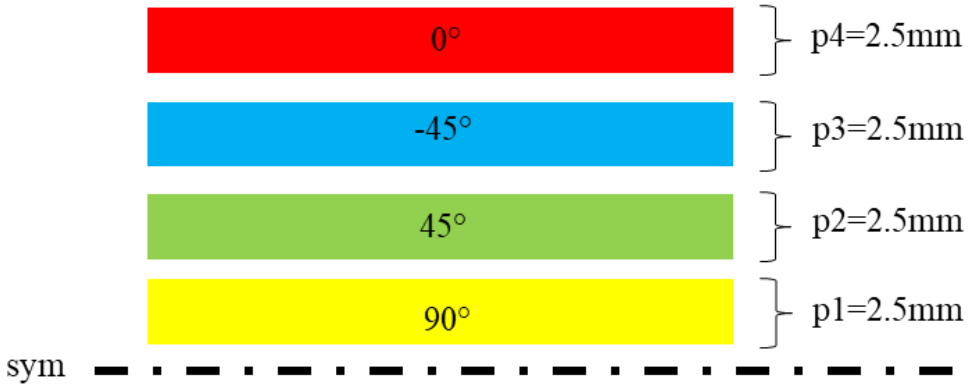

Figure 14. *Baseline ply configuration of torque tube.*

The analysis and optimization phases will incorporate a balance and symmetry condition as a constraint. As a result, the final laminate, much like the one utilized in the flexbeam, will be symmetric and balanced. Furthermore, aerospace standards specify specific drop-off ratios and maximum numbers of successive plies. In this study, these values remain the same as in the flexbeam design, with a drop-off ratio of 1:20 in the main load direction and 1:10 in the perpendicular direction, and a maximum successive number of plies for each orientation set to 2. Finally, Carbon-Epoxy material is nominated for torque tube design.

Following the analysis setup, the initial analysis for the baseline design was executed. Figure 15 briefly indicates the displacements of the flexbeam, torque tube, and snubber, respectively.

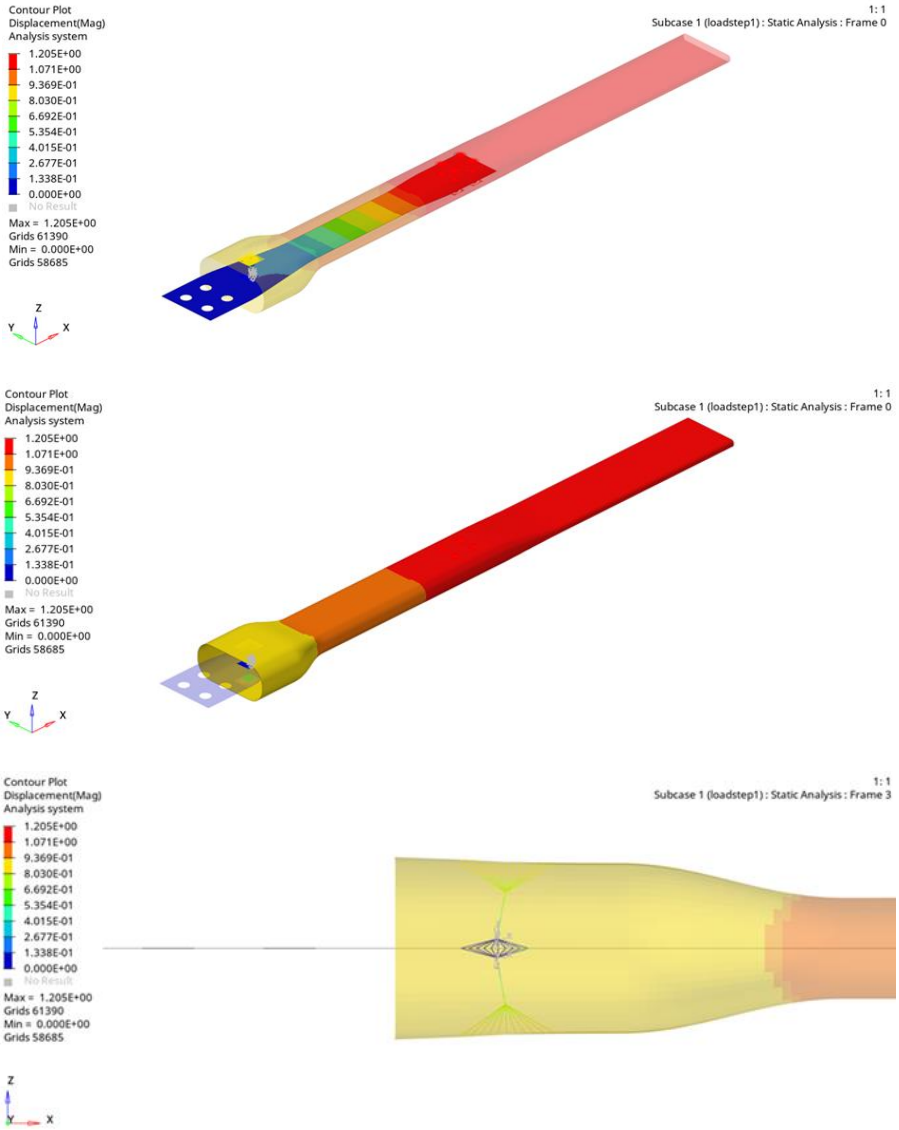

Figure 15. *Displacements of flexbeam, torque tube and snubber components under centrifugal load, respectively.*

Additionally, the stresses and strains were analysed after the initial assessment, as illustrated in Figure 16. The root region, which is the most critical region in terms of strength, showed no indications of strain or stress issues.

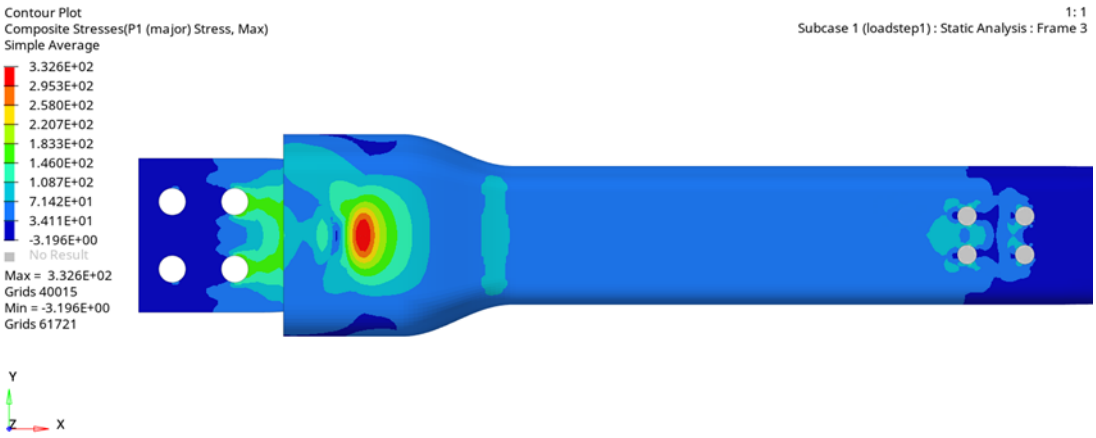

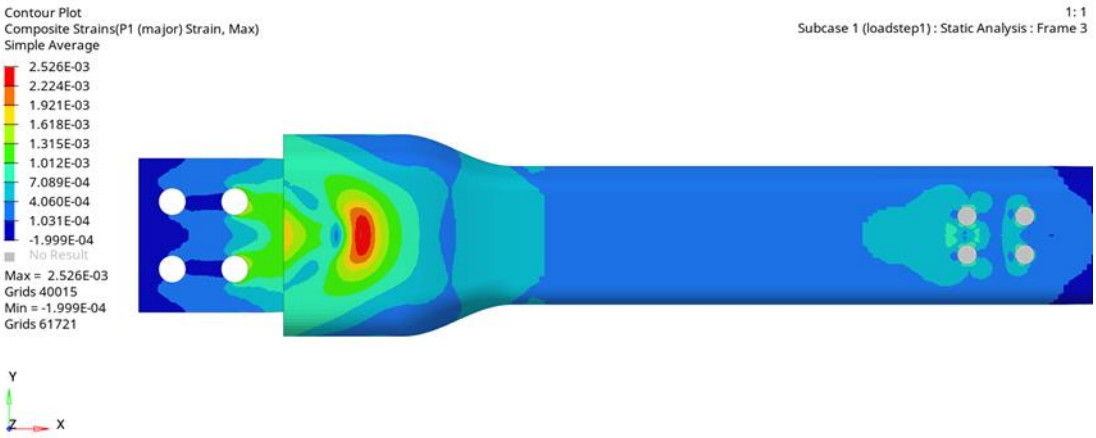

Figure 16. *Stress and strain levels on torque tube root under centrifugal load.*

7. Structural Optimization of Flexbeam and Torque Tube

The optimization will follow the sequential steps; free size, size and shuffling optimization. For all optimization steps, entire flexbeam and torque tube model will give as design space to the solver. For flexbeam, as a design constrain, the minimum laminate thickness is given as 10 mm as well as maximum values is 40 mm. Performing a non-linear static analysis to the baseline design gives much information about what should be the thickness range is. Moreover, the balance, symmetry, and the drop off ratio is given as inputs.

The optimization process aims to minimize mass, compliance, and keep the static displacement in range in the z direction (flapwise direction). It is essential to keep the tip deflection of the flexbeam between 45-50 mm in the flapwise direction and is considered an engineering constraint in the optimization process as a design constraint at the beginning.

It is essential to monitor the iterations, outputs, and deviations from objectives at the beginning of each optimization step. Analysing each iteration step in detail from the output text file is vital since it provides valuable information about the optimization's direction for the structure and what might cause the optimization to fail. The mass and compliance outputs were thoroughly investigated in this study by analysing the output text file. Moreover, the effect of the manufacturing constraints on the engineering parameters was assessed and controlled, as presented in Figure 17.

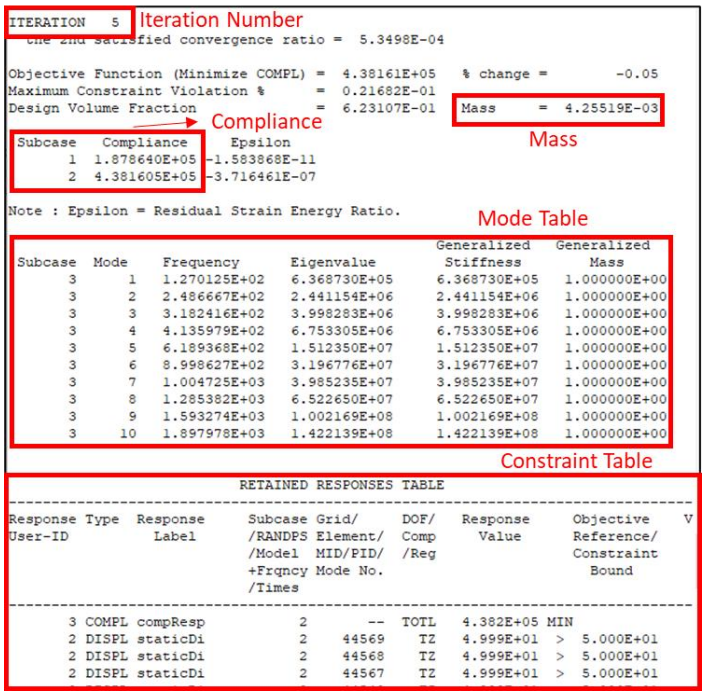

Figure 17. *Flexbeam optimization parameters control panel.*

In Figure 18, the thickness distribution of 0°-90° and ±45° plies can be observed after the free size optimization.

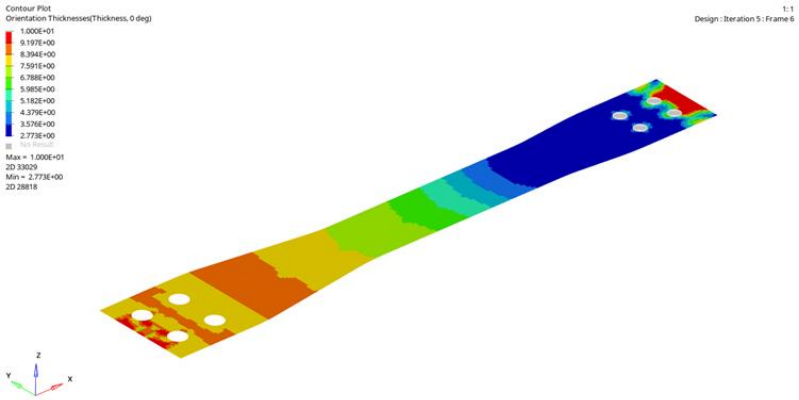

(a) 0°-90° superply thickness output.

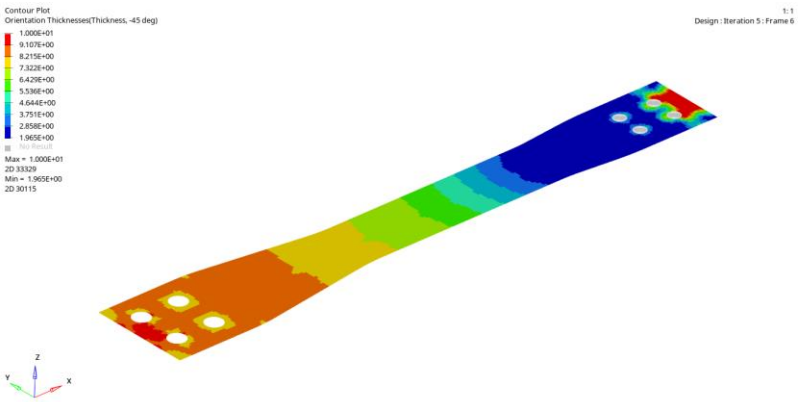

(b) ±45° superply thickness output.

Figure 18. *Flexbeam laminate and ply thickness output from free size optimization.*

One of the most important outcomes of performing size optimization is to understand the load paths, as mentioned before. It is quite significant that the HAR, ITR, PR, OTR and BAR regions are shaped automatically (without giving any additional constraints) as mentioned before. This is a milestone for the optimization since it clearly indicates that the boundary conditions, manufacturing and engineering constraints are applied correctly. As it is predicted previously, the thicknesses of HAR and BAR regions are quite thicker than the other flexbeam regions. In Figure 18, the thicknesses of the 0° - 90° and -45° - +45° plies are not separated each other because this is a symmetric and balanced laminate and it is enough to only indicate one of them. Moreover, during the optimization, the software identifies the reason for optimization failure if a feasible design cannot be reached due to engineering or manufacturing constraints, making it straightforward to resolve during the analysis.

Both 0° and 45° plies have thickest regions of 10 mm and thinnest regions of 2.773 mm and 1.965 mm, respectively. Currently, the optimization loop does not include constraints for manufacturable or cured ply thickness, but this information will be incorporated in the size optimization step. The output of the free size optimization is presented in Figure 19.

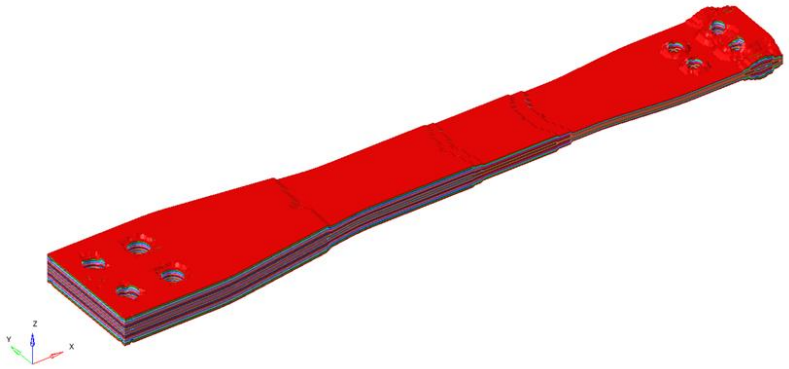

Figure 19. *Output of the free size optimization for flexbeam.*

As stated earlier, the free size optimization typically does not produce designs that are easy to manufacture. Nonetheless, this stage is critical for understanding the function and load distribution. The plies identified by the free size optimization presented in Figure 19 will be refined through size optimization and with the help of manual modifications.

Figure 20 indicates that the ply shapes is to reorganized and adjusted to address practical manufacturability concerns. To achieve this, some modifications to the FEM are necessary, consisting of adding or subtracting elements from the 2D FEM model. This process must be performed for each ply generated during the size optimization step and according to experience it gives more accurate results to perform in manually.

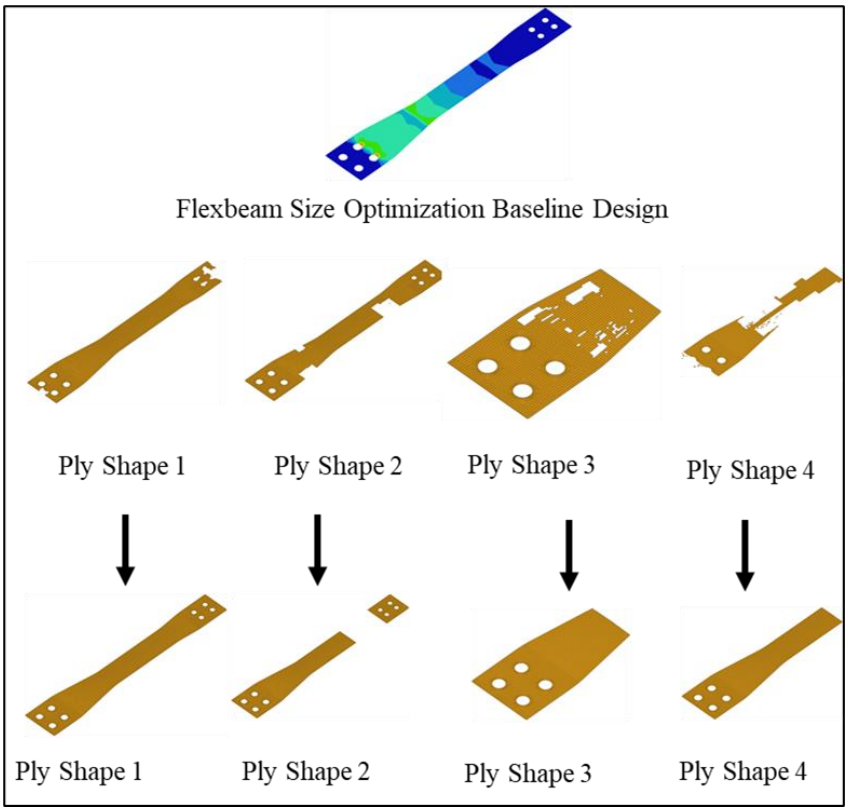

Figure 20. *Edition of flexbeam ply shapes manually.*

The weight of the flexbeam was lowered from 8.474 kg to 4.255 kg in this step, demonstrating that the baseline structure was over-engineered as a laminate. Other important point of discussion is that during the optimization, the structure's compliance hardly changes; it was initially 438160 mm/N and increased to 586160 mm/N. This suggests that the weight of the structure was nearly halved while the stiffness remained in range. After obtaining the all results from free size optimization, this information could be transferred to the sizing optimization. An easy and swift way to perform this is to using FSTOSZ control card. All information from free size optimization could be transferred to the sizing optimization with adding that control card to the output card section. Afterwards, a new analysis window could be opened and the free sizing results solver deck could be directly imported to the new sizing optimization study.

One notable aspect of the free size optimization phase is the discrepancy in the number of plies between the two stages. As explained earlier, the baseline design only had four plies, but after free size optimization, the number of plies increased to 16. The variation results from the solver dividing all the superplies into four subgroups. This segmentation leads to more distinct ply quantities after the sizing optimization process, where the manufacturable ply thicknesses are set. Additionally, the solver incorporates one design variable for each ply, which represents the design space. In summary, there are 16 design variables for 16 plies.

Furthermore, the menu depicted in Figure 21 enables the user to specify the manufacturable ply thickness for each ply. Additionally, the thickness assigned to each ply by the solver is visible in this menu. The menu also allows to show the pre assigned thickness that is coming from free size optimization, basically user able to see the thickness of each superply generated by free size optimization. During this phase, alterations can be made to the design space, ply shapes, ply orientation, and base material. Nonetheless, these parameters are maintained the same as in the free size optimization in this study. Lastly, the manufacturable

ply thickness parameter is set to 0.5 mm for all optimizations that is performed in this study. The industrial ply thicknesses are varying between 0.1 mm to 0.25 mm (there could be exceptions), however, using such thin ply thicknesses in the optimization loop extending the process time, consumes more CPU memory and slows down the procedure. To overcome that issue, a simple approach will be used: 0.5 mm single ply would also mean two times 0.25 mm ply and five times 0.1 mm ply. If any practical reasons could require some changes in the optimizations, this will be handled by using that "multiples" approach.

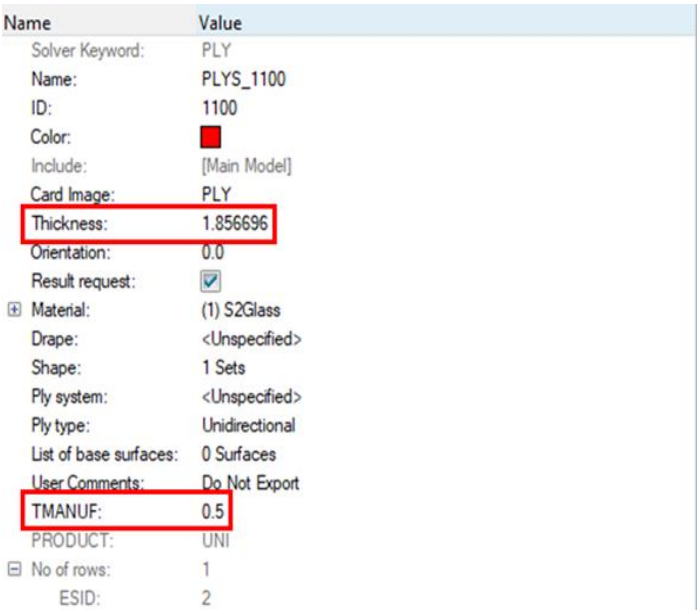

Figure 21. *Manufacturable ply thickness input to the flexbeam size optimization.*

The ply shapes and thickness distribution along the flexbeam can be observed in Figure 22 after all parameters are defined and some plies are modified manually for practicality.

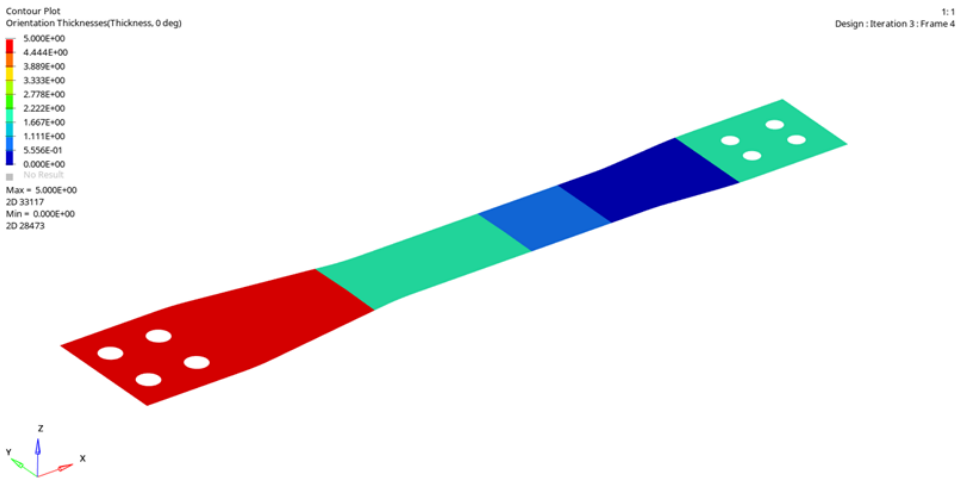

(a) 0° and 90° ply thickness distributions

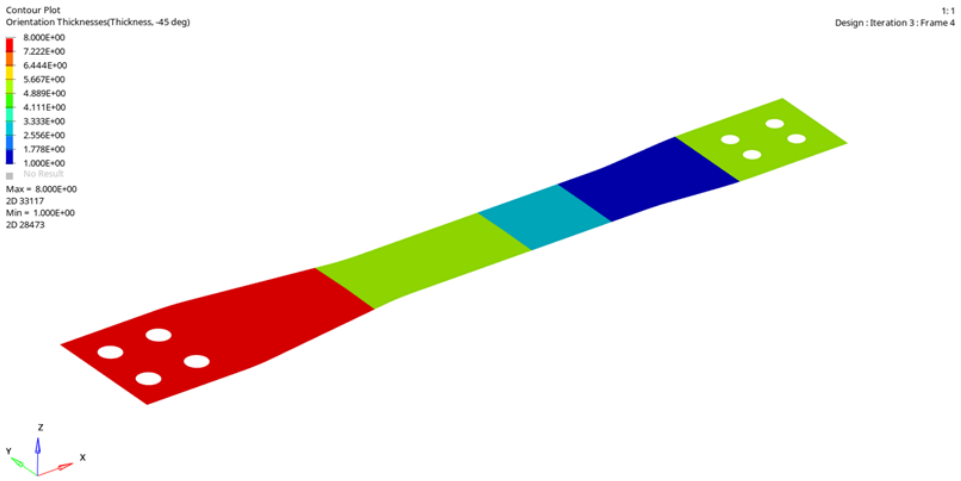

(b) 45° and -45° ply thickness distributions

Figure 22. *Ply thickness distributions after sizing optimization of flexbeam*

The 3D shape of the flexbeam after sizing optimization is depicted in Figure 23. The weight of the structure decreases from 4.255 kg to 3.375 kg in this phase. Furthermore, the compliance increases from 586160 mm/N to 626639 mm/N. The structure experiences a slight softening after the sizing optimization, but this is advantageous in terms of the engineering targets for the flapwise and torsion wise directions. Also, a weight reduction of around 20% is accomplished in this stage, which is highly beneficial for the overall weight of the rotor blade.

As performed during the transition between free-size to sizing optimization, there is one control card that could transfer all the information of results coming from sizing optimization. SZTOSH control card will perform this transfer and the output of the sizing optimization could be imported as a solver deck directly to the new shuffling optimization step.

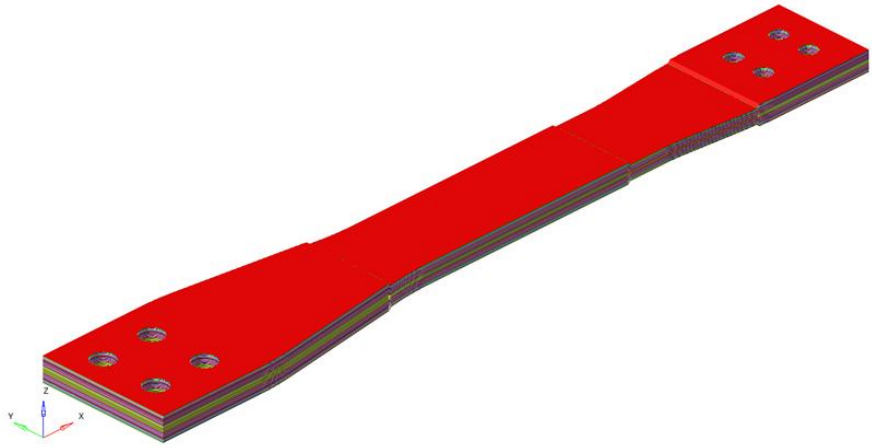

Figure 23. *Output shape of flexbeam after sizing optimization*

The shuffling optimization environment demonstrates that the number of plies has been altered again after importing the size optimization solver deck. The user can manage this parameter by imposing a manufacturing thickness constraint. As shown in Figure 24, the number of plies is changed from 16 to 30. This is an outcome of the solver has applied 0.5 mm manufacturable thickness constrain to all superplies.

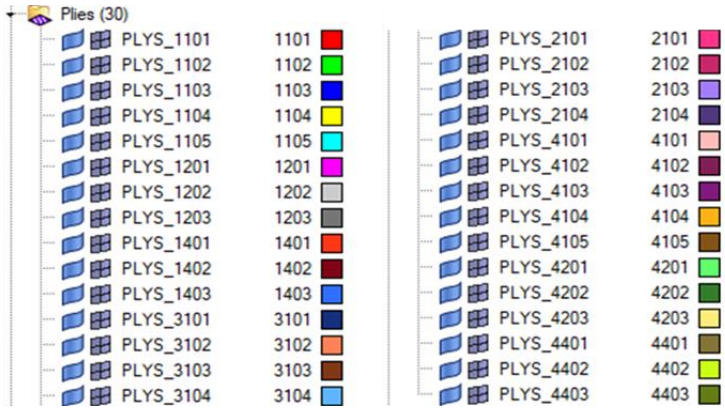

Figure 24. *New ply configuration after sizing optimization.*

This step also includes placing limitations on the maximum successive ply and the pairing of 45° and -45° ply. During this optimization phase, the maximum successive plies for each orientation are restricted to 2. Besides, another parameter is defined for using 45° and -45° plies as the outermost covers since it would enhance the damage tolerance of the structure. The setting of these parameters is demonstrated in Figure 25 and 26

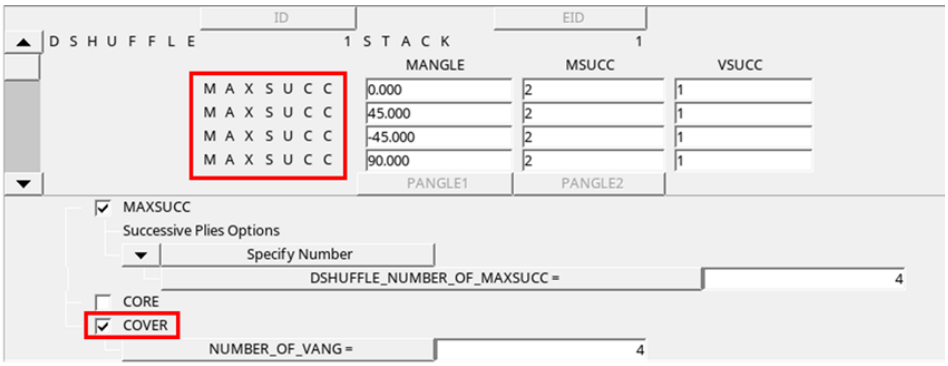

Figure 25. *Setting of maximum successive plies and cover ply for each orientation.*

Figure 26. *Setting of pairing for 45° and -45° plies as design constraint.*

With the shuffling optimization setup complete, the solver can initiate the optimization process that comprises shuffling optimization and non-linear analysis, yielding results as depicted in Figure 27.

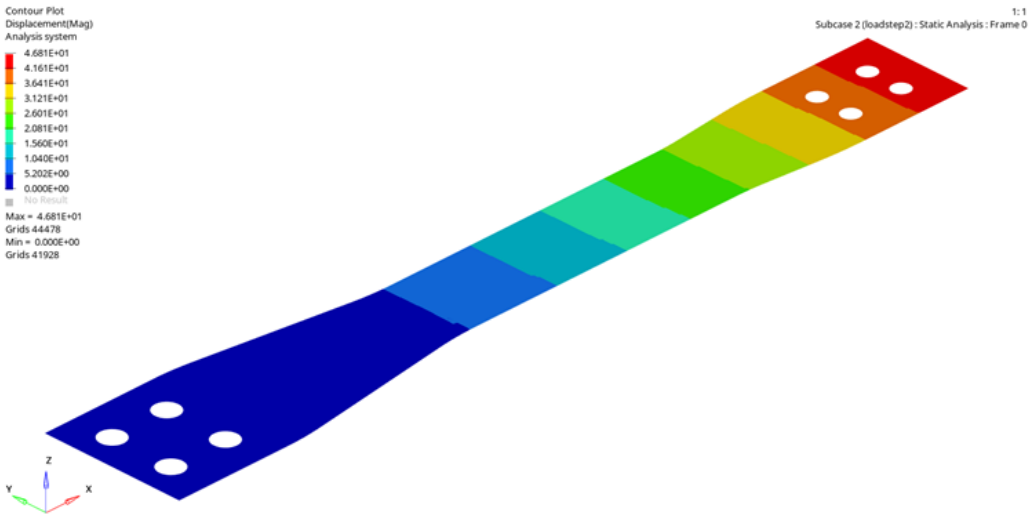

(a) Displacements.

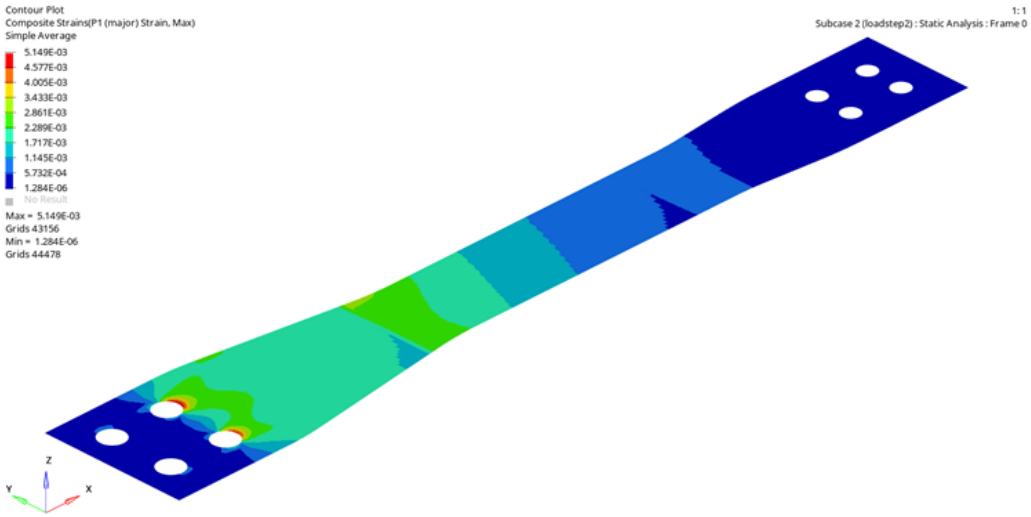

(b) Composite strains.

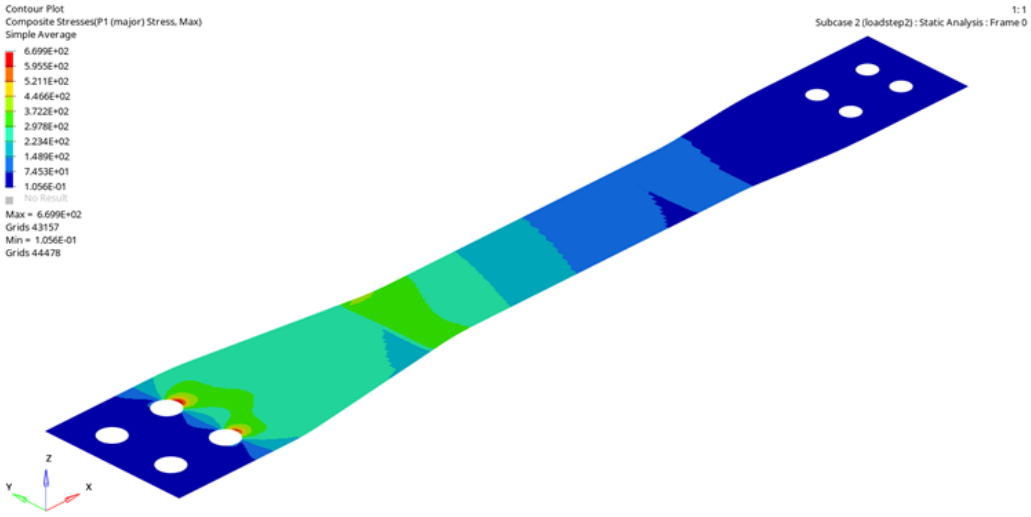

(c) Composite stresses.

Figure 27. *Displacements, composite strains and stresses after shuffling optimization of flexbeam*

Eventually, the mass is reduced from 3.375 kg to 3.36 kg during this step. The compliance has remained almost the same at 645256 mm/N. Thus, the structure has become softer to some extent, but this doesn't significantly impact its behaviour since the difference is negligible. Following all of the optimization steps, the final flexbeam structure is presented in Figures 28 and 29.

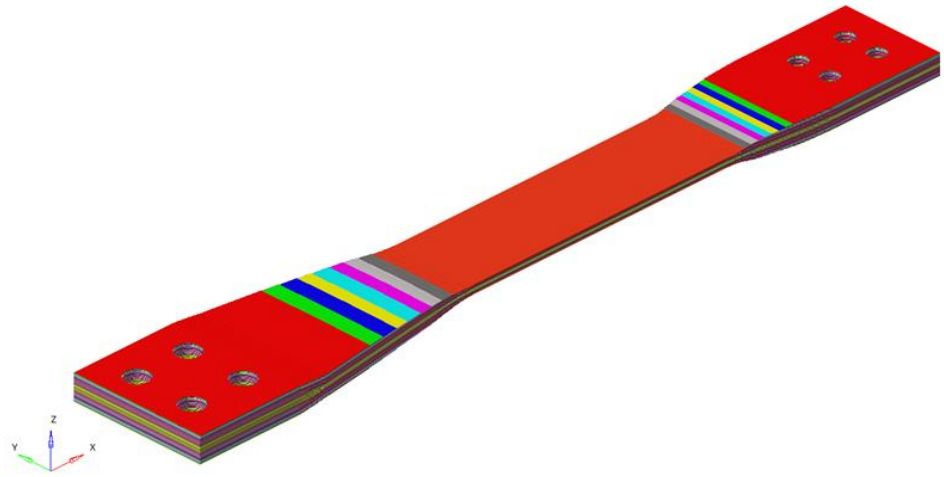

Figure 28. Final flexbeam structure after optimization.

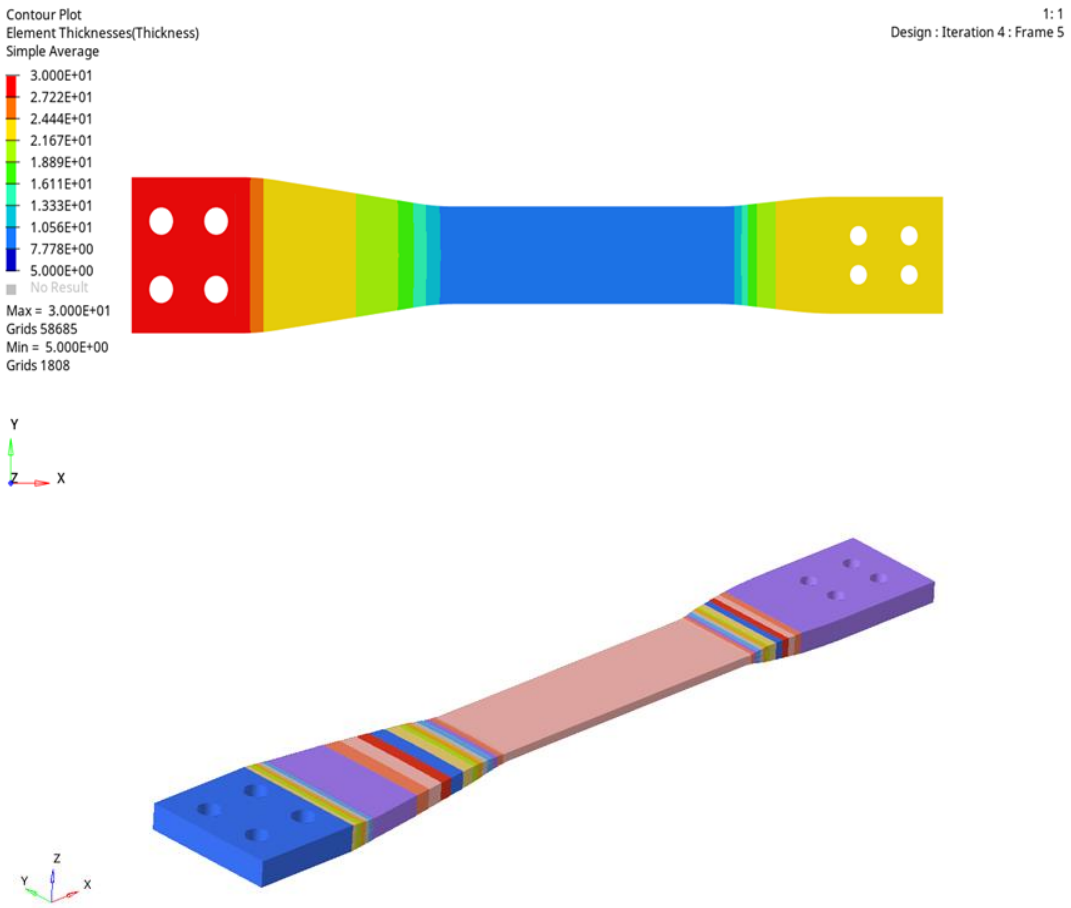

Figure 29. *Thickness distribution of flexbeam after optimization.*

In addition, the drop-off regions play a vital role in preventing any structural failures. It is crucial to verify that the constraints are being applied correctly during each shuffling

optimization step. Figure 30 confirms that the drop-off constraints have been accurately implemented in the spanwise direction.

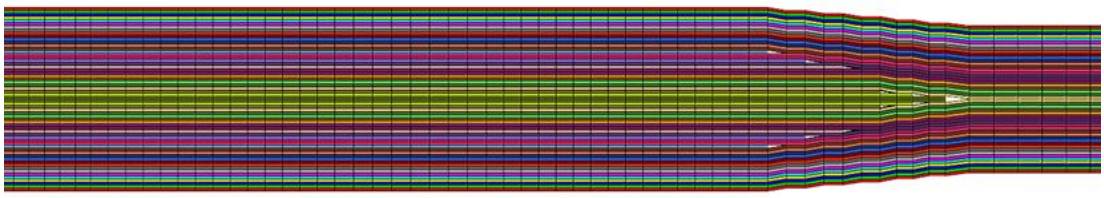

(a) Transition from HAR to ITR-2

(b) Transition from ITR to PR

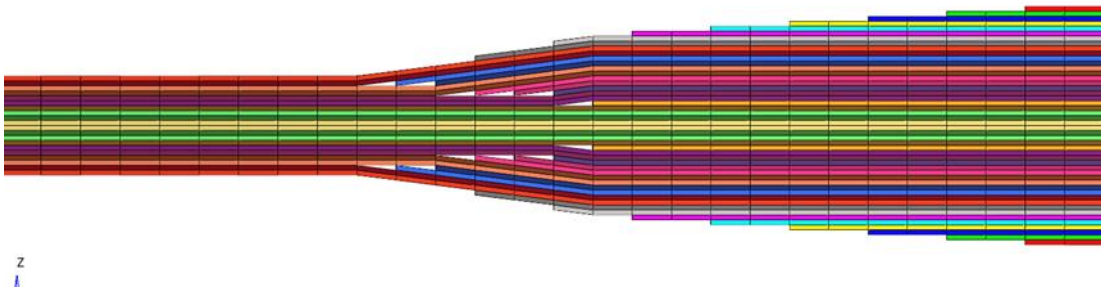

(c) Transition from PR to OTR and BAR

Figure 30. *The transition regions among the flexbeam after shuffling optimization*

As did in flexbeam optimization, similar steps will be followed also in torque tube optimization. The same steps that are followed with flexbeam is not extensively explained in that section in order to prevent any repetition. It is aimed to show the milestones that is specific to the torque tube design.

The torque tube's element and orientation thicknesses are depicted in Figure 31 after the free sizing optimization stage. The figure reveals that the maximum laminate thickness is 15.84 mm, whereas the lowest laminate thickness is 5 mm. The snubber region, particularly in the root area, has a significantly greater thickness than the functional portion of the torque tube, as anticipated. Furthermore, the bolted joint area has an insufficient thickness since it was not specified as a design space parameter for the solver. This decision was made to avoid a significant increase in solving time, and it will be analysed during the size optimization phase.

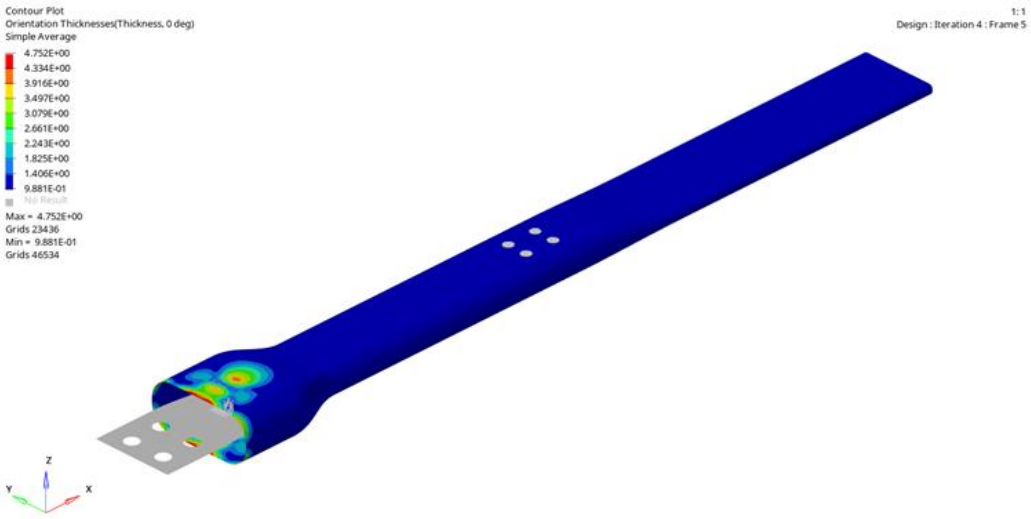

(a) 0° - 90° superply thickness output.

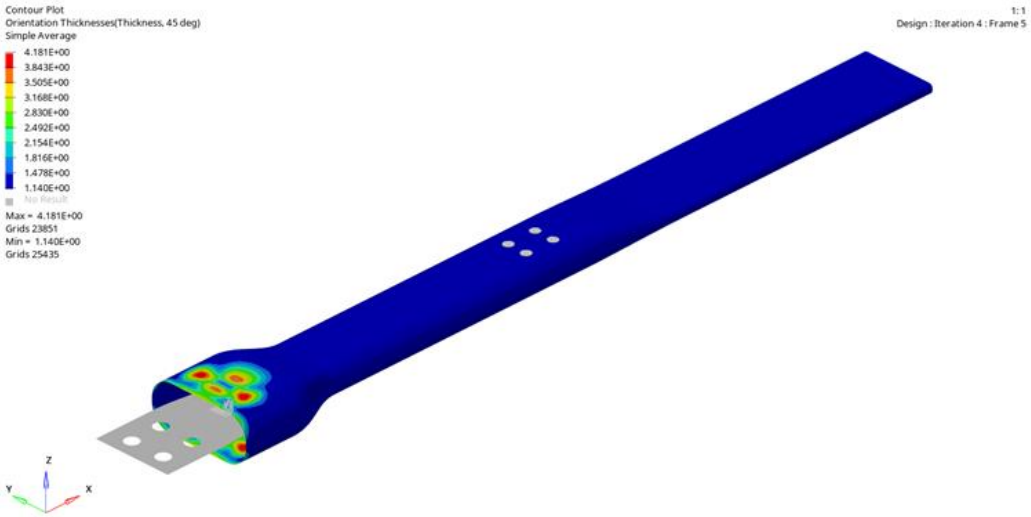

(b) ±45° superply thickness output.

Figure 31. *Torque Tube laminate and ply thickness output from free size optimization*

As indicated in flexbeam section, the number of 0° and 90° plies are equal to each other as well as +45° and -45° plies. After successfully passing the centrifugal load safety check, it was determined that the 45° and -45° plies are more influential than the 0° and 90° plies in improving the torque tube's torsional stiffness. The thickness of the 0° and 90° plies fluctuates between 4.752 mm and 0.988 mm, whereas the thickness of the 45° and -45° plies ranges from 4.181 mm to 1.140 mm. After performing the free size optimization, the overall shape and thickness distribution is shown in Figure 32.

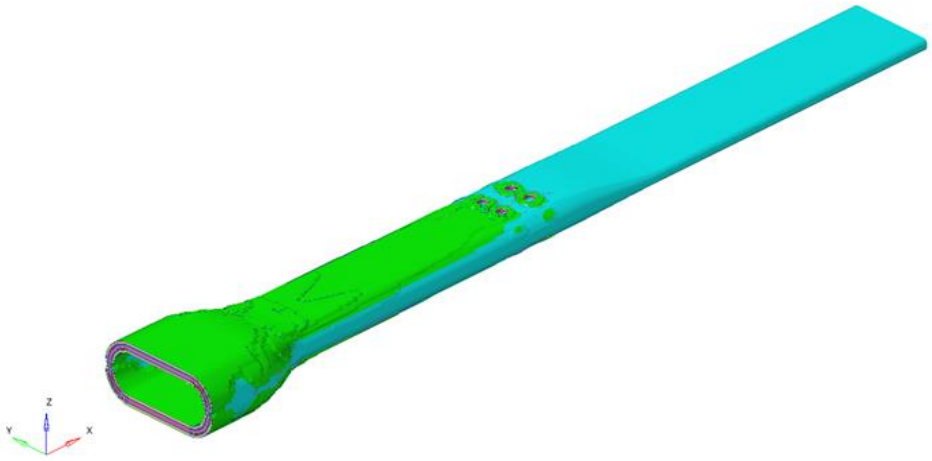

Figure 32. *Output of the free size optimization for torque tube.*

Based on the outcomes of the free size optimization, modifications were made to the shapes of certain plies, similar to the flexbeam optimization. This procedure was implemented for all the plies generated during the free size optimization, and a few of the changes are illustrated in Figure 33.

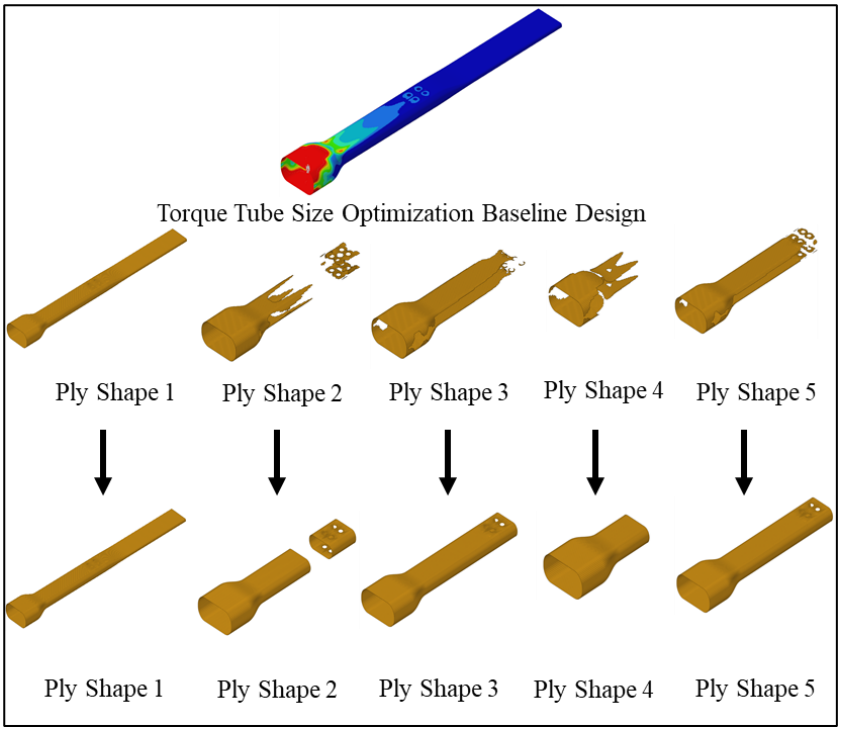

Figure 33. *Edition of torque tube ply shapes manually.*

The weight of the flexbeam was reduced from 17.41 kg to 7.627 kg after the free size optimization. Since a significant amount of material was removed from the structure, the compliance of the torque tube increased from 259634 mm/N to 502905 mm/N. However, even the stiffness of the structure is decreased, it remains still in the safe zone. Moreover, this is also another proof that the baseline design is overdesigned at the beginning, this was also proven with non-linear static analysis for baseline design. As did in flexbeam optimization, the transition between free size and size optimizations is possible with using FSTOSZ output control card. After performing size optimization with using the same design and manufacturing constrains that is used in flexbeam optimization, the results could be seen in Figure 34.

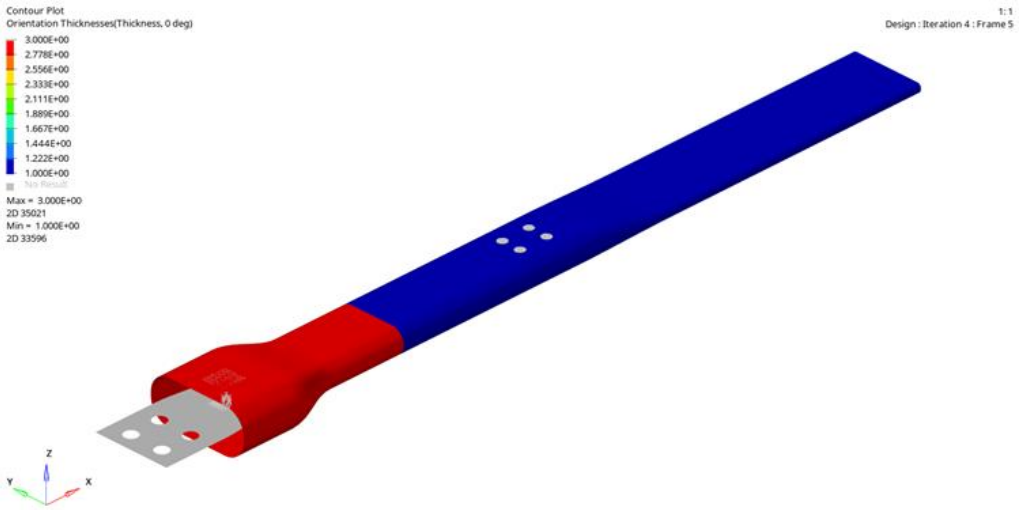

(a) 0° and 90° ply thickness distributions

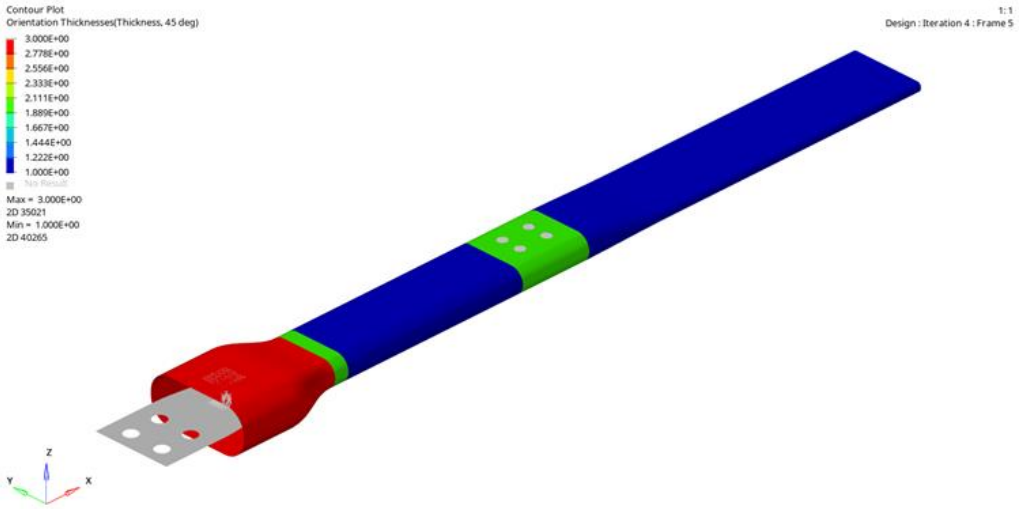

(b) 45° and -45° ply thickness distributions

Figure 34. *Ply thickness distributions after sizing optimization of torque tube.*

The weight of the torque tube decreased from 7.627 kg to 4.719 kg after the sizing optimization. Additionally, there was no significant stiffness alteration in the component, with a previous value of 502905 mm/N and a current value of 545233 mm/N. The final shape of the torque tube after the size optimization can be viewed in Figure 35.

Figure 35. *Output shape of torque tube after sizing optimization.*

The last checkpoint of the optimization process is again shuffling optimization. The shuffling optimization setup commences with the arrangement of successive plies and pairing plies. Once the shuffling optimization is complete, the solver automatically performs a non-linear static analysis of the torque tube, and the constraints are examined to ensure they meet the desired levels. The results of the shuffling optimization can be seen in Figure 36.

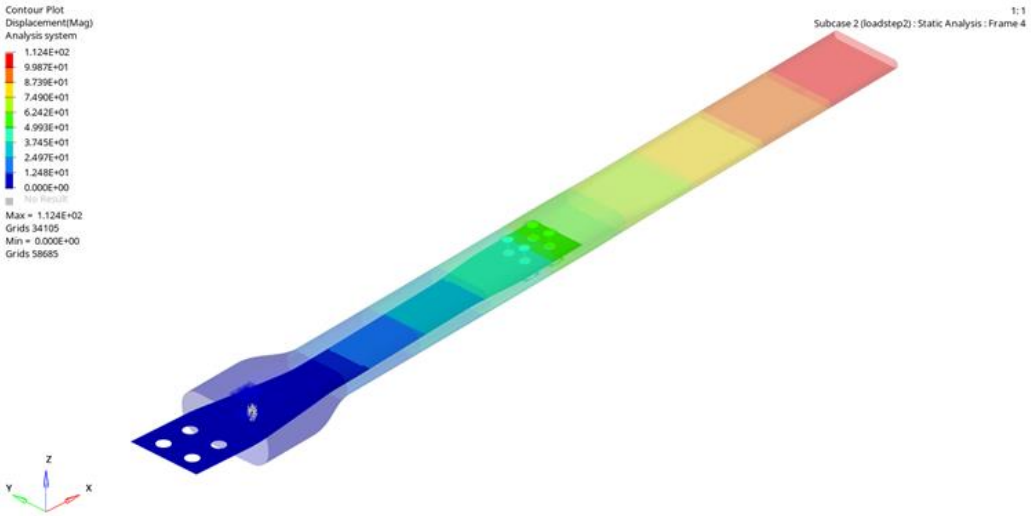

(a) Displacements.

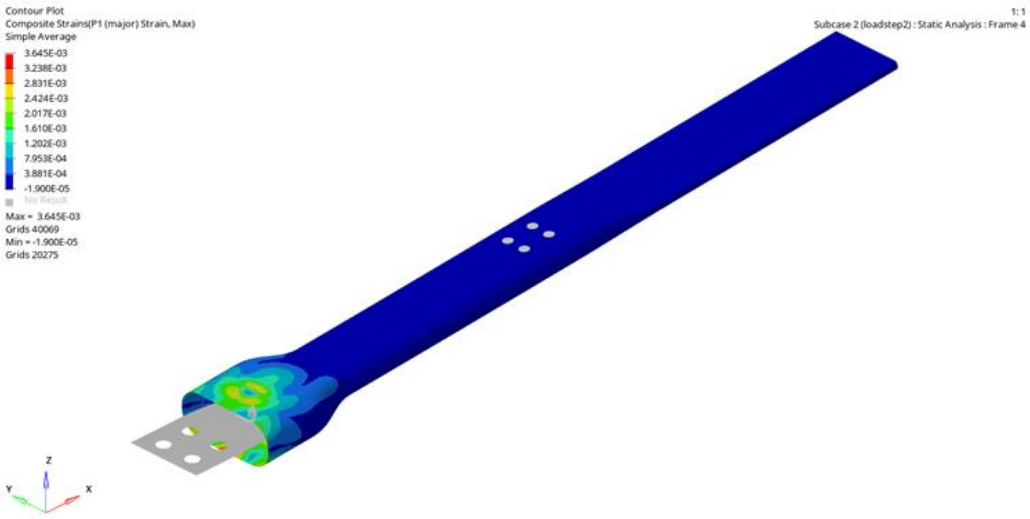

(b) Composite strains.

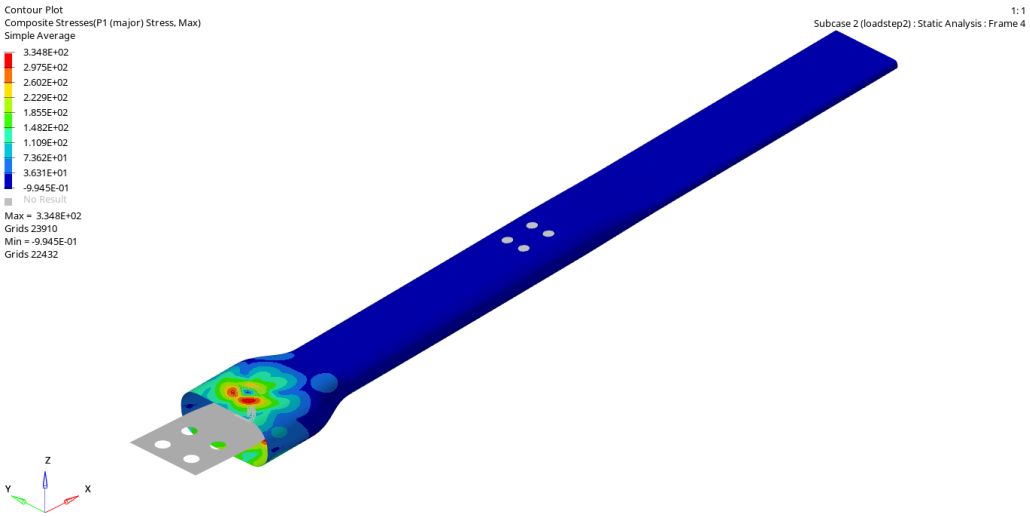

(c) Composite stresses.

Figure 36. *Displacements, composite strains and stresses after shuffling optimization of torque tube.*

The final weight of the torque tube structure is 4.802 kg after completion of the optimization. Although there is a minor weight increase in the structure due to the shuffling optimization constraints, it can be observed that most of the constraints have been satisfied. Additionally, the compliance has decreased from 545233 mm/N to 501270 mm/N. The final ply configuration for the root region, bolted joint region, and functional region are depicted in Figure 37, 38, and 39, respectively.

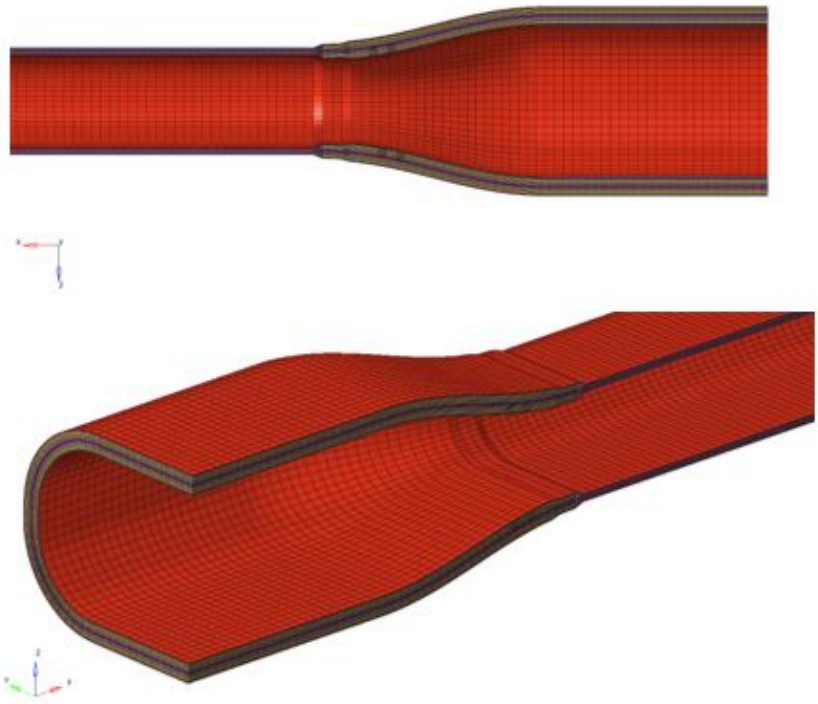

Figure 37. *Root region of optimized torque tube.*

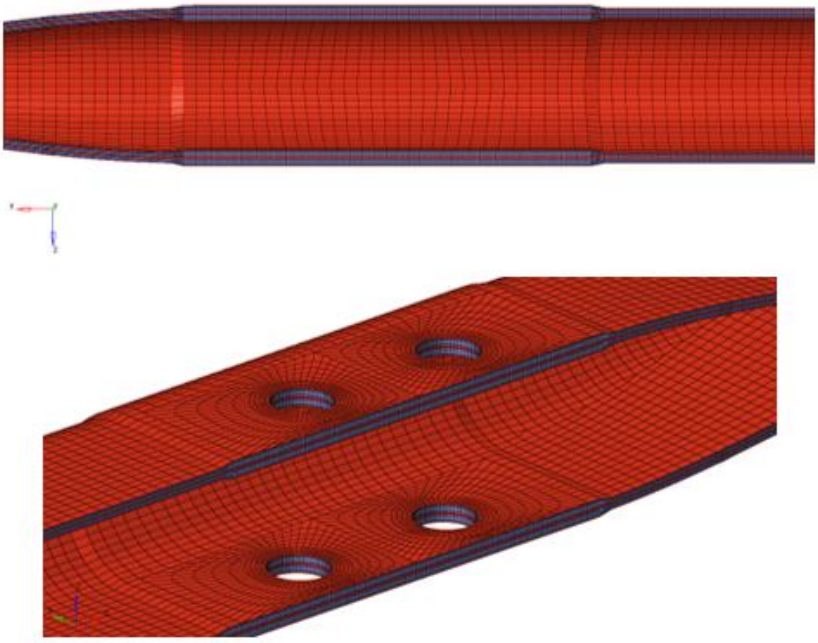

Figure 38. *Bolted joint region of optimized torque tube.*

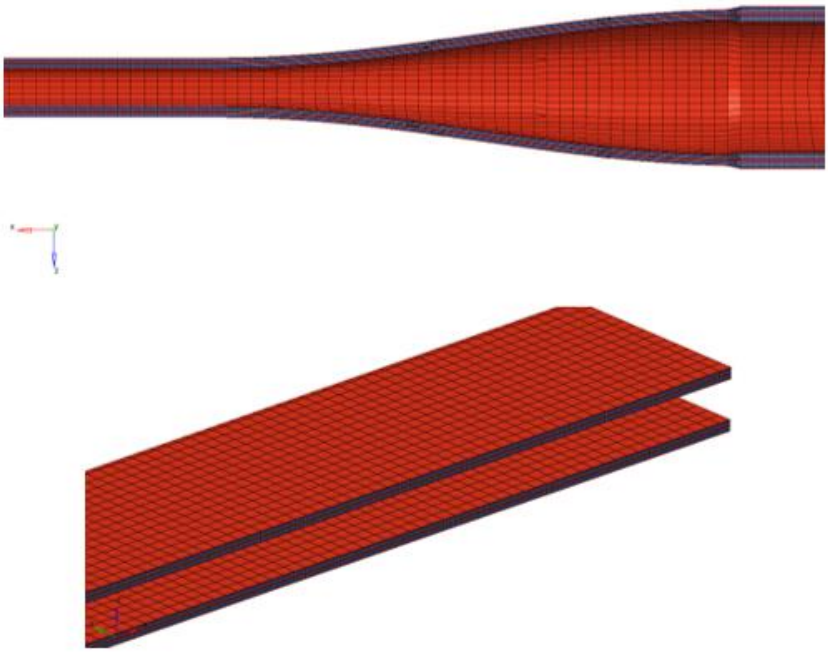

Figure 39. *Functional region of optimized torque tube.*

8. Conclusion

In this study, a comprehensive design and optimization process is performed for a bearingless tail rotor system considering the loads, stability and safety. Briefly, bearingless rotor system eliminates the usage of bearings, hinges and attachment links that are using in conventional articulated rotor systems.

With the optimization process, the overall weight of the entire bearingless rotor system is also reduced within a certain value. Three different optimization steps (free-size, size and shuffling) are performed for two primary structures which is flexbeam and torque tube. Both components are the heaviest components of the entire rotor structure, therefore these two components are targeted to optimize. After optimization, weight reduction of 60.35% for flexbeam and 72.43% for torque tube is achieved. Note that these are the weight reduction percentages compared to the baseline design and final design. The weight reduction comparison could also be performed after the free-size optimization to see efficiency of the further steps. This step is also required since the baseline design is prepared for an overdesign structure and comparing the weight reduction starting from baseline design could not be informative as intended. For flexbeam and torque tube, these values are 18% and 37%, respectively. In overall, including the weight savings from optimization and elimination of bearings, hinges and attachment links, the overall rotor structure becomes 23.08% lighter compared to the conventional articulated rotor systems.

Finally, bearingless rotor system development is closely following the advances on material science since usage of advanced materials allows to develop bearingless system. Therefore, with the developments of material science, the utilization of bearingless rotor systems in helicopters will find an enormous place in the future. Moreover, development of bearingless rotor systems influences also two trending industries; e-VTOL (Electrical Vertical Take-off and Landing) and VTOL (Vertical Take-off and Landing) because of the cost effectiveness and simplicity of the system in terms of design.

References

Bramwell, A. R. S., Done, G., Balmford, D., (2001). *Bramwell's helicopter dynamics*. Butterworth-Heinemann.

Brynes, F.E., D'Anna F.P. (1992). Flexbeam helicopter rotor with improved snubber-vibration damper between the torque tube and the flexible spar member. (Patent No. US005092738A). U.S. Patent and Trademark Office, 1-12.

Brynes, F.E., Federici, F.D., Schmaling, D.N. (1994a). Optimized composite Flexbeam for helicopter tail rotors (Patent No. US005690474A). U.S. Patent and Trademark Office, 1-19.

Brynes, F.E., Schmaling, D.N. (1994b). Spar-to-hub joint for a flexbeam helicopter rotor (Patent No. US005286167A). U.S. Patent and Trademark Office, 1-16.

Cheney Jr., M.C. (1976). Results of preliminary studies of a bearingless helicopter rotor concept. United Aircraft Research Laboratories, Connecticut, USA, 1-11.

Eckert, B. (2007). *Analytical and a numerical ground resonance analysis of a conventionally articulated main rotor helicopter* (Published Master's Thesis). Stellenbosch University, Stellenbosch, South Africa.

Emmerling, S., Kuntze-Fechner, G. The H145 bearingless main rotor – earnings of the H135 heritage. *45th European Rotorcraft Forum,* Warsaw, Poland, 1-13.

Goelke M. (2021). *Introduction to practical aspects of composites with Altair Optistruct*. Altair Engineering, Inc.

Hodges, D. H. (1990). A review of composite rotor blade modeling. *AIAA Journal, 28(3),* 561-565.

Ichihashi, T., Bandoh, S. (1992). Design, fabrication and testing of the composite bearingless rotor system for rotary-wing aircraft. *18th European Rotorcraft Forum*, Avignon, France, 1-14.

Johnson, W. (2013). *Rotorcraft aeromechanics*. Cambridge University Press.

Kim., D., Kim., S. (2014). The overview of KARI bearingless main rotor hub system. Korea Aerospace Research Institute (KARI), Daejeon, Korea, 1-12.

Klöppel, V., Huber, H., Enenkl, B. (1983). Development of bearingless tail rotors. Messerschmitt-Bölkow-Blohm GmbH, Munich, Germany, 1-14.

Mangalgiri, P. D. (1999). Composite materials for aerospace applications. *Bulletin of Materials Science, 22(3),* 657-664.

Narayana, K.S., Pranesh, B., Maiti, N.K. (1998), Dynamic validation of a stiff-in-plane bearingless tail rotor of advanced light helicopter. *24th European Rotorcraft Forum*, Marseilles, France, 1-10.

Xiaocheng, X. (1999). Random response analysis of pre-stressed structures using MSC/NASTRAN. *MSC Aerospace Users' Conference Proceedings*, 1-5.

Investigation of the Effect of Process and Design Parameters on the Mechanical Properties of PETG Materials Produced by Fused Deposition Modeling

Cem GÜDÜR[1]
Türker TÜRKOĞLU[2]
İlker EREN[3]

Additive Manufacturing (Additive Manufacturing) is a method of producing the desired part by adding layers on top of each other (Özer, 2020; Sezer, Eren, & Börklü, 2016). Today, there are many additive manufacturing methods and FDM (Fused Deposition Modelling) Method is one of them (Kaygusuz & Özerinç, 2018; Sezer et al., 2016). FDM 3D printers are the most widely used 3D printers due to their low cost, fast printing and easy accessibility (Evlen, 2019; Kamer, Yaykaşlı, Kaya, & Akay, 2022). It is possible to produce models with complex structures with FDM 3D Printers. FDM Technology is rapidly becoming widespread in many fields such as automotive, aerospace and aviation, biomedical engineering, and architectural structures (Kamer et al., 2022; Kaygusuz & Özerinç, 2018). In the FDM, thermoplastic materials called filaments wrapped around the spool are used. PLA (Polylactic Acid), ABS (Acrylonitrile Butadiene Styrene), PET-G (Polyethylene Terephthalate Glycol), PC (Polycarbonate) materials are used as filaments in FDM Technology. When the market research and literature review is conducted, it is seen that the filament diameters also vary (1.75 mm, 2.85 mm) (Başçı & Yamaoglu, 2021; Evlen, 2019). The filament to be used in the FDM Method is first placed in the extrusion head. Here, the filament, which liquefies with the help of a heater, easily passes through the nozzle and starts to form the first layer. After the filament passes through the nozzle, it cools and solidifies. When the layer is completed, the table part goes down as much as the layer thickness. This process continues until the desired part is formed. After the part is completed, it is separated from the table part and the support parts, if any, are cleaned and the part is finalized (Cano-Vicent et al., 2021).

In this study, PETG materials were successfully produced by FDM method under different design and manufacturing parameters. The effects of lattice structures and production parameters on the tensile test results were analysed. As a result of the findings, it was determined that both lattice designs and manufacturing parameters have a significant effect on mechanical properties.

Material and Method

In this study, samples in accordance with ISO 527 Standard were produced with PETG filament with a diameter of 1.75 mm. The PETG filament used is a filament compatible with FDM (Fused Deposition Modelling) Method. Ender 3 Pro was used as a 3D printer in the production of the samples and all samples were printed on the same printer. Ultimaker Cura

[1] Postgraduate Researcher, Balikesir University, Department of Mechanical Engineering
[2] Assistant Professor, Balikesir University, Department of Mechanical Engineering
[3] Assistant Professor, Balikesir University, Department of Mechanical Engineering

was used as the slicer programme in the production of the samples. Some parameters were kept constant for all samples in Ultimaker Cura Programme. Layer height (0.2 mm), nozzle (0.4 mm), table temperature (70 °C), support Status (Off), cooling fan (On), flow (100%) are the parameters kept constant in the Ultimaker Cura programme and these parameters are shown in Table 1.

After all adjustments were completed in the Ultimaker Cura Slicer Programme, G codes were created in the Ultimaker Cura Programme, transferred to the 3D Printer and printed. The printed samples were subjected to tensile test in ZwickRoell Z250 device. The tensile test was performed at a speed of 5 mm/s. All specimens were processed in the same tensile machine and at the same speed. The tensile machine used and the specimen produced are shown in the Figure 1.

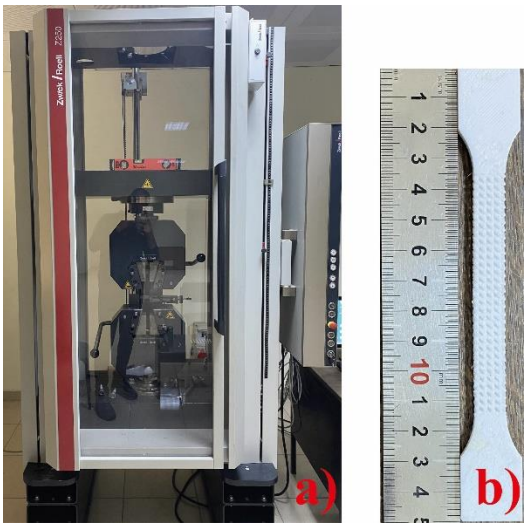

Figure 4. a) Tensile test machine b)Sample

Table 1. Fixed production conditions

Layer Height	0.2 mm
Nozzle	0.4 mm
Table Temperature	70 °C
Support Status	Off
Cooling Fan	On
Flow	100 %

Results and discussion

The sample numbers created for the experimental designs of PETG materials in the study are given in Table 2. Each factor consists of three levels. Lattice designs were differentiated as gyroid, lidinoid and schwarz. The production temperature varies between 230-240-250 °C and the production speed varies between 40-50-60 mm/s. All samples with different design and production parameters produced by the additive manufacturing process were manufactured according to the order specified in Table 2. The parameters selected in the study were found to be effective on the tensile strength determined as output.

***Table 2** Production parameters for PETG material*

Sample No.	Latis Structure	Temperature (°C)	Speed (mm/s)
1	Lidinoid	230	40
2	Schwarz	230	40
3	Lidinoid	250	40
4	Schwarz	250	40
5	Lidinoid	230	60
6	Schwarz	230	60
7	Lidinoid	250	60
8	Schwarz	250	60
9	Lidinoid	240	50
10	Schwarz	240	50
11	Diamond	230	50
12	Diamond	250	50
13	Diamond	240	40
14	Diamond	240	60
15	Diamond	240	50

Figure 2 shows the tensile test results of the specimens produced in the study. Data were collected on a graphical stress-strain scale. As a result of the comparison between the PETG samples produced by FDM, it was determined that the lattice design played a dominant role on the mechanical properties. While maximum tensile strength value was obtained in schwarz lattice design, minimum tensile strength value was determined in diamond lattice design. TPMS structures are diversified through their mathematical formulations and maximum properties can be obtained at optimum input values. Due to their exceptional properties, they have recently been applied in many fields. It is also known that the lattice structures are renowned for their excellent strength-to-weight ratio and capacity for absorbing energy. Inadequate design may result in serious engineering failures like crack growth. It is crucial to identify the ideal parameters before applying lattice structure. The lattice thickness values of the designs selected in the study were determined as 1 mm.

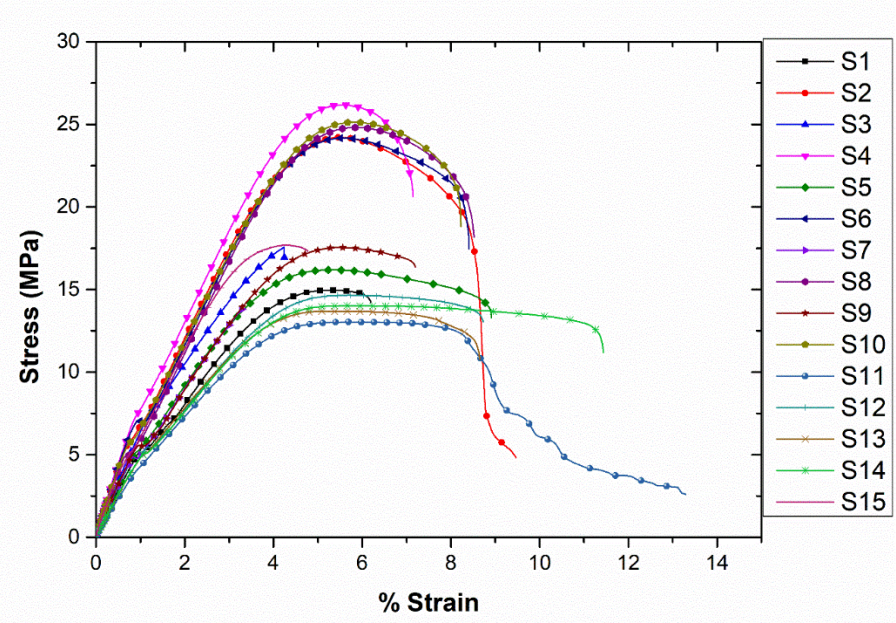

Figure 5 Tensile strength test data

PETG malzemeden farklı tasarım ve üretim parametreleri altında üretilmiş numunelerin çekme test sonuçlarına latis tasarımının yanı sıra üretim sıcaklığı ve üretim hızının da etkin olduğu belirlenmiştir.

Maximum tensile strength of specimens produced by FDM with schwarz lattice design, 250 °C (S4), which was produced at a production temperature of 240 °C and a production speed of 40 mm/s. In the tensile strength comparison, the second place was taken by specimen S10 (lattice design: schwarz, production temperature: 240 °C, production speed: 40 mm/s), while the third place was obtained from specimen S8 with schwarz lattice design, produced at a production temperature of 250 °C and a production speed of 60 mm/s. It can be seen that the schwarz structure is present in all of the combinations that give the maximum tensile strength.

The minimum tensile strength value obtained in the study was obtained from sample S11 with diamond lattice design, 230 °C production temperature and 50 mm/s production speed. This sample was followed by sample S13 (lattice design: diamond, production temperature: 240 °C, production speed: 40 mm/s) and sample S7 (lattice design: diamond, production temperature: 250 °C, production speed: 60 mm/s). It was found that the lowest tensile strength values of the specimens produced by FDM method were obtained from the specimens produced using diamond lattice design. Higher temperatures are believed to improve layer cohesion and, as a result, increase the mechanical properties of materials. The maximum tensile strength value was obtained at a production temperature of 250 °C. In accordance with the literature, the positive effect of relatively high temperatures on tensile strength was also reported in the study of Pang et al. (Pang, Lai, Ismail, & Yap, 2022).

Conclusions

In this study, PETG materials were successfully produced by FDM method under the specified production parameters. No manufacturing defects were detected in post-production visual inspections. Weight reduction was achieved by applying lattice structures in the sample design. The production parameters with the highest tensile strength were determined as schwarz lattice design, 250 °C production temperature and 40 mm/s production speed. It was reported that the highest tensile strength values were obtained with the Schwarz lattice structure. It was observed that the production temperature was effective on the tensile strength and 250 °C represents the production temperature at which the maximum tensile strength was obtained.

References

Başçı, G., & Yamaoglu, R. (2021). Yeni Nesi Üretim Teknolojisi: FDM ile Eklemeli İmalat. *INTERNATIONAL JOURNAL OF 3D PRINTING TECHNOLOGIES AND DIGITAL INDUSTRY*, 5(2), 339–352. Retrieved from https://doi.org/10.46519/ij3dptdi.838281

Cano-Vicent, A., Tambuwala, M. M., Hassan, S. S., Barh, D., Aljabali, A. A. A., Birkett, M., … Serrano-Aroca, Á. (2021). Fused deposition modelling: Current status, methodology, applications and future prospects. *Additive Manufacturing*, 47(August). Retrieved from https://doi.org/10.1016/j.addma.2021.102378

Evlen, H. (2019). Doluluk Oranının 3B Yazıcıda Üretilen TPU ve TPE Numunelerinin Mekanik Özellikleri Üzerine Etkilerinin İncelenmesi Investigation of the Effect of Infill Rate on Mechanical Properties of TPU and TPE Specimens Produced in 3D Printer. *DEUFMD*, 21(63), 793–804. Retrieved from https://doi.org/10.21205/deufmd.2019216310

Kamer, M. S., Yaykaşlı, H., Kaya, A., & Akay, O. E. (2022). Comparison of mechanical properties of tensile test specimens produced with ABS and PLA material at different printing speeds in 3D printer 3B yazıcıda farklı yazdırma hızlarında ABS ve PLA malzeme ile üretilen çekme test numunelerinin mekanik özellikleri. *Journal of the Faculty of Engineering and Architecture of Gazi University*, 3, 1197–1211. Retrieved from https://doi.org/10.17341/gazimmfd.961981

Kaygusuz, B., & Özerinç, S. (2018). 3 Boyutlu Yazıcı ile Üretilen PLA Bazlı Yapıların Mekanik Özelliklerinin İncelenmesi. *MAKİNA TASARIM VE İMALAT DERGİSİ*, 16(1), 1–6.

Özer, G. (2020). Eklemeli üretim teknoloj ileri üzerine bir derleme. *Nigde Omer Halisdemir University Journal of Engineering Sciences*, 9(1), 606–621. Retrieved from https://doi.org/10.28948/ngumuh.626011

Pang, R., Lai, M. K., Ismail, K. I., & Yap, T. C. (2022). The Effect of Printing Temperature on Bonding Quality and Tensile Properties of Fused Deposition Modelling 3d-Printed Parts. *IOP Conference Series: Materials Science and Engineering*, 1257(1), 012031. Retrieved from https://doi.org/10.1088/1757-899x/1257/1/012031

Sezer, K., Eren, O., & Börklü, R. (2016). Carbon Fiber Reinforced ABS Filament Manufacturing and Investigation of Mechanical Properties and Investigation of Mechanical Properties. In *1. 3B BASKI TEKNOLOJİLERİ ULUSLARARASI SEMPOZYUMU (3B-BTS2016)* (p. 12).

Investigation of Enhancing Energy Absorption in Aerospace Applications through Gradient Lattice Structures

Erkan TUR[1]

Introduction

The significance of energy absorption in aerospace contexts is of utmost importance and cannot be overemphasized. The research focus on the development of materials and structures with superior energy absorption properties has become crucial due to the increasing demands for safety, efficiency, and performance. The present article offers a comprehensive exploration of the augmentation of energy absorption in aerospace contexts through the utilization of gradient lattice structures. Over the course of numerous decades, the aerospace sector has been at the forefront of investigating novel materials and structures in order to satisfy progressively rigorous safety and performance standards. The process of energy absorption holds significant importance in various situations such as crashworthiness and debris impact, as it serves as a crucial protective mechanism. The utilization of materials and structures with efficient energy absorption capabilities can significantly impact the outcome of a situation, potentially preventing catastrophic failure and enabling controlled damage mitigation. affecting not only structural integrity but also passenger safety and survivability (Suresh, 2001). The present materials utilized in aerospace applications, for instance, aluminum and carbon-fiber composites, have conferred considerable enhancements in performance, however, their capacity to absorb energy is restricted. In order to address these constraints and achieve improved energy absorption, the industrial sector has initiated an investigation into novel categories of material configurations. Among these, gradient lattice structures have exhibited significant promise. Functionally graded lattice structures, commonly referred to as gradient lattice structures, exhibit micro-architectures that vary spatially, resulting in mechanical properties that are superior to those of uniform lattice structures. These objects are designed with a continuous variation in both structural and material properties, which facilitates a more effective distribution of stress, resulting in heightened energy absorption. The efficacy of gradient lattice structures is derived from their distinctive characteristic of customizing material dispersion within the structure, thereby enabling them to efficiently regulate energy absorption. The aforementioned characteristic renders them exceedingly appropriate for aerospace applications wherein weight efficiency is of utmost importance, and energy absorption prerequisites can exhibit substantial variations throughout the structure (Rahman et. al., 2021).

This study aims to delve deeper into the aforementioned potential. The objective of our investigation is to establish a thorough comprehension of the techniques employed to manipulate and optimize the characteristics of gradient lattice structures in order to achieve maximum energy absorption in aerospace contexts. The objective of our study is not solely to establish the efficacy of gradient lattice structures, but also to furnish pragmatic recommendations for their design and implementation in the aerospace sector. The study conducted by Xu and colleagues in 2022. The present study employs a combination of theoretical and experimental approaches, complemented by sophisticated computational simulations, to enhance our comprehension of the energy absorption potential of gradient lattice structures. This study explores the material science aspects of these structures, including their

[1] Erkan Tur, Middle East Technical University, Department of Natural and Applied Sciences, Orcid: 0000-0002-3764-2184

mechanical properties, and evaluates the influence of various design parameters on their energy absorption capacity. The research endeavors to offer a novel viewpoint on the augmentation of energy absorption in aerospace contexts. Through the utilization of gradient lattice structures, we anticipate a forthcoming era in which aerospace structures can endure severe circumstances and collisions with improved durability and security. The present article commences by providing an overview of the existing knowledge regarding energy absorption in aerospace contexts, as well as the constraints of current materials and structures. Subsequently, a comprehensive exposition of gradient lattice structures is presented, encompassing their distinctive characteristics and elucidating their potential as a viable option for augmenting energy absorption. Subsequently, we explicate the methodology employed in our inquiry, succeeded by the exposition and discourse of our discoveries. Ultimately, our study culminates in the presentation of our findings and subsequent recommendations for potential avenues of inquiry. The escalating requirements for aerospace performance and safety have intensified the necessity for structures that possess exceptional energy absorption properties. The study of gradient lattice structures presents a viable solution for addressing this requirement, with the potential to transform the landscape of aerospace design and engineering. We extend an invitation to participate in our endeavor to investigate and discover resolutions that surpass the existing limitations in aerospace implementations.

Methodology

The present investigation utilized a comprehensive computational approach, employing the ABAQUS Finite Element Analysis (FEA) software, to examine the energy absorption capacity of gradient lattice structures in the context of aerospace applications. The investigation of the distinctive characteristics of said structures and their influence on energy absorption was conducted via meticulous computational modeling, facilitating the attainment of a comprehensive comprehension of their performance across diverse scenarios (Xiao and Song, 2018).

Uniform Lattice Structures:

Homogeneous lattice structures, commonly referred to as uniform lattice structures, are composed of a recurring pattern of a solitary unit cell throughout the entirety of the structure. The structures exhibit uniform characteristics across their entirety, indicating that each unit cell within the structure possesses identical material properties and geometry. The entities in question may exhibit either a two-dimensional or three-dimensional nature, and their geometric arrangement may manifest in a diverse array of forms, such as cubic, tetrahedral, and octahedral, among other possibilities. The utilization of these structures has been extensive across diverse applications owing to their lightweight properties and their capacity to endure various forms of loading. Hollow structures are highly desirable in weight-sensitive fields like aerospace due to their superior stiffness-to-weight and strength-to-weight ratios when compared to solid structures. Uniform lattice structures exhibit certain limitations with respect to their energy absorption capabilities, particularly when subjected to non-uniform stress distributions or high-impact scenarios. (Seharing et. al., 2020).

Gradient Lattice Structures:

Functionally graded lattice structures, commonly referred to as gradient lattice structures, exhibit distinct characteristics from uniform lattice structures due to their spatially varying properties throughout the structure. It is possible to regulate the diversity of characteristics to conform to a specific gradient profile, such as linear, exponential, or sinusoidal. This regulation may encompass modifications in the geometry of the unit cells, the material properties, or both.

The implementation of functional grading in properties enables gradient lattice structures to exhibit superior stress distribution management capabilities in comparison to their uniform lattice structure counterparts. Structures can be engineered to effectively manage stress distribution by strategically directing it towards regions with greater strength or away from critical areas. This approach can result in superior structural performance and increased capacity for energy absorption. The ability to customize the distribution of materials within the structure enables gradient lattice structures to effectively conform to particular loading circumstances. Moreover, the utilization of functional grading renders gradient lattice structures highly advantageous for aerospace applications, wherein the energy absorption prerequisites can exhibit substantial variations across the structure. Efficient energy absorption and dissipation are essential in various applications, especially in situations that involve crashworthiness and debris impact. The complexity of designing and manufacturing gradient lattice structures is comparatively higher than that of uniform lattice structures, owing to the presence of spatially varying properties (Bai et. al., 2020)

To summarize, although uniform and gradient lattice structures possess their respective merits, gradient lattice structures exhibit superior capabilities in managing stress distribution and energy absorption, rendering them highly promising for advanced applications such as aerospace.

Modeling and Simulation of Gradient Lattice Structures:

The first step in our methodology involved creating detailed 3D models of the gradient lattice structures using ABAQUS/CAE. (Alaña et. al., 2021) Our models incorporated functionally graded micro-architectures, allowing for continuous variation in structural and material properties. As the lattice design, FCC was considered as unit cell. The lattice structures were designed with different gradient profiles, such as linear, exponential, and sinusoidal, varying in properties like density and modulus (Al-Qrimli et. al., 2015).

Figure 1 – FCC Unit Cell

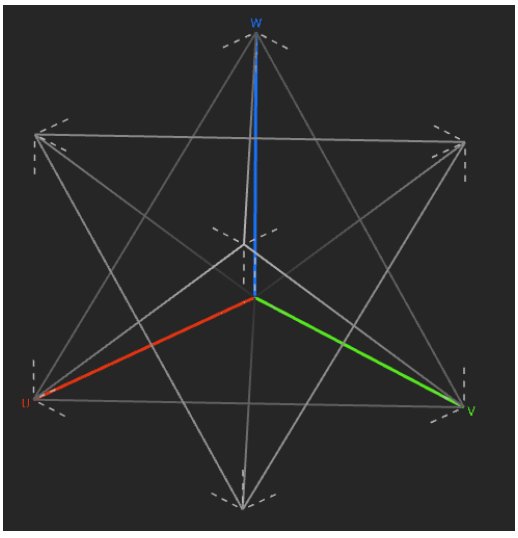

Table 1 – Strut size and cell sizes

Cubic Unit Cell Size, μm	Strut Dimensions			
	Diameter	Strut Angles	Strut Length	Strut Design
24.8 x 24.8 x 24.8	5 μm	45^o	17.54 μm	FCC

Figure 2 – All Direct and All Principal Conditions

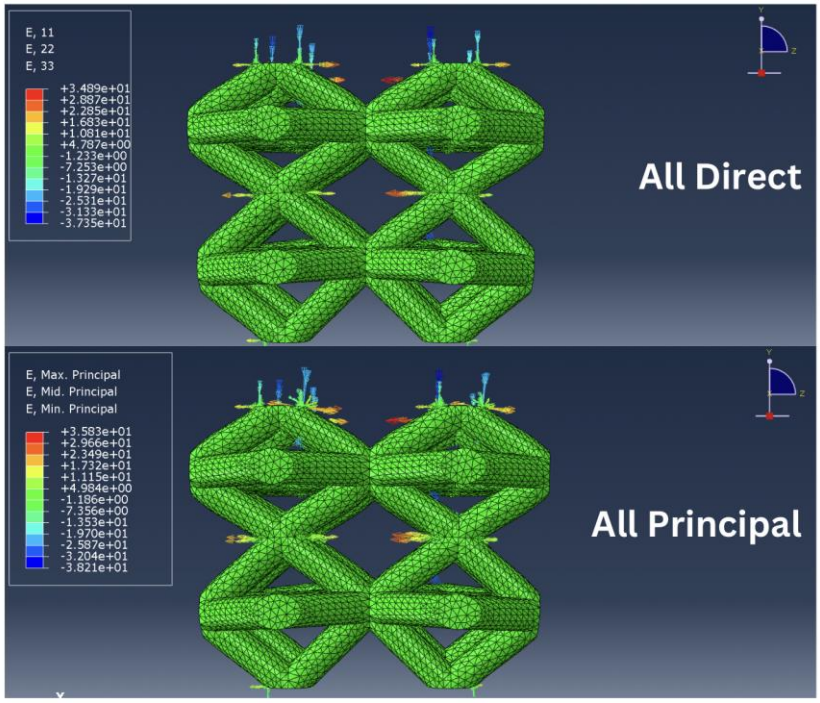

Material properties for the models were defined based on the aerospace-grade materials used in the industry. We made use of user-defined material subroutines in ABAQUS (UMAT and VUMAT) for defining the functionally graded material properties (Alwattar et. al., 2019).

Zable 2 – Materials Properties

Material	Plastic Properties		Elastic Properties	
	Young's Modulus E (GPa)	Tensile Yield Strength (MPa)	Poisson Ratio, v	Plastic Strain, ε_p
ABS	0.862	33.33	0.35	0.045

Load Application and Boundary Conditions:

In order to replicate real-life aerospace scenarios, our models were exposed to diverse loading and boundary conditions, with a particular emphasis on compressive forces. The load application was developed with the purpose of emulating various scenarios that a structure could potentially face in an aerospace environment, including but not limited to, collision, debris impact, and high-velocity projectile impact. The aforementioned procedure facilitated the evaluation of the energy absorption properties of the lattice structures across a wide range of circumstances.

Analysis Type:

The FEA simulations were run using static structural (ABAQUS/Standard) solvers, depending upon the nature of loading conditions. The static analysis provided insights into the deformation and stress distribution under slow, quasi-static loadings.

Energy Absorption Calculation:

The energy absorption of the lattice structures was calculated by integrating the area under the stress-strain curve obtained from the simulation results. We made use of ABAQUS' capability to track the energy quantities (like internal, kinetic, and strain energy) throughout the simulation. This facilitated the calculation of energy absorption and understanding the energy distribution within the lattice structure. In SI unit system, total energy absorption (tea), is calculated in kilojoules, Specific energy absorption has the unit kJ/kg and volumetric energy absorption unit is kg/m^3 (Al-Qrimli et. al., 2015).

Table 3 – Energy Absorption Equations

Total Energy Absorption	Specific Energy Absorption	Volumetric Energy Absorption
$tea = \int P_{av} \equiv P_{av} * (d_f - d_i)$	$sea = \frac{tea}{mass}$	$vea = \frac{tea}{volume}$

Parameter Study:

In addition, our research encompassed a comprehensive examination of parameters. The study involved the manipulation of crucial design parameters, including the unit cell configuration, gradient distribution, strut width, and material characteristics. This study facilitated comprehension of the impact of said parameters on the energy absorption capacities of gradient lattice structures. Through the utilization of ABAQUS software, our research conducted a thorough and meticulous evaluation of the viability of gradient lattice structures in augmenting energy absorption within the realm of aerospace. The utilization of numerical simulations has facilitated the resolution of fabrication and testing constraints, thereby providing an opportunity to assess the efficacy of complex gradient lattice structures that would have been arduous to produce or experimentally examine.

Results and Discussion

The study employed a thorough methodology that utilized the ABAQUS Finite Element Analysis software to investigate the energy absorption capacity of gradient lattice structures in the context of aerospace applications. The findings of the study were enlightening. The simulation outcomes obtained from ABAQUS demonstrated significant dissimilarities in energy dissipation capabilities between gradient lattice configurations and their uniform equivalents. The energy absorption capabilities of gradient lattice structures were found to be consistently superior under different loading and boundary conditions.

The stress distribution in gradient lattice structures was found to be more homogeneous than that in uniform lattice structures under quasi-static loading. Consequently, there was an increase in energy dissipation effectiveness and improved deformation control, leading to a corresponding enhancement in energy absorption. The simulations conducted indicated that lattice structures with gradients exhibited enhanced energy absorption capabilities. The deformation modes exhibited by the object were distinct and capable of efficiently absorbing compressive energy, indicating potential for averting disastrous outcomes in the event of such scenarios, particularly under varying flight loads. The investigation of parameters revealed the impact of the configuration of the unit cell, the gradient profile, and the thickness of the strut on the capacity for energy absorption. The utilization of an exponential gradient profile in the design of the face centered cubic unit cell resulted in the highest level of energy absorption

when compared to the uniform FCC model variants that were subjected to testing. The aforementioned results hold significant value in the context of developing and enhancing gradient lattice configurations intended for employment in the aerospace sector.

Figure 3 – Stress Strain Graphs for Simulation Results

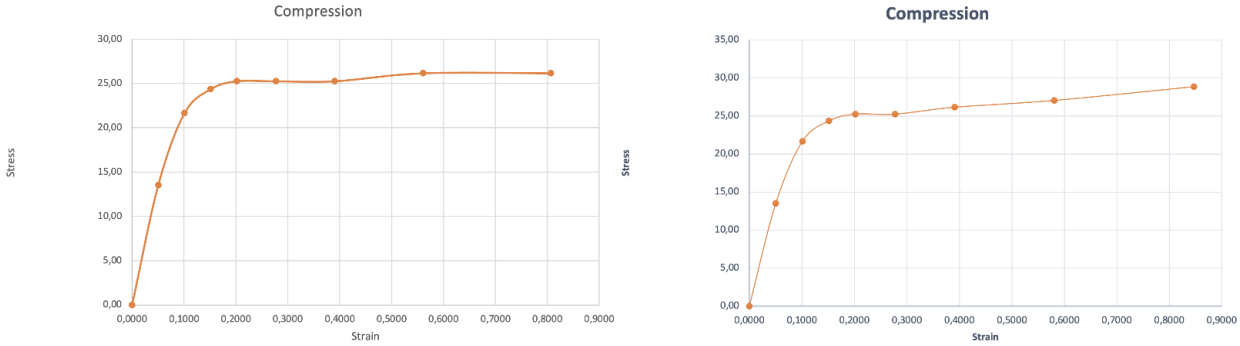

Figure 4 – AC Yield Results

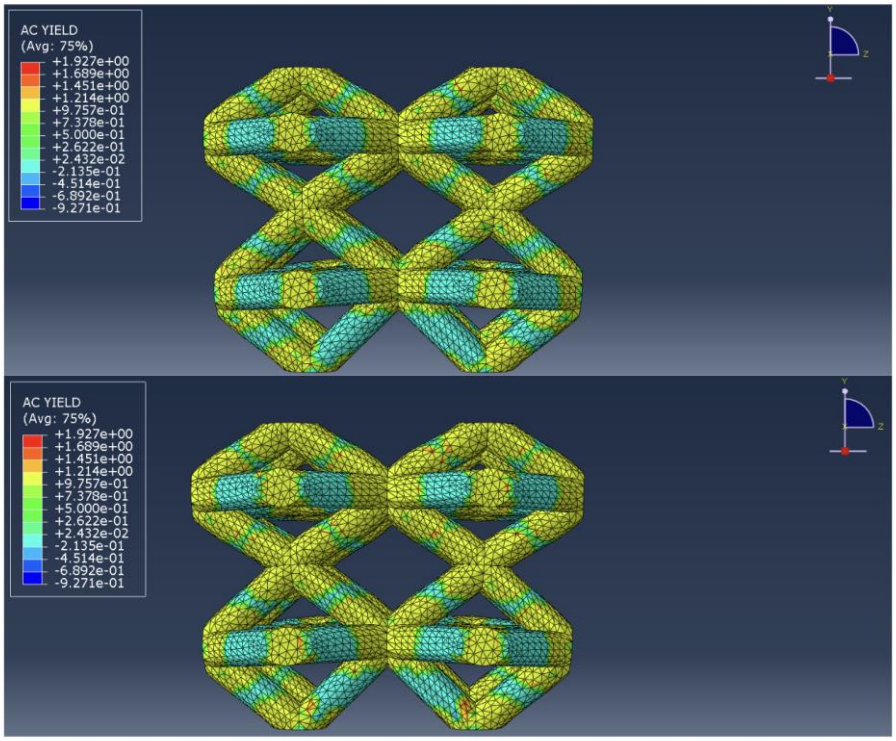

Figure 5 – Results for Tresca Criterion (Stress)

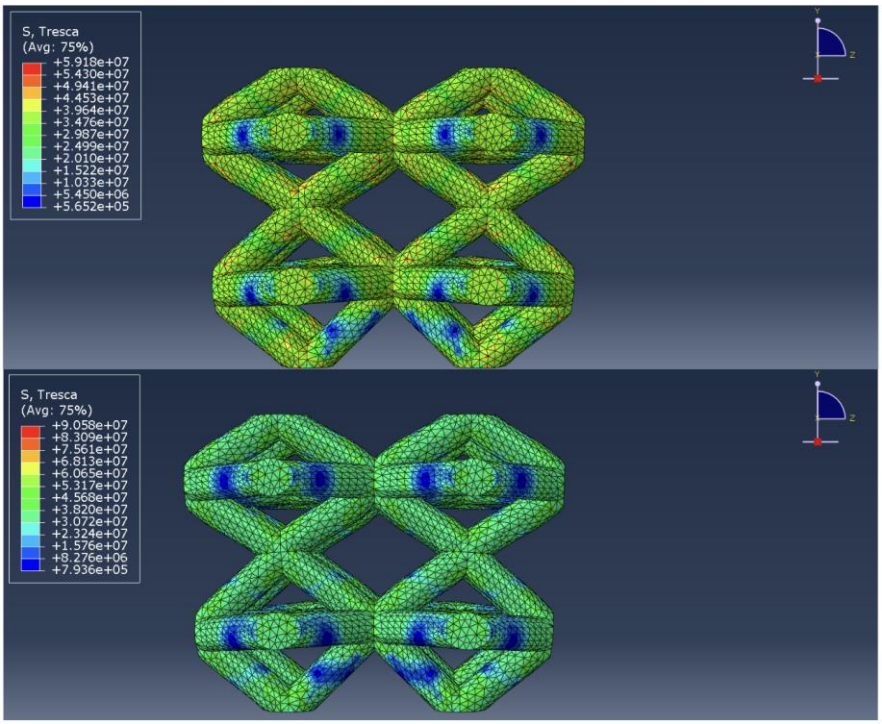

Figure 6 – Results for von Mises (Stress)

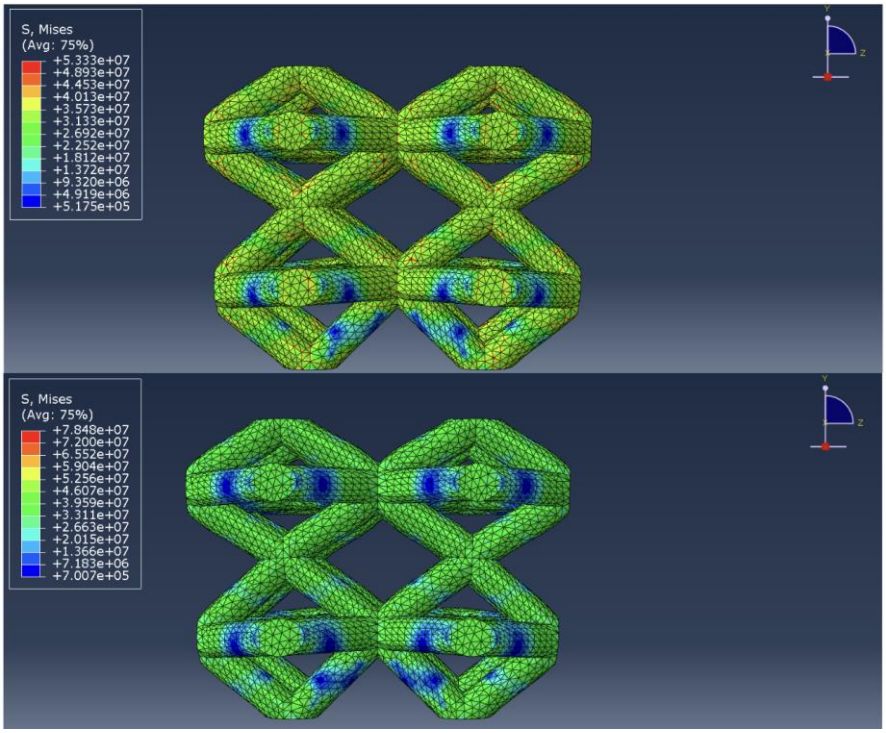

Figure 7 – Results of Resultant Displacement, by Magnitude

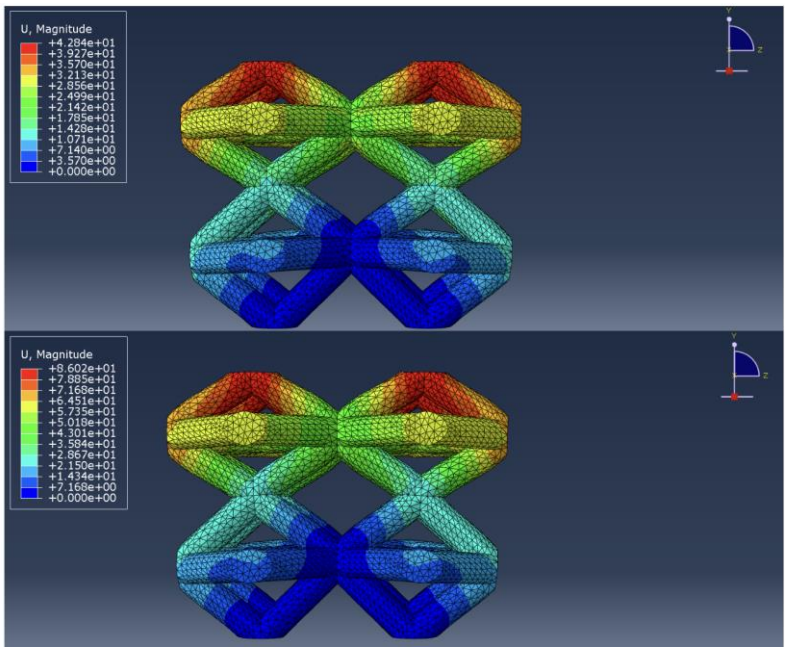

The study employed a thorough methodology that utilized the ABAQUS Finite Element Analysis software to investigate the energy absorption capacity of gradient lattice structures in the field of aerospace. The findings were enlightening. The simulation outcomes obtained from ABAQUS demonstrated significant dissimilarities in energy absorption between gradient lattice structures and their uniform equivalents. The energy absorption capabilities of gradient lattice structures were found to be consistently superior under different loading and boundary conditions.

The enhanced capacity of gradient lattice structures to absorb energy can be ascribed to their micro-architecture that is functionally graded. This distinctive characteristic facilitates a heightened efficacy in the dispersion of stress, resulting in proficient dissipation of energy and improved management of deformation. In addition, the capacity of materials to absorb energy can be enhanced by tailoring the distribution of material within their structure. This provides them with a competitive advantage over uniform lattice structures. The simulations conducted on high-speed impacts were highly informative, demonstrating the efficacy of gradient lattice structures in efficiently absorbing impact energy. This attribute holds significant importance in the aerospace industry. The capacity of these structures to withstand extreme loading conditions highlights their potential to augment safety protocols in aerospace contexts. The conducted parameter study yielded significant findings regarding the optimization of energy absorption through the manipulation of design parameters. The aforementioned results can be utilized to direct the formation and enhancement of gradient lattice configurations in the context of aerospace implementations, thereby facilitating the creation of aerospace structures that are both more secure and more effective.

In brief, the outcomes of our study furnish convincing proof endorsing the utilization of gradient lattice configurations in aerospace sectors to augment energy absorption. The study highlights the superior energy absorption capabilities of gradient lattice structures compared to conventional uniform lattice structures, thereby advocating for their integration into forthcoming aerospace design and manufacturing methodologies. Nevertheless, additional investigation is required to thoroughly examine their capabilities and to establish feasible techniques for their integration in practical aerospace scenarios.

REFERENCES

Al-Qrimli, H. F. A., Khalid, K. S., & Mahdi, F. A. (2015). The effect of cone angle on composite tubes subjected to axial loading. British Journal of Applied Science and Technology, 7(4), 351-363.

Alaña, M., Cutolo, A., Ruiz de Galarreta, S., & Van Hooreweder, B. (2021). Influence of relative density on quasi-static and fatigue failure of lattice structures in Ti6Al4V produced by laser powder bed fusion. Scientific Reports, 11(1), 19314.

Alwattar, T. A., & Mian, A. (2019). Development of an elastic material model for BCC lattice cell structures using finite element analysis and neural networks approaches. Journal of composites science, 3(2), 33.

Bai, L., Gong, C., Chen, X., Sun, Y., Xin, L., Pu, H., ... & Luo, J. (2020). Mechanical properties and energy absorption capabilities of functionally graded lattice structures: Experiments and simulations. International Journal of Mechanical Sciences, 182, 105735.

Rahman, H., Yarali, E., Zolfagharian, A., Serjouei, A., & Bodaghi, M. (2021). Energy absorption and mechanical performance of functionally graded soft–hard lattice structures. Materials, 14(6), 1366.

Seharing, A., Azman, A. H., & Abdullah, S. (2020). A review on integration of lightweight gradient lattice structures in additive manufacturing parts. Advances in Mechanical Engineering, 12(6), 1687814020916951.

Suresh, S. (2001). Graded Materials for Resistance to Contact Deformation and Damage. Science, 292(5526), 2447-2451.

Xiao, L., & Song, W. (2018). Additively-manufactured functionally graded Ti-6Al-4V lattice structures with high strength under static and dynamic loading: Experiments. International Journal of Impact Engineering, 111, 255-272.

Xu, Z., Razavi, S. M. J., & Ayatollahi, M. R. (2022). 00019 Functionally Graded Lattice Structures: Fabrication Methods, Mechanical Properties, Failure Mechanisms and Applications. International Journal of Impact Engineering, 125, 163-172.

Current Debates on Natural and Engineering Sciences

9